The Phase-Averaged Velocity Measurement and the Estimation of Pressure Force of a Periodically Moving Body

August 2011

Alexandre Suryadi

A Thesis for the Degree of Ph.D. in Engineering

The Phase-Averaged Velocity Measurement and the Estimation of Pressure Force of a Periodically Moving Body

August 2011

Graduate School of Science and Technology
Keio University

Alexandre Suryadi

DISSERTATION

Submitted to the School of Science for Open and Environmental Systems, Keio University, in partial fulfillment of the requirements for the degree of Doctor of Philosophy

Acknowledgment

This research has been financially supported by the Japanese government (Monbukagakusho) scholarship and by the Keio Leading-Edge Laboratory of Science and Technology, Research Grant.

I am truly grateful to my supervisor Professor Shinnosuke Obi for allowing me to take on this project and supporting me throughout my graduate studies with his advice and encouragement. His support has been very important to the completion of the present thesis. I would also like to express my gratitude to Professor Toshihisa Ueda, Professor Koji Fukagata, and Professor Kenjiro Takemura for their constructive comments.

I would like to thank the members of Masuda-Obi Laboratory and Obi-Fukagata Laboratory for making life in Japan more enjoyable. In particular, I would like to thank Dr. Yoshitsugu Naka who helped me in troubleshooting the experiment device problems and to Ms. Hui Jing for discussion of any topics.

I would also like to thank my friends, who came to this university from overseas, for sharing their experience in living in Japan.

Finally, I would like to thank my family who have supported me all the time.

Abstract

Motivated to engineer micro-air vehicles, the relationship of the vorticity distribution with force generated by a flapping rigid plate was investigated with stereo particle image velocimetry. Measurements were conducted under the hovering condition with a flapping rigid plate for the wing model and a sinusoidal function as the flapping motion. The full deformation tensor was obtained by measuring the velocity vectors at three measurement planes offset in the out-of-plane direction. The unsteady state of the flow was resolved by phase averaging. Thus, the governing equations were decomposed into the average and fluctuation terms.

Vortex structures were identified using the second invariant of the deformation tensor and two-dimensional streamlines. Control volume analysis shows the interaction of the vortex structures with the flapping plate as represented by the force acting on the control volume. There is a phase difference between the generated force and flapping motion for all the measured sections of the plate. Maximum force is generated when the plate is at the start of either upstroke or downstroke, ie. the flapping motion is at low velocity. On the leading edge, the unsteady term of the force increases with increasing Reynolds number

The pressure field distribution around the flapping plate was visualized from the velocity field by integrating the Poisson equation using two overlapping meshes. For comparison, the torque of the flapping axis was calculated using the pressure estimation and strain gauge measurement. In this study, qualitative agreement of the two methods is shown for the mid-chord section of the plate. The visualization of the pressure field shows that the vortex flow increases the force generation at low flapping velocity by creating a stagnation pressure from the flow induced by the vortices or *inter-vortex stream*. This mechanism is responsible for the phase difference between the force and the flapping motion. After the initial motion, there are pressure stagnations on the front and rear surface of the plate. Front stagnation is produced by flow stagnation because of the motion of the plate and rear stagnation is generated by the inter-vortex stream.

Contents

List of Figures

List of Tables

Chapter 1

Introduction

1.1 Introduction

1.1.1 Micro-air vehicles and animal flight principles

A micro-air vehicle (MAV) is defined as an autonomous flying vehicle with dimensions of less than 15 cm in length, width, and height (McMichael and Francis, 1997). It functions as a platform for observations in close proximity or over an obstructed field of view by at most two operators. Due to its size, MAV flies in low Reynolds number regime similar to the flight of small birds and large insects. Animal flight is considered for propulsion and lift as an alternative to conventional aerodynamics in designing an MAV.

There is a fundamental difference between animal flight and the flight of fixed-wing aircrafts. By definition, a fixed-wing aircraft does not flex its wing for generating lift and a separate propulsion system is required for generating thrust. In animal flight, animals use the motion of their wings to generate lift and to propel their body forward. There are many variations in animal flight kinematics. Variations occur between species and small variations within a species (Ellington, 1984; Azuma, 1992). Bird flight imposes an active flexibility to the wing but insect flight has relatively simpler kinematics. Because of this, much attention has been placed toward insect flight. A flapping stroke plane is defined as the plane parallel with the path of the flapping stroke. Each flapping stroke

consists of an upstroke and a downstroke. Based on the orientation of the flapping stroke plane relative to an inertial plane, three flapping strokes have been defined: horizontal, vertical, and inclined stroke.

An example of flapping on the horizontal stroke plane can be seen in hummingbirds, *Chlorostilbon aureoventris*, which hover with an eight-figure stroke path (Ellington, 1984). Detailed studies of flapping flight have been conducted for normal hovering by Dickinson et al (1999); Birch and Dickinson (2001); Sane and Dickinson (2001, 2002); Birch et al (2004); Poelma et al (2006) for the flight of *Drosophila melanogaster* or fruitflies and by Ellington et al (1996); van den Berg and Ellington (1997); Van Den Berg and Ellington (1997); Willmott et al (1997); Bomphrey et al (2005); Sane and Jacobson (2006) for the flight of *Manduca sexta* or hawkmoths.

An example of flapping on the vertical stroke plane have been observed in butterflies (Ellington, 1984; Srygley and Thomas, 2002; Mao and Xin, 2003), which show a vertical stroke plane during the downward motion. In a vertical stroke plane, the wing motion is perpendicular to the chord. At the start of the motion, the wings are clapped together and then flung open and at the end of the downstroke the wings are almost clapped together again. This motion produces a vortex ring. This flight mechanism is called *clap-fling* and although initially observed to be utilized by butterflies, it is not restricted to vertical stroke planes. Clap-fling mechanism at normal hovering was studied by Lehmann et al (2005); Miller and Peskin (2005). This mechanism is used optimally for low Reynolds number flight. At Re=32, the leading edge vortex forms and remains attached to the wing compared for the flight at Re=64, where the leading edge vortex is shed during each wing stroke, reducing the aerodynamic forces on the wing.

Studies of flapping wing mechanics of a dragon fly have shown an asymmetric wing kinematics during the upstroke and downstroke in an inclined stroke plane (Azuma et al, 1985; Wang, 2004). This asymmetry produces different mean force for each stroke. The vertical component of the force in inclined hovering is greater than the one generated in normal hovering, which explains why dragonflies are among the best hoverers in the insect world.

Animals fly by actively changing the shape of their wings by bending and twisting to get the optimum thrust or lift (Shyy et al, 1999). Birds and bats change the shape of

their wings with muscle tissue to deal with rapid changes of the flight environment. Bats control their wing surface by changing the degree of surface tension of their wing membrane, thereby changing the wing profile's curvature by passive aeroelastic response of the wing to aerodynamics loading. Flow control of MAV has been proposed using adaptive feedback control and actuators to change the shape of the wing (Ho et al, 2003). It was found that the level of stiffness of the wing profile is essential in producing thrust for an oscillating wing (Ho et al, 2003; Heathcote et al, 2004; Heathcote and Gursul, 2007) and careful control of the spanwise flexibility of the wing with respect to the wing motion kinematics can enhance propulsive efficiency (Bandyoypadhyay, 2009; Heathcote et al, 2008). Other ways to produce thrust are pitching rigid airfoils and purely plunging airfoils (Lai and Platzer, 1999, 2000). Pitching airfoils have the prospect of producing both lift and thrust at the same time when paired with the vertical oscillation motion of the wing (Guglielmini and Blondeaux, 2004).

A variety of flight modes have also been observed depending on the behavior of the insect: hovering flight, forward flight, and maneuver flight have been observed. Hovering flight in flight vehicle is defined as flight with zero forward velocity as a result of balancing the lift force and weight of the vehicle. Hovering in animal flight is defined more loosely, where velocity and acceleration vectors of the body is low. In forward steady flight the thrust balances the body drag of the insect. The ratio of the forward velocity to the mean flapping velocity of the wing is called *advance ratio*. Hovering flight can be defined when the advance ratio is almost zero. The mechanism of maneuver flight has been investigated by Tobalske (2009). A yaw is defined as rotation of the body on the vertical axis, which may happen due to gust or wind or by an asymmetric force produced by the wings. A torque in the counter direction, called *flapping counter torque*, is required to stop the yaw motion. Because of the rotation of the body, symmetric motion of the wing relative to the body produces higher velocity on one of the wings, which produces greater aerodynamic force compared to the other wing, which is moving at lower velocity. The result is a torque of the body in the direction opposite of the yaw motion, effectively stopping the yaw motion. The prediction of yaw damping as well as pitch and roll damping have been formulated by Sunada et al (2010) experimentally using a mechanical dragonfly and analytically using blade element theory.

Two designs of micro air vehicle based on flapping wing are prevalent. The first is the hybrid design using a plunging airfoil to generate thrust and a body in the shape of a wing to generate lift while the vehicle is in forward motion. Lift and thrust generation from a plunging airfoil was studied by Knoller (1909) and Betz (1912) separately and is called the Knoller–Betz effect (Jones et al, 1998). The flow has been reproduced experimentally by Jones et al (1998); Lai and Platzer (1999). The flow downstream of the airfoil was visualized by dye flow visualization and was quantified by laser doppler measurements. A jet flow, instead of a wake, is produced from the shedding of vortices from the trailing edges of a plunging airfoil above a critical flapping frequency. Thereby, generating thrust instead of drag (Lai and Platzer, 1999). This jet flow is slanted providing a normal force component or lift on the wing at higher flapping frequency. The profile of the wing is an important factor in the generation of thrust in hovering condition. Lai and Platzer (2000) had measured the velocity profile in front of the leading edge and behind the trailing edge of a symmetrical airfoil and a circular cylinder. The former produces thrust and the latter does not. The difference is that the circular cylinder has a symmetrical profile. The MAV design based on the Knoller-Betz phenomena was discussed in Jones and Platzer (1997); Jones et al (2001); Jones and Platzer (2009). Because forward motion is necessary to generate lift, this design lacks the maneuvering capabilities that an insect or a bird has. These capabilities are potentially achievable by the second design.

The second design mimics the kinematics of small birds or insects by solely using the flapping wing to generate lift and thrust. This design mimics the flight characteristics of insects and small birds. The design of a biologically inspired flapping wing was discussed by Bandyoypadhyay (2009). The maneuvering capabilities of flapping birds or insects can help the operation of MAV in tight and narrow spaces. The aerodynamic study of MAV design has also given more information for zoologist because of the similarities with animal flight.

1.1.2 Measurement history

Flapping wing research have mostly been done by zoologist in search of the mechanics of insect and bird flight. The flight of insects has been studied at the Reynolds number of

1000–10000 using qualitative visualizations of a tethered hawkmoth and a mechanical scaled-up wing modeled after the same insect shows a conical vortex bubble stabilized by a *spanwise flow* formed closely behind the leading edge of the wing and associated with lift enhancement while the wing has a high angle of attack (Ellington et al, 1996; van den Berg and Ellington, 1997; Van Den Berg and Ellington, 1997; Willmott et al, 1997; Bomphrey et al, 2005; Sane and Jacobson, 2006). The spanwise flow direction from the base of the flapping wing to the tip limits the growth of the leading-edge vortex by removing the energy from the vortex core. This mechanism is generated during the translational phase of the wing. The spanwise flow decelerates indicating a breakdown of the vortex bubble near the tip of the plate.

The flapping kinematics of a fruit fly is similar to that of a hawkmoth. In observations of mechanical wing of a fruit fly at Re=136, additional lift generating mechanisms called *wing rotation* increases the flow circulation and *wake capture* interacts with the separated vortex at the start of a stroke (Dickinson et al, 1999; Birch and Dickinson, 2001; Sane and Dickinson, 2001, 2002; Birch et al, 2004; Poelma et al, 2006). This theory is taken as a generalized theory of insect flight with variations of the start of the wing rotation to compensate for variations of species. The timing of the wing rotation with the end of the stroke influences the increase of lift. Delaying the start of the wing rotation produces 70% less lift than advancing the wing rotation and 65% less lift when the wing rotates in conjunction with the end of the stroke. The position of the axis of rotation of the wing also influences the induced circulation. Rotating the wing on the leading edge have been shown to induce the highest added circulation and rotating the wing on its trailing edge actually produces negative added circulation. Wake capture enhances the lift of the flapping wing at the start of each stroke because of the induced flow of the surrounding fluid from the shed vortices of the previous stroke. The flow induced by these vortices is called *inter-vortex stream*. The effect of wake capture to the force generation is a distinct force peak that develops immediately after the wing changes the direction of motion. At Re=136, the axial flow of the vortex bubble is not clearly distinguishable due to the prominence of viscosity whereas, at Re=1400, the axial flow phenomena is prevalent during the translational phase of the flapping stroke (Birch et al, 2004). At Re=1400, the spanwise flow from the base of the flapping wing

to the tip limits the growth of the leading edge vortex by removing the energy of the vortex core. While at Re=136 the spanwise flow is not clearly observed and the stability of the leading edge vortex is postulated due to the downwash of the tip vortex, which reduces the effective angle of attack of the wing.

Hovering motion in an inclined stroke plane shows relatively higher lift and aerodynamic efficiency. Two-dimensional numerical simulations of wing kinematics, modeled after a dragonfly at Re=1350, have shown that the increase in lift is explained by the contribution of drag to the vertical component of force (Sun and Lan, 2004; Wang, 2004).

The inclined stroke plane improves the performance of insects at hovering conditions. The flow generated by an accelerating vertical stroke plane was visualized by Ringuette et al (2007) with the effect of tip vortex put under scrutiny. The tip vortex is responsible for the increase of drag and suppression of the tip vortex reduces the drag component. It shows that the tip vortex improves the stability of the attached leading edge vortex and the three-dimensional effect may increase the vertical force.

Studies by Dickinson et al (1999); Ellington et al (1996); Wang (2004) were done using qualitative visualization, force measurements using load cells, and numerical investigation. Flapping wing inspired MAV designs and analysis have been studied (Tsai and Fu, 2009; Ansari et al, 2009; Ho et al, 2003). Aerodynamic experiments to obtain the flow field generated by a two-dimensional profile of flapping wings have been done by Poelma et al (2006), which visualizes the time-resolved and three-dimensional vortex structure generated by flapping wing, and by van Oudheusden et al (2007); David et al (2009); Spedding and Hedenström (2009); Jardin et al (2009) using particle image velocimetry and momentum integration approach. The experiments have also focused on quantifying the uncertainty of the available data. The momentum integration approach,

$$\mathbf{F}(t) = -\int_V \frac{\partial \rho \mathbf{u}}{\partial t}\, dV - \int_S \rho \mathbf{u}(\mathbf{u}\cdot\mathbf{n})\, dS + \int_S (-p\mathbf{n} + \tau\cdot\mathbf{n})\, dS \tag{1.1}$$

utilized by Unal et al (1997); van Oudheusden et al (2007), uses the available velocity data from planar measurements and spatially integrates the pressure gradient,

$$-\nabla p = \rho \frac{\partial \mathbf{u}}{\partial t} + \rho \mathbf{u}(\mathbf{u}\cdot\mathbf{n}) - \mu \nabla^2 \mathbf{u} \tag{1.2}$$

to obtain the pressure on the control surface, S, where the control volume and control surface is given in Fig. 1.1.

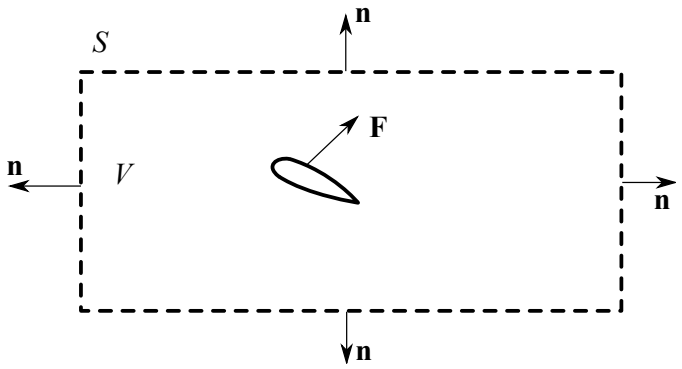

Figure 1.1: The definition of control volume and control surface for Eq. (1.1).

A finite wing will produce a three-dimensional flow, which in the qualitative visualization of Ellington et al (1996), shows an increase of vortex size along the spanwise of the wing and vortex separation closer to the wing tip. Only a few three-dimensional measurements have been conducted. Experimentation remains a challenge in the progress for an efficient design of MAV (Platzer et al, 2008). One of the challenges in the measurement of the performance of an MAV is the investigation of its aerodynamic characteristics. Recent measurements of forces have used a scaled-up model of the wing of a certain species of birds or insects, where force balance can be applied. Customized force sensing have been developed for the measurement and use in feedback control of MAV up to 25mm in wingspan (Wood and Fearing, 2001; Steltz et al, 2006; Haddab et al, 2009). However, commercial intrusive sensors cannot be used for the actual MAV because not only they are not sensitive enough, but also their dimension and wirings will disturb the flow. For an MAV with a semi wing-span of 7.5cm (McMichael and Francis, 1997), the lift force of 0.39mN was estimated (Wang, 2001). This is about 0.4% of the smallest range of a thin film micro load cell (Cooper Instruments, 2007); therefore, low signal to noise ratio can be expected.

Flow visualization methods provide the dissemination of flow structures non-intrusively, thereby experiments can be conducted without worry of the sensor disturbing the flow. Some methods, such as dye or ink injection, provide qualitative information for the investigation of flow behavior. Quantitative methods, such as PIV, provide visual information as well as estimations of the flow properties such as stress tensor, vorticity

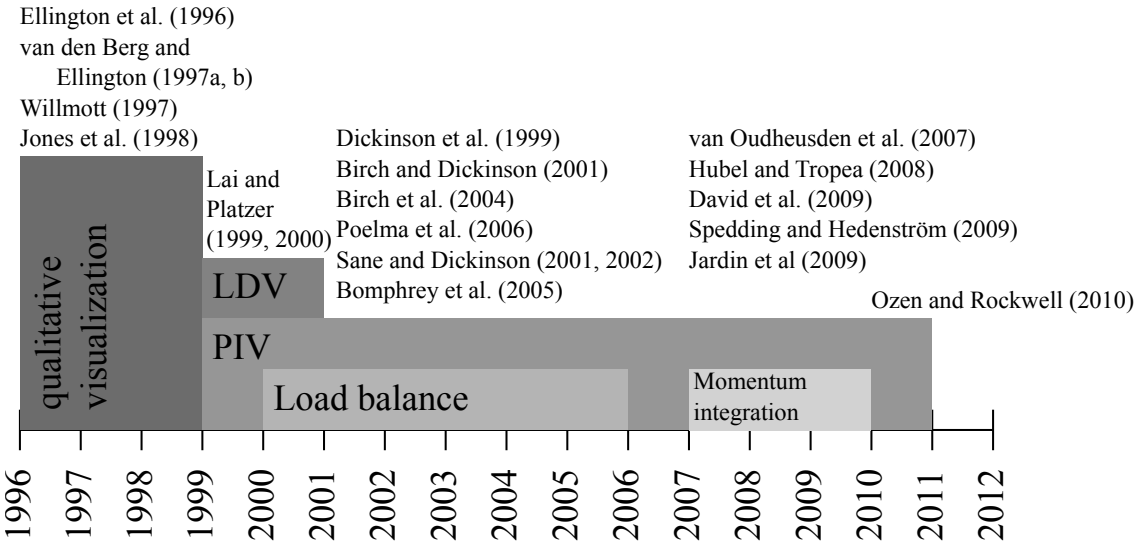

Figure 1.2: Summary of measurement techniques in flapping wing research.

vector, circulation, and force. Three-dimensional flow analysis and the estimation of force can provide information on the interaction of vortex and rigid structure, which is helpful in the engineering of an MAV. This interaction is one of the foundations of flapping flight. In this case, rigid structure can be the wing or body of an MAV. Visualization and force estimation can provide ingenious ways to increase the aerodynamic efficiency of MAV.

The measurement history of flapping wing research is summarized in Fig. 1.2. Early measurements had used qualitative visualization tools, which enabled the study of the evolution of flow structures. Better measurement tools, such as laser doppler velocimetry (LDV) and PIV, were available afterwards and quantitative visualization has been conducted ever since. The measurement of force utilizes load balance and only recently utilizes the control volume analysis of the measured velocity.

Two-dimensional computational studies of flapping flight have been conducted by solving the vorticity and stream function equation on an elliptical coordinate system (Wang, 2000, 2001), using the immersed boundary method (Miller and Peskin, 2005; Sudhakar and Vengadesan, 2010), overset grid method (Mao and Xin, 2003). Three-dimensional solutions of the Navier-Stokes equations have been solved using overset grid method (Sun and Lan, 2004) and using the Navier-Stokes equations on a non-

inertial frame of reference and body conformed grid (Sun and Tang, 2002; Wu and Sun, 2004; Mu-lin et al, 2006).

1.2 Objectives

The objectives of this study are two folds. First, to establish a quantitative method for flow observation and force evaluation of a periodically flapping plate. Past studies have focused on the measurement of force and the visualization of the vorticity distribution around the flapping plate. However, the relation of vortices to the generation of force has never been fully detailed. To answer this problem, the effect of vortices to force will be studied by (1) Control volume analysis of the near field of a flapping plate, (2) by estimating the surface pressure of the wing, and (3) temporally resolved measurements of the flow field using particle image velocimetry.

In this study, the integration of the flow field and the arbitrary selection of the size of the control volume within the flow field is explored to quantify the dynamics of the flow generated by a flapping plate. The result of the control volume analysis is the force acting on a control volume.

The mechanism to generate aerodynamic force is the pressure difference on the surface of the body and the viscous force. The viscous force can be investigated directly from a spatially accurate velocity field and is negligible except for very small Reynolds numbers. The investigation of force from the pressure difference requires the calculation of the pressure that is expressed in the Poisson equation (Fujisawa et al, 2005; Obi and Tokai, 2006; de Kat et al, 2008). The proposed method was designed to estimate the pressure field of a flapping wing modeled as a rigid plate from a set of velocity measurements to estimate the aerodynamic forces. The pressure field was estimated by solving the three-dimensional Poisson equation evaluated on the phase-averaged velocity field. The pressure field represents the pressure distribution on a planar field around the flapping plate. The combination of two numerical meshes, one was at a fixed position and the other was moving with the flapping plate, were required to solve the Poisson equation on a moving boundary. The performance of the pressure integration was compared with measurement using strain gauges.

The flow was measured with stereo PIV due to its capability of measuring three-velocity components at multiple points instantaneously on a planar field. To measure the full deformation tensor, including the velocity derivatives with respect to the out-of-plane direction, measurements were conducted on a set of measurement planes offset along the out-of-plane direction.

The second objective is to estimate the force acting on the flapping wing using information acquired using velocity measurements. This is considered because the engineering of MAV requires the measurement of an actual size MAV to optimize the aerodynamic, structure, and flight control. The technical difficulties of applying load sensors to measure the force on an actual MAV are intrusiveness of the sensor and the sensitivity of the sensor.

1.3 Methodology

A simplified wing in the shape of a rigid flat plate and a simplified wing kinematics was visualized both qualitatively and quantitatively. Dye was injected manually from a pipette near the spanwise of the plate to visualize the nearby vortex structure. Independently, seeded flow was recorded using stereo particle image velocimetry. Phase-locked measurements were applied to the recording, referring to the velocity measurement of the individual phase angle associated with the flapping plate. As explained in §1.1, the flow around a finite flapping plate is fully three-dimensional. A volumetric measurement was approximated by measuring the flow in slices as the measurement plane or laser sheet was positioned along the direction chordwise to the plate. The slices are required in order to estimate the velocity gradients in the out-of-plane direction and to integrate the three-dimensional Poisson equation. At the same time with stereo PIV measurement, the torque produced by the flapping wing was measured by two strain gauges attached on the rotational axis of the flapping wing.

The velocity field was treated with statistical tools. The average of the cycle-to-cycle velocity field of each phase angle will be referred as the phase-averaged velocity field and the process to obtain it is called phase-averaging. The phase-averaged velocity field is a function of the spatial location and the phase angle of the plate. Hence, the phase-

averaged velocity field of a group of planar measurements represents the evolution of velocity distribution of the flow around a flapping plate. Due to phase-averaging, the cycle-to-cycle velocity field can be decomposed as an average value and fluctuating value. Hence, the governing equations are decomposed into terms including the phase-averaged terms and fluctuation terms.

In flow measurements, the fluctuation of the velocity components can be of two kinds:

1. Random velocity fluctuation, which is distributed according to the normal distribution.
2. Non-random velocity fluctuation, which has a probability density with embedded structures that deviates the normal distribution.

The first type can be neglected in the governing equations and in the process of analysis is represented as measurement uncertainty (Bevington, 1969; Coleman and Steele, 1995; Bendat and Piersol, 2000). The second kind, which could indicate vortical wake or turbulent structure, is relevant to the understanding of flow dynamics and can not be neglected (Pope, 2000; Bernard and Wallace, 2002).

Probability density functions are commonly used to indicate the normality of a sample, e.g. the time history of a velocity component. Several requirements for this statement are that the flow was measured in steady state and at a defined spatial position of the flow. In PIV, the flow was measured at multiple spatial positions and particular to this study, low Reynolds number flow was measured close to the solid boundary that it would be unwise to randomly pick the spatial locations to analyze the distribution of the velocity components. A statistical test was applied to identify normal distributions of every spatial location on the flow field of each phase angle. The statistical test is the Shapiro–Wilk test and calculation of kurtosis and skewness (Shapiro and Wilk, 1965; Masuda, 2006).

Quantitative flow visualization was presented by:

1. The second invariance of the deformation tensor, $\langle Q \rangle$, which is also the laplacian of the pressure.
2. The vorticity in y-direction, ω_y, to visualize the evolution of the leading edge vortex.

3. Two-dimensional streamlines.
4. Pressure field.

The pressure field was visualized numerically by integrating the three-dimensional Poisson equation for pressure. Overlapping mesh was proposed to obtain the pressure on the surface of the plate, where the pressure obtained away from the surface was used to resolve the pressure within the mesh close to the surface. The non-slip condition was applied for the boundary condition of the surface of the plate. The pressure field was validated by comparing the torque from the integration of the estimated surface pressure distribution with the torque measured by strain gauges.

1.4 Thesis outline

Chapter 2 will discuss the governing flow equations that were used for control volume analysis, surface pressure integration, and vortex visualization from a measured velocity field distribution. The unsteady state was resolved by phase-averaging the velocity field. Therefore, the governing equations were decomposed into the average and fluctuation terms. The estimation of pressure field that was introduced in the previous chapter will be further discussed in Chapter 3. The Poisson equation for pressure is formulated to estimate the pressure around a circular cylinder. The flow around a flapping wing was measured using stereo PIV. Simultaneously, the torque of the flapping axis was measured with strain gauges. These experimental setups are discussed in Chapter 4. In Chapter 5, the velocity field was analyzed using qualitative and quantitative visualization methods and using the control volume analysis. In Chapter 6, the estimation of the pressure field of the flow generated by a flapping rigid plate is formulated. Samples of the flapping wing at certain flapping phase is presented. The discussion of the torque calculated by the integration of the surface pressure is given in Chapter 7. Finally, conclusions and recommendations derived from this study is given in Chapter 8.

Chapter 2

Theory

This chapter discusses the governing equations for control volume analysis, pressure field visualization, and vortex visualization in §2.1. To represent one cycle of the flapping motion, a large number of flapping cycles were recorded and the result was averaged for each phase angle. This is discussed in §2.2.

2.1 Governing flow equations

Micro-air vehicles operate in $1000 < \mathrm{Re} < 10000$, which is within the flight operation of small birds and insects. In the hovering mode, birds and insects generate aerodynamic forces solely due to flapping wing. Hence, it is suggested that the unsteady term will play a major role in the governing flow equation. The viscous effect of the flow caused by a flapping wing is negligible for $\mathrm{Re} > 136$. So, incompressible and inviscid flow can be assumed at all instants. The governing flow equations are the continuity equation,

$$\frac{\partial u_i}{\partial x_i} = 0 \tag{2.1}$$

and the momentum conservation equation,

$$\rho \frac{\partial u_i}{\partial t} + \rho u_j \frac{\partial u_i}{\partial x_j} = -\frac{\partial p}{\partial x_i} \tag{2.2}$$

where u_i is the instantaneous velocity component, t is the temporal variable, x_i is the spatial variable, ρ is the density of the fluid, and μ is the kinematic viscosity of the fluid.

Equations (2.1) and (2.2) are governing flow equations in the inertial frame of reference. With a stationary observer, the flow is measured relative to an inertial frame of reference. However, in an unsteady motion such as a flapping wing, one is interested in understanding the forces that the wing is experiencing. In this case, an observer has to move with the wing. In other words, flow information is in the non-inertial frame of reference. Direct measurements following the motion of the wing is practically difficult. Therefore, in this study the information in the non-inertial frame of reference is constructed using measurements from the inertial frame of reference. The governing flow equations in the non-inertial frame of reference are the continuity condition,

$$\frac{\partial u_i'}{\partial x_i'} = 0 \tag{2.3}$$

and the momentum conservation equation,

$$\rho\frac{\partial u_i'}{\partial t} + \rho u_j'\frac{\partial u_i'}{\partial x_j'} = -\frac{\partial p}{\partial x_i'} + \mu\frac{\partial^2 u_i'}{\partial {x_j'}^2} - \rho\left[\frac{\partial^2 R_i}{\partial t^2} - \frac{\partial \Omega_i}{\partial t} r_j \varepsilon_{ijk} + 2\Omega_i u_j' \varepsilon_{ijk} + \Omega_l(\Omega_i r_j \varepsilon_{ijk})\varepsilon_{lkm}\right] \tag{2.4}$$

where the subscript u_i' indicates the velocity in the non-inertial frame of reference. The acceleration and rotation of the non-inertial frame of reference, $O'x'y'z'$, are $\partial^2 R_i/\partial t^2$ and Ω_i, respectively. The non-inertial frame of reference and its parameters are shown in Fig. 2.1, where the inertial frame of reference is $Oxyz$.

2.1.1 Control volume analysis

In the analysis of flows, it is sometimes necessary to integrate Eq. (2.2) or Eq. (2.4) within a control volume to investigate the forces acting on the flow. A control volume is a defined volume in space that may move or deform independently from the flow field. Mass, momentum, or energy may flow across the boundary of the control volume, called the control surface. Through mathematical manipulations, the force acting on the surface of the body inside a control volume or the force acting on the control volume can be known. Control volume analysis provide a simple way to study aerodynamics.

To study the effect of a periodically moving body, force was calculated with control volume analysis of a fixed control volume, cf. Fig. 2.2,

$$F_i = \rho\int_V \frac{\partial u_i}{\partial t}\,dV + \rho\int_S u_i u_j \hat{n}_j\,dS \tag{2.5}$$

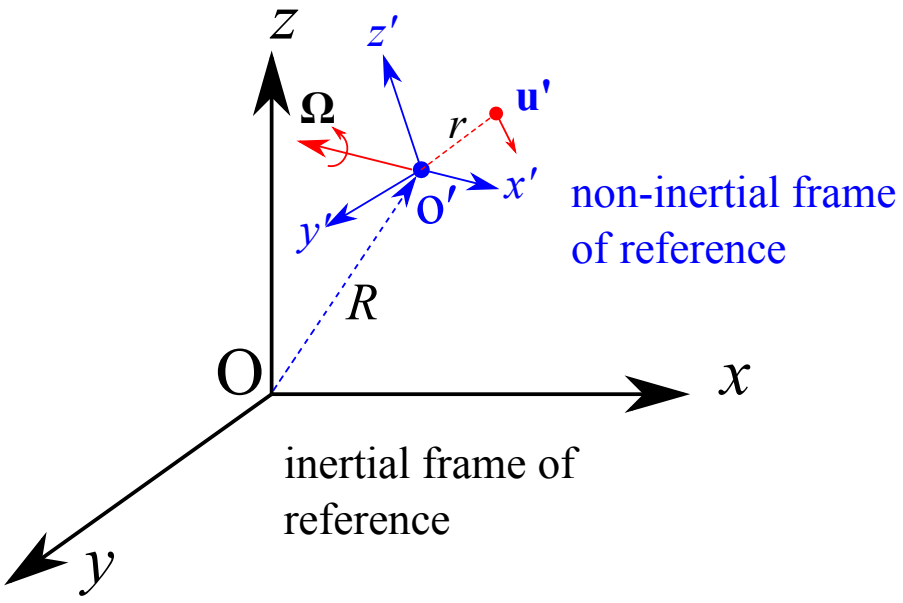

Figure 2.1: Non-inertial frame of reference

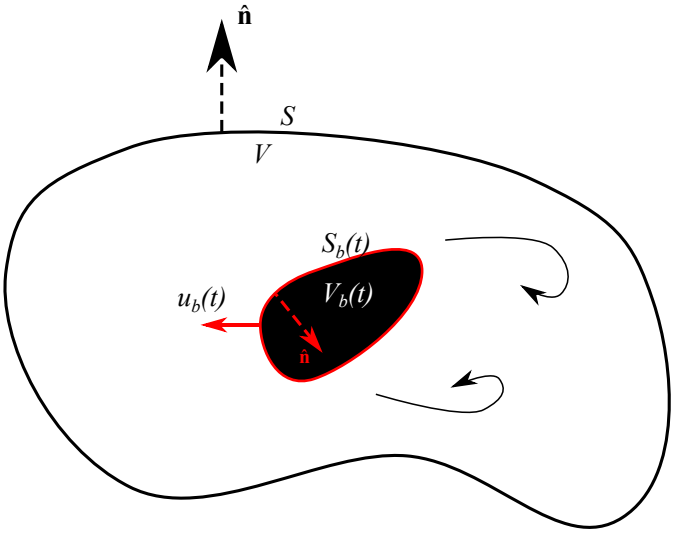

Figure 2.2: Control volume surrounding an unsteady moving body such as flapping wing. V is the control volume of the field and S is its control surface. $V_b(t)$ is the volume of the body as a function of time and $S_b(t)$ is its control surface. The body is moving at $u_b(t)$.

Table 2.1: scaling parameters to non-dimensionalize Eqs. (2.1) and (2.2)

Scaling parameter	Description	Primary dimensions
L	Characteristic length	$\{\mathrm{L}\}$
V	Characteristic speed	$\{\mathrm{Lt}^{-1}\}$
f	Characteristic frequency	$\{\mathrm{t}^{-1}\}$
$p_0 - p_\infty$	Reference pressure difference	$\{\mathrm{mL}^{-1}\mathrm{t}^{-2}\}$

where V is the control volume of the flow field and S is its control surface. The non-dimensional form of Eq. (2.5) is

$$\frac{F_i}{1/2\rho U^2 bc} = \frac{1}{1/2 U^2 bc}\int_V \frac{\partial u_i}{\partial t}\,dV + \frac{1}{1/2 U^2 bc}\int_S u_i u_j \hat{n}_j\,dS \tag{2.6}$$

The right hand side of the non-dimensional terms of Eq. (2.6) can be interpreted by transforming Eq. (2.2) into its non-dimensional form. For completeness the viscous effect is taken into account. Introducing the non-dimensional variables

$$t^* = ft; \quad x^* = \frac{x}{L}; \quad u^* = \frac{u}{U}; \quad p^* = \frac{p - p_\infty}{p_0 - p_\infty}; \quad \frac{\partial}{\partial x_i^*} = L\frac{\partial}{\partial x_i} \tag{2.7}$$

where the scaling parameters are summarized in Table 2.1.

Rearranging Eq. (2.7) in terms of the dimensional variables,

$$t = \frac{t^*}{f}; \quad x = Lx^*; \quad u = Uu^*; \quad p = p_\infty + (p_0 - p_\infty)p^*; \quad \frac{\partial}{\partial x_i} = \frac{1}{L}\frac{\partial}{\partial x_i^*} \tag{2.8}$$

Substitute Eq. (2.8) to Eq. (2.1) to obtain

$$\frac{1}{L}\frac{\partial}{\partial x_i^*} U u_i^* = 0 \tag{2.9}$$

$$\frac{U}{L}\frac{\partial u_i^*}{\partial x_i^*} = 0 \tag{2.10}$$

$$\frac{\partial u_i^*}{\partial x_i^*} = 0 \tag{2.11}$$

and to Eq. (2.2) to obtain

$$\rho U f\frac{\partial u_i^*}{\partial t^*} + \frac{\rho U^2}{L}\left(u_j^*\frac{\partial}{\partial x_j^*}\right)u_i^* = -\frac{p_0 - p_\infty}{L}\frac{\partial p^*}{\partial x_i^*} + \frac{\mu U}{L^2}\frac{\partial^2 u_i^*}{\partial x_j^{*2}} \tag{2.12}$$

Table 2.2: Non-dimensional numbers in Eq. (2.13)

Non-dimensional number	Description
St= $\frac{fL}{U}$	Strouhal number (ratio of vortex oscillation to mean speed)
Eu= $\frac{p_0-p_\infty}{\rho U^2}$	Euler number (ratio of pressure drop to dynamic pressure)
Re= $\frac{\rho UL}{\mu}$	Reynolds number (ratio of flow inertia to fluid viscosity)

multiplying every term by $L/\rho U^2$ and after some rearrangement,

$$\left[\frac{fL}{U}\right]\frac{\partial u_i^*}{\partial t^*}+u_j^*\frac{\partial u_i^*}{\partial x_j^*}=-\left[\frac{p_0-p_\infty}{\rho U^2}\right]\frac{\partial p^*}{\partial x_i^*}+\left[\frac{\mu}{\rho UL}\right]\frac{\partial^2 u_i^*}{\partial x_i^*\partial x_j^*} \tag{2.13}$$

The products of the characteristic parameters are defined in Table 2.2. Equation 2.13 is rearranged into,

$$[\mathrm{St}]\frac{\partial u_i^*}{\partial t^*}+u_j^*\frac{\partial u_i^*}{\partial x_j^*}=-[\mathrm{Eu}]\frac{\partial p^*}{\partial x_i^*}+\left[\frac{1}{\mathrm{Re}}\right]\frac{\partial^2 u_i^*}{\partial x_j^{*2}} \tag{2.14}$$

Only the left hand side of Eq. (2.14) is represented by Eq. (2.6). The first term on the right hand side of Eq. (2.6) is the unsteady term and the non-dimensional parameter that represents this term is the Strouhal number. The second term is the diffusion term and is expected to be unaffected with increasing flow frequency.

2.1.2 Integration of the surface pressure

The force acting on the surface of the flapping wing can be evaluated using control volume analysis, as shown in Fig. 2.2. The control volume, V, is differentiated as control volume of the body, V_b, and the control volume of the flow, $V-V_b$. The control surface, S_b is the surface of the control volume V_b. Thus, the force acting on the body, F_i, is

$$\begin{aligned}F_i=&-\rho\int_V\frac{\partial u_i}{\partial t}\,dV-\rho\int_S u_iu_j\hat{n}_j\,dS-\int_S p\hat{n}_i\,dS\\&-\rho\int_{S_b(t)}(u_i-u_b(t))u_j\hat{n}_j\,dS\end{aligned} \tag{2.15}$$

where u_i is the velocity in the inertial frame of reference, the shape and size of the control volume and surface is a function of time, and the control volume is moving at $u_b(t)$. The last term on the right hand side reflects the transfer of momentum on the surface of the body, which is due to suction and/or blowing. In the absence of both, the last term can be omitted.

The equivalent form of Eq. (2.15) is

$$F_i = -\int_{S_b(t)} -p\hat{n}_i \, dS \tag{2.16}$$

In the calculation of Eq. (2.16), the surface of the body and the pressure field down to the surface of the body have to be defined. The study by Obi and Tokai (2006) calculated the pressure field from a set of measured velocity field by integrating the Poisson equation for the pressure, which is derived by taking the divergence of Eq. (2.2),

$$\begin{aligned} \frac{\partial}{\partial x_i}\left(\frac{\partial p}{\partial x_i}\right) &= -\frac{\partial}{\partial x_i}\left(\frac{\partial u_i}{\partial t}\right) - \frac{\partial}{\partial x_i}\left(u_j \frac{\partial u_i}{\partial x_j}\right) \\ &= -\cancel{\frac{\partial}{\partial t}\left(\frac{\partial u_i}{\partial x_i}\right)} - \frac{\partial u_j}{\partial x_i}\frac{\partial u_i}{\partial x_j} \\ \frac{\partial^2 p}{\partial x_i^2} &= -\frac{\partial u_j}{\partial x_i}\frac{\partial u_i}{\partial x_j} \end{aligned} \tag{2.17}$$

where the omitted term is due to the continuity condition, $\partial u_i / \partial x_i = 0$. Solving the Poisson equation on the surface of an unsteady body is practically difficult because the numerical solver needs to be created for every phase angle and the velocity distribution close to the wall must be resolved. In this study, to evaluate the pressure force and the surface pressure distribution, the pressure field will be defined by solving Eq. (2.17) using two overlapping meshes: a rectangular mesh and a mesh that conforms to the surface of the body and is a subset of the rectangular mesh. The Poisson equation is integrated from the velocity information that is known on the rectangular mesh. The use of overlapping meshes will be discussed in Chapter 3. The advantage of the proposed pressure estimation method to calculate force is the insight that can be obtained from evaluating the pressure distribution of the flow field.

2.1.3 Vortex visualization

Flow separation behind a bluff body creates a region of strongly rotational flow. In

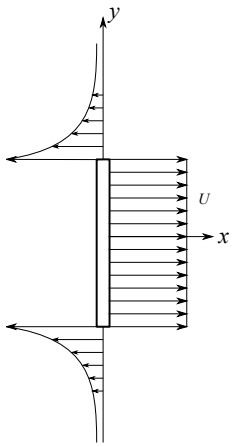

Figure 2.3: Velocity profile created by the motion of the plate. The discontinuity creates a strong rotational flow behind the body.

Fig. 2.3, the discontinuity of the velocity profile at the tips creates a strong rotational flow downstream of the body. The motion of this fluid is described by the curl of the velocity,

$$\omega_k = \nabla \times \mathbf{u} = \frac{\partial}{\partial x_i} u_j \hat{e}_k \varepsilon_{ijk} \tag{2.18}$$

The symbol ω_k is defined as the vorticity of the flow. Qualitatively, a vortex is defined as a connected fluid region with high concentration of vorticity compared to its surrounding.

A velocity field can be given as the sum of its rotational elements and its irrotational elements,

$$\mathbf{u}(\mathbf{x},t) = \mathbf{u}_v(\mathbf{x},t) + \nabla\psi \tag{2.19}$$

The irrotational element, $\nabla\psi$, is the potential flow problem. And the rotational element is defined as

$$\mathbf{u}_v = \frac{1}{4\pi} \int \frac{\omega(\mathbf{x}',t) \times (\mathbf{x}-\mathbf{x}')}{|\mathbf{x}-\mathbf{x}'|^3} d\mathbf{x}' \tag{2.20}$$

where $\mathbf{x}-\mathbf{x}'$ is the distance between the vorticity element, ω to the fluid element induced by the rotational effect of ω. Equation (2.20) is illustrated in Fig. 2.4. The effect of rotation is inversely proportional to the square of the distance between the vortex element to a fluid element.

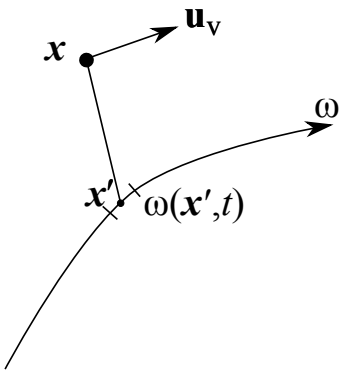

Figure 2.4: The definition of Eq. (2.20).

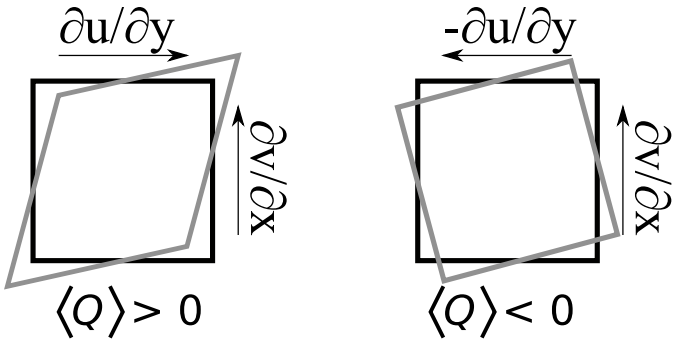

Figure 2.5: The physical interpretation of Eq. (2.21).

When formed, a vortex plays an important role in organizing the flow. Thus, the identification of a vortex provide an important information to the entire fluid mechanics. The vortex element is identified by calculating the second invariance of the deformation tensor.

$$\begin{aligned} Q &= (\|\Omega\|^2 - \|\mathbf{S}\|^2) \\ &= \left\| \frac{1}{2}\left(\frac{\partial u_i}{\partial x_j} - \frac{\partial u_j}{\partial x_i}\right) \right\|^2 - \left\| \frac{1}{2}\left(\frac{\partial u_i}{\partial x_j} + \frac{\partial u_j}{\partial x_i}\right) \right\|^2 \\ &= -\frac{\partial u_i}{\partial x_j}\frac{\partial u_j}{\partial x_i} \end{aligned} \tag{2.21}$$

where Ω is the rotational tensor and $\mathbf{S}$ is the strain tensor. The second invariance Q denotes dominance of the strength of rotation compared with that of the strain as illustrated in Fig. 2.5. The identification of the vortex element can also be done by taking

the divergence of the momentum conservation equation, which will lead to Eq. (2.17). Thus, the second invariance is equal to the Laplacian of the pressure.

Another useful method of visualization is streamlines. Along a streamline, the instantaneous velocity vector is tangential to that streamline. Streamlines show the direction of a fluid element. A two-dimensional streamline is defined as,

$$\frac{dx}{u} = \frac{dy}{v} \tag{2.22}$$

Streamlines depicts the motion of instantaneous fluid motion. For the presentation of the measurement results, streamlines are used with phase-averaged velocity vectors. Therefore, giving different streamlines for every flapping phase angle. The phase-averaging of the velocity vectors is described in the next section.

2.2 Phase-averaging

To improve the certainty of the measurement, ensemble averaging is commonly done when presenting the result. For periodic flows, the averaging can be done for one phase angle of every period of the source of disturbance. This is called *phase-averaging*. In this study, the source of disturbance is the flapping plate. The phase-averaging of velocity is

$$\langle \mathbf{u} \rangle (\mathbf{x}, \phi) = \lim_{N \to \infty} \frac{1}{N} \sum_{n=1}^{N} \mathbf{u} [\mathbf{x}, (n + \phi)/f] \tag{2.23}$$

where $\langle \mathbf{u} \rangle$ denotes the phase-averaged velocity and $\mathbf{u}$ is the instantaneous velocity. The fluctuative velocity is defined as the difference between the two, $\mathbf{u}' = \mathbf{u} - \langle \mathbf{u} \rangle$. The phase angle of the flapping plate is $0 \leq \phi < 2\pi$. The phase-averaging operation is illustrated in Fig. 2.6.

Because of phase-averaging, the governing flow equations has to be decomposed into the averaged value and the fluctuative value. For the momentum conservation equation,

$$\rho \frac{\partial \langle u_i \rangle}{\partial t} + \rho \langle u_j \rangle \frac{\partial \langle u_i \rangle}{\partial x_j} = -\frac{\partial \langle p \rangle}{\partial x_i} - \rho \frac{\partial \langle u_i' u_j' \rangle}{\partial x_j} \tag{2.24}$$

where the last term on the right hand side appears as the product of the fluctuative

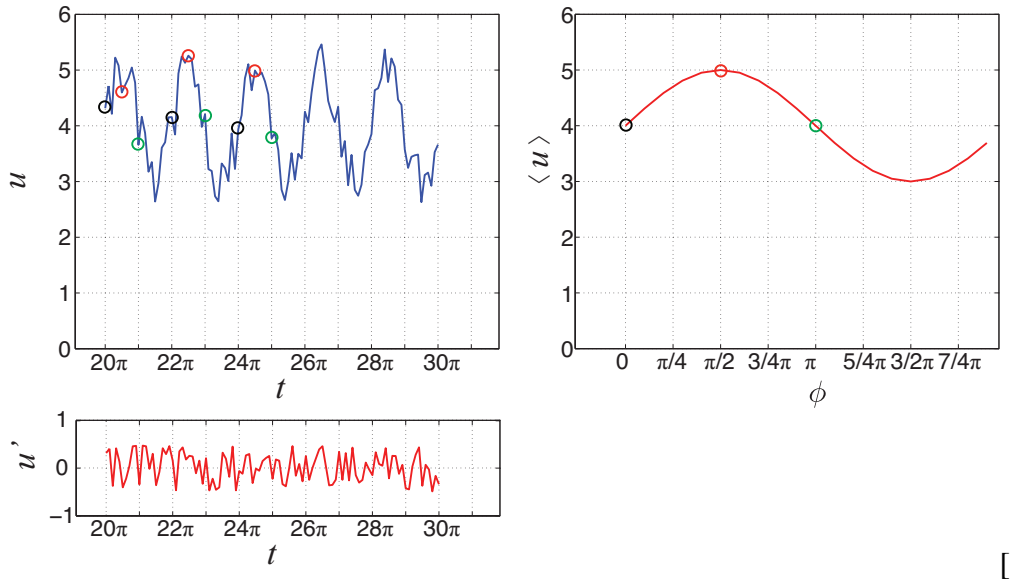

[!t]

Figure 2.6: Phase averaging of an instantaneous velocity component, u, the phase-averaged velocity, $\langle u \rangle$, and the fluctuating velocity, u'.

velocity components. Thus, the Poisson equation for pressure is also decomposed,

$$\frac{\partial^2 \langle p \rangle}{\partial x_i^2} = -\frac{\partial \langle u_i \rangle}{\partial x_j}\frac{\partial \langle u_j \rangle}{\partial x_i} - \frac{\partial^2 \langle u_i' u_j' \rangle}{\partial x_i \partial x_j} \tag{2.25}$$

And for vortex visualization, the second invariance of the deformation tensor is equal to the right hand side of Eq. (2.25).

$$\langle Q \rangle = -\frac{\partial \langle u_i \rangle}{\partial x_j}\frac{\partial \langle u_j \rangle}{\partial x_i} - \frac{\partial^2 \langle u_i' u_j' \rangle}{\partial x_i \partial x_j} \tag{2.26}$$

Chapter 3

Estimation of the pressure field by the integration of the Poisson equation on two overlapping meshes

The two-meshes method to solve the pressure field on the surface of a body is explained in §3.1. The method is evaluated in §3.2 for a circular cylinder in potential flow with the discrete form of the governing equation explained in §3.3. The discrete equation set was solved using numerical method explained in §3.4 and the results are shown in §3.5. Finally remarks are given in §3.6.

3.1 Pressure Estimation

The pressure field can be estimated from the PIV velocity field by integrating the Poisson equation of pressure as briefly described in §2.1.1. The Poisson equation is derived by taking the divergence of the Euler equation, which in this chapter is formulated in the

decomposed form,

$$\begin{aligned}\nabla\cdot\left(\frac{\partial\langle\mathbf{u}\rangle}{\partial t}+\langle\mathbf{u}\rangle\cdot\langle\mathbf{u}\rangle\right)&=\nabla\cdot\left(-\nabla\frac{1}{\rho}\langle p\rangle-\langle\mathbf{u}'\mathbf{u}'\rangle\right)\\ \nabla\langle\mathbf{u}\rangle\left(\nabla\langle\mathbf{u}\rangle\right)^T&=-\frac{1}{\rho}\nabla^2\langle p\rangle-\nabla\cdot\langle\mathbf{u}'\mathbf{u}'\rangle\\ \nabla^2\langle p\rangle&=-\rho\left[\nabla\langle\mathbf{u}\rangle\left(\nabla\langle\mathbf{u}\rangle\right)^T+\nabla\cdot\langle\mathbf{u}'\mathbf{u}'\rangle\right]\end{aligned}\tag{3.1}$$

and in its tensorial form,

$$\frac{\partial^2\langle p\rangle}{\partial x_i^2}=-\rho\frac{\partial\langle u_i\rangle}{\partial x_j}\frac{\partial\langle u_j\rangle}{\partial x_i}-\rho\frac{\partial^2\langle u_i'u_j'\rangle}{\partial x_i\partial x_j}\tag{3.2}$$

The solution is calculated by integrating Eq. (3.2) with the pressure gradient normal to the boundary,

$$\frac{1}{\rho}\frac{\partial\langle p\rangle}{\partial\hat{n}}=-\frac{\partial u_{\hat{n}}}{\partial t}-u_{\hat{n}}\frac{\partial u_{\hat{n}}}{\partial\hat{n}}-u_{\hat{s}}\frac{\partial u_{\hat{n}}}{\partial\hat{s}}-u_{\hat{z}}\frac{\partial u_{\hat{n}}}{\partial\hat{z}}-\frac{\partial\langle u_{\hat{n}}u_{\hat{n}}\rangle}{\partial\hat{n}}-\frac{\partial\langle u_{\hat{n}}u_{\hat{s}}\rangle}{\partial\hat{s}}-\frac{\partial\langle u_{\hat{n}}u_{\hat{z}}\rangle}{\partial\hat{z}}\tag{3.3}$$

where $\hat{n}$, $\hat{s}$, and $\hat{z}$ are in the normal, tangential, and z-direction of the numerical boundary.

The discrete form of Eq. (3.2) is solvable using an iterative solver, where the convergence of the solution is evaluated by the rate of the absolute value of the residual, R. The residual is

$$\nabla^2\langle p\rangle=\Phi+R\tag{3.4}$$

$$R=\nabla^2\langle p\rangle-\Phi\tag{3.5}$$

where Φ is the right hand side of Eq. 3.1. The convergence is

$$\varepsilon=\frac{\|R(k)-R(k-1)\|}{R(3)}\tag{3.6}$$

where k is the iteration number and the difference is normalized by $R(k=3)$. For the purpose of the estimation of surface pressure integration, the pressure on the surface of the plate needs to be resolved. The Poisson equation is solved on two connecting numerical meshes. The first mesh, which will be called *global mesh*, is a rectangular mesh defined avoiding the surface of the plate and the second mesh, which will be called *local mesh*, is attached to the plate and is moving with it. Spatial continuity of the pressure

between the meshes is preserved by interpolating the pressure solution of the global mesh to the numerical boundary of the local mesh. The out-of-plane derivatives are approximated using the two adjacent measurement planes in the out-of-plane direction.

In PIV measurements, the velocity vectors are spatially distributed in a rectangular mesh. This rectangular mesh is the global mesh that will be used to integrate Eq. (3.2). Taking the rectangular coordinate system,

$$\langle \mathbf{u} \rangle = (\langle u \rangle, \langle v \rangle, \langle w \rangle) \tag{3.7}$$

$$\mathbf{x} = (x, y, z) \tag{3.8}$$

for the velocity components and coordinate bases. The governing equation to be solved in the global mesh is,

$$\begin{aligned}
&\frac{\partial^2 \langle p \rangle}{\partial x^2} + \frac{\partial^2 \langle p \rangle}{\partial y^2} + \frac{\partial^2 \langle p \rangle}{\partial z^2} = \\
&\quad -\rho \left[\left(\frac{\partial \langle u \rangle}{\partial x} \right)^2 + \left(\frac{\partial \langle v \rangle}{\partial y} \right)^2 + \left(\frac{\partial \langle w \rangle}{\partial z} \right)^2 \right. \\
&\qquad + 2 \left(\frac{\partial \langle u \rangle}{\partial y} \frac{\partial \langle v \rangle}{\partial x} + \frac{\partial \langle u \rangle}{\partial z} \frac{\partial \langle w \rangle}{\partial x} + \frac{\partial \langle v \rangle}{\partial z} \frac{\partial \langle w \rangle}{\partial y} \right) \\
&\qquad + \left(\frac{\partial^2 \langle u'u' \rangle}{\partial x^2} + \frac{\partial^2 \langle v'v' \rangle}{\partial y^2} + \frac{\partial^2 \langle w'w' \rangle}{\partial z^2} \right) \\
&\qquad \left. + 2 \left(\frac{\partial^2 \langle u'v' \rangle}{\partial y \partial x} + \frac{\partial^2 \langle u'w' \rangle}{\partial z \partial x} + \frac{\partial^2 \langle v'w' \rangle}{\partial z \partial y} \right) \right]
\end{aligned} \tag{3.9}$$

Because the boundaries of the global mesh are parallel to either x, y, or z-axis, the boundary conditions are pressure gradients normal to the x, y, and z-axis.

$$\begin{aligned}
\frac{\partial \langle p \rangle}{\partial x} = -\rho \left[\frac{\partial \langle u \rangle}{\partial t} + \langle u \rangle \frac{\partial \langle u \rangle}{\partial x} + \langle v \rangle \frac{\partial \langle u \rangle}{\partial y} + \langle w \rangle \frac{\partial \langle u \rangle}{\partial z} \right. \\
\left. + \frac{\partial \langle u'u' \rangle}{\partial x} + \frac{\partial \langle u'v' \rangle}{\partial y} + \frac{\partial \langle u'w' \rangle}{\partial z} \right]
\end{aligned} \tag{3.10}$$

$$\begin{aligned}
\frac{\partial \langle p \rangle}{\partial y} = -\rho \left[\frac{\partial \langle v \rangle}{\partial t} + \langle u \rangle \frac{\partial \langle v \rangle}{\partial x} + \langle v \rangle \frac{\partial \langle v \rangle}{\partial y} + \langle w \rangle \frac{\partial \langle v \rangle}{\partial z} \right. \\
\left. + \frac{\partial \langle u'v' \rangle}{\partial x} + \frac{\partial \langle v'v' \rangle}{\partial y} + \frac{\partial \langle v'w' \rangle}{\partial z} \right]
\end{aligned} \tag{3.11}$$

$$\frac{\partial\langle p\rangle}{\partial z} = -\rho\left[\frac{\partial\langle w\rangle}{\partial t} + \langle u\rangle\frac{\partial\langle w\rangle}{\partial x} + \langle v\rangle\frac{\partial\langle w\rangle}{\partial y} + \langle w\rangle\frac{\partial\langle w\rangle}{\partial z} + \frac{\partial\langle u'w'\rangle}{\partial x} + \frac{\partial\langle v'w'\rangle}{\partial y} + \frac{\partial\langle w'w'\rangle}{\partial z}\right] \tag{3.12}$$

The local mesh encompasses a small area from to the surface of the body. It is constrained and conforms to the shape of the body. For the investigation of a periodically moving body, the local mesh is defined in the non-inertial frame of reference (ξ_1,ξ_2,ξ_3). The velocity components $(\upsilon_1,\upsilon_2,\upsilon_3)$ in the local mesh is obtained using the bi-linear interpolation from the measured values. The velocity interpolation process requires three steps. First, the coordinates of the local mesh (ξ_1,ξ_2,ξ_3) is transformed to the coordinates in the global mesh (x',y',z').

$$\begin{pmatrix} x' \\ y' \\ z' \end{pmatrix} = \mathcal{F}(\xi_1,\xi_2,\xi_3,x,y,z) \tag{3.13}$$

Second, the velocity components in the global mesh is interpolated on (x',y',z').

$$\begin{pmatrix} u(x',y',z') \\ v(x',y',z') \\ w(x',y',z') \end{pmatrix} = \mathcal{G}(u,v,w,x,y,z,x',y',z') \tag{3.14}$$

Finally, the interpolated velocity components are transformed to the local mesh coordinates, (ξ_1,ξ_2,ξ_3).

$$\begin{pmatrix} \upsilon_1 \\ \upsilon_2 \\ \upsilon_3 \end{pmatrix} = \mathcal{F}(u(x',y',z'),v(x',y',z'),w(x',y',z'),x',y',z',\xi_1,\xi_2,\xi_3) \tag{3.15}$$

The governing equation to be solved in the local mesh is in the non-inertial frame of reference. Assuming that this frame of reference has an orthogonal basis, the pressure gradient of inviscid and incompressible flow is,

$$\frac{1}{\rho}\frac{\partial\langle p\rangle}{\partial\xi_i} = -\frac{\partial\langle\upsilon_i\rangle}{\partial t} - \langle\upsilon_j\rangle\frac{\partial\langle\upsilon_i\rangle}{\partial\xi_j} - \frac{\partial\langle\upsilon_i'\upsilon_j'\rangle}{\partial\xi_j} - \varepsilon_{ijk}\Omega_i\xi_j - \Omega_i\Omega_j\xi_j + \Omega_j^2\xi_i - \frac{\partial^2 R_i}{\partial t^2} - 2(\varepsilon_{ijk}\Omega_i\upsilon_j) \tag{3.16}$$

where the variables are given in Fig. 2.1. Taking the divergence of Eq. 3.16,

$$\begin{aligned}\frac{1}{\rho}\frac{\partial}{\partial\xi_i}\frac{\partial\langle p\rangle}{\partial\xi_i} =& \frac{\partial}{\partial\xi_i}\Bigg(-\frac{\partial\langle\upsilon_i\rangle}{\partial t}-\langle\upsilon_j\rangle\frac{\partial\langle\upsilon_i\rangle}{\partial\xi_j}-\frac{\partial\langle\upsilon_i'\upsilon_j'\rangle}{\partial\xi_j}\\ &-\varepsilon_{ijk}\Omega_i\xi_j-\Omega_i\Omega_j\xi_j+\Omega_j^2\xi_i-\frac{\partial^2 R_i}{\partial t^2}-2(\varepsilon_{ijk}\Omega_i\upsilon_j)\Bigg)\end{aligned} \tag{3.17}$$

the Poisson equation of the local mesh is

$$\begin{aligned}\frac{1}{\rho}\frac{\partial^2\langle p\rangle}{\partial\xi_i^2} =& -\frac{\partial\langle\upsilon_i\rangle}{\partial\xi_j}\frac{\partial\langle\upsilon_j\rangle}{\partial\xi_i}-\frac{\partial^2\langle\upsilon_i'\upsilon_j'\rangle}{\partial\xi_i\partial\xi_j}\\ &-\frac{\partial}{\partial\xi_k}\left(\varepsilon_{ijk}\Omega_i\xi_j\right)-\frac{\partial}{\partial\xi_j}\left(\Omega_j\Omega_i\xi_i-\Omega_i^2\xi_j\right)-2\frac{\partial}{\partial\xi_k}\left(\varepsilon_{ijk}\Omega_i\upsilon_j\right)\end{aligned} \tag{3.18}$$

where $\xi_i=(\xi_1,\xi_2,\xi_3)$ is constrained to the shape of the surface. For example, $\xi_i=(r,\theta,z)$ for cylindrical coordinate system or $\xi_i=(\xi,\eta,\zeta)$ for a rectangular coordinate system. To solve Eq. (3.18), the pressure gradient normal to the surface of the body is,

$$\begin{aligned}\frac{\partial\langle p\rangle}{\partial\xi_{\hat{n}}} =& -\left(\Omega_{\hat{s}}\xi_{\hat{z}}-\Omega_{\hat{z}}\xi_{\hat{s}}\right)-\left(\Omega_{\hat{n}}\Omega_{\hat{s}}\xi_{\hat{s}}-\Omega_{\hat{s}}^2\xi_{\hat{n}}+\Omega_{\hat{n}}\Omega_{\hat{z}}\xi_{\hat{z}}-\Omega_{\hat{z}}^2\xi_{\hat{n}}\right)\\ &-\frac{\partial^2 R_{\hat{n}}}{\partial t^2}-2\left(\Omega_{\hat{s}}\upsilon_{\hat{z}}-\Omega_{\hat{z}}\upsilon_{\hat{s}}\right)\end{aligned} \tag{3.19}$$

The subscript $(\hat{n},\hat{s},\hat{z})$ are in the normal, tangential, and out-of-plane direction of the local mesh. Assuming the non-slip condition, $\upsilon_{\hat{n}}=0$, $\upsilon_{\hat{s}}=0$, and $\upsilon_{\hat{z}}=0$ on the surface of the body. Ω and $\partial R_{\hat{n}}/\partial t$ is the angular and translational velocity of the non-inertial frame of reference, respectively. The surface pressure is calculated by extrapolating the resolved pressure on the center node to the surface of the body using the second order Lagrangian extrapolation.

The procedures of the method is summarized in Fig. (3.1). The Poisson equation, Eq. (3.2), is solved using the velocity field measured with stereo PIV in the global mesh with boundary conditions in Eq. (3.10)–(3.12). The local mesh is defined in the non-inertial frame of reference, the velocity components in the local mesh are defined from the global mesh using interpolation and coordinate transformation. For each phase of one period, the velocity field is transformed from the rectangular grid of the global mesh to the relative velocity of the local mesh. The Poisson equation of the local mesh, Eq. (3.18) is solved using the Neumann-Dirichlet boundary condition. The Neumann

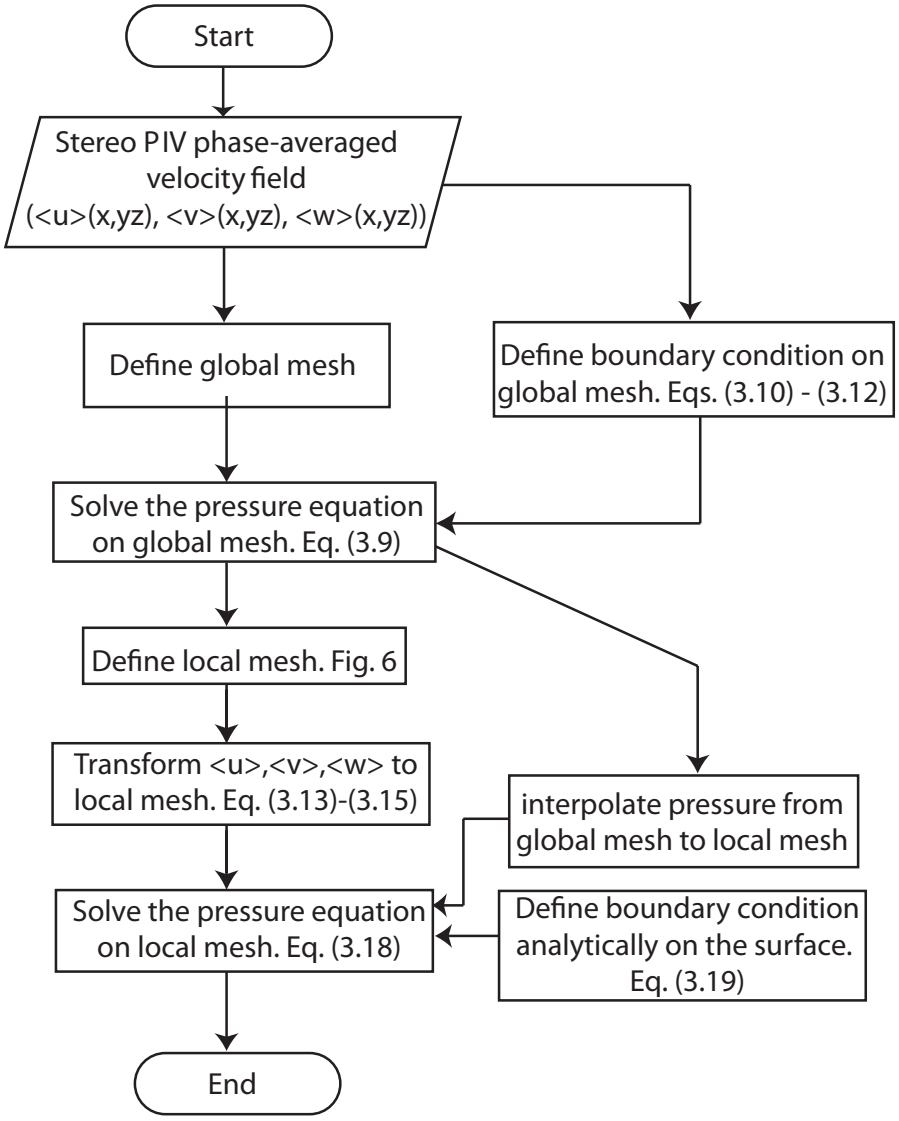

Figure 3.1: Flowchart for the general description for the estimation of phase-averaged pressure based on stereo PIV velocity field.

boundary condition for the local mesh is given by Eq. (3.19) on the surface of the plate. The Dirichlet boundary condition is the pressure interpolated from the global mesh applied to the numerical boundary of the local mesh.

3.2 Cylinder in potential flow

The steady potential flow around a circular cylinder was used to proof the concept of the overlapping meshes system that was explained in the previous section. The components of the velocity field of the potential flow over a circular cylinder in polar coordinates were given as

$$U_r = \left(1 - \frac{R^2}{r^2}\right) U_\infty \cos\theta \tag{3.20}$$

$$U_\theta = -\left(1 + \frac{R^2}{r^2}\right) U_\infty \sin\theta \tag{3.21}$$

where U_r is the radial velocity, U_θ is the tangential velocity, R is the cylinder's radius, and U_∞ is the freestream velocity. The components in Cartesian coordinate was obtained from Eqs. (3.20)–(3.21),

$$\begin{pmatrix} u \\ v \end{pmatrix} = \begin{bmatrix} \sin\theta & -\cos\theta \\ \cos\theta & \sin\theta \end{bmatrix} \begin{pmatrix} U_r \\ U_\theta \end{pmatrix} \tag{3.22}$$

and the velocity components inside the cylinder were set to zero,

$$u(x,y) = 0, \quad v(x,y) = 0 \quad ; \text{if } \sqrt{x^2+y^2} < R \tag{3.23}$$

The velocity field defined by Eqs. (3.22) and (3.23) were used to simulate the velocity field of PIV as shown in Fig. 3.2.

The Navier-Stokes equation in cartesian coordinate is

$$u_j \frac{\partial u_i}{\partial x_j} = -\frac{1}{\rho}\frac{\partial p}{\partial x_i} \tag{3.24}$$

and the Poisson equation is the divergence of Eq. (3.24),

$$\frac{\partial^2 p}{\partial x_i^2} = -\rho \frac{\partial u_j}{\partial x_i}\frac{\partial u_i}{\partial x_j} \tag{3.25}$$

expanding the tensorial indices $i = 1,2$ and $j = 1,2$, where $x_i = (x_1, x_2) = (x, y)$ and $u_i = (u_1, u_2) = (u, v)$,

$$\frac{\partial^2 p}{\partial x^2} + \frac{\partial^2 p}{\partial y^2} = 2\rho \left(\frac{\partial u}{\partial x}\frac{\partial v}{\partial y} - \frac{\partial u}{\partial y}\frac{\partial v}{\partial x}\right) \tag{3.26}$$

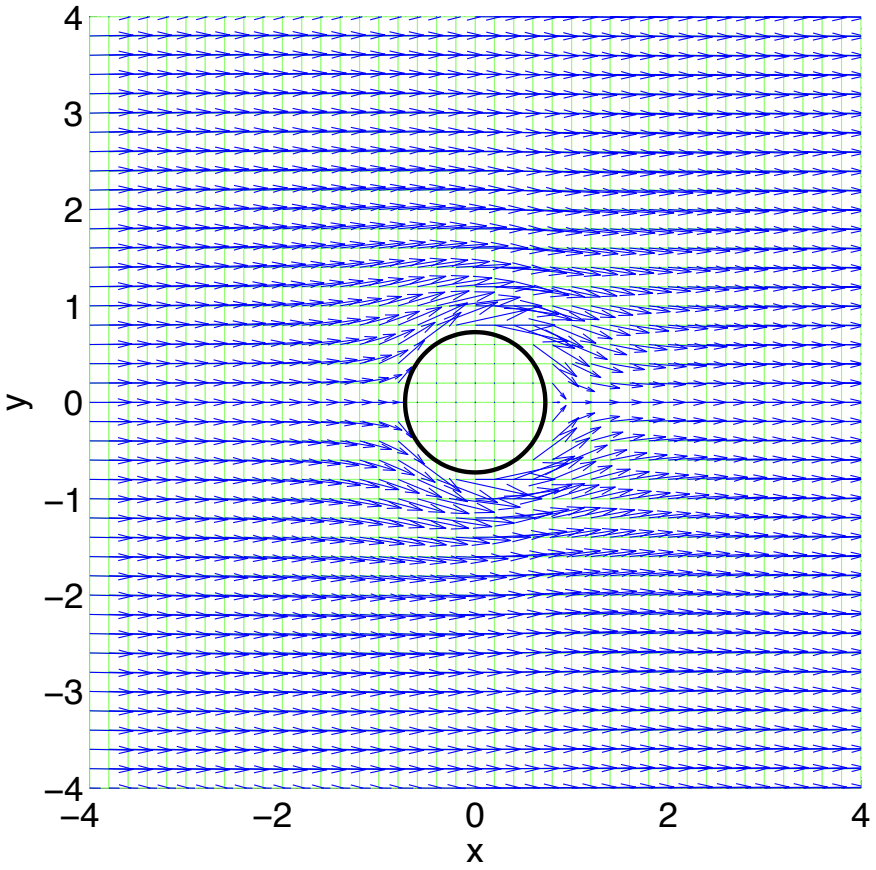

Figure 3.2: Numerical velocity used to simulate PIV velocity field.

To solve Eq. (3.26) in the global mesh, the boundary condition is the pressure gradient normal to the boundary,

$$\frac{\partial p}{\partial \hat{n}} = -\rho \left(\frac{\partial u_{\hat{n}}}{\partial t} + u_{\hat{n}} \frac{\partial u_{\hat{n}}}{\partial \hat{n}} + u_{\hat{s}} \frac{\partial u_{\hat{n}}}{\partial \hat{s}} \right) \tag{3.27}$$

with $\hat{n}$ and $\hat{s}$ are the bases in the normal and tangential direction of the boundary, respectively. The velocity component $u_{\hat{n}}$ and $u_{\hat{s}}$ are the component associated with their respective bases. The boundary conditions of the global mesh are

$$\frac{\partial p}{\partial x} = -\rho \left(\frac{\partial u}{\partial t} + u \frac{\partial u}{\partial x} + v \frac{\partial u}{\partial y} \right) \tag{3.28}$$

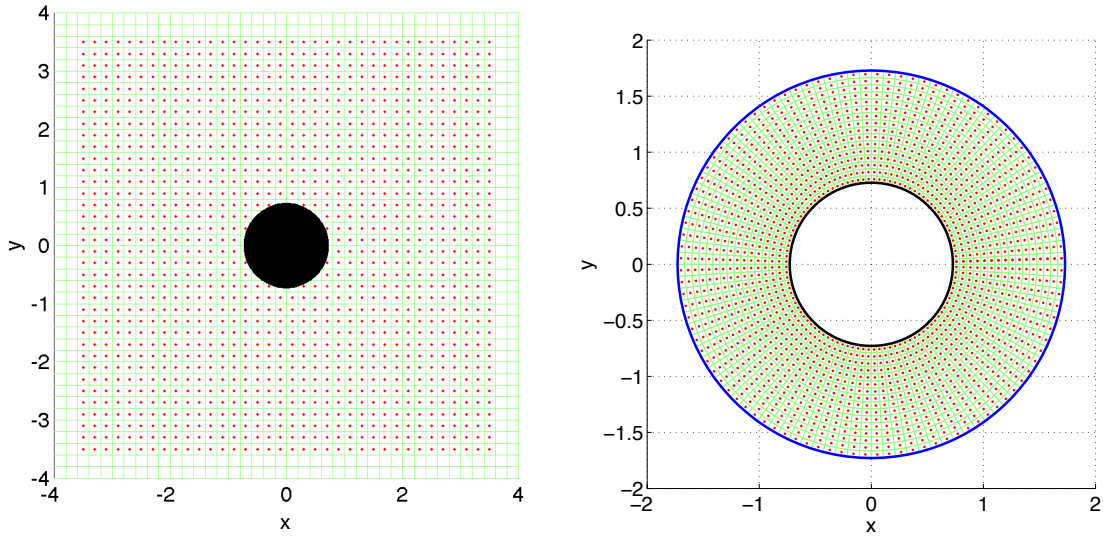

(a) Global mesh.

(b) Local mesh.

Figure 3.3: Definition of numerical meshes.

for the boundaries parallel to the y-direction and

$$\frac{\partial p}{\partial y} = -\rho\left(\frac{\partial v}{\partial t} + u\frac{\partial v}{\partial x} + v\frac{\partial v}{\partial y}\right) \tag{3.29}$$

for the boundaries parallel to the x-direction.

In this numerical evaluation, the numerical mesh to solve the pressure equation was divided into two: the global mesh as shown in Fig. 3.3(a) and the local mesh as shown in Fig. 3.3(b). The velocity distribution in the local mesh was interpolated from the global mesh using

$$\begin{aligned} f(x,y) \approx & \frac{f(x_1,y_1)}{\Delta x\Delta y}(x_2-x)(y_2-y) + \frac{f(x_2,y_1)}{\Delta x\Delta y}(x-x_1)(y_2-y) \\ & + \frac{f(x_1,y_2)}{\Delta x\Delta y}(x_2-x)(y-y_1) + \frac{f(x_2,y_2)}{\Delta x\Delta y}(x-x_1)(y-y_1) \end{aligned} \tag{3.30}$$

and this equation is illustrated in Fig. 3.4. The pressure was solved on the nodes (red dots) in Fig. 3.3. The pressure in the global mesh is solved only on the visible nodes and outside the cylinder. The velocity field in the local mesh was given in Fig. 3.5 where sparser vector density is shown here to easily illustrate the velocity field.

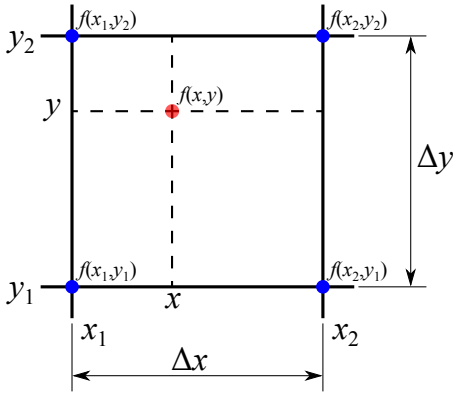

Figure 3.4: Illustration for bilinear interpolation. Bilinear interpolation uses the information of 4 nodes closest to the unknown node.

The Navier-Stokes equations in polar coordinate are given in r and θ direction as

$$\frac{\partial p}{\partial r} = \rho(h_r + b_r) \tag{3.31}$$

$$\frac{\partial p}{\partial \theta} = \rho(h_\theta + b_\theta) \tag{3.32}$$

where

$$h_r = -\frac{1}{r}\frac{\partial}{\partial r}(r u_r u_r) - \frac{1}{r}\frac{\partial}{\partial \theta}(u_\theta u_r) \tag{3.33}$$

$$b_r = \frac{u_\theta^2}{r} \tag{3.34}$$

$$h_\theta = -\frac{1}{r}\frac{\partial}{\partial r}(r u_r u_\theta) - \frac{1}{r}\frac{\partial}{\partial \theta}(u_\theta u_\theta) \tag{3.35}$$

$$b_\theta = -\frac{u_r u_\theta}{r} \tag{3.36}$$

The pressure equation is obtained by taking the divergence of the Navier-Stokes equation,

$$\begin{aligned}
\frac{1}{r}\frac{\partial}{\partial r}\left(r\frac{\partial p}{\partial r}\right) + \frac{1}{r}\frac{\partial}{\partial \theta}\left(\frac{1}{r}\frac{\partial p}{\partial \theta}\right) &= \rho\left[\frac{1}{r}\frac{\partial}{\partial r}[r(h_r + b_r)] + \frac{1}{r}\frac{\partial}{\partial \theta}(h_\theta + b_\theta)\right] \\
\frac{1}{r}\frac{\partial r}{\partial r}\frac{\partial p}{\partial r} + \frac{r}{r}\frac{\partial^2 p}{\partial r^2} + \frac{1}{r^2}\frac{\partial^2 p}{\partial \theta^2} &= \rho\left[\frac{1}{r}\frac{\partial r}{\partial r}h_r + \frac{\partial h_r}{\partial r} + \frac{1}{r}\frac{\partial r}{\partial r}b_r + \frac{\partial b_r}{\partial r} + \frac{1}{r}\frac{\partial h_\theta}{\partial \theta} + \frac{1}{r}\frac{\partial b_\theta}{\partial \theta}\right] \\
\frac{1}{r}\frac{\partial p}{\partial r} + \frac{\partial^2 p}{\partial r^2} + \frac{1}{r^2}\frac{\partial^2 p}{\partial \theta^2} &= \rho\left[\frac{h_r + b_r}{r} + \frac{\partial h_r + b_r}{\partial r} + \frac{1}{r}\frac{\partial}{\partial \theta}(h_\theta + b_\theta)\right]
\end{aligned} \tag{3.37}$$

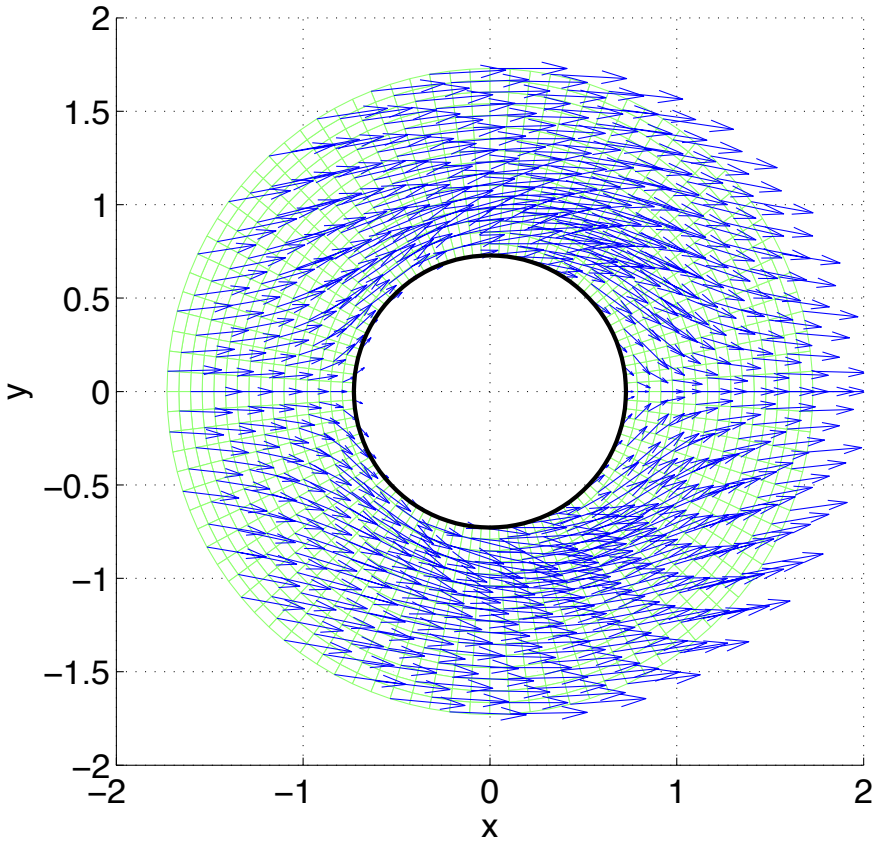

Figure 3.5: Velocity field in local mesh, interpolated from the global mesh using Eq. (3.4)

The pressure gradient normal to the boundary of the local mesh is

$$\frac{\partial p}{\partial r} = \rho(h_r + b_r) \tag{3.38}$$

where

$$h_r = -\frac{1}{r}\frac{\partial}{\partial r}(r u_r u_r) - \frac{1}{r}\frac{\partial}{\partial \theta}(u_\theta u_r) \tag{3.39}$$

$$b_r = \frac{u_\theta^2}{r} \tag{3.40}$$

because of the slip condition of the potential flow, Eq. (3.38) can be simplified to

$$\frac{\partial p}{\partial r} = \rho \frac{u_\theta^2}{r} \tag{3.41}$$

where u_θ on the wall is

$$u_\theta = -2U_\infty \sin\theta \tag{3.42}$$

The boundary condition on the numerical boundary of the local mesh is the pressure values interpolated from the global mesh.

The analytical coefficient of pressure of the flow field is

$$C_p = 1 - \frac{U^2}{U_\infty^2} \tag{3.43}$$

and on the surface of the cylinder,

$$C_p = 1 - 4\sin^2\theta \tag{3.44}$$

The numerical procedure in this section is summarized using the flowchart in Fig. 3.6.

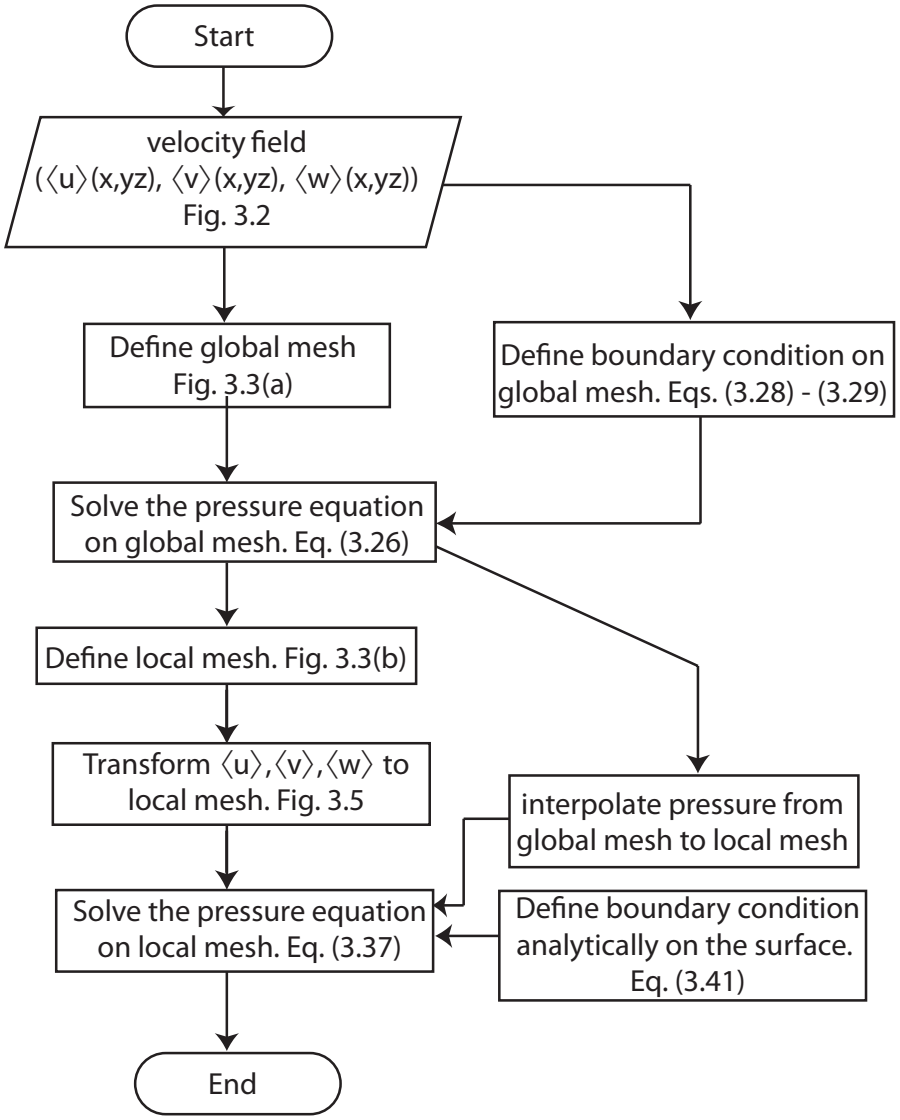

Figure 3.6: Flowchart for the estimation of the pressure field around a circular cylinder in potential flow.

3.3 Finite differentiation

The finite differentiation scheme of the governing equation was needed to solve the partial differential equation using an iterative solver. The Poisson equation was solved using the Gauss-Seidel method on the center of the grid. The coordinates of the grid are

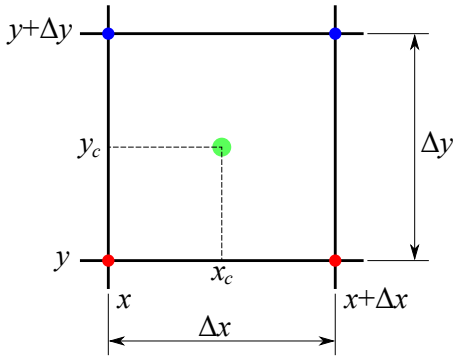

Figure 3.7: Definition of the node coordinates, x^c, y^c.

(x,y) and the coordinates of the grid center are (x^c, y^c),

$$x^c = \frac{(x)+(x+\Delta x)}{2} \tag{3.45}$$

$$y^c = \frac{(y)+(y+\Delta y)}{2} \tag{3.46}$$

and illustrated in Fig. 3.7

Two iterative solvers are required to solve the finite form of the Poisson equation, one for each mesh.

3.3.1 Governing equations in global mesh

The Poisson equation of the global mesh is given as

$$\frac{\partial^2 p}{\partial x^2} + \frac{\partial^2 p}{\partial y^2} = 2\rho\left(\frac{\partial u}{\partial x}\frac{\partial v}{\partial y} - \frac{\partial u}{\partial y}\frac{\partial v}{\partial x}\right) \tag{3.47}$$

The right hand side of Eq. (3.47) will be denoted as ψ_{global}. Equation (3.47) was discretized as

$$\frac{p(x^c-\Delta x,y^c)-2p(x^c,y^c)+p(x^c+\Delta x,y^c)}{\Delta x^2}+ \frac{p(x^c,y^c-\Delta y)-2p(x^c,y^c)+p(x^c,y^c+\Delta y)}{\Delta y^2} = \psi(x^c,y^c)_{global} \tag{3.48}$$

Where the spatial derivatives on the right hand side of Eq. (3.47) were approximated as

$$\frac{\partial f}{\partial x} \approx \frac{\Delta f}{\Delta x} = \frac{f(x+\Delta x,y+\Delta y)+f(x+\Delta x,y)-f(x,y+\Delta y)-f(x,y)}{2\Delta x} \tag{3.49}$$

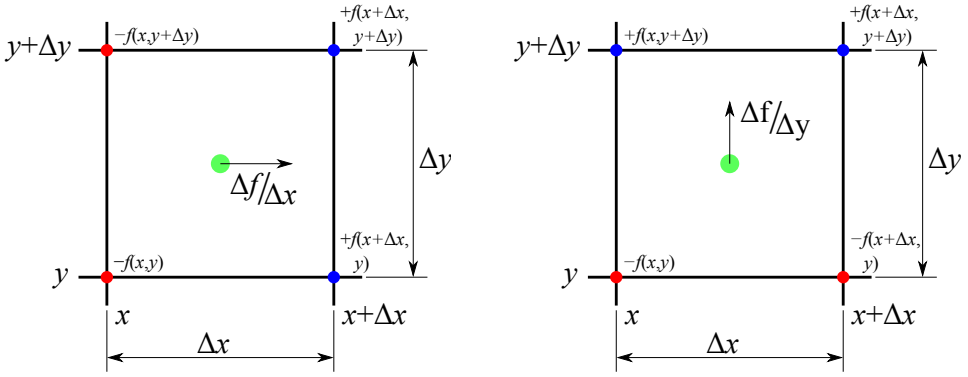

(a) Illustration of $\frac{\Delta f}{\Delta x}$ (b) Illustration of $\frac{\Delta f}{\Delta y}$

Figure 3.8: Illustration of Eqs. (3.49) and (3.50), respectively.

$$\frac{\partial f}{\partial y} \approx \frac{\Delta f}{\Delta y} = \frac{f(x+\Delta x, y+\Delta y) + f(x, y+\Delta y) - f(x+\Delta x, y) - f(x,y)}{2\Delta y} \tag{3.50}$$

Equations (3.49) and (3.50) is illustrated in Figs. 3.8(a) and 3.8(b), respectively. In those figures, the gradient is proportional to the sum of the 4 neighboring points. Next to the numerical boundaries, Eq. (3.48) was treated with the Neumann boundary condition of the approximated form of the pressure gradient as

$$\frac{\partial p}{\partial x} \approx \frac{\Delta p}{\Delta x} = -\rho \left(u\frac{\Delta u}{\Delta x} + v\frac{\Delta u}{\Delta y} \right) \tag{3.51}$$

$$\frac{\partial p}{\partial y} \approx \frac{\Delta p}{\Delta y} = -\rho \left(u\frac{\Delta v}{\Delta x} + v\frac{\Delta v}{\Delta y} \right) \tag{3.52}$$

The treatment of Eq. (3.48) near the boundary depends on the orientation of the respective boundary. The boundaries treatment were

1. Forward scheme along the x-direction. For $x^c = x^c{}_2$, next to the numerical boundary, and $x^c = x^c_{k-1}$, next to the surface of the cylinder, as shown in Fig. 3.9.

$$\frac{1}{\Delta x^2}\Big(p(x^c_1, y^c) - 2p(x^c_2, y^c) + p(x^c_3, y^c)\Big) \\ \frac{1}{\Delta y^2}\Big(p(x^c_2, y^c - \Delta y) - 2p(x^c_2, y^c) + p(x^c_2, y^c + \Delta y)\Big) \\ = \psi(x^c_2, y^c) \tag{3.53}$$

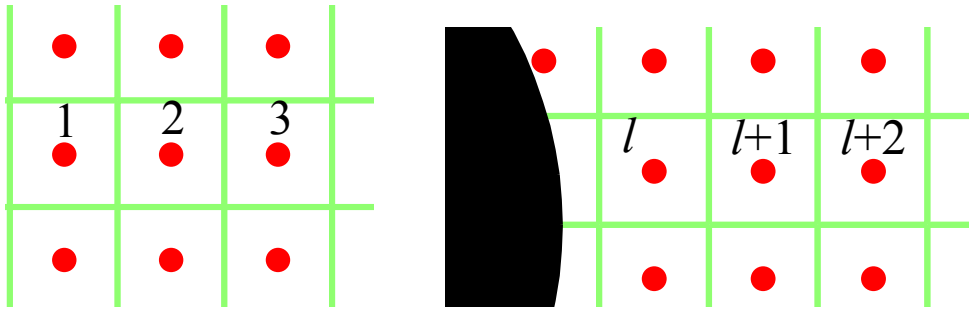

(a) next to the numerical boundary. (b) next to the cylinder.

Figure 3.9: Positions in the global mesh where the forward scheme along x was applied.

Substitute $p(x_1^c, y^c)$ with the one-sided pressure gradient,

$$\begin{aligned} \left.\frac{\Delta p}{\Delta x}\right|_1 &= \frac{-3p(x_1^c,y^c)+4p(x_2^c,y^c)-p(x_3^c,y^c)}{2\Delta x} \\ p(x_1^c,y^c) &= -\frac{2\Delta x}{3}\left.\frac{\Delta p}{\Delta x}\right|_1 + \frac{4}{3}p(x_2^c,y^c) - \frac{1}{3}p(x_3^c,y^c) \end{aligned} \tag{3.54}$$

Thus, Eq. (3.53) becomes

$$\begin{aligned} &\frac{1}{\Delta x^2}\left(-\frac{2}{3}p(x_2^c,y^c)+\frac{2}{3}p(x_3^c,y^c)\right) \\ &\qquad \frac{1}{\Delta y^2}\Big(p(x_2^c,y^c-\Delta y)-2p(x_2^c,y^c)+p(x_2^c,y^c+\Delta y)\Big) \\ &\qquad\qquad = \psi(x_2^c,y^c)+\frac{2}{3\Delta x}\left.\frac{\Delta p}{\Delta x}\right|_1 \end{aligned} \tag{3.55}$$

and the derivation was similar for the other boundary orientation.

2. Backward scheme in x-direction, where $x^c = {x^c}_{M-1}$, next to the boundary, and $x^c = x_{k-1}^c$, next to the surface of the cylinder, as shown in Fig. 3.10.

$$\begin{aligned} &\frac{1}{\Delta x^2}\left(\frac{2}{3}p({x^c}_{M-2},y^c)-\frac{2}{3}p({x^c}_{M-1},y^c)\right) \\ &\quad +\frac{1}{\Delta y^2}\Big(p({x^c}_{M-1},y^c+\Delta y)2p({x^c}_{M-1},y^c)+p({x^c}_{M-1},y^c-\Delta y)\Big) \\ &\qquad = \psi({x^c}_M,y^c)-\frac{2}{3\Delta x}\left.\frac{\Delta p}{\Delta x}\right|_M \end{aligned} \tag{3.56}$$

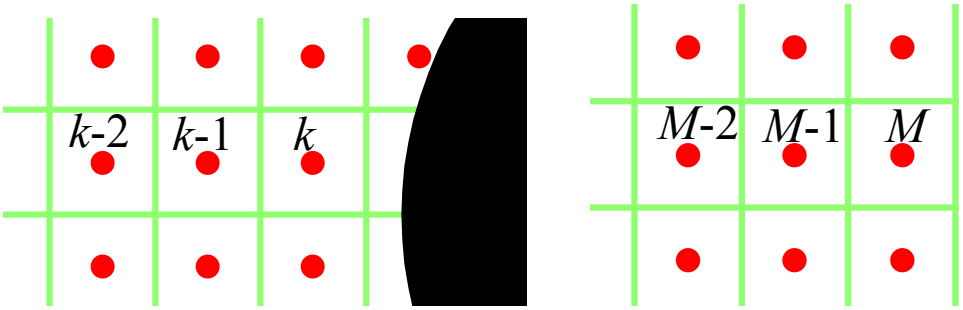

(a) next to the cylinder. (b) next to the numerical mesh.

Figure 3.10: Positions in the global mesh where the backward scheme was applied.

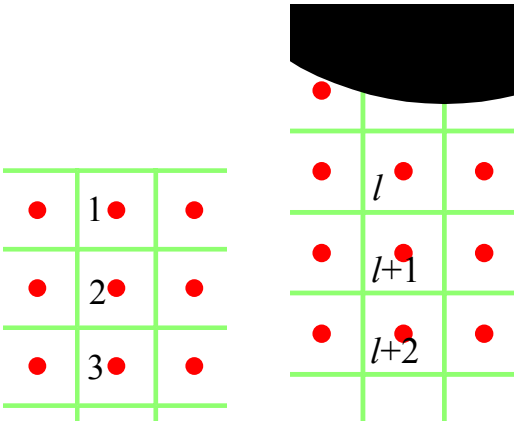

(a) next to the numerical mesh. (b) next to the cylinder.

Figure 3.11: Positions in the global mesh where the forward scheme was applied.

3. Forward scheme in y-direction, where $y^c = y^c{}_1$, next to the boundary, and $y^c = y^c_{l+1}$, next to the surface of the cylinder, as shown in Fig. 3.11.

$$\frac{1}{\Delta x^2}\Big(p(x^c+\Delta x, y^c{}_1)2p(x^c, y^c{}_1)+p(x^c-\Delta x, y^c{}_1)\Big) + \frac{1}{\Delta y^2}\left(-\frac{2}{3}p(x^c, y^c{}_1)+\frac{2}{3}p(x^c, y^c{}_1+\Delta y)\right) = \psi(x^c, y^c{}_1)+\frac{2}{3\Delta y}\frac{\Delta p}{\Delta y}\bigg|_1 \quad (3.57)$$

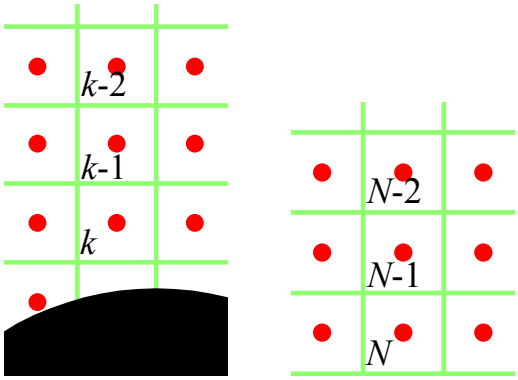

(a) next to the cylinder.

(b) next to the numerical mesh.

Figure 3.12: Positions in the global mesh where the backward scheme was applied.

4. Backward scheme in y-direction, $y^c = y^c_{M-1}$, next to the boundary, and $y^c = y^c_{k-1}$, next the surface of the cylinder, as shown in Fig. 3.12.

$$\frac{1}{\Delta x^2}\left(p(x^c+\Delta x, {y^c}_{M-1}) 2p(x^c, {y^c}_{M-1}) + p(x^c-\Delta x, {y^c}_{M-1})\right) + \frac{1}{\Delta y^2}\left(\frac{2}{3}p(x^c, {y^c}_{M-2}) - \frac{2}{3}p(x^c, {y^c}_{M-1})\right) = \psi(x^c, {y^c}_M) - \frac{2}{3\Delta y}\frac{\Delta p}{\Delta y}\bigg|_M \quad (3.58)$$

3.3.2 Governing equations in local mesh

The Poisson equation in the local mesh,

$$\frac{1}{r}\frac{\partial p}{\partial r} + \frac{\partial^2 p}{\partial r^2} + \frac{1}{r^2}\frac{\partial^2 p}{\partial \theta^2} = \rho\left[\frac{h_r + b_r}{r} + \frac{\partial h_r + b_r}{\partial r} + \frac{1}{r}\frac{\partial}{\partial \theta}(h_\theta + b_\theta)\right] \quad (3.59)$$

where

$$h_r = -\frac{1}{r}\frac{\partial}{\partial r}(r u_r u_r) - \frac{1}{r}\frac{\partial}{\partial \theta}(u_\theta u_r) \quad (3.60)$$

$$b_r = \frac{u_\theta^2}{r} \quad (3.61)$$

$$h_\theta = -\frac{1}{r}\frac{\partial}{\partial r}(r u_r u_\theta) - \frac{1}{r}\frac{\partial}{\partial \theta}(u_\theta u_\theta) \quad (3.62)$$

$$b_\theta = -\frac{u_r u_\theta}{r} \quad (3.63)$$

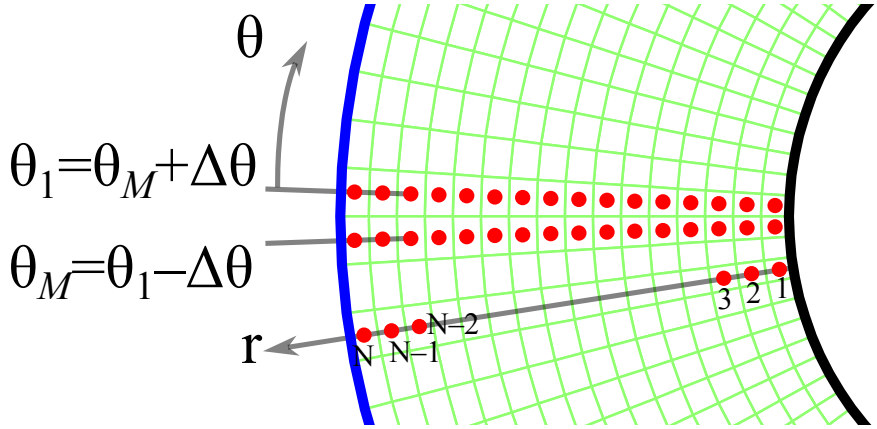

Figure 3.13: The notation for the local mesh.

In the following derivation, the right hand side will be symbolized as ψ_{local}. Equation. (3.59) was discretized as

$$\frac{1}{r}\frac{p(r+\Delta r,\theta)-p(r-\Delta r,\theta)}{2\Delta r} + \frac{p(r+\Delta r,\theta)-2p(r,\theta)+p(r-\Delta r,\theta)}{\Delta r^2} + \frac{1}{r^2}\frac{p(r,\theta-\Delta\theta)-2p(r,\theta)+p(r,\theta+\Delta\theta)}{\Delta\theta^2} = \psi(r,\theta)_{local} \quad (3.64)$$

The boundary condition in the r-direction was the surface pressure gradient and in the θ-direction, periodic boundary was applied,

$$\theta_1 = \theta_M + \Delta\theta \quad (3.65)$$

$$\theta_M = \theta_1 - \Delta\theta \quad (3.66)$$

where the subscript M is the last node along θ. The boundary condition on the numerical boundary, $r = r_N$, was the pressure values interpolated from the global mesh. The boundary condition next to the surface, $r = r_1$, was

$$\frac{\partial p}{\partial r} \approx \frac{\Delta p}{\Delta r}\bigg|_w = \rho\left(-\frac{\Delta h_{r1}}{\Delta r} - \frac{1}{r}\frac{\Delta h_{r2}}{\Delta\theta} + \frac{u_\theta^2}{r}\right) \quad (3.67)$$

The notation of the local mesh is given in Fig. 3.13.

The Poisson equation was treated for the boundary condition on $r = r_2$,

$$\frac{1}{r}\frac{\frac{4}{3}p(r_3,\theta)-\frac{4}{3}p(r_2,\theta)}{2\Delta r}+\frac{-\frac{2}{3}p(r_2,\theta)+\frac{2}{3}p(r_3,\theta)}{\Delta r^2}+ \\ \frac{1}{r^2}\frac{p(r_2,\theta-\Delta\theta)-2p(r_2,\theta)+p(r_2,\theta+\Delta\theta)}{\Delta\theta^2}=\psi(r_2,\theta)_{local}+\frac{2}{3}\left(\frac{1}{\Delta r}-\frac{1}{2r}\right)\left.\frac{\Delta p}{\Delta r}\right|_1 \tag{3.68}$$

and on the numerical boundary $r = r_{N-1}$,

$$-\frac{1}{r}\frac{p(r_{N-2},\theta}{2\Delta r}+\frac{-2p(r_{N-1},\theta)+p(r_{N-2},\theta)}{\Delta r^2} \\ +\frac{1}{r^2}\frac{p(r_{N-1},\theta)-2p(r_{N-1},\theta)+p(r_{N-1},\theta+\Delta\theta)}{\Delta\theta^2} \\ =\psi(r_{N-1},\theta)-\left(\frac{1}{2r\Delta r}+\frac{1}{\Delta r^2}\right)p(r_N,\theta) \tag{3.69}$$

The pressure on the surface of the cylinder was extrapolated from the pressure solved on the center nodes,

$$p|_w=\frac{15}{8}p(r_1,\theta)-\frac{5}{4}p(r_2,\theta)+\frac{3}{8}p(r_3,\theta) \tag{3.70}$$

where

$$p(r_1,\theta)=-\frac{2}{3}\left.\frac{\Delta p}{\Delta r}\right|_w\Delta r+\frac{4}{3}p(r_2,\theta)-\frac{1}{3}p(r_3,\theta) \tag{3.71}$$

and the non-dimensional pressure coefficient was

$$C_p=\frac{p|_w}{\frac{1}{2}\rho U_\infty^2} \tag{3.72}$$

3.4 Numerical solution to Poisson equation

The pressure was solved using the Gauss-Seidel method. For the next discussion, the matrix is symbolized as

$$A\mathbf{x}=\mathbf{b} \tag{3.73}$$

In the Gauss-Seidel method, the matrix A is split into A_1 and A_2,

$$A=A_1-A_2 \tag{3.74}$$

where

$$A_1 = D - L \tag{3.75}$$

$$A_2 = U \tag{3.76}$$

and D is the matrix consisting of the diagonal elements of A, L is the matrix consisting of the negative of the lower triangular elements of the matrix A, and U is the matrix consisting of the negative of the upper triangular element of the matrix A. The unknown variable $\mathbf{x}$ is solved by

$$\mathbf{x}^{k+1} = A_1^{-1} A_2 \mathbf{x}^k + A_1^{-1} b \tag{3.77}$$

where k is the iteration number.

The iteration was stopped when the convergence criteria has been achieved. The convergence criteria was defined according to the rate of the absolute value of the residual. The residual was defined as

$$A\mathbf{x}^k = b + R^k \tag{3.78}$$

$$R^k = A\mathbf{x}^k - b \tag{3.79}$$

where R^k is the residual of the k^{th} iteration, and the convergence is normalized with R of the third iteration.

$$\varepsilon = \frac{\sum \|R^k - R^{k-1}\|}{R^3} \tag{3.80}$$

$$\tag{3.81}$$

The convergence criteria was $\varepsilon \leq 1 \times 10^{-3}$ for both global mesh and local mesh.

3.5 Numerical results

The velocity distribution around a circular distribution was defined using Eqs. (3.21)–(3.23). The flow parameters to create this distribution were $U_\infty = 3000$, $R = 0.7284$. The size of the global mesh was $-4 \leq x \leq 4$ and $-4 \leq y \leq 4$, where $\Delta x = \Delta y = 0.2$. The size of the local mesh was $R \leq r \leq R + 16\Delta r$, where $\Delta R = 0.25$ and $0 < \theta \leq 2\pi$, where $\Delta\theta = \pi/50$.

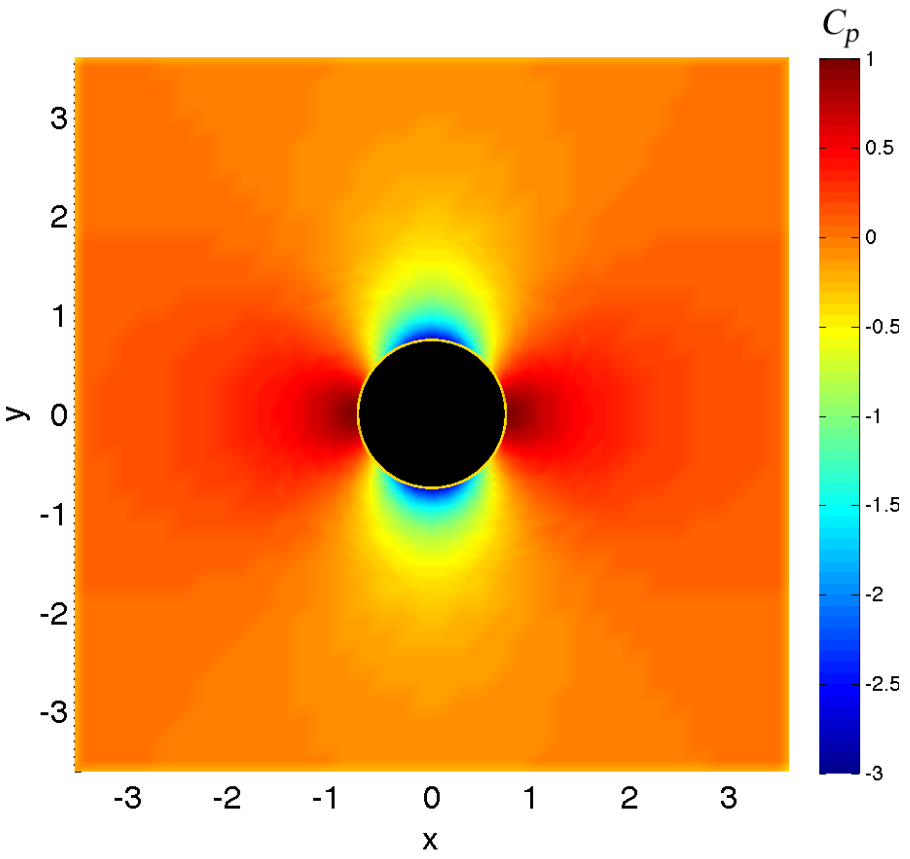

Figure 3.14: The estimated pressure field.

The result of the numerical evaluation of the overlapping mesh method using the potential flow over a circular cylinder is given in Fig. 3.14. The contour depicts the coefficient of pressure and the circular cylinder is depicted as a black circle. In this figure, the pressure distributions of the global and local meshes are plotted together giving smooth pressure distribution on the surface of the cylinder as resolved in the local mesh and no apparent discontinuity between the global and local meshes. The estimated pressure distribution shows two stagnation pressure points on the leading and trailing edge of the cylinder and two low pressure regions on the top and bottom surface of the cylinder.

The absolute error of the pressure distribution is given in Fig. 3.15 where the error is the difference of the absolute values of the estimated pressure field with that of the

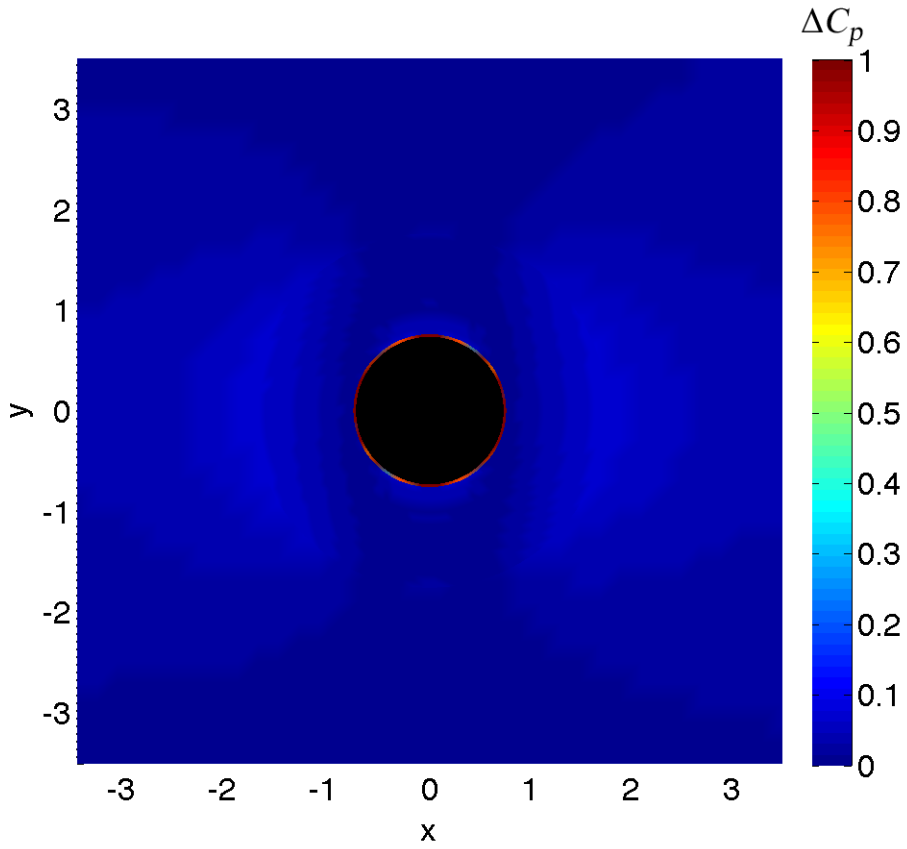

Figure 3.15: The absolute error between Fig. 3.14 and the analytical pressure distribution.

analytical. The maximum error of the estimation is $\Delta C_p \approx 0.07$.

The estimated pressure distribution on the surface of the cylinder is shown in Fig. 3.16 from the trailing edge, counter-clockwise. This distribution is compared with the analytical pressure distribution and they show good agreement with each other.

The pressure profile Fig. 3.17 is the pressure distribution along x at $y = 0$. There is continuous pressure distribution from the global mesh to the local mesh. Comparison of the estimated pressure distribution of both meshes with the analytical pressure distribution shows good agreement with each other. The pressure profile in Fig. 3.18 is the pressure distribution along y at $x = 0$, which similar to the last figure shows good agreement with the analytical pressure distribution.

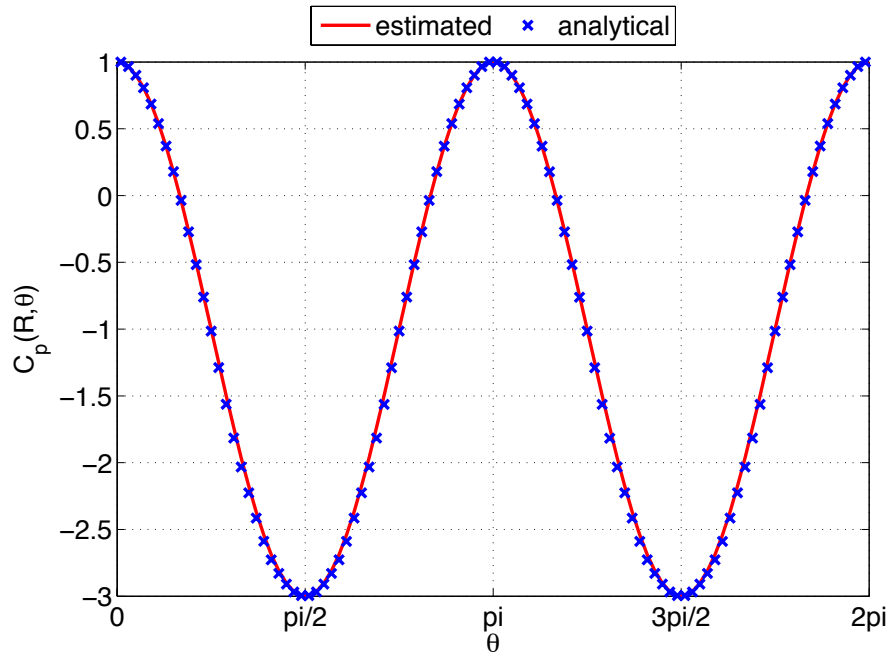

Figure 3.16: Pressure distribution on the surface of the cylinder.

3.6 Concluding remarks

The procedure to solve the Poisson equation with overlapping meshes was evaluated using a circular cylinder in a potential flow. Using potential flow the analytical velocity and pressure distribution were known. To emulate the condition of measurement, the velocity vectors were distributed in a grid system as if they were measured with PIV. Continuous pressure distribution was achieved between the global and local mesh. Comparison of the estimated pressure distribution and the analytical one shows good agreement on the surface of the plate and on all parts of the flow.

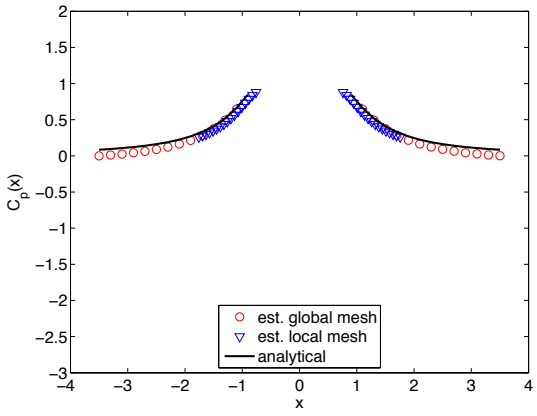

Figure 3.17: Pressure distribution along x at $y = 0$.

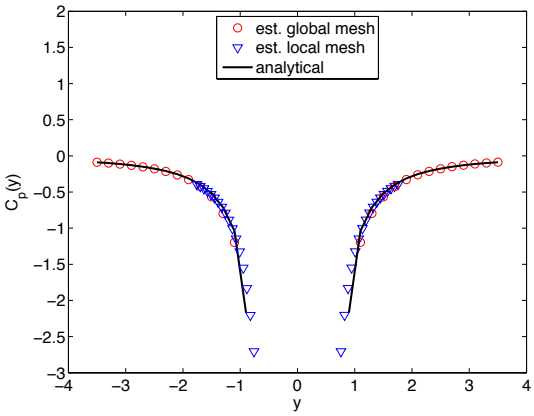

Figure 3.18: Pressure distribution along y at $x = 0$.

Chapter 4

Experimental Setup

The facility is explained in §4.1, which include the tank where the measurement took place, the flapping wing model and its kinematics. Followed by, §4.2 discussing the basic theory of PIV and stereo PIV measurement setup, and finally §4.3 explaining about the strain gauge measurement setup.

4.1 Facility

The hovering condition was recreated by conducting experiments inside an all around transparent tank. The volume of the tank was $310 \times 310 \times 270\text{mm}^3$ volume and was filled with tap water. The wing was modeled as a rectangular transparent plate with span length, b, of 40mm, chord length, c, of 20 mm, and thickness of 2 mm. The plate was fully immersed in water and it maintained its rigidity during all flapping cycle. The sinusoidal motion of the wing was defined as

$$\theta = \Theta \sin(2\pi f t) \tag{4.1}$$

$$x = r\cos(\theta) \tag{4.2}$$

$$y = r\sin(\theta) \tag{4.3}$$

where θ is the instantaneous flapping angle of the plate, Θ is defined as the amplitude of the flapping angle, f is the flapping frequency, and t is the time variable. The instantaneous position of the plate in Cartesian coordinate is represented by x and y, which

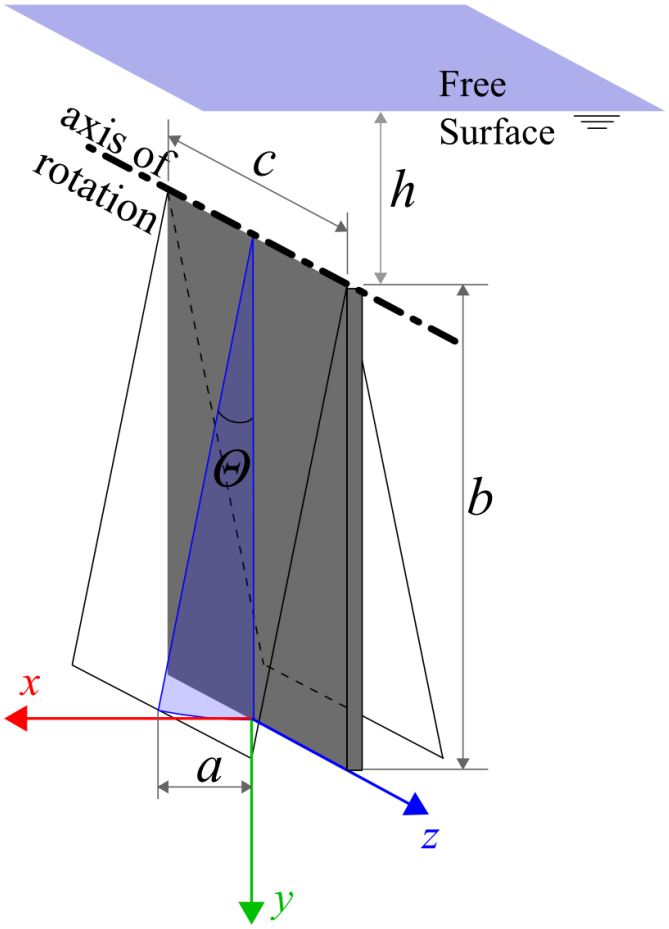

Figure 4.1: The geometry of the flapping plate and definition of the flapping kinematics.

corresponds to θ, where the coordinate orientation is defined in Fig. 4.1, and r is in the spanwise direction of the plate, where $0 \leq r \leq b$, $r = 0$ is the hub of the flapping plate and $r = b$ is the tip of the plate.

The velocity of the plate in the normal direction of the plate is

$$\begin{aligned} u_{plate} &= \dot{\theta} r \\ &= 2\pi f \Theta r \cos(2\pi f t) \end{aligned} \tag{4.4}$$

Of particular interest is the maximum velocity of the tip, where $r = b$ and $\theta = 0$. Which gives $u_{plate,tip} = 2\pi f(b\Theta)$. Here, $b\Theta$ is the amplitude of the flapping wing. This velocity

is used as the reference velocity, $U = u_{plate,tip}$, for the definition of the Reynolds number,

$$\mathrm{Re} = \frac{cU}{\nu} \tag{4.5}$$

where ν is the kinematic viscosity of water. The plate was immersed in water 80 mm below the free surface. TiO_2 powder was used for tracer particles.

The motion of the plate was actuated by a 5-phase stepping motor series, RK566BA, from Oriental Motor Co.,Ltd (2002). The motion was synchronized with PIV measurement using National Instruments' PCI 7332 motion control board and motion control software, NI–motion (2006). Due to indirect compatibility of the motor and the motion controller, the input from the motion controller was relayed through National Instruments' Universal Motion Interface, UMI-7664 (2010).

For the purpose of this study, a sinusoidal motion of the plate was required by using the circular arc motion in NI–motion. The circular arc interpolates a circular motion when used with two motors that are at 90° out of phase with each other. In this case, only one of the two motion axis was used, which created a sinusoidal motion for the flapping wing. The key settings of the circular arc motion are,

1. circular arc
2. travel angle
3. starting position
4. start angle
5. arc radius
6. ending position

The arc radius sets how far the motor of each axis have to travel. The start angle is the starting angle of the arc. The travel angle is the angle to be traversed, which ranges from -4096 to 4095 revolutions. Positive travel angle is defined as counter-clockwise rotation in the xy plane.

The circular motion can be defined as follows,

$$\text{for axis 1: } x_1 = R\sin(\omega t) \tag{4.6}$$

$$\text{for axis 2: } x_2 = R\cos(\omega t) \tag{4.7}$$

where R is the arc radius. For this study, only one axis was needed to generate the flapping motion. The maximum flapping deflection, Θ can be adjusted by adjusting the arc radius,

$$\Theta = \frac{360^{\circ}(R)}{2(Resolution)} \tag{4.8}$$

Where R is in steps and $Resolution$ is the number of steps to complete one revolution. To ensure smoothness, a resolution of $125,000$ steps per revolution was used, which gives fine motion of $0.00288^{\circ}/\text{step}$.

The motion control system and PIV measurement system were synchronized using the Real Time System Integration (RTSI) cable connecting the motion controller, NI-7332, with digital timing board, NI PCI-6602 (2009; 1999).

4.2 Particle Image Velocimetry

In qualitative flow visualization, flow markers, usually injected into the flow upstream of a body or injected from the surface a body, are used to highlight certain regions of interest when the flow passes over the body. These markers, such as dye or smoke, highlight certain structures in the flow that contribute to the flow physics. Some examples of the use of this technique are: visualization of mixing layers, wake behind cylinder, or transient flow over an airfoil.

For future use of the knowledge of flow structures, the visualizations are recorded by film photography or by moving images. Long exposure recordings of the markers will produce streaklines. Because of that, streaklines do not indicate the instantaneous structure of the flow. The long exposure creates flow structures that are produced on the surface of the body because of shearing forces. Shear stress causes the markers to deform and creates unique shapes that we recognize as vortices. The vortices are convected downstream and they retain their shape in weak shear stress or no shear at all.

A short exposure of the flow markers can estimate the flow streamlines. Streamlines are better indicators of flows because it temporally localizes the flow structure where it is produced and shows the spatial evolution of the flow from upstream to the downstream of the body. Because of the short exposure, streamlines are visualized using a homogeneously distributed particles in the flow.

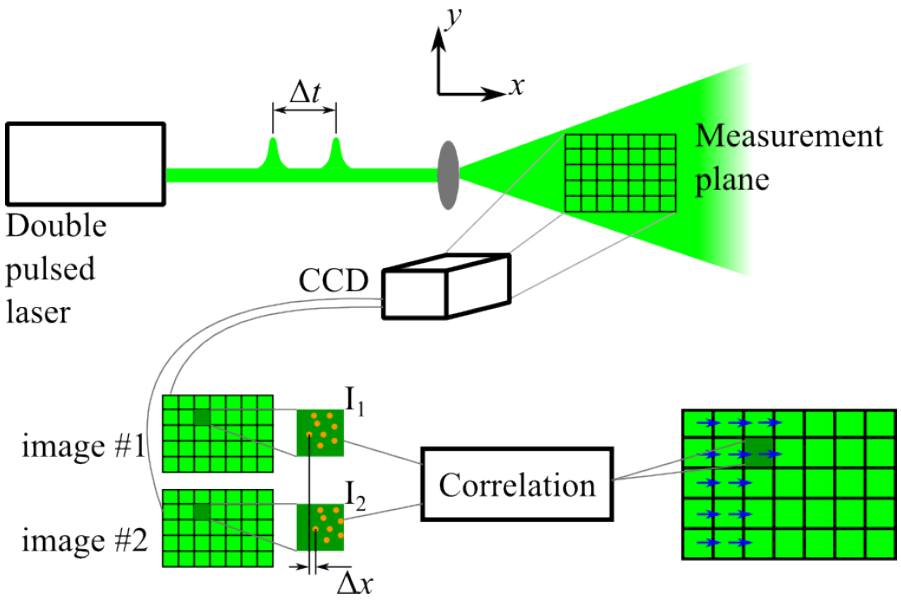

Figure 4.2: Principles of PIV measurement.

Particle image velocimetry (PIV) quantifies flow visualization by measuring the displacement of tracers that are in the form of discrete particles. Physically, velocity is defined as

$$u = \frac{\partial x}{\partial t} \tag{4.9}$$

and its discrete version is

$$v = \frac{x(t) - x(t + \Delta t)}{\Delta t} \tag{4.10}$$

with limit theory, $\Delta t \rightarrow 0$,

$$v \approx u \tag{4.11}$$

PIV records the flow in two short exposures consecutively. The exposures are separated within a short time span, Δt, for good approximation of the flow velocity. Since Willert and Gharib (1991), digital PIV has been in use for flow research. Each exposure is stored as a digital grayscale images and the velocity field is approximated by two consecutive digital images. Figure 4.2 shows how PIV works.

A digital image is a discrete representation of an analog image. Intensity of light is represented by integer values from 0 to 255. For a digital grayscale image, the color black is represented by the value 0, the color white is represented by the value 255, and

(a) The character "x".

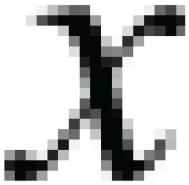

(b) Digital image representation.

255	255	255	241	191	144	96	98	255	255	255	255	255	237	103	70	181
255	255	222	81	35	4	4	4	154	255	255	255	202	22	4	4	23
255	255	255	255	255	203	6	4	21	255	255	220	21	69	52	9	104
255	255	255	255	255	255	123	4	4	201	252	44	162	255	255	255	255
255	255	255	255	255	255	222	4	4	125	130	117	255	255	255	255	255
255	255	255	255	255	255	255	29	4	29	40	249	255	255	255	255	255
255	255	255	255	255	255	255	94	4	4	179	255	255	255	255	255	255
255	255	255	255	255	255	255	158	4	4	186	255	255	255	255	255	255
255	255	255	255	255	255	255	203	4	4	128	255	255	255	255	255	255
255	255	255	255	255	255	255	91	4	4	69	255	255	255	255	255	255
255	255	255	255	255	255	201	55	77	4	12	254	255	255	255	255	255
255	255	255	255	255	255	60	205	138	4	4	207	255	255	255	255	255
255	255	255	255	255	140	105	255	195	4	4	150	255	255	241	191	255
255	255	255	255	198	24	241	255	249	6	4	80	255	255	77	187	255
158	74	192	236	33	186	255	255	255	62	4	9	235	124	96	255	255
26	4	4	13	149	255	255	255	255	139	4	4	6	72	249	255	255
120	5	41	158	255	255	255	255	255	242	36	8	110	249	255	255	255

(c) Discrete values of intensity

Figure 4.3: The character "x" and its representation as a digital image. A digital image can be represented by colors or by numbers. The latter is enlarged to visualize pixels and the intensity.

there are 254 gray tones between them. Constant intensity is contained within a discrete unit called *pixel* as shown in Fig. 4.3

The velocity is approximated by correlating a localized area of the image, called interrogation window. In Eq. (4.12), the interrogation window of the first image is represented with I_1 and for the second image with I_2. The result of the correlation function of Eq. (4.12) is the correlation map, $C(\delta i, \delta j)$, as shown in Fig. 4.4

$$C(\delta i, \delta j) = \frac{\sum_{i=1}^{M} \sum_{j=1}^{N} I_1(i,j) * I_2(i+\delta i, j+\delta j)}{\sqrt{\sum_{i=1}^{M} (I_1(i,j))^2} \sqrt{\sum_{i=1}^{N} (I_2(i,j))^2}} \tag{4.12}$$

where i, j are the indices for row and column matrix of a digital image, respectively

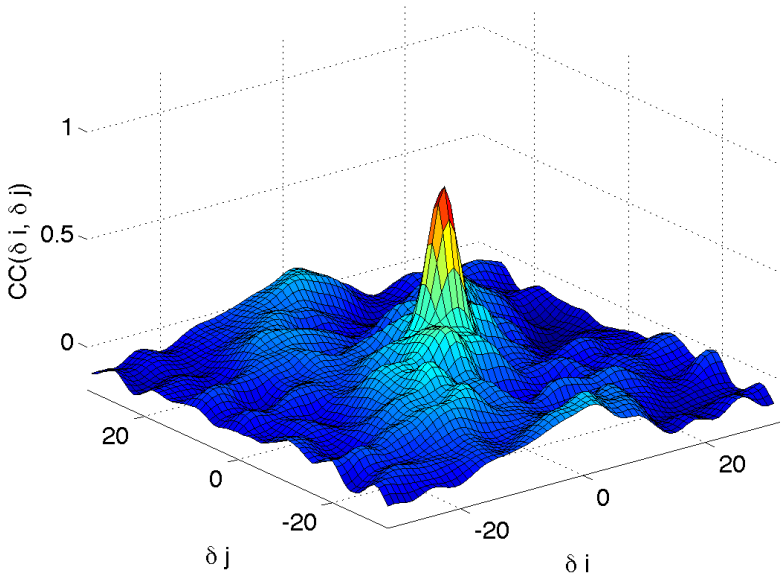

Figure 4.4: Cross-correlation map that corresponds with $-32 \leq \delta i \leq 32$ and $-32 \leq \delta j \leq 32$, produced from two successive particle images.

and the size of the interrogation window is $M \times N$ pixels and $M > 1$ pixel and $N > 1$ pixel. The correlation map was calculated by displacing the second image by $\delta i, \delta j$ pixel ranging from $-M$ to M pixel and $-N$ to N pixel, respectively. When the particles completely overlap, Eq. (4.12) will produce good correlation, ie. $C(\delta i, \delta j) = 1$, and for no correlation, ie. $C(\delta i, \delta j) = 0$. Average displacement of particles from I_1 to I_2, is indicated by index of the maximum correlation, (δ'_i, δ'_j). The average displacement is the nominator of Eq. (4.10) and Δt is the denominator.

The size of the interrogation window is a disadvantage in PIV. A rule of thumb exist where the size of the interrogation window should be at least be 4 times of the displacement. However, this is no longer a concern since research-grade digital cameras can capture two images within 2ms, which would give a very short displacement. With such cameras, the main concern is the amount particles within the interrogation window. An interrogation window is required to contain a few particles in order to produce good correlation map and each window will be represented by one velocity vector in the

vector field. Thereby, the velocity vector is an average of the individual velocity of a few particles in an interrogation window. An interrogation window of $32 \times 32\text{pixel}^2$ is commonly used.

The discrete unit of pixel causes low spatial resolution of the velocity that is overcame by using a Gaussian weighted interpolation,

$$x_0 = i + \frac{\ln(C(i-1,j)) - \ln(C(i+1,j)}{2\ln C(i-1,j) - 4\ln C(i,j) + 2\ln C(i+1,j)} \tag{4.13}$$

$$y_0 = j + \frac{\ln(C(i,j-1)) - \ln(C(i,j+1)}{2\ln C(i,j-1) - 4\ln C(i,j) + 2\ln C(i,j+1)} \tag{4.14}$$

The resolution is improved up to 0.01 pixel with Gaussian weighted interpolation.

Because the correlation map was calculated by shifting the second image one pixel at a time for both vertical and horizontal directions of the image, the areas near the edge of the image experience a lost of signal quality. In order to maintain any form of quality, the size of I_2 is usually made twice larger than I_1. One can make the size of I_2 as large as possible, however this may give false positive correlations. This means good correlation maybe found far from the first interrogation area giving large velocity vector, which is due to the random nature of particle patterns obtained in the flow recording.

Improvements to correlation can be achieved by moving the interrogation window of the second image by the amount of corresponding displacement (Westerweel et al, 1997). This method requires at least two correlations. First, as a rough measure of displacement and the interrogation window of the second image is shifted using this information. The second correlation will give a correlation map closer to a Gaussian profile. Thereby, giving better interpolation result.

In using Eq. (4.12), the mathematical operation is performed $4MN$ times. To improve the speed of the operation, the correlation can be performed using Fourier transform. In digital imaging, the two dimensional discrete Fourier transform is used,

$$F(u,v) = \frac{1}{MN} \sum_{i=1}^{M} \sum_{j=1}^{N} f(i,j) e^{-\sqrt{-1}2\pi(ui/M + vj/N)} \tag{4.15}$$

and the inverse transform is

$$f(i,j) = \sum_{u=1}^{M} \sum_{v=1}^{N} F(u,v) e^{\sqrt{-1}2\pi(ui/M + vj/N)} \tag{4.16}$$

The transformation is symbolized by $\mathcal{F}$ and the inverse transformation is $\mathcal{F}^{-1}$. Commonly fast Fourier transform is used for PIV. The correlation is formulated as

$$R = \mathcal{F}^{-1}(\mathcal{F}(I_1) * \mathcal{F}^*(I_2)) \tag{4.17}$$

and the normalized correlation map is

$$C = \frac{R}{\sqrt{\sum_{i=1} M(I_1(i,j))^2}\sqrt{\sum_{i=1} N(I_2(i,j))^2}} \tag{4.18}$$

where $\mathcal{F}^*$ is the complex conjugate of $\mathcal{F}$.

In three-dimensional flow, the velocity component normal to the measurement plane is as important as the other components. To measure the normal component (Willert, 1997) configured PIV for stereoscopic use; this configuration is called stereo PIV.

In stereo PIV, two cameras are pointed to a point on the laser sheet illuminating the flow. The projection of the flow in the object plane onto the image plane of each camera provides two views of the flow which can be reconstructed using stereo projection. In optical terms, the object plane is the location of the real object perpendicular to the optical axis and the image plane is the surface of the sensor where the real object is projected in the optical system. The cameras are commonly in an angular configuration known as the Scheimpflug configuration, which improves the focus of an image by setting the lens plane at an angle respective to the image plane (Zang and Prasad, 1997). The Scheimpflug configuration specifies that object, lens, and image planes intersect with each other as shown in Fig. 4.5.

For each camera two-dimensional images are recorded and two-dimensional displacement vectors are obtained by using the image analysis explained in §4.2. Three-dimensional velocity vectors can be obtained by reconstructing from two sets of two-dimensional velocity vector field that are acquired simultaneously from two viewing angles. The reconstruction method is related to the position of the cameras with respect to the object plane. In Soloff et al (1997), the reconstruction method is related to the camera calibration by approximating the projective function from images obtained from

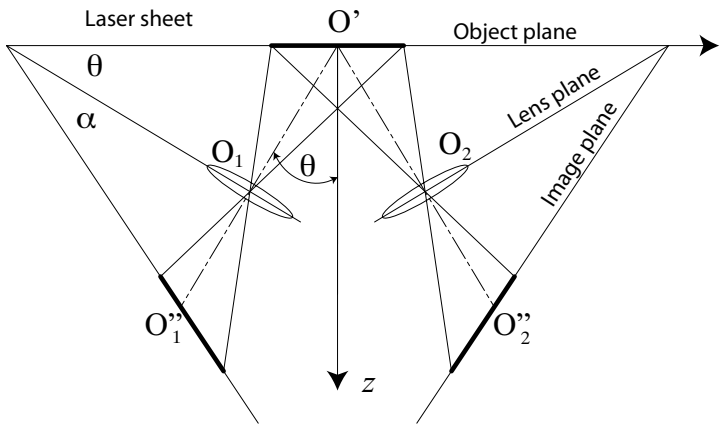

Figure 4.5: The Scheimpflug configuration for stereo PIV.

the calibration process.

$$\begin{aligned}\mathbf{F}(x) =& \mathbf{a}_0 + \mathbf{a}_1 x_1 + \mathbf{a}_2 x_2 + \mathbf{a}_3 x_3 + \mathbf{a}_4 x_1^2 \\ &+ \mathbf{a}_5 x_1 x_2 + \mathbf{a}_6 x_2^2 + \mathbf{a}_7 x_1 x_3 + \mathbf{a}_8 x_2 x_3 \\ &+ \mathbf{a}_9 x_3^2 + \mathbf{a}_{10} x_1^3 + \mathbf{a}_{11} x_1^2 x_2 + \mathbf{a}_{12} x_1 x_2^2 \\ &+ \mathbf{a}_{13} x_2^3 + \mathbf{a}_{14} x_1^2 x_3 + \mathbf{a}_{15} x_1 x_2 x_3 + \mathbf{a}_{16} x_2^2 x_3 \\ &+ \mathbf{a}_{17} x_1 x_3^2 + \mathbf{a}_{18} x_2 x_3^2\end{aligned} \tag{4.19}$$

where $\mathbf{a}_i$ are vector valued coefficients that are obtained from the calibration and x_i are the coordinates in the objects plane, (x_1, x_2, x_3). The projective function relates the object plane with the image plane.

$$\mathbf{X} = \mathbf{F}(x) \tag{4.20}$$

where $\mathbf{X}$ is a four element vector representing the coordinates of the image plane, $\mathbf{X} = (X_1^1, X_2^1, X_1^2, X_2^2)$, where the superscript $(1), (2)$ is the notation for camera 1 and 2, respectively. From the calibration plane, $\mathbf{x}$ is known and from the calibration images, $\mathbf{X}$ is known. The coefficients, $\mathbf{a}_i$ from Eq. (4.19), can be calculated using the least square approach.

The particle image displacement is

$$\Delta\mathbf{X} = \mathbf{F}(\mathbf{x} + \Delta\mathbf{x}) - \mathbf{F}(\mathbf{X}) \tag{4.21}$$

$$\Delta\mathbf{X} \approx \nabla\mathbf{F}(\mathbf{x})\Delta\mathbf{x} \tag{4.22}$$

in tensor form, $\nabla \mathbf{F}$, is formulated as

$$\nabla \mathbf{F} = (\nabla F)_{ij} = \frac{\partial F_i}{\partial x_j} = F_{i,j} \tag{4.23}$$

with $i = 1,2$ and $j = 1,2,3$. In index notation,

$$\begin{bmatrix} \Delta X_1^{(1)} \\ \Delta X_2^{(1)} \\ \Delta X_1^{(2)} \\ \Delta X_2^{(2)} \end{bmatrix} = \begin{bmatrix} F_{1,1}^{(1)} & F_{1,2}^{(1)} & F_{1,3}^{(1)} \\ F_{2,1}^{(1)} & F_{2,2}^{(1)} & F_{2,3}^{(1)} \\ F_{1,1}^{(2)} & F_{1,2}^{(2)} & F_{1,3}^{(2)} \\ F_{2,1}^{(2)} & F_{2,2}^{(2)} & F_{2,3}^{(2)} \end{bmatrix} \begin{bmatrix} \Delta x_1 \\ \Delta x_2 \\ \Delta x_3 \end{bmatrix} \tag{4.24}$$

The equation solves for the three dimensional particle displacement. With an overestimated system such as Eq. (4.24), the displacement is calculated by the least square method.

$$\Delta \mathbf{x} = \left(\nabla \mathbf{F}^T \nabla \mathbf{F}\right)^{-1} \nabla \mathbf{F}^T \Delta \mathbf{X} \tag{4.25}$$

The out-of-plane displacement, Δx_3, is given by recording the calibration plate at several out-of-plane positions. The advantage of the calibration method is that the aberration of the image caused by the lens will be included in the projection function giving high accuracy in the velocity reconstruction.

The stereo PIV configuration allows the measurement of three velocity components on a plane. It depicts a slice of three-dimensional flow. The investigation of three-dimensional flow also requires the measurement of the velocity gradient normal to the measurement plane. This gradient can be measured by investigating the three-dimensional flow on several measurement planes offset along the normal direction.

A home built stereo PIV was used in the measurement of flow velocity. Two Redlake Megaplus ES 1.0 digital cameras were used in Scheimpflug configuration to obtain images with good focus for every points in the measurement plane (Zang and Prasad, 1997; Prasad, 2000). The Scheimpflug condition was fulfilled with Nikkor 85mm special perspective lenses attached to each camera (Foo, 2001). Each camera was focused on an area close to the tip of the wing. The size of the viewing plane for each camera was $1,017 \times 1,008$ pixels (Redlake MASD, Inc, 2001). Each camera was connected to a frame grabber National Instruments PCI-1422 which has an 8-bit image depth (National Instruments Co., 2001). Illumination was provided by a 5mm thick Nd:YaG laser

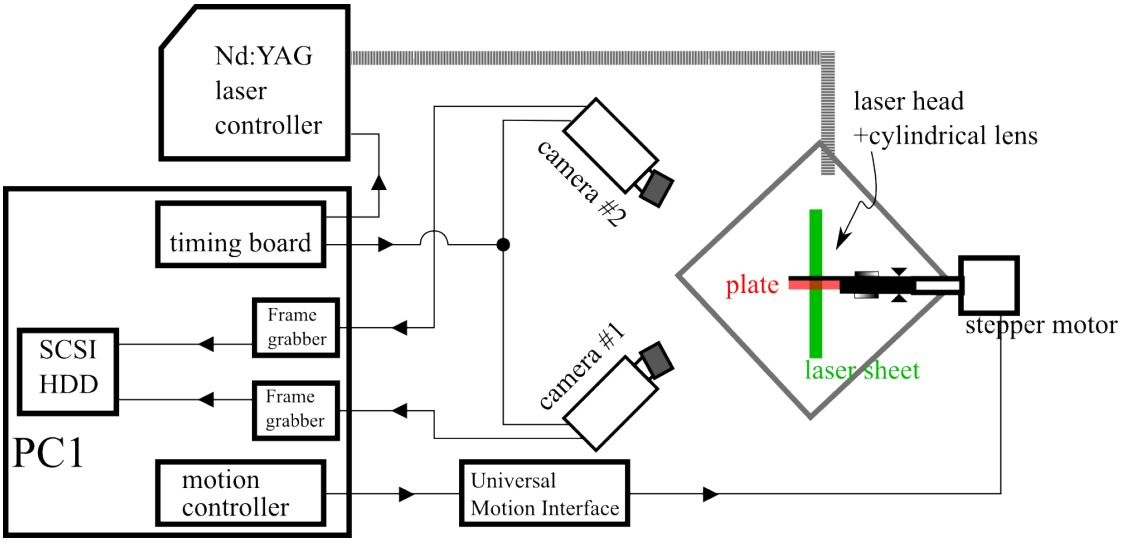

Figure 4.6: Setup of PIV measurement system.

pulsed through a biconcave lens to produce a light sheet (New Wave Research, 2003), TiO_2 tracer particles, which has particle diameter of 20-200 μm and specific density of 0.01-0.04, were used and produced images of particles of approximately 3-4 pixel diameter (Ishihara Sangyo Kaisha, 2006). The particles were homogeneously distributed at a concentration of approximately 0.018%. After approximately 1000 flapping cycles, a thin layer of particles appeared on the floor of the tank. However sufficient particles remain suspended in the water. From this layer, we assume no large-scale circulation of flow occurred within the tank. The measurement configuration is illustrated in Fig. 4.6.

To measure the velocity gradients in all three directions of space. Measurements were conducted on several measurement planes separated a few millimeters in the normal direction of the measurement area. For accurate displacement of the measurement plane and in order not to repeat the calibration process for every displacement, the laser sheet position relative to the tank was fixed and the actuating mechanism, motor and flapping axis, were set on a single axis traversing stage with 0.05mm traverse accuracy. To ensure that the position of the flapping plate was fixed during the measurement, the traversing stage was equipped with a clamp and the frame that housed the rotation axis was clamped as well.

An inertial damper was attached on one end of the motor and a coupling were at-

tached on the other end, where the rotation of the motor's axis was transferred to the flapping axis by a polyurethane timing belt to minimize the effect of vibration from the motor.

One flapping cycle, $0 \leq \phi < 2\pi$, was discretized into 20 phase angles with the phase angle step $\Delta\phi = 0.05f$. Each measurement collected a large number of image pairs. The recording of an image pair was separated by $\Delta t = 2$ms for each exposure. The normalized phase angle was $\hat{\phi} = 0, 0.05, \cdots, 0.95$ to represent one flapping cycle, $0 \leq \hat{\phi} < 1$.

Particle images were processed with a two-step algorithm (Westerweel et al, 1997) with $32 \times 32\text{pixel}^2$ interrogation window and the calibration method (Soloff et al, 1997) was used to reconstruct the 3D velocity field with five calibration planes, $z = (-2.5, -1, 0, 1, 2.5)$mm, to approximate a fourth order projection polynomial. Phase averaging was used to minimize the random error and a new term appeared in the governing equation because of that. In turbulence, this term is called the Reynolds stress, which is a product of the fluctuative velocity. The velocity fluctuation, is the difference of the instantaneous velocity with the phase-averaged velocity.

The calibration plate was made from water resistant paper and the calibration image was printed on it. The calibration image consisted of white dots to mark the position of the calibration points as shown in Fig. 4.8. These markers were 1.5mm in diameter and were set 3mm apart. The markers were circular and had constant intensity value of 255. The marker at the center of the calibration plate was shaped as a square to indicate the center of the recorded images. The calibration paper was attached to an aluminum plate with double sided adhesive tape. Additional thickness of the paper and the adhesive tape was taken into account by carefully positioning the calibration image at the middle of the laser sheet. The calibration plate was positioned by attaching it to a two-axis traversing stage which has traversing accuracy of 0.05mm.

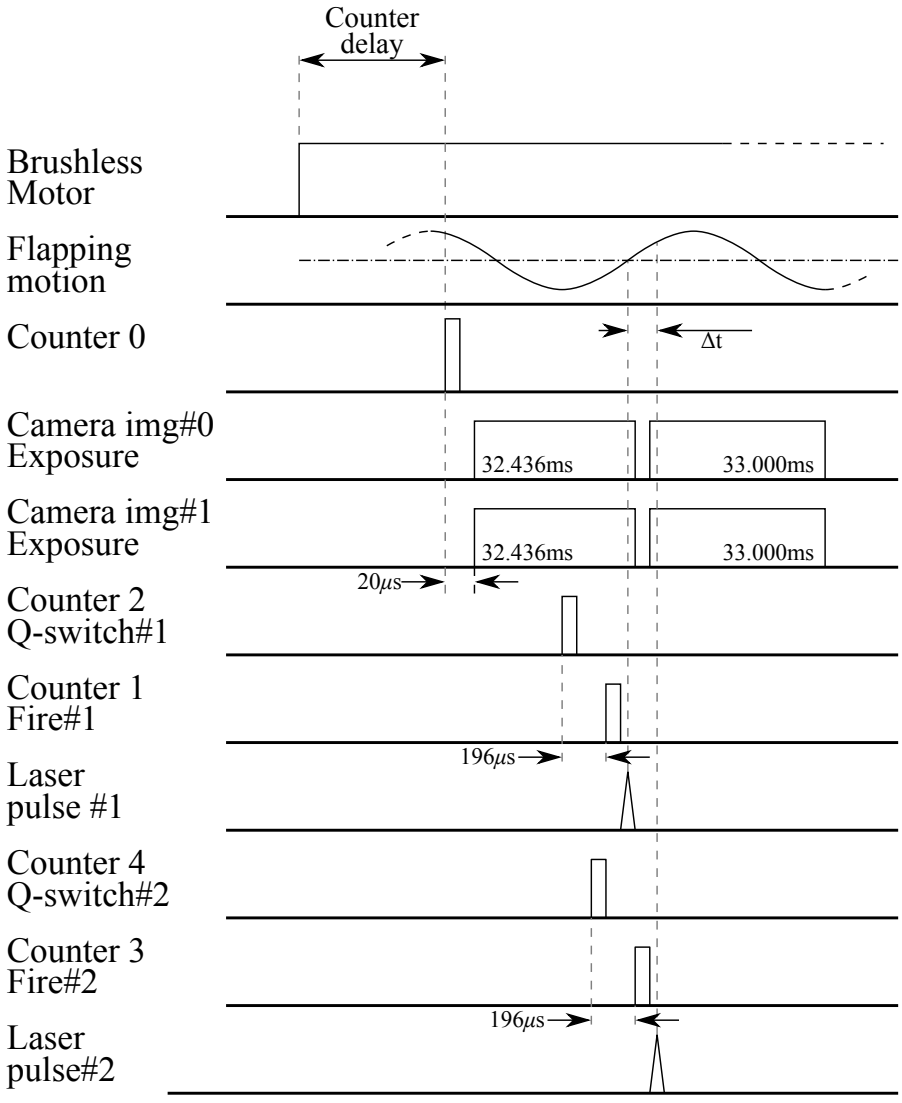

Figure 4.7: Timing chart of to synchronize PIV with flapping motion.

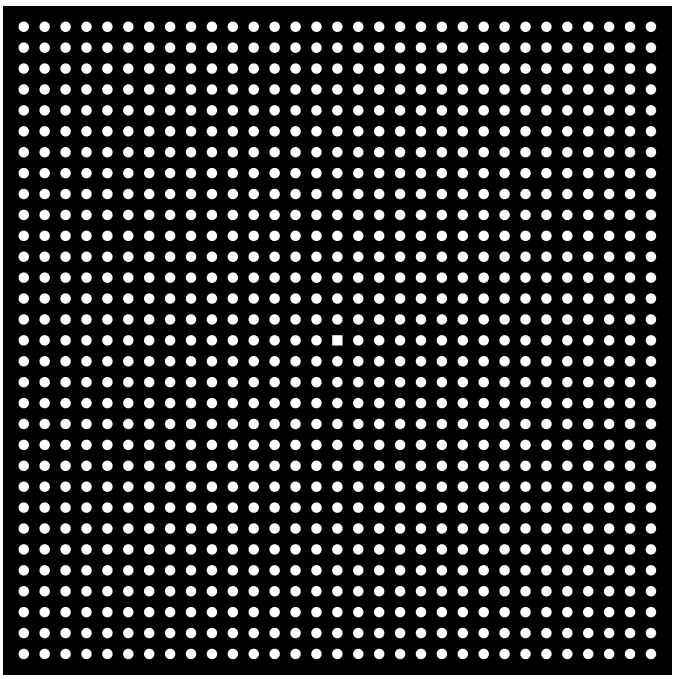

Figure 4.8: Calibration image. The center marker of the plate was set to square to indicate the center of the recorded image.

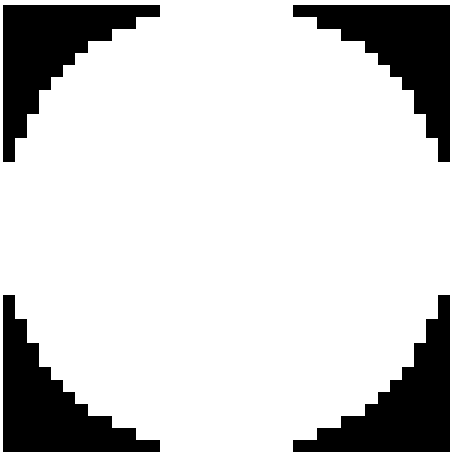

Figure 4.9: Markers indicate calibration position to estimate the projective function of stereo PIV.

4.3 Strain gauge measurement

To validate the method, the torque of the flapping axis was calculated from PIV information and compared with load measurement. Load was measured with micro strain measuring gauges, KSP-2-120-E3, with the approximate gage factor of 120 (Kyowa Electronic Instruments Co., Ltd., 2010b). The gauges were wired to the Wheatstone bridge to record the shearing moment on the axis of rotation because of the forces acting normal to the surface of the wing (Kyowa Electronic Instruments Co., Ltd., 2010a). Strain gauges were applied at opposite sides of the rotational axis at approximately 10 mm off the edge of the plate. Measurement sampling rate was 30 Hz and sampling time of 100 cycles was used. PIV measurements and strain gauge measurements were conducted simultaneously. The Wheatstone bridge was connected to the strain amplifier, DPM-700B (Kyowa Electronic Instruments Co., Ltd., 2004), where the voltage signal was stored on a PC by using a data acquisition system (National Instruments Co., 2000).

The motion of the flapping was measured by using a linear displacement laser sensor from Keyence Corporation (2006). The laser was targeted not on the flapping plate but onto a plate that was attached to the vibration absorbing damper that was installed on the rotating part of the motor. The rotation of the target plate was off the axis of rotation, therefore the directly measured displacement was not symmetrical. With the motor off, the laser hit the position of the target at 25.38 mm radial distance and 1.2 mm above the rotational axis as shown in Fig. 4.10. The analytical displacement in mm, Δ, is

$$\Delta = -\left(-1.2\tan(\pi+\theta)+\frac{25.38}{\cos(\pi+\theta)}\right) \tag{4.26}$$

The direct measurement was compared by analyzing the off-axis displacement, as shown in Fig. 4.11.

The strain gauge measurement setup is given in Fig. 4.12. The strain gauges were set 10mm behind the flapping plate. The load of the rotational axis was calculated by the configuration showed in Fig. 4.13. The bending moment caused tensile extension on one and compression on the other. The torsional moment caused the tensile extension of both of the strain gauges. The combined resistance of the strain gauges is

$$\begin{aligned} R_{serial} &= R_A + R_B \\ &= 2R \end{aligned} \tag{4.27}$$

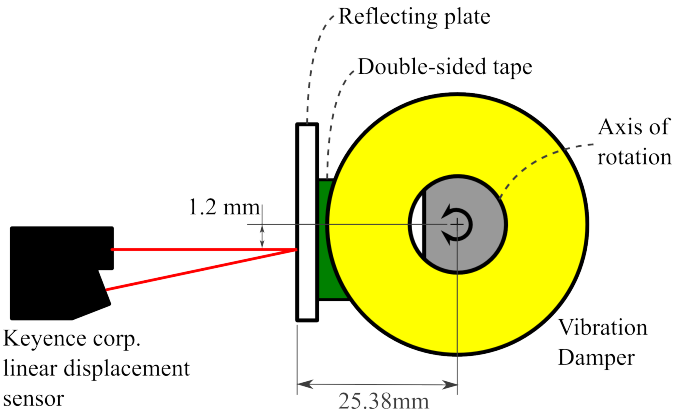

Figure 4.10: Setup for the measurement of flapping plate phase angle using linear displacement sensor.

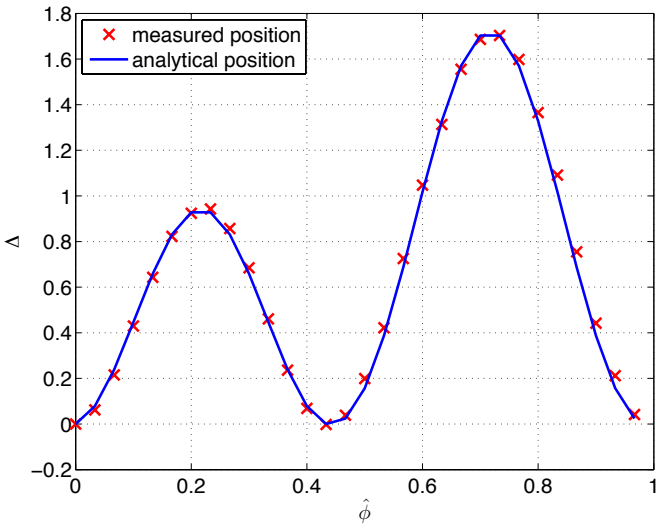

Figure 4.11: Comparison of the measured displacement and analytical displacement based on the position where the laser was targeted, Eq. (4.26).

and the change of the strain gauge because of strain is

$$\begin{aligned} R_{serial} + \Delta R_{serial} &= R_A + \Delta R_{bending} + \Delta R_{torsion} + R_B - \Delta R_{bending} + \Delta R_{torsion} \\ &= 2R + 2\Delta R_{torsion} \end{aligned} \tag{4.28}$$

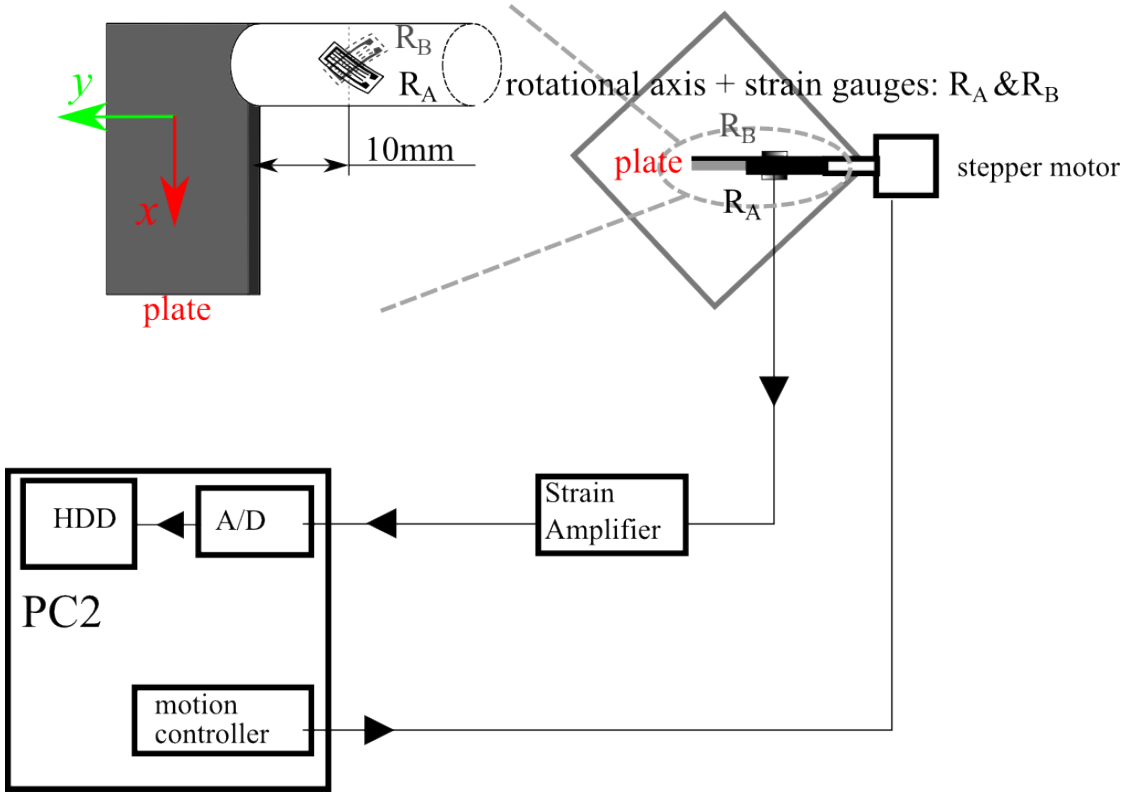

Figure 4.12: Setup for strain gauge measurement.

and the measured voltage when there is no strain is

$$\begin{aligned} V_G &= \left(\frac{R_{serial}}{R_{serial}+R} - \frac{R}{R+R/2} \right) V_S \\ &= \left(\frac{2R}{3R} - \frac{R}{3/2R} \right) V_S \\ &= 0 \end{aligned} \tag{4.29}$$

and when there is strain,

$$\begin{aligned} V_G &\approx \left(\frac{R_{serial}+\Delta R_{serial}}{R_{serial}+R} - \frac{R}{R+R/2} \right) V_S \\ &\approx \left(\frac{2R+2\Delta R_{torsion}}{3R} - \frac{R}{3/2R} \right) V_S \\ &\approx \left(\frac{2\Delta R_{torsion}}{3R} \right) V_S \end{aligned} \tag{4.30}$$

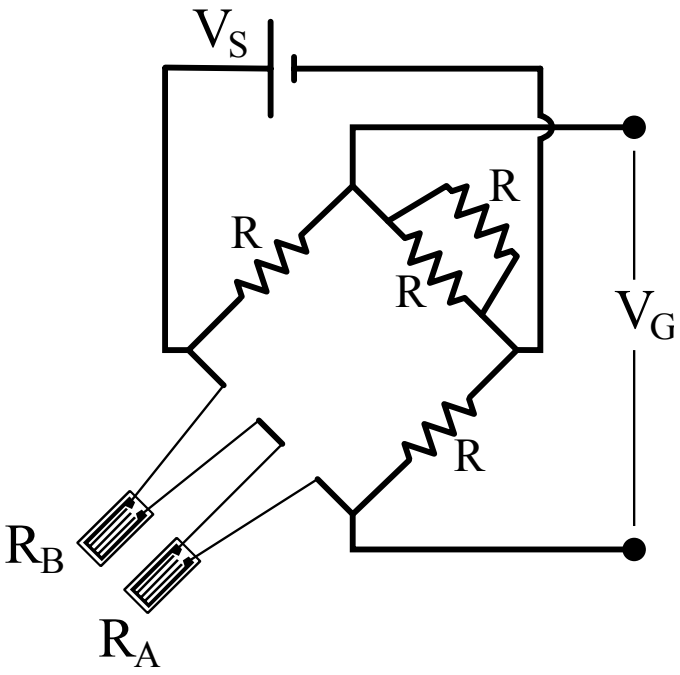

Figure 4.13: Electrical setup for the measurement of torque.

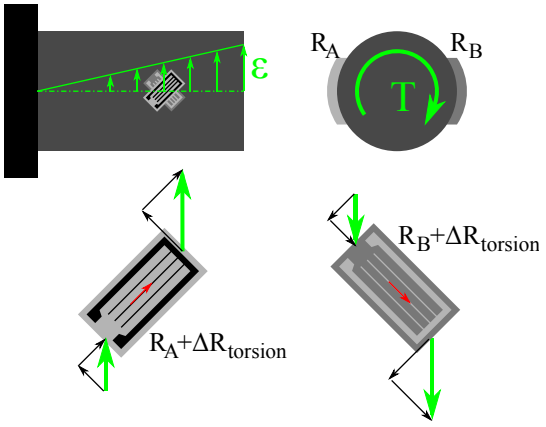

Figure 4.14: Calculation of torsion.

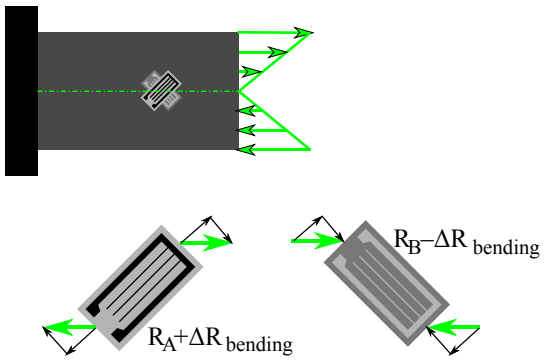

Figure 4.15: Calculation of bending.

To ensure that enough strain was exerted on the flapping axis. The flapping axis was made of Polyacetal, which has an elastic modulus of 2.76GPa. The value of the elastic modulus is 4% than that of an aluminum alloy 2017, 72.4GPa.

Chapter 5

Control volume analysis

This chapter presents the qualitative and quantitative visualization and analysis by control volume analysis of the flow generated by a flapping rigid plate. The measurement setup is explained in §5.1 and the accuracy and measurement uncertainty is discussed in §5.2. Qualitative visualization with dye ink is presented in §5.3. The result of stereo PIV is processed to visualize the flow structures quantitatively in §5.4. The dynamics of the vortex flow is investigated in §5.5 and final remarks are given in §5.6.

5.1 Measurement setup

Stereo PIV measurements were done parallel to the *xy*-planes to produce the three dimensional planar field around the mid-chord section and leading edge section. The aeronautical terms leading edge and wing tip are borrowed to indicate the edge of the wing and its tip.

For the control volume analysis, the flow along three *xy*-planes were measured at $z = (0, 5, 10)$mm to analyze the three dimensional effect of the half-size of the plate as shown in Fig. 5.1. In this case, the measurement planes were set apart because there is no need to calculate the components of velocity derivative for the control volume analysis.

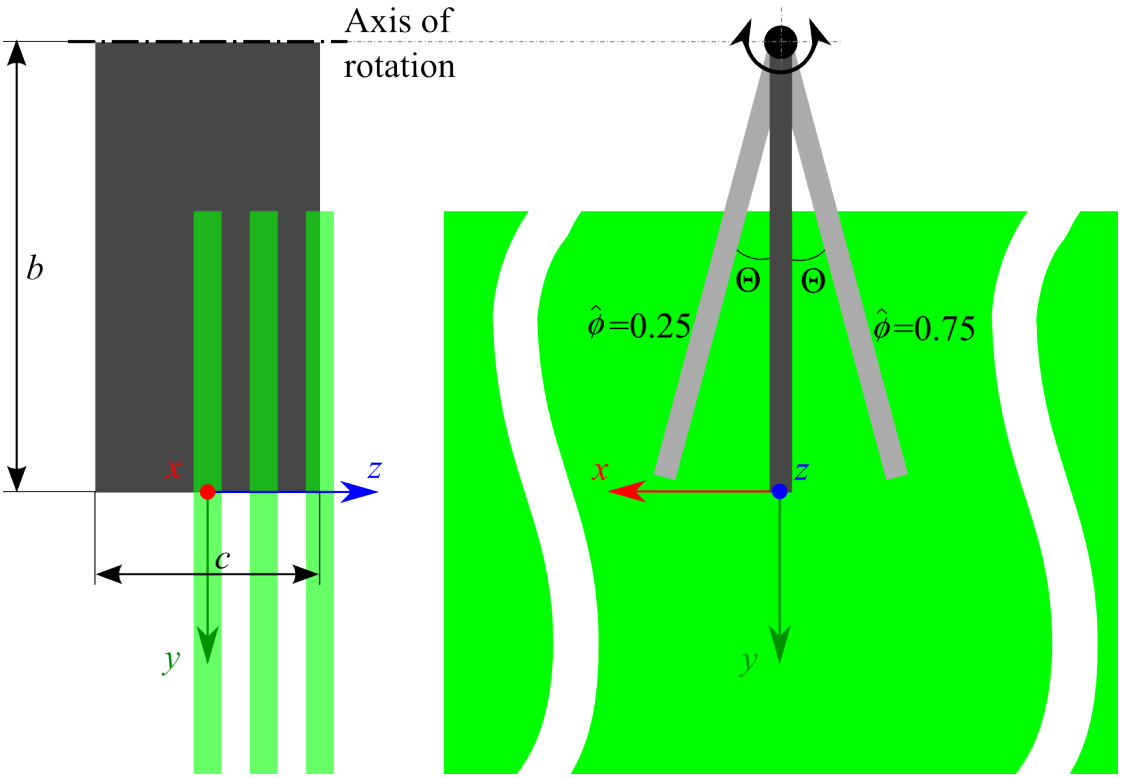

Figure 5.1: Position of measurement planes parallel to *xy*-plane measured for control volume analysis. The plate is illustrated in *dark gray*.

5.2 Accuracy and measurement uncertainty

Several factors affect the accuracy of the measurements. Misalignment was measured using the method described in Coudert and Schon (2001) with a set of 50 images taken by the left and right cameras of one phase angle. The average misalignment was found to be 0.14mm (5% of the interrogation area) in the horizontal direction of the image and 0.18mm(6.4% of the interrogation area) in the vertical direction leading to uncertainties of the velocity measurement as high as 0.15% in $\langle u \rangle$, 0.12 % in $\langle v \rangle$, and 0.12% in $\langle w \rangle$ relative to U. Another factor that affects the accuracy of our measurement is the wing tip reflection that was observed at high phase angles. Reflection of the laser light at the wing tip was detected by using a median intensity filter and the intensity of the reflection was substituted with background intensity.

Measurement uncertainty was determined by the measurement of fifteen groups of

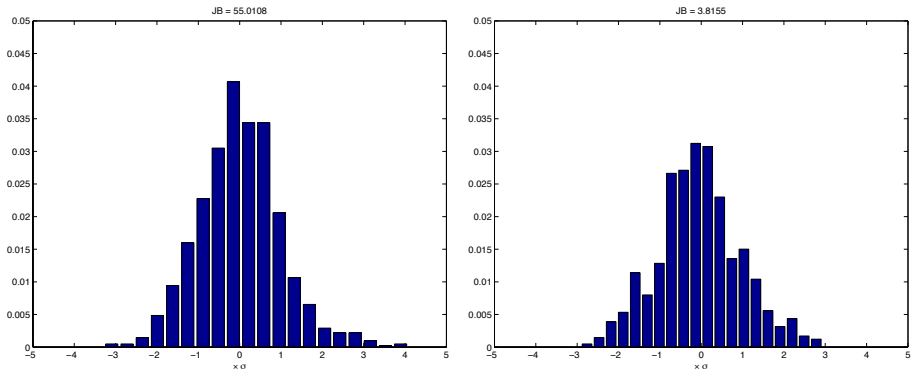

(a) Before treatment (b) After treatment

Figure 5.2: Velocity distribution at $X = 0$ and $Y = 0.5$.

velocity at one phase angle (Coleman and Steele, 1995). Each group recorded 1000 cycles of data and the velocity data was treated as described in the previous section. With a 95% confidence level, measurement uncertainties of phase-averaged velocities relative to U of an area randomly selected at $x/c = 0$, $y/c = 0.5$ are 3% for $\langle u \rangle$, 2% for $\langle v \rangle$ and 2% for $\langle w \rangle$. The temperature of the water tank was measured before and after the stereo PIV measurement and shows that the temperature fluctuation was 0.1°C at most during the whole run of the stereo PIV measurement. The probability density function of the velocity is shown in Fig. 5.2. Gaussian distribution of this data was confirmed using the Jarque-Bera test as formulated in Eq. (5.1).

$$JB = \frac{n}{6}\left(S^2 + \frac{(K-3)^2}{4}\right) \tag{5.1}$$

$$S = \frac{\hat{\mu}_3}{(\hat{\sigma}^2)^{3/2}} \tag{5.2}$$

$$K = \frac{\hat{\mu}_4}{(\hat{\sigma}^2)^2} \tag{5.3}$$

where n is the number of observation, S and K represent the sample's skewness and kurtosis, respectively. $\hat{\mu}_3$ and $\hat{\mu}_4$ are the estimates of the third and fourth central moments and $\hat{\sigma}^2$ is the estimate of the variance. Values of JB closer to zero indicates better resemblance to the Gaussian distribution.

After treatment, the sample closely approximates the Gaussian distribution as shown

Table 5.1: calculation of Skewness (S), Kurtosis (K), and the Jarque-Bera test (JB). For Gaussian distribution, S = 0, K = 3, and JB = 0.

	before treatment			after treatment		
	S	K	JB	S	K	JB
u	0.36	3.90	55.01	0.14	3.14	3.80
v	-0.39	2.94	26.14	-0.10	2.83	1.26
w	-0.39	3.32	30.04	-0.26	2.98	11.59

in Table 5.1. This approximate agreement indicates that the variables measured can be considered to be random. Thus, the measurement of one phase angle for every cycle is considered to be, within reason, free of other organized structures, such as reflected vortices.

5.3 Qualitative visualization

Qualitative flow visualization was achieved by injecting blue pen ink next to the rotational axis. The ink was injected at approximately 2mm below the rotational axis from a pipette, which has an inner diameter of 1.5mm, as shown in Fig. 5.3. The flow was recorded separately, from the front and from the top of the plate, with a 30fps digital camera.

The evolution of the flow phenomena around the flapping plate is shown in Fig. 5.3(b) –(c) at $\hat{\phi} \approx 0.25$, when the plate is at the end of its flapping motion, and Fig. 5.3(d)–(e) at $\hat{\phi} \approx 0.45$, when the plate starts its return stroke. Streaklines were visualized using blue dye and, in the snapshots, the plate is highlighted by a yellow frame and the tip of the plate by a red line. The combination of views suggest a helical vortex structure on the edge of the plate. Figure 5.3(b) and (d) shows the front view and Fig. 5.3(c) and (e) shows the slanted top view. These viewpoints are depicted in Fig. 5.3(a) as well as the point of dye injection.

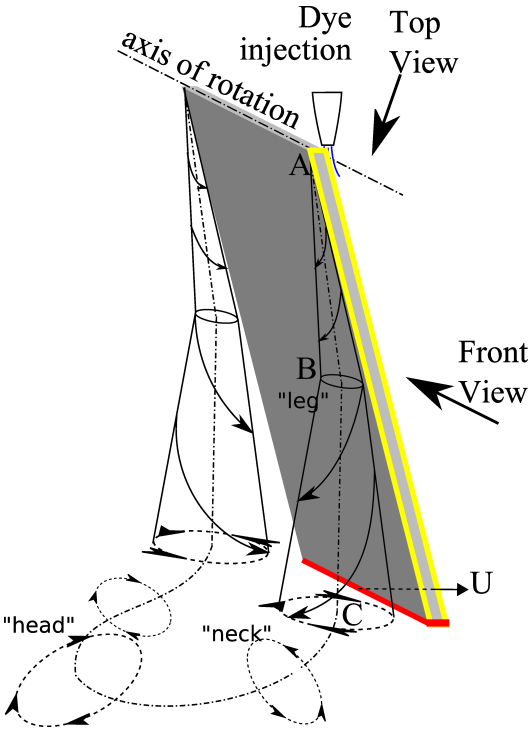

(a) Illustration of the vortex structure generated by the flapping plate.

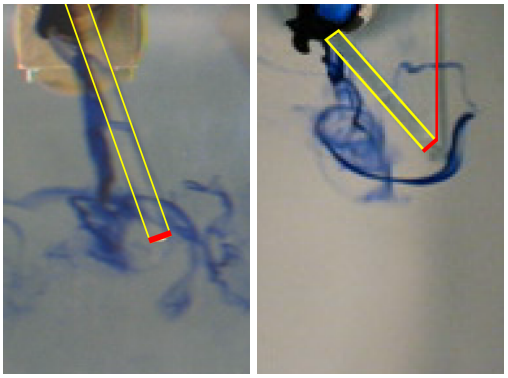

(b) Front view, $\hat{\phi} \approx 0.25$.

(c) Top view, $\hat{\phi} \approx 0.25$.

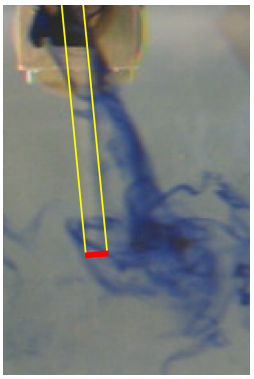

(d) Front view, $\hat{\phi} \approx 0.45$.

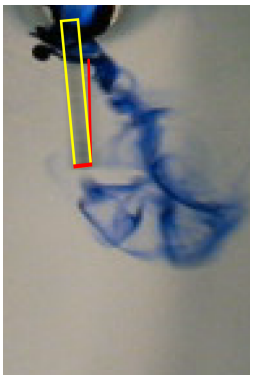

(e) Top view, $\hat{\phi} \approx 0.45$.

Figure 5.3: Snapshots of visualization of the flow around the wing with blue dye. The wing is marked with yellow highlight and the wingtip with red.

The dye was injected while the plate was moving and was quickly diffused toward the tip of the plate along its edge. The dye produced streaklines as shown in Fig. 5.3(b)–(e). The streaklines at $\hat{\phi} \approx 0.25$ behave as a steady stream flowing along the edge of the plate, Fig. 5.3(b) and as a rotating structure in the clockwise direction, Fig. 5.3(c). The dye was diffused near the tip of the plate. In the return stroke, the dye was convected around the edge of the plate as shown in Fig. 5.3(d)–(e).

Based on dye visualization, a possible flow structure is sketched in Fig. 5.3(a). The "legs" extend along the edges of the plate with opposite rotation and are connected with

the “neck” and “head”.

5.4 Quantitative visualization

5.4.1 Discretization of the quantitative visualization

The second invariance denotes the dominance between the strength of the rotation compared with that of the strain as indicated in Eq. (2.21) and rewritten in this section as Eq. (5.4).

$$\begin{aligned} Q &= (\|\Omega\|^2 - \|\mathbf{S}\|^2) \\ &= \left\| \frac{1}{2}\left(\frac{\partial u_i}{\partial x_j} - \frac{\partial u_j}{\partial x_i}\right) \right\|^2 - \left\| \frac{1}{2}\left(\frac{\partial u_i}{\partial x_j} + \frac{\partial u_j}{\partial x_i}\right) \right\|^2 \\ &= -\frac{\partial u_i}{\partial x_j}\frac{\partial u_j}{\partial x_i} \end{aligned} \tag{5.4}$$

For the phase-averaged velocity field, Eq. (5.4) was decomposed into

$$\langle Q \rangle = -\frac{\partial \langle u_i \rangle}{\partial x_j}\frac{\partial \langle u_j \rangle}{\partial x_i} - \left\langle \frac{\partial u_i'}{\partial x_j}\frac{\partial u_j'}{\partial x_i} \right\rangle \tag{5.5}$$

Equation (5.5) was discretized as

$$\langle Q \rangle \approx -\frac{\Delta \langle u_i \rangle}{\Delta x_j}\frac{\Delta \langle u_j \rangle}{\Delta x_i} - \left\langle \frac{\Delta u_i'}{\Delta x_j}\frac{\Delta u_j'}{\Delta x_i} \right\rangle \tag{5.6}$$

where

$$\frac{\partial f}{\partial x} \approx \frac{\Delta f}{\Delta x} = \frac{f(x+\Delta x, y, z) - f(x-\Delta x, y, z)}{2\Delta x} \tag{5.7}$$

$$\frac{\partial f}{\partial y} \approx \frac{\Delta f}{\Delta y} = \frac{f(x, y+\Delta y, z) - f(x, y-\Delta y, z)}{2\Delta y} \tag{5.8}$$

$$\frac{\partial f}{\partial z} \approx \frac{\Delta f}{\Delta z} = \frac{f(x, y, z+\Delta z) - f(x, y, z-\Delta z)}{2\Delta z} \tag{5.9}$$

and next to the boundary, the one-sided formulation was used,

$$\frac{\partial f}{\partial x} \approx \frac{\Delta f}{\Delta x} = \frac{-3f(x,y,z)+4f(x+\Delta x,y,z)-f(x+2\Delta x,y,z)}{2\Delta x} \tag{5.10}$$

$$\frac{\partial f}{\partial y} \approx \frac{\Delta f}{\Delta y} = \frac{-3f(x,y,z)+4f(x,y+\Delta y,z)-f(x,y+2\Delta y,z)}{2\Delta y} \tag{5.11}$$

$$\frac{\partial f}{\partial z} \approx \frac{\Delta f}{\Delta z} = \frac{-3f(x,y,z)+4f(x,y,z+\Delta z)-f(x,y,z+2\Delta z)}{2\Delta z} \tag{5.12}$$

where $\Delta z = \Delta z$ or $\Delta z = -\Delta z$ according to the orientation of the boundary.

5.4.2 Result of visualization

Figure 5.4 shows a snapshot of the velocity field around the flapping plate at $\hat{\phi} = 0.55$. In this figure, a part of the flapping plate is represented by the gray square. The arrows indicate the in-plane components of velocity, $\langle u \rangle / U$ and $\langle v \rangle / U$, and the color indicate the out-of-plane component of velocity, $\langle w \rangle / U$. Three measurement planes are presented from the bottom plane in Fig. 5.4 to the top: the mid-chord plane $z/c = 0$, the one-quarter chord plane $z/c = 0.25$, and the leading-edge plane $z/c = 0.5$. Several terms related to the flapping plate are *leading-edge* and *tip* for the spanwise edge of the plate and the chordwise edge of the plate, respectively. The surface of the plate moving towards the fluid will be called the *front-surface* and the opposite surface will be called the *rear-surface*. Figure 5.4 shows three-dimensional velocity distribution around the plate. Most notable features are the rotational structure around the leading-edge of the plate indicated by the distribution of $\langle w \rangle$, the spanwise flow towards the tip of the plate, chordwise velocity distribution near the tip of the plate, and the rotational structure around the tip of the plate.

The rotational flow structures were visualized by the second invariance, Eq. (2.21), and by streamlines, Eq. (2.22), in Fig. 5.5 for the downstroke sequence on the measurement plane at $z/c = 0.5$. The downstroke of the flapping plate is defined for $0.25 \leq \hat{\phi} < 0.75$.

The contour in Fig. 5.5 represents the magnitudes of $\langle Q \rangle$ given in the legend. Two dimensional streamlines are represented by red lines depicting the flow motion along the x and y directions. In the figure, the plate is represented by the gray patch. Regions

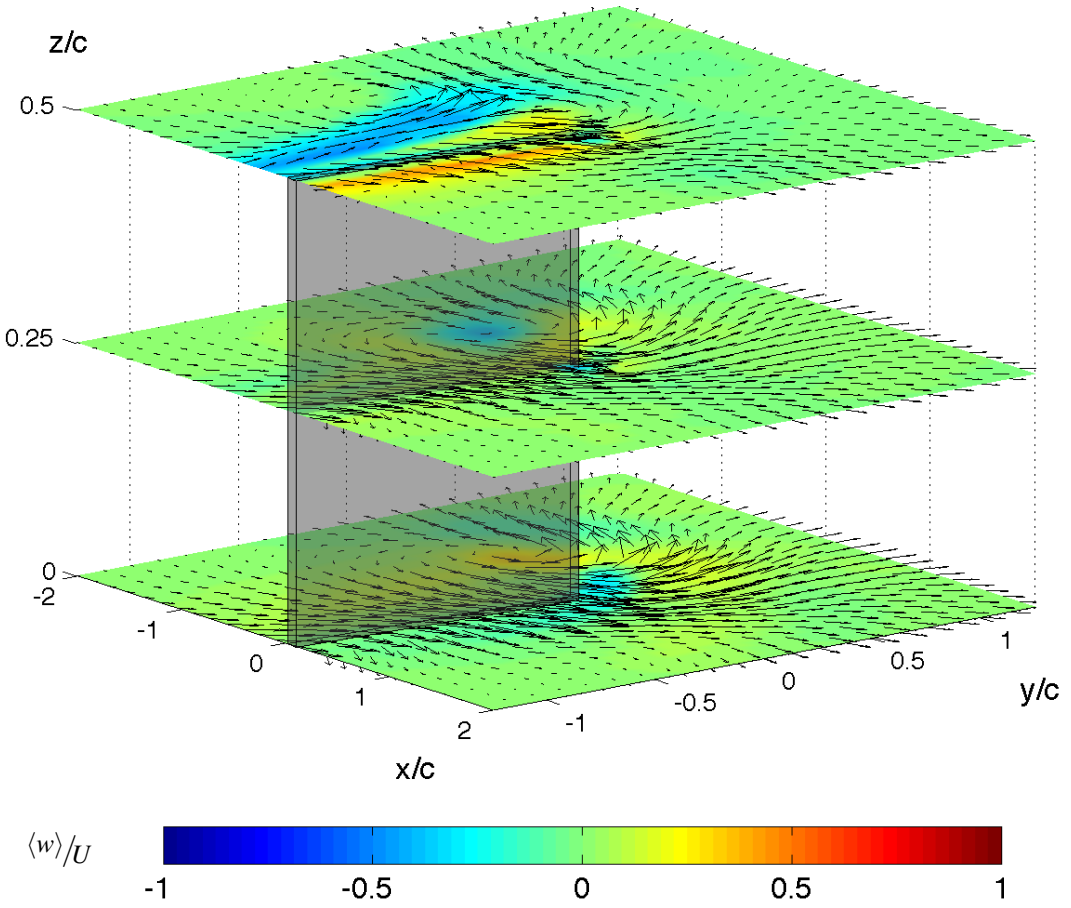

Figure 5.4: Three dimensional velocity distribution at $\hat{\phi} = 0.55$. $\langle u \rangle / U$, $\langle v \rangle / U$ are represented by vectors and $\langle w \rangle / U$ by the colors represented in the legend.

where $\langle Q \rangle < 0$ are the location of the vortical structures. Additional structures are visualized by the streamlines that forms rotational lines. These curves are symbolized with **TV** with "+" and "−" signs to indicate the counter-clockwise and clockwise rotation.

The region around the plate in Fig. 5.5 has $\langle Q \rangle < 0$ caused by shear flow which develops into a vortex. This vortex disappears for a while at $0.35 \leq \hat{\phi} \leq 0.45$ and reappears afterwards on the rear-surface of the plate. At $\hat{\phi} = 0.35$, the streamlines changed direction moving towards the rear-surface of the plate and a rotational structure begins to develop as depicted by both streamlines and $\langle Q \rangle$ as shown by **TV2+** in Fig. 5.5(f). The vortex at $0.55 \leq \hat{\phi} \leq 0.65$ follows the motion of the plate and bifurcates away from the

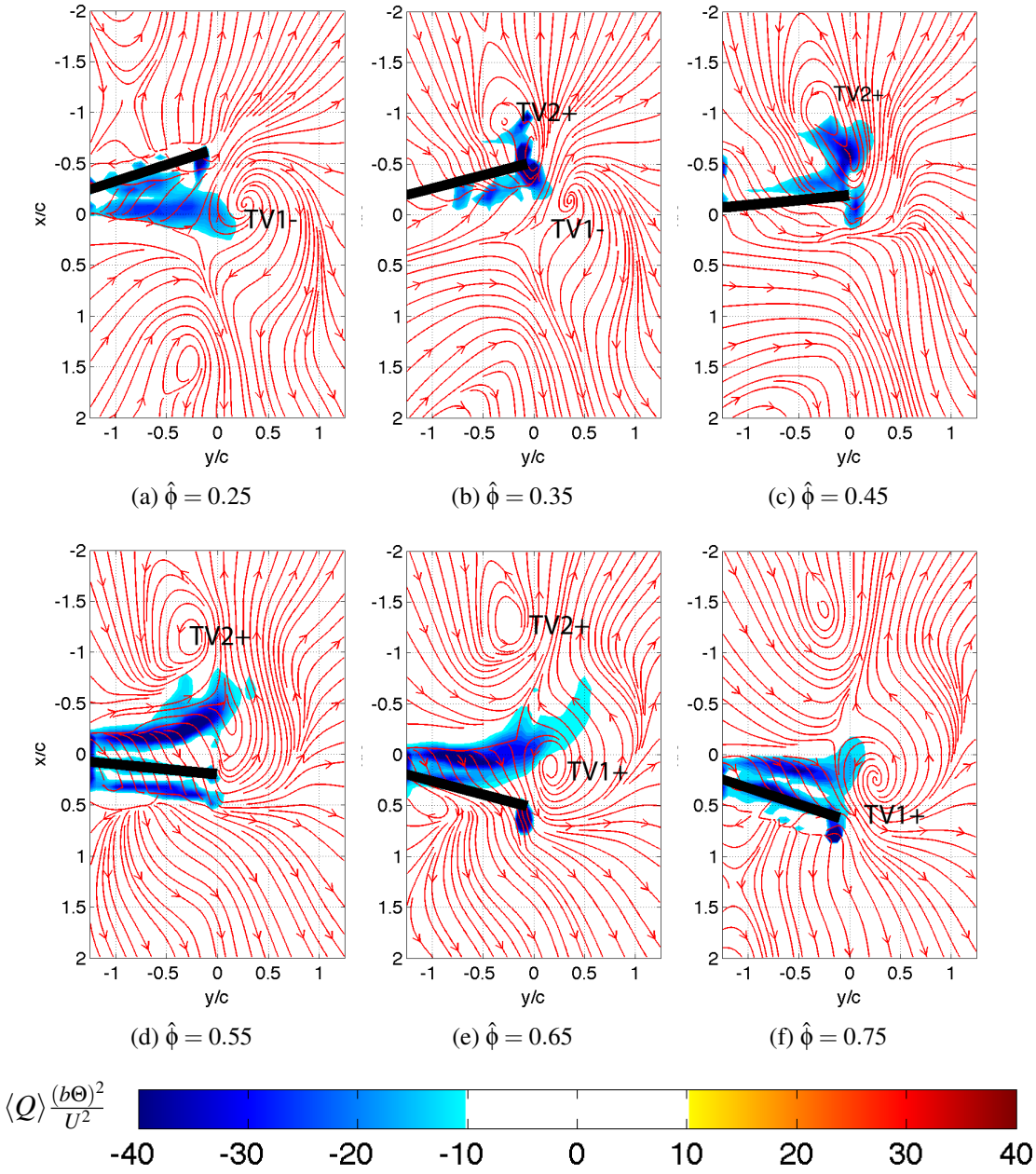

(a) $\hat{\phi} = 0.25$ (b) $\hat{\phi} = 0.35$ (c) $\hat{\phi} = 0.45$

(d) $\hat{\phi} = 0.55$ (e) $\hat{\phi} = 0.65$ (f) $\hat{\phi} = 0.75$

Figure 5.5: Vortex identification at $z/c = 0.5$ by $\langle Q \rangle$ presented as a contour. Streamlines are depicted in the field as *red lines* that do not relate to the contour legend. Legend depicts the magnitude of $\langle Q \rangle \, {}^{(b\Theta)^2}/_{U^2}$.

plate close to the tip. At $\hat{\phi} = 0.75$, when the downstroke ends, the vortex moves closer to the plate from its downward momentum as observed by the streamlines in the region where $\langle Q \rangle < 0$. Rotational streamlines are observed above the top of the vortices in counter-clockwise direction (**TV2+**) as shown in Fig. 5.5(c)–5.5(e). At $0.65 \leq \hat{\phi} \leq 0.75$ a second counter-clockwise rotating streamlines appear near the tip, **TV1+**. In the region where $\langle Q \rangle < 0$ where the vortex has "fully-developed", the streamlines are grouped together showing a relatively fast flow in that region moving toward the tip. From this region several streamlines diverge, moving toward the surface as a result of the vortex moving with the plate.

In Fig. 5.6, observations of the streamlines at $z/c = 0$ show less rotational elements in the streamlines and the flow moves toward the rear-surface of the plate and away from the front-surface of the plate. The vortex is observed around the tip and is weaker than the one on $z/c = 0.5$.

The flow structure of Figs. 5.5–5.6 are sketched in Fig. 5.7 for all the measured phase angle. The plate is represented as the red line, the vortex at $z/c = 0.5$ is represented by the blue line, which will be called the *leading-edge vortex* and symbolized with **LEV**, and the vortex at $z/c = 0$ is represented by the dashed-blue line, which will be called the *mid-chord vortex* and symbolized with **TV**.

Observations of $\langle Q \rangle$ in Fig. 5.7 shows that the evolution of the vortex system can be broken down into several phases relative to the motion of the plate:

1. accelerating phase, $0.25 \leq \hat{\phi} < 0.50$ and $0.75 \leq \hat{\phi} < 0$
2. decelerating phase, $0 \leq \hat{\phi} < 0.25$ and $0.5 \leq \hat{\phi} < 0.75$
3. resting phase, when $U = 0$, $\hat{\phi} = 0.25$ and $\hat{\phi} = 0.75$

Figure. 5.7 shows two vortices on the leading edge of the plate at $\hat{\phi} = 0.05$ to $\hat{\phi} = 0.15$. One large leading-edge vortex and a smaller one are rotating in the same direction. These vortices are indicated as **LEV**$+$. The larger of the two is extended to $z/c = 0$ (**TV**$-$) and grows up to 150% of the flapping wing amplitude as the plate approaches the resting phase. The smaller one does not show any extension. It is most likely that only one large structure on the rear-surface of the plate exists. This description of the leading-edge vortex is due to the measurement configuration giving the cross-section of the leading-edge vortex on the measurement plane. At $\hat{\phi} = 0.20$, a vortex attached to the

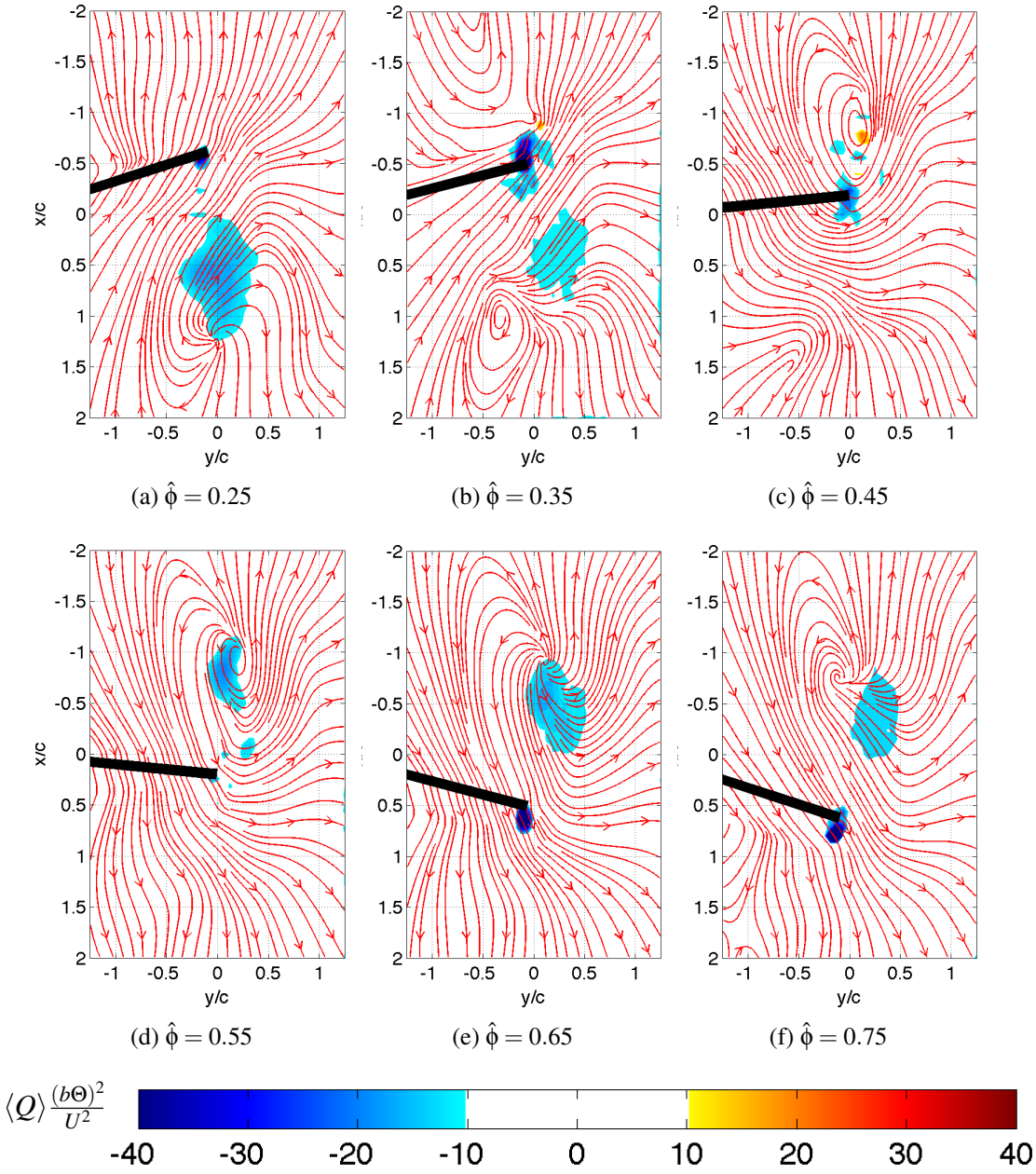

(a) $\hat{\phi} = 0.25$ (b) $\hat{\phi} = 0.35$ (c) $\hat{\phi} = 0.45$

(d) $\hat{\phi} = 0.55$ (e) $\hat{\phi} = 0.65$ (f) $\hat{\phi} = 0.75$

Figure 5.6: Vortex identification at $z/c = 0$ by $\langle Q \rangle$ presented as a contour. Streamlines are depicted in the field as *red lines* that do not relate to the contour legend. Legend depicts the magnitude of $\langle Q \rangle \, {}^{(b\Theta)^2}/_{U^2}$.

edge of the plate (**LEV**$-$) appears in the opposite direction of the leading-edge vortex. This opposite vortex is extended to the mid-chord plane (**TV**$-$).

At $\hat{\phi} = 0.30$, the leading-edge vortex develops into a separated counter-clockwise rotating vortex. From qualitative visualization, it was known that the leading edge vortex is diffused around the edge of the plate and dissipates. The mid-chord vortex grows weaker and is stretched up to 200% of the flapping amplitude. At $\hat{\phi} = 0.35$ and $\hat{\phi} = 0.40$, the mid-chord vortex reverses its rotational direction and moves to the rear-surface of the plate. Throughout the accelerating phase, a leading edge vortex is observed on the front-surface of the plate.

The decelerating phase of $0.5 \leq \hat{\phi} < 0.75$ shows the opposite vortical structures as $0 \leq \hat{\phi} < 0.25$. The leading-edge vortex on the front-surface of the plate during the accelerating plate is diffused to the rear-surface of the plate and the mid-chord vortex strengthen then weakens at $\hat{\phi} = 0.70$.

The accelerating phase of $0.75 \leq \hat{\phi} < 0$ also shows the opposite vortical structure as the other accelerating phase at $0.25 \leq \hat{\phi} < 0.50$. Weak mid-chord vortices are observed and the leading-edge vortex appears on the front-surface of the plate before being diffused to the rear-surface at $\hat{\phi} = 0.95$.

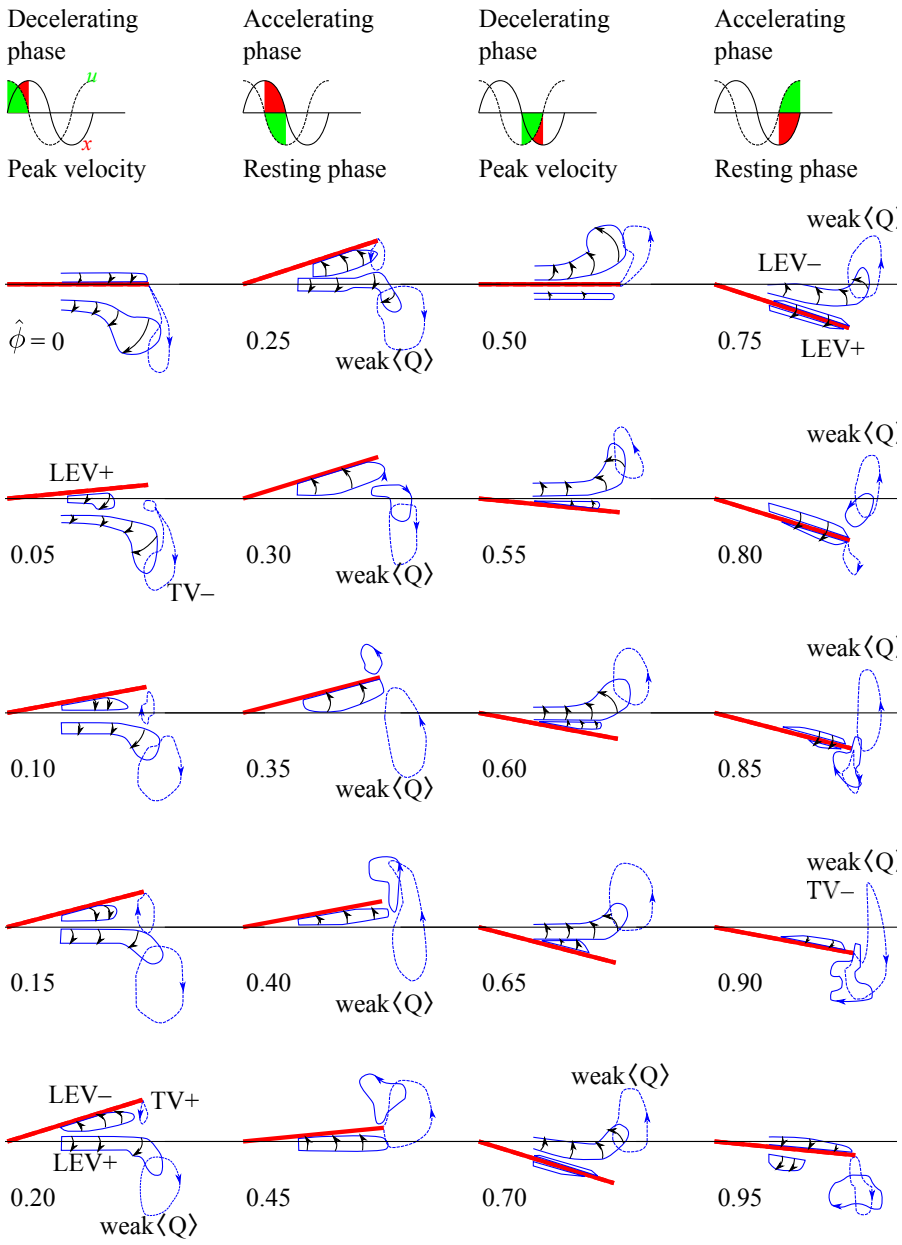

Figure 5.7: Sketch of vortex structure from $\hat{\phi} = 0$ – 0.95. The sequence should be read from *top* to *down* and from *left* to *right*. Vortices at $z/c = 0.5$ are represented by continuous *blue lines*, leading-edge vortex (**LEV**), and at $z/c = 0$ by *blue dashed lines*, mid-chord vortex (**TV**). The plate is represented by a *red line*. *Arrows* indicate the rotational direction. For the leading-edge vortex, the rotational axis is in the spanwise direction.

5.5 Control volume analysis

5.5.1 Discretized control volume analysis

Force can be calculated within a specific part of the flow by defining a control volume as shown in Eq. (2.5). The force is defined by the integral of the momentum within a control volume, which is rewritten here as Eq. (5.13),

$$F_i = \rho \int_V \frac{\partial \langle u_i \rangle}{\partial t} dV + \rho \int_S \langle u_i \rangle \langle u_j \rangle \hat{n}_j dS \tag{5.13}$$

After decomposing the momentum equation to the phase averaged component and fluctuating component,

$$\langle F \rangle_i = \rho \frac{\partial \phi}{\partial t} \int_V \frac{\partial \langle u_i \rangle}{\partial \phi} dV + \rho \int_S \langle u_i \rangle \langle u_j \rangle \hat{n}_j dS + \rho \int_S \langle u_i' u_j' \rangle \hat{n}_j dS \tag{5.14}$$

The first term on the left hand side of Eq. (5.14) is the average unsteady term, the second term is the average convection term, and the last term is the average of the variation of the convection from the product of the fluctuating velocity component.

The integration was done with finite volume method, where the unsteady term is formulated as

$$\int_V \frac{\partial \langle u_i \rangle}{\partial \phi} dV = \sum_{i=1}^{N} \frac{\Delta \langle u_i \rangle}{\Delta \phi} \Delta V \tag{5.15}$$

where i indicates the node number and $N = {}^{V}/_{\Delta V}$ is the number of nodes. Expanding the discrete form of the unsteady term to its components, $\langle u_i \rangle = \langle u \rangle^c, \langle v \rangle^c, \langle w \rangle$,

$$F_{unsteady,x} = \sum_{i=1}^{N} \frac{\Delta \langle u \rangle^c}{\Delta \phi} \Delta V \tag{5.16}$$

$$F_{unsteady,y} = \sum_{i=1}^{N} \frac{\Delta \langle v \rangle^c}{\Delta \phi} \Delta V \tag{5.17}$$

$$F_{unsteady,z} = \sum_{i=1}^{N} \frac{\Delta \langle w \rangle^c}{\Delta \phi} \Delta V \tag{5.18}$$

The convection term is discretized as

$$\int_S \langle u_i \rangle \langle u_j \rangle \hat{n}_j dS = \sum_{k=1}^{3} \sum_{l=0}^{1} \sum_{i=1}^{N} (-1)^l \langle u_i \rangle \langle u_j \rangle \hat{n}_j \Delta S \tag{5.19}$$

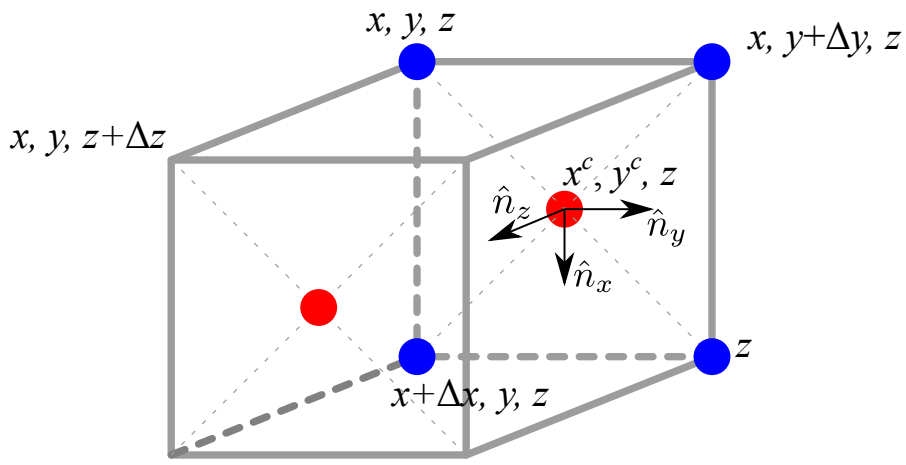

Figure 5.8: Control volume definition and the orientation of x, y, and z

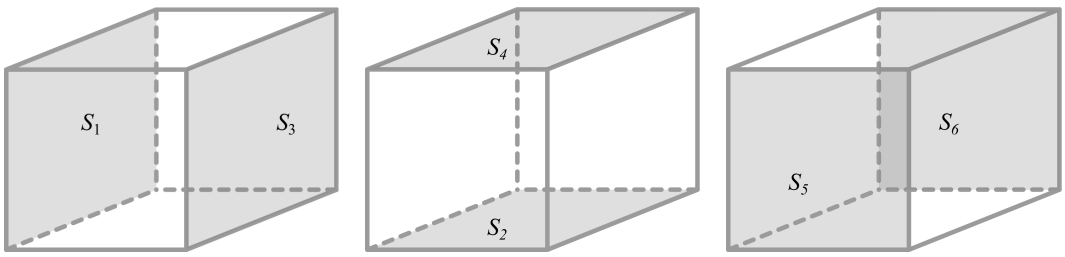

(a) Definition of S_1 and S_3. (b) Definition of S_2 and S_4. (c) Definition of S_5 and S_6.

Figure 5.9: Definition of the control surface for each faces of control volume, V.

where k is the direction of the convection force, l is the surface orientation. Equation 5.19 is better explained when it is expanded to its vector form in Eqs. (5.20)–(5.22), where the orientation of (x,y,z) and S_1 to S_6 are shown in Figs. 5.8 and 5.9.

$$
\begin{aligned}
F_{convection,x} &= \int_S \Big(\langle u\rangle\langle u\rangle n_x + \langle u\rangle\langle v\rangle n_y + \langle u\rangle\langle w\rangle n_z \Big)\, dS \\
&= \int_{S_2} \langle u\rangle\langle u\rangle(-1)\, dS + \int_{S_4} \langle u\rangle\langle u\rangle(+1)\, dS \\
&\quad + \int_{S_1} \langle u\rangle\langle v\rangle(+1)\, dS + \int_{S_3} \langle u\rangle\langle v\rangle(-1)\, dS \\
&\quad + \int_{S_5} \langle u\rangle\langle w\rangle(+1)\, dS + \int_{S_6} \langle u\rangle\langle w\rangle(-1)\, dS \\
&= \sum_{i=1}^{N} \frac{\Delta y \Delta z}{2} \Big[\langle u\rangle\langle u\rangle(x+\Delta x, y+\Delta y, z) + \langle u\rangle\langle u\rangle(x+\Delta x, y, z) \Big] \\
&\qquad - \sum_{i=1}^{N} \frac{\Delta y \Delta z}{2} \Big[\langle u\rangle\langle u\rangle(x, y+\Delta y, z) + \langle u\rangle\langle u\rangle(x, y, z) \Big] \\
&\quad + \sum_{i=1}^{N} \frac{\Delta x \Delta z}{2} \Big[\langle u\rangle\langle v\rangle(x, y+\Delta y, z) + \langle u\rangle\langle v\rangle(x+\Delta x, y+\Delta y, z) \Big] \\
&\qquad - \sum_{i=1}^{N} \frac{\Delta x \Delta z}{2} \Big[\langle u\rangle\langle v\rangle(x, y, z) + \langle u\rangle\langle v\rangle(x+\Delta x, y, z) \Big] \\
&\quad + \sum_{i=1}^{N} \Delta x \Delta y \Big[\langle u\rangle\langle w\rangle(x^c, y^c, z+\Delta z) - \langle u\rangle\langle w\rangle(x^c, y^c, z) \Big]
\end{aligned}
\tag{5.20}
$$

$$
\begin{aligned}
F_{convection,y} &= \int_S \Big(\langle v \rangle \langle u \rangle n_x + \langle v \rangle \langle v \rangle n_y + \langle v \rangle \langle w \rangle n_z \Big)\, dS \\
&= \int_{S_2} \langle v \rangle \langle u \rangle (-1)\, dS + \int_{S_4} \langle v \rangle \langle u \rangle (+1)\, dS \\
&\quad + \int_{S_1} \langle v \rangle \langle v \rangle (+1)\, dS + \int_{S_3} \langle v \rangle \langle v \rangle (-1)\, dS \\
&\quad + \int_{S_5} \langle v \rangle \langle w \rangle (+1)\, dS + \int_{S_6} \langle v \rangle \langle w \rangle (-1)\, dS \\
&= \sum_{i=1}^{N} \frac{\Delta y \Delta z}{2} \Big[\langle v \rangle \langle u \rangle (x + \Delta x, y + \Delta y, z) + \langle v \rangle \langle u \rangle (x + \Delta x, y, z) \Big] \\
&\qquad - \sum_{i=1}^{N} \frac{\Delta y \Delta z}{2} \Big[\langle v \rangle \langle u \rangle (x, y + \Delta y, z) + \langle v \rangle \langle u \rangle (x, y, z) \Big] \\
&\quad + \sum_{i=1}^{N} \frac{\Delta x \Delta z}{2} \Big[\langle v \rangle \langle v \rangle (x, y + \Delta y, z) + \langle v \rangle \langle v \rangle (x + \Delta x, y + \Delta y, z) \Big] \\
&\qquad - \sum_{i=1}^{N} \frac{\Delta x \Delta z}{2} \Big[\langle v \rangle \langle v \rangle (x, y, z) + \langle v \rangle \langle v \rangle (x + \Delta x, y, z) \Big] \\
&\quad + \sum_{i=1}^{N} \Delta x \Delta y \Big[\langle v \rangle \langle w \rangle (x^c, y^c, z + \Delta z) - \langle v \rangle \langle w \rangle (x^c, y^c, z) \Big]
\end{aligned}
\tag{5.21}
$$

$$
\begin{aligned}
F_{convection,z} &= \int_S \Big(\langle w\rangle\langle u\rangle n_x + \langle w\rangle\langle v\rangle n_y + \langle w\rangle\langle w\rangle n_z \Big)\, dS \\
&= \int_{S_2} \langle w\rangle\langle u\rangle(-1)\, dS + \int_{S_4} \langle w\rangle\langle u\rangle(+1)\, dS \\
&\quad + \int_{S_1} \langle w\rangle\langle v\rangle(+1)\, dS + \int_{S_3} \langle w\rangle\langle v\rangle(-1)\, dS \\
&\quad + \int_{S_5} \langle w\rangle\langle w\rangle(+1)\, dS + \int_{S_6} \langle w\rangle\langle w\rangle(-1)\, dS \\
&= \sum_{i=1}^{N} \frac{\Delta y \Delta z}{2} \Big[\langle w\rangle\langle u\rangle(x+\Delta x, y+\Delta y, z) + \langle w\rangle\langle u\rangle(x+\Delta x, y, z) \Big] \\
&\qquad - \sum_{i=1}^{N} \frac{\Delta y \Delta z}{2} \Big[\langle w\rangle\langle u\rangle(x, y+\Delta y, z) + \langle w\rangle\langle u\rangle(x, y, z) \Big] \\
&\quad + \sum_{i=1}^{N} \frac{\Delta x \Delta z}{2} \Big[\langle w\rangle\langle v\rangle(x, y+\Delta y, z) + \langle w\rangle\langle v\rangle(x+\Delta x, y+\Delta y, z) \Big] \\
&\qquad - \sum_{i=1}^{N} \frac{\Delta x \Delta z}{2} \Big[\langle w\rangle\langle v\rangle(x, y, z) + \langle w\rangle\langle v\rangle(x+\Delta x, y, z) \Big] \\
&\quad + \sum_{i=1}^{N} \Delta x \Delta y \Big[\langle w\rangle\langle w\rangle(x^c, y^c, z+\Delta z) - \langle w\rangle\langle w\rangle(x^c, y^c, z) \Big]
\end{aligned}
\tag{5.22}
$$

The differentiation of the last term of Eq. (5.14) follows similarly with the convection term.

$$
\begin{aligned}
F_{variation,x} &= \int_S \Big(\langle u'u' \rangle n_x + \langle u'v' \rangle n_y + \langle u'w' \rangle n_z \Big)\, dS \\
&= \int_{S_2} \langle u'u' \rangle (-1)\, dS + \int_{S_4} \langle u'u' \rangle (+1)\, dS \\
&\quad + \int_{S_1} \langle u'v' \rangle (+1)\, dS + \int_{S_3} \langle u'v' \rangle (-1)\, dS \\
&\quad + \int_{S_5} \langle u'w' \rangle (+1)\, dS + \int_{S_6} \langle u'w' \rangle (-1)\, dS \\
&= \sum_{i=1}^{N} \frac{\Delta y \Delta z}{2} \Big[\langle u'u' \rangle (x + \Delta x, y + \Delta y, z) + \langle u'u' \rangle (x + \Delta x, y, z) \Big] \\
&\qquad - \sum_{i=1}^{N} \frac{\Delta y \Delta z}{2} \Big[\langle u'u' \rangle (x, y + \Delta y, z) + \langle u'u' \rangle (x, y, z) \Big] \\
&\quad + \sum_{i=1}^{N} \frac{\Delta x \Delta z}{2} \Big[\langle u'v' \rangle (x, y + \Delta y, z) + \langle u'v' \rangle (x + \Delta x, y + \Delta y, z) \Big] \\
&\qquad - \sum_{i=1}^{N} \frac{\Delta x \Delta z}{2} \Big[\langle u'v' \rangle (x, y, z) + \langle u'v' \rangle (x + \Delta x, y, z) \Big] \\
&\quad + \sum_{i=1}^{N} \Delta x \Delta y \Big[\langle u'w' \rangle (x^c, y^c, z + \Delta z) - \langle u'w' \rangle (x^c, y^c, z) \Big]
\end{aligned}
\tag{5.23}
$$

$$
\begin{aligned}
F_{variation,y} &= \int_S \Big(\langle v'u' \rangle n_x + \langle v'v' \rangle n_y + \langle v'w' \rangle n_z \Big)\, dS \\
&= \int_{S_2} \langle v'u' \rangle (-1)\, dS + \int_{S_4} \langle v'u' \rangle (+1)\, dS \\
&\quad + \int_{S_1} \langle v'v' \rangle (+1)\, dS + \int_{S_3} \langle v'v' \rangle (-1)\, dS \\
&\quad + \int_{S_5} \langle v'w' \rangle (+1)\, dS + \int_{S_6} \langle v'w' \rangle (-1)\, dS \\
&= \sum_{i=1}^{N} \frac{\Delta y \Delta z}{2} \Big[\langle v'u' \rangle (x+\Delta x, y+\Delta y, z) + \langle v'u' \rangle (x+\Delta x, y, z) \Big] \\
&\qquad - \sum_{i=1}^{N} \frac{\Delta y \Delta z}{2} \Big[\langle v'u' \rangle (x, y+\Delta y, z) + \langle v'u' \rangle (x, y, z) \Big] \\
&\quad + \sum_{i=1}^{N} \frac{\Delta x \Delta z}{2} \Big[\langle v'v' \rangle (x, y+\Delta y, z) + \langle v'v' \rangle (x+\Delta x, y+\Delta y, z) \Big] \\
&\qquad - \sum_{i=1}^{N} \frac{\Delta x \Delta z}{2} \Big[\langle v'v' \rangle (x, y, z) + \langle v'v' \rangle (x+\Delta x, y, z) \Big] \\
&\quad + \sum_{i=1}^{N} \Delta x \Delta y \Big[\langle v'w' \rangle (x^c, y^c, z+\Delta z) - \langle v'w' \rangle (x^c, y^c, z) \Big]
\end{aligned}
\tag{5.24}
$$

$$
\begin{aligned}
F_{variation,z} &= \int_S \Big(\langle w'u' \rangle n_x + \langle w'v' \rangle n_y + \langle w'w' \rangle n_z \Big)\, dS \\
&= \int_{S_2} \langle w'u' \rangle (-1)\, dS + \int_{S_4} \langle w'u' \rangle (+1)\, dS \\
&\quad + \int_{S_1} \langle w'v' \rangle (+1)\, dS + \int_{S_3} \langle w'v' \rangle (-1)\, dS \\
&\quad + \int_{S_5} \langle w'w' \rangle (+1)\, dS + \int_{S_6} \langle w'w' \rangle (-1)\, dS \\
&= \sum_{i=1}^{N} \frac{\Delta y \Delta z}{2} \Big[\langle w'u' \rangle (x+\Delta x, y+\Delta y, z) + \langle w'u' \rangle (x+\Delta x, y, z) \Big] \\
&\qquad - \sum_{i=1}^{N} \frac{\Delta y \Delta z}{2} \Big[\langle w'u' \rangle (x, y+\Delta y, z) + \langle w'u' \rangle (x, y, z) \Big] \\
&\quad + \sum_{i=1}^{N} \frac{\Delta x \Delta z}{2} \Big[\langle w'v' \rangle (x, y+\Delta y, z) + \langle w'v' \rangle (x+\Delta x, y+\Delta y, z) \Big] \\
&\qquad - \sum_{i=1}^{N} \frac{\Delta x \Delta z}{2} \Big[\langle w'v' \rangle (x, y, z) + \langle w'v' \rangle (x+\Delta x, y, z) \Big] \\
&\quad + \sum_{i=1}^{N} \Delta x \Delta y \Big[\langle w'w' \rangle (x^c, y^c, z+\Delta z) - \langle w'w' \rangle (x^c, y^c, z) \Big]
\end{aligned}
\tag{5.25}
$$

The total force is

$$
\langle F_i \rangle = \rho \left[\frac{\Delta \phi}{\Delta t} \langle F_i \rangle_{unsteady} + \langle F_i \rangle_{convection} + \langle F_i \rangle_{variation} \right] \tag{5.26}
$$

and the normalized force is

$$
\begin{aligned}
\tilde{C}_{\langle F_i \rangle} &= \frac{\langle F_i \rangle}{1/2 \rho U^2 bc} \\
&= \frac{\rho}{1/2 \rho U^2 bc} \left(\frac{2\pi f \Delta t}{\Delta t} \langle F_i \rangle_{unsteady} + \langle F_i \rangle_{convection} + \langle F_i \rangle_{variation} \right) \\
&= \frac{4\pi f}{U^2 bc} \langle F_i \rangle_{unsteady} + \frac{2}{U^2 bc} \Big(\langle F_i \rangle_{convection} + \langle F_i \rangle_{variation} \Big)
\end{aligned}
\tag{5.27}
$$

Equation (5.27) is expanded to its bases x, y, and z,

$$
\begin{bmatrix} \tilde{C}_x(\hat{\phi}_i) \\ \tilde{C}_y(\hat{\phi}_i) \\ \tilde{C}_z(\hat{\phi}_i) \end{bmatrix} = \begin{bmatrix} \tilde{C}_x^{u,t}(\hat{\phi}_i) \\ \tilde{C}_y^{u,t}(\hat{\phi}_i) \\ \tilde{C}_z^{u,t}(\hat{\phi}_1) \end{bmatrix} + \begin{bmatrix} \tilde{C}_x^{uu}(\hat{\phi}_i) \\ \tilde{C}_y^{uu}(\hat{\phi}_i) \\ \tilde{C}_z^{uu}(\hat{\phi}_1) \end{bmatrix} + \begin{bmatrix} \tilde{C}_x^{u'u'}(\hat{\phi}_i) \\ \tilde{C}_y^{u'u'}(\hat{\phi}_i) \\ \tilde{C}_z^{u'u'}(\hat{\phi}_i) \end{bmatrix} \tag{5.28}
$$

where the superscript "u,t" is the rate of change of momentum, "uu" is the momentum flux, and "$u'u'$" is the product of the fluctuating velocity. The force coefficient $\tilde{C}_{\langle F_i \rangle}$ is shortened as $\tilde{C}_{x_i}$.

A three-point moving average smoothing function was applied to the force coefficients,

$$C_{x_i}(\hat{\phi}_k) = \frac{\tilde{C}_{x_i}(\hat{\phi}_k - \Delta\hat{\phi}_k) + 2\tilde{C}_{x_i}(\hat{\phi}_k) + \tilde{C}_{x_i}(\hat{\phi}_k + \Delta\hat{\phi}_k)}{4} \tag{5.29}$$

where $\hat{\phi}_k$ is the discrete phase angle. The analysis follows the arbitrary choice of control volume size and location in the PIV velocity field to analyze the physics of the flow generated by flapping motion as shown in the next section.

5.5.2 Result of control volume analysis

The out-of-plane velocity distribution provides a way to assess the flow three-dimensionally. The size of the control volume was defined to partially include the plate in order to evaluate the physics of the flow and the effect of the plate's inertia on the flow inside the control volume. Equation (5.27) was used to calculate the force acting on the control volume, which included the pressure and viscous terms acting on the control surface. As a consequence, the calculation is dependent on the size of the control volume. This dependence is exploited for the evaluation of flow physics. Equation (5.27) calculates the force due to the flow within a control volume fixed in space, not the force acting on the plate. Thus, in this study the added mass was not compensated.

As explained, Eq. (5.27) is dependent on the control volume used for the analysis. The control volume analysis on each z positions of the measurement planes are defined as

$$-1.84 \leq x \leq 1.84, \qquad -1.12 \leq y \leq 1.12 \tag{5.30}$$

as shown in Fig. 5.10. Figures 5.11–5.13 are the results given by the conditions above.

The evolution of C_x and C_y are presented in Fig. 5.11. At $z/c = 0$ and $z/c = 0.25$, C_x has a sinusoidal form and is equal in magnitude and phase for both Reynolds numbers and C_y is smaller than C_x. The streamlines show that the flow is diffused along the x-direction more prominently than in the y-direction. Comparison of C_x for both Reynolds numbers at $z/c = 0.5$ shows that the magnitude of C_x depends on the Reynolds number

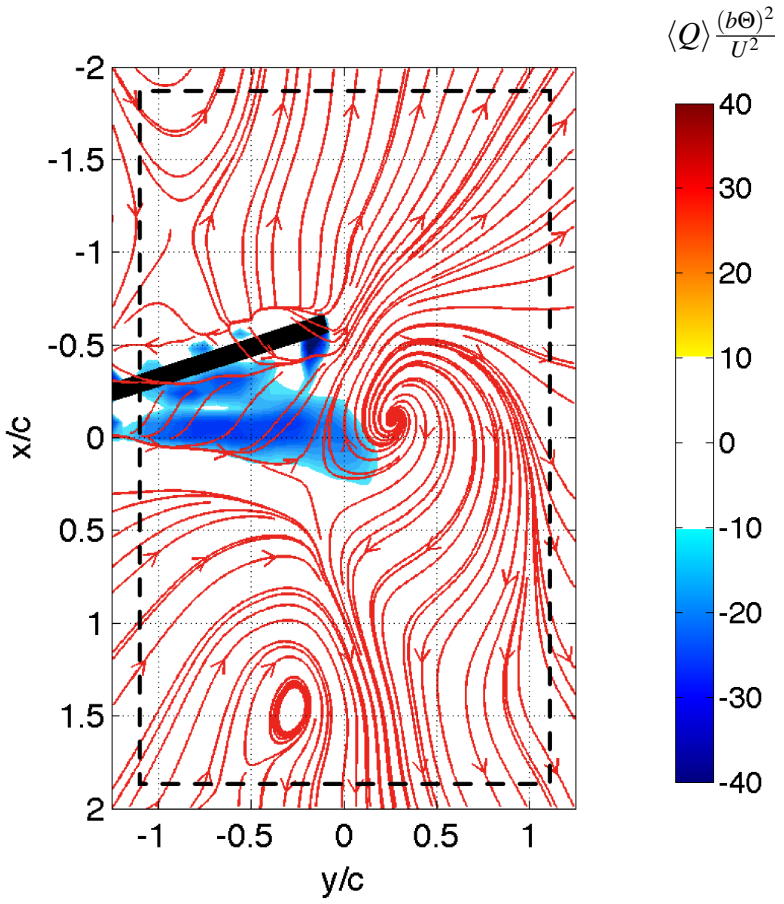

Figure 5.10: The control volume defined in Eq. 5.30.

at $0.25 < \hat{\phi} < 0.45$ and $0.75 < \hat{\phi} < 0.95$ while, at other phases, it is equal in magnitude to that of C_y.

Force coefficients at $z/c = 0.5$ are presented in Fig. 5.12, which compares C_x of both Reynolds numbers with the path of the wing tip. In this figure, the phase lag between maximum force and maximum acceleration of the wing is observed to be approximately $\Delta\hat{\phi} = 0.1$.

In Fig. 5.13, the results of Fig. 5.12 are decomposed into its individual terms as pointed out in Eq. (5.27). Here, $C_x^{u,t}$ represents the unsteady term, C_x^{uu} represents the average momentum flux, and $C_x^{u'u'}$ represents the turbulent momentum flux. Figure 5.13

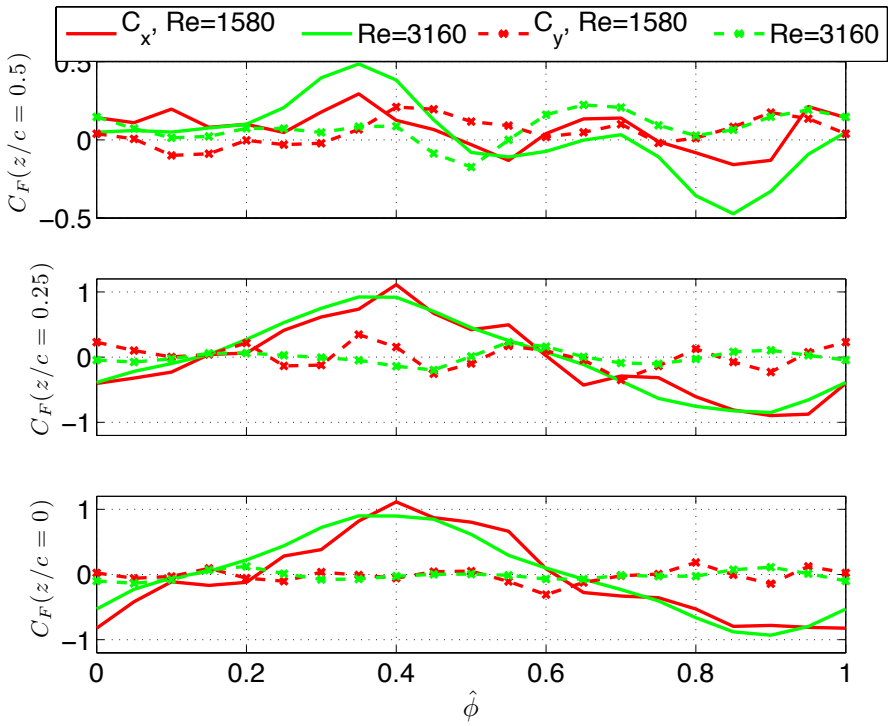

Figure 5.11: Force coefficients for $z/c = 0$ (mid-chord), $z/c = 0.25$ (1/4 chord), and $z/c = 0.5$ (leading edge). Results are after the moving average.

shows local increases for $C_x^{u,t}$ at $0.3 \leq \hat{\phi} \leq 0.45$ and $0.8 \leq \hat{\phi} \leq 0.95$. These increases can be observed in Fig. 5.6 where the leading edge vortex at $\hat{\phi} = 0.25$ disappear due to outward diffusion as also shown by the dye visualization in Fig. 5.3(d)–(e).

In Fig. 5.13, C_x^{uu} shows no distinguishable flow phenomena throughout the flapping phase. To describe the mechanism of momentum transfer, we now select a smaller control volume so that the momentum flux is explicitly evaluated. Forces in Fig. 5.15 were evaluated using a smaller control volume,

$$-0.64 \leq x \leq 0.64, -1.12 \leq y \leq 1.12 \tag{5.31}$$

This control volume is defined in Fig. 5.14

Figure 5.15 shows large magnitudes of C_x^{uu} around $\hat{\phi} = 0.4$ and $\hat{\phi} = 0.8$, as compared to Fig. 5.13, due to the flux of average momentum passing across the control surface. C_x^{uu} is delayed further than $C_x^{u,t}$ reaching values as high as $\Delta\hat{\phi} = 0.05$. The relation of the magnitude of C_x^{uu} to the phase angle is related to the size of the selected control volume.

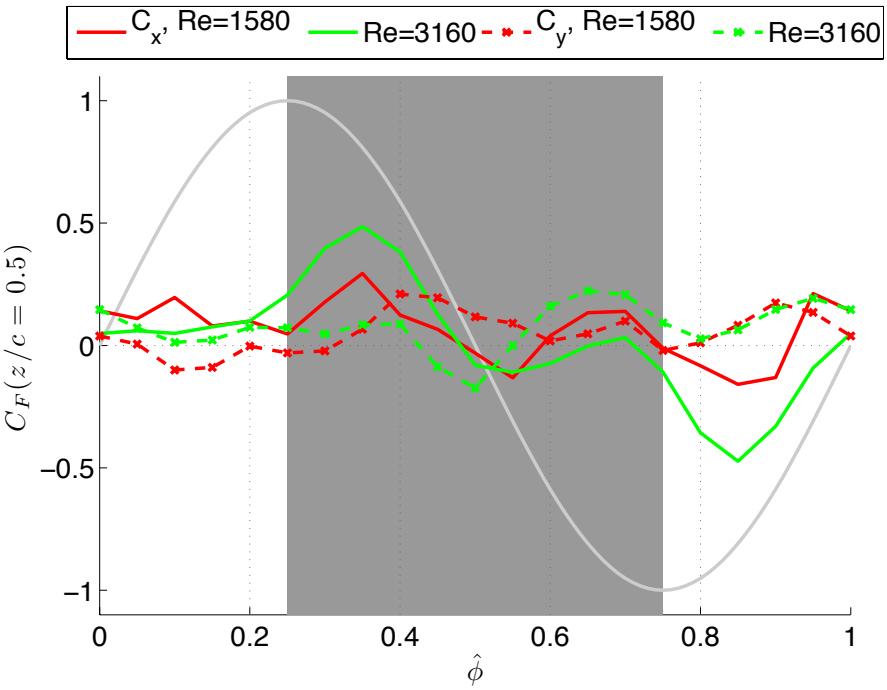

Figure 5.12: Force coefficients for $z/c = 0.5$ (leading edge). Results are after the moving average.

The selection of a smaller control volume will detect the momentum flux more strongly due to the diffusion of the vortex to the surrounding fluid at rest.

To evaluate the flow structures around the edge and near the tip, Eq. (5.31) was divided into two control volumes,

$$-0.64 \leq x \leq 0.64, \qquad -1.12 \leq y < -0.4 \tag{5.32}$$

$$-0.64 \leq x \leq 0.64, \qquad -0.4 \leq y \leq 1.12 \tag{5.33}$$

These control volumes are defined in Fig. 5.16 where the volume defined by Eq. (5.31) will be called $\mathcal{V}$, by Eq. (5.32) will be called $\mathcal{V}_e$, and by Eq. (5.33) will be called $\mathcal{V}_t$. Thus, $\mathcal{V} = \mathcal{V}_e + \mathcal{V}_t$, where $\mathcal{V}_e$ is the volume covering the edge of the plate and $\mathcal{V}_t$ is the volume covering the tip and the region beyond the tip.

In Figs. 5.17–5.20, three rows represent force evaluation in $\mathcal{V}$, $\mathcal{V}_e$, and $\mathcal{V}_t$ from top to bottom. Figure 5.17 shows that the unsteady term, $C_x^{u,t}$, at $z/c = 0.5$, is higher at the region encompassed by $\mathcal{V}_e$ than that by $\mathcal{V}_t$. Therefore, the vortex around the edge

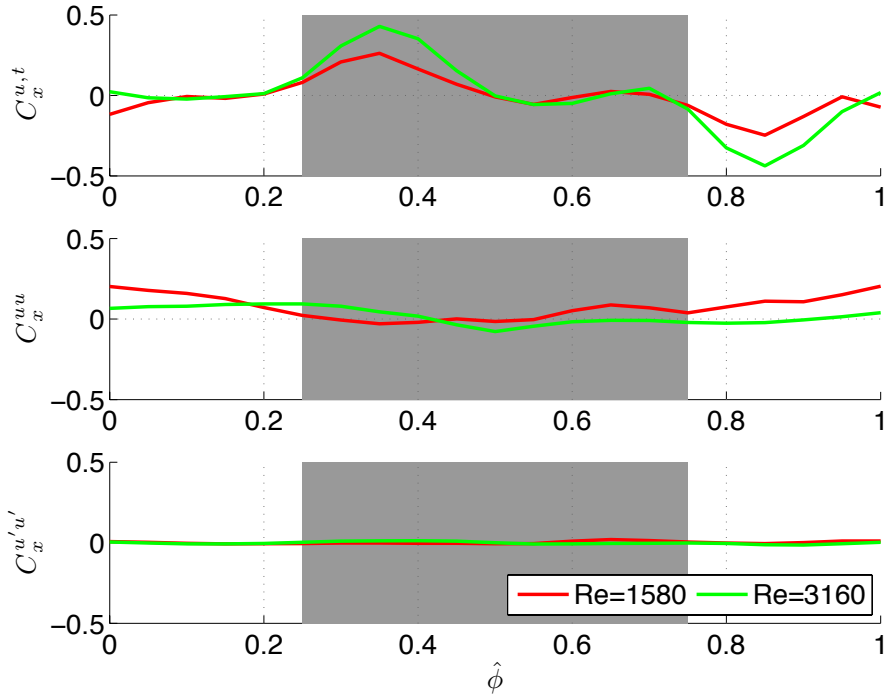

Figure 5.13: Force coefficients for $z/c = 0.5$ decomposed into: unsteady term $C_x^{u,t}$, average momentum flux C_x^{uu}, and turbulent momentum flux $C_x^{u'u'}$. Calculated under the condition in Eq. (5.30).

of the plate is the main source of the unsteady term because it experiences massive changes more than the flow in $\mathcal{V}_t$. The unsteady term of $\mathcal{V}_t$ shows that at $0.5 \leq \hat{\phi} \leq 0.75$ and $0 \leq \hat{\phi} \leq 0.25$ the unsteady term is minimum, which depicts a "developed" vortex structure behind the plate, as sketched in Fig. 5.7. In Fig. 5.17 the "developed" state is reached more quickly for the low Reynolds number.

C_z at $z/c = 0.5$ is plotted in Fig. 5.18 where by calculating Eq. (5.27) in $\mathcal{V}$, a positive force at $0.3 \leq \hat{\phi} \leq 0.45$ and a negative force $0.8 \leq \hat{\phi} \leq 0.95$ are observed. Decomposing $\mathcal{V}$ to $\mathcal{V}_e$ and $\mathcal{V}_t$, negative force is observed at $\mathcal{V}_e$ and positive force is observed at $\mathcal{V}_t$ for the aforementioned phase angles. Figure 5.7 shows that the flow encompassed by $\mathcal{V}_t$ at $0 \leq \hat{\phi} \leq 0.25$ and $0.5 \leq \hat{\phi} \leq 0.75$ includes a vortex structure that appears to be an extension of the leading edge vortex moving outward (positive z-direction). The sketch also shows that in the region of $\mathcal{V}_e$, the leading edge vortex is not observed because it was diffused outward and, as a consequence, $C_z(\mathcal{V}_e)$ of Fig. 5.18 is negative

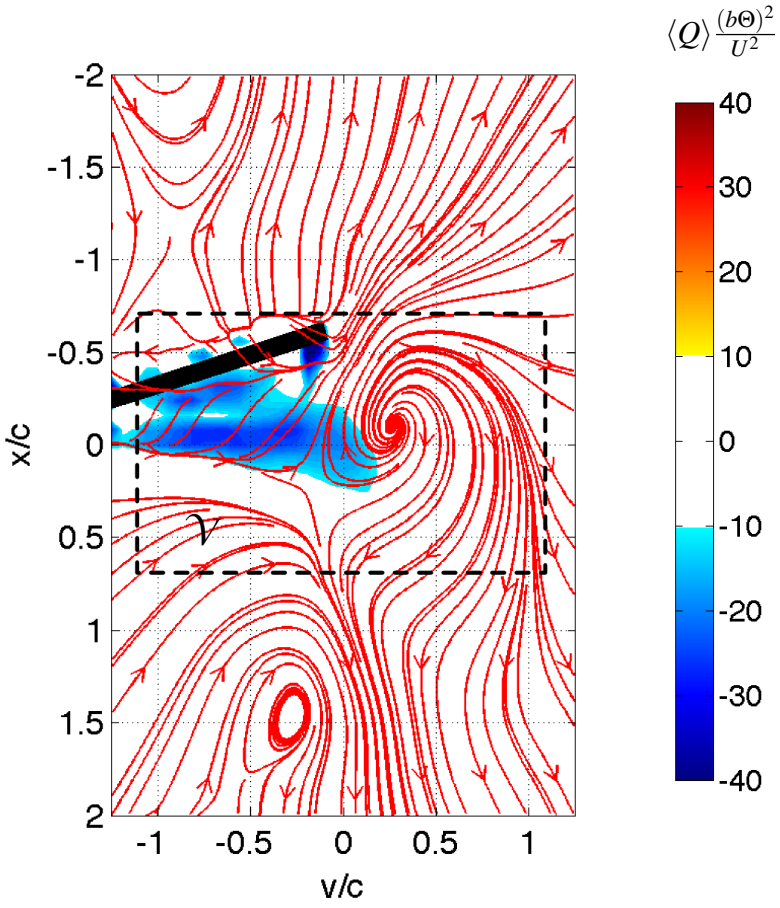

Figure 5.14: The control volume defined by Eq. (5.31).

due to the existence of the new vortex formed around the edge of the plate. However, the dynamics of the leading edge vortex are still distinguishable from the evaluation of $\mathcal{V}_t$. This dynamic is also observable in Fig. 5.3(b)–(e). The dye is behind the plate in Fig. 5.3(b)–(c) and is diffused around the edge of the plate in Fig. 5.3(d)–(e) indicating the existence of a vortex attached to the edge of the plate with opposite rotation to that of the leading edge vortex.

Forces in y-direction are of particular interest since the velocity profile at this direction has been studied by Jones et al (1998) and Lai and Platzer (1999), among others, as part of the study of flow caused by fluttering. They clarified the existence of the

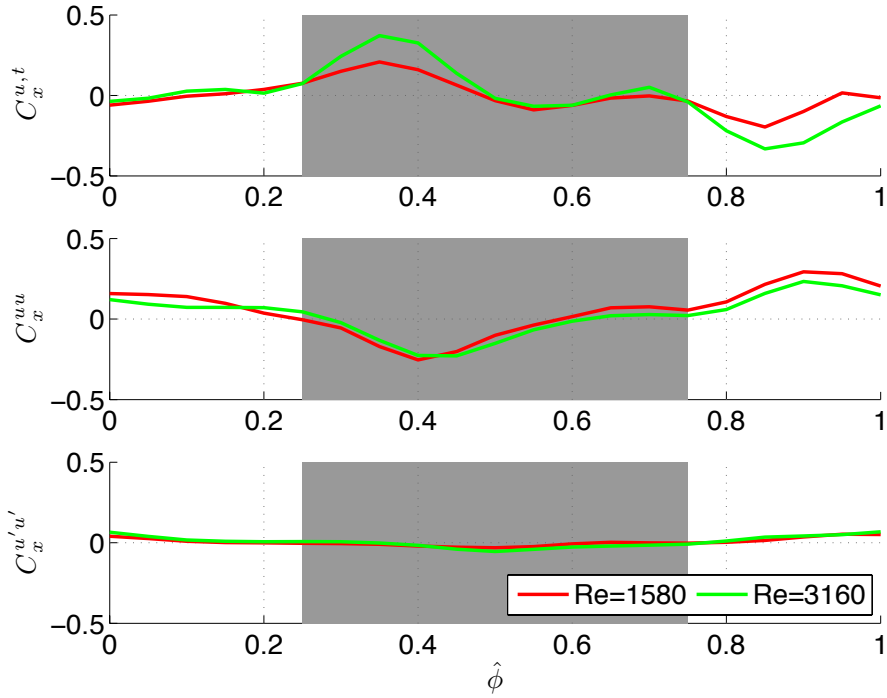

Figure 5.15: Force coefficients for $z/c = 0.5$ decomposed into: unsteady term $C_x^{u,t}$, average momentum flux C_x^{uu}, and turbulent momentum flux $C_x^{u'u'}$. Calculated under the condition in Eq. (5.31).

Knoller-Betz effect, which is a thrust producing effect for a plunging or oscillating airfoil. To see the same effect, the phase-averaged momentum flux, C_y^{uu}, on $z/c = 0.5$ is presented in Fig. 5.19 with the same volume decomposition explained by Eqs. (5.32) and (5.33). C_y^{uu} at $\mathcal{V}$ shows different graphs between low and high Reynolds numbers. C_y^{uu} calculated with $\mathcal{V}_e$ of low and high Reynolds numbers fits well. C_y^{uu} of $\mathcal{V}_e$ produces drag at $0.25 \leq \hat{\phi} \leq 0.55$ and $0.75 \leq \hat{\phi} \leq 0.05$. The existence of drag at these phase angles is related to the appearance of vortex attached on the windward surface of the plate. Although C_y^{uu} of $\mathcal{V}_t$ shows discrepancies between the Reynolds number, it still produces jet flow. This discrepancy is associated with the change of the flapping frequency of the plate.

C_y^{uu} on $z/c = 0$ is shown in Fig. 5.20. In one cycle, C_y^{uu} on $\mathcal{V}$ has greater magnitude from $0 \leq \hat{\phi} \leq 0.4$ compared to $0.6 \leq \hat{\phi} \leq 1$ and is negative at $0.45 \leq \hat{\phi} \leq 0.55$ for high Reynolds number. At low Reynolds number a different graph is observed. Similar to

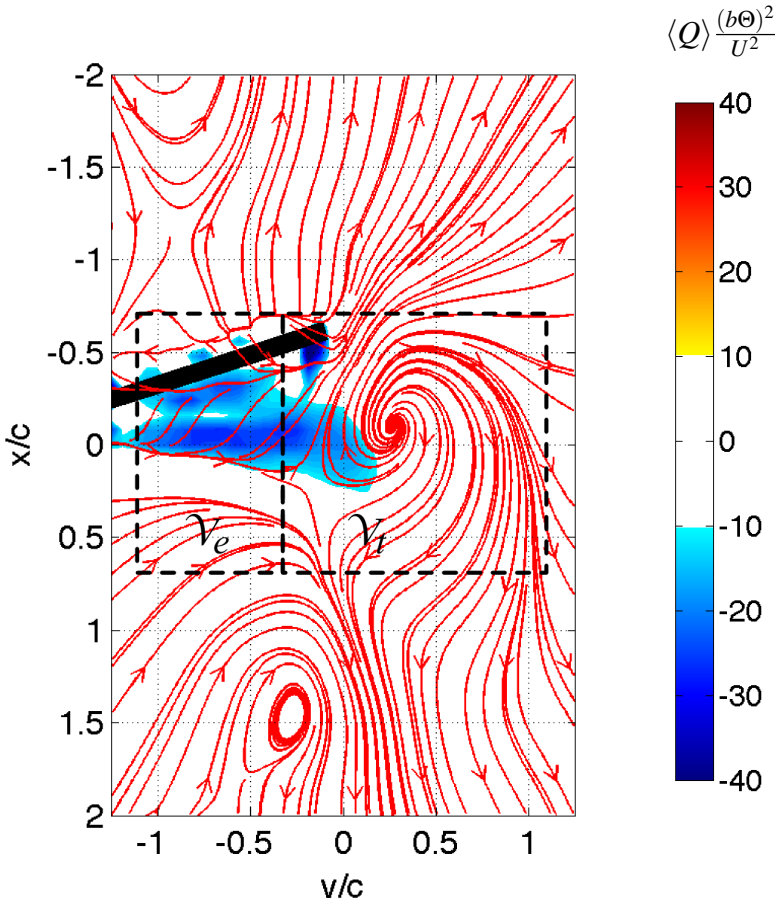

Figure 5.16: The control volume defined by Eqs. (5.32)–(5.33).

Fig. 5.19, the differences can be observed by performing an evaluation on $\mathcal{V}_e$ and $\mathcal{V}_t$. In $\mathcal{V}_e$, C_y^{uu} of low and high Reynolds numbers fit nicely. However, in $\mathcal{V}_t$, C_y^{uu} for low and high Reynolds numbers produce different curves, indicating a difference between the two flow regimes similar to that depicted in Fig. 5.20. However, the effect of momentum flux on y-direction over time is the same, which produces a force directed along the positive y-axis, regardless of Reynolds number or position, as shown in Table 5.2. Thrust producing flow is depicted by the direction of the streamlines in Fig. 5.5–5.6. Here, source elements are observed around the edge of the plate for the duration of flapping.

Table 5.3 shows the time averaged force resulting from C_x for both Reynolds num-

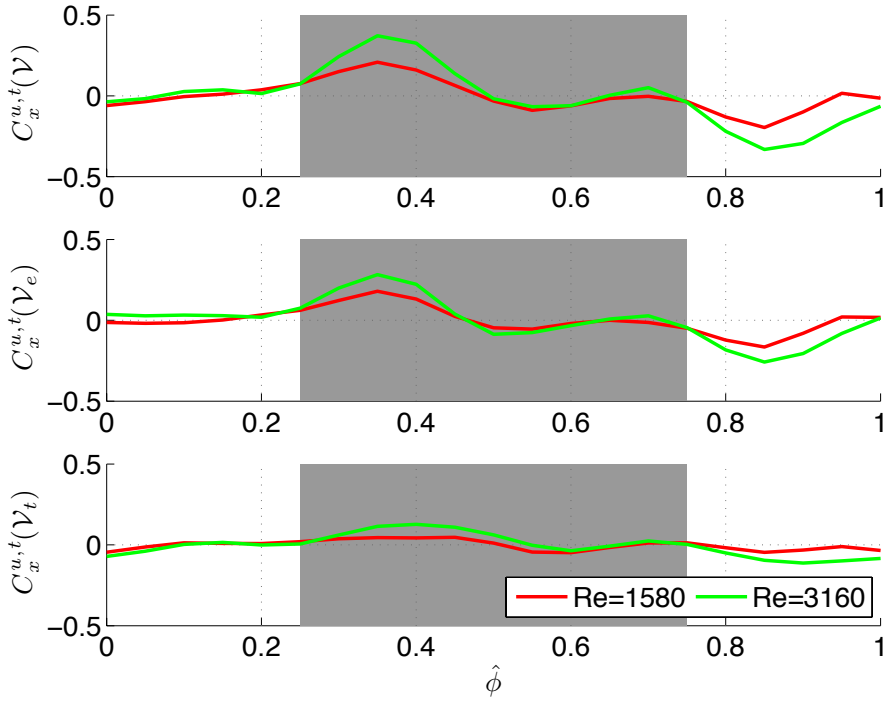

Figure 5.17: $C_x^{u,t}$ at $z/c = 0.25$ calculated with $\mathcal{V}$ and decomposed into $\mathcal{V}_e$ and $\mathcal{V}_t$.

Table 5.2: Time-averaged C_y^{uu} at $z/c = 0$ and $z/c = 0.5$

	$z/c = 0$	$z/c = 0.5$
Re=1580	0.02	0.02
Re=3160	0.02	0.04

bers on the edge of the plate. The values of C_x in Table 5.3 highlight the slight asymmetry of the vortex shedding, which was also reported by Lai and Platzer (2000) for a plunging symmetric airfoil at zero free-stream velocity. By decomposition of $\mathcal{V}$, the value of C_x is seen to be negative for $\mathcal{V}_e$ and positive for $\mathcal{V}_t$. For $\mathcal{V}_e$, the value of C_x is higher in magnitude at higher Reynolds number. Conversely, for $\mathcal{V}_t$, it is higher at lower Reynolds numbers. This depicts the nature of the leading edge vortex where the flow follows the motion of the plate and, around the tip, the flow is moving in the opposite direction of the plate.

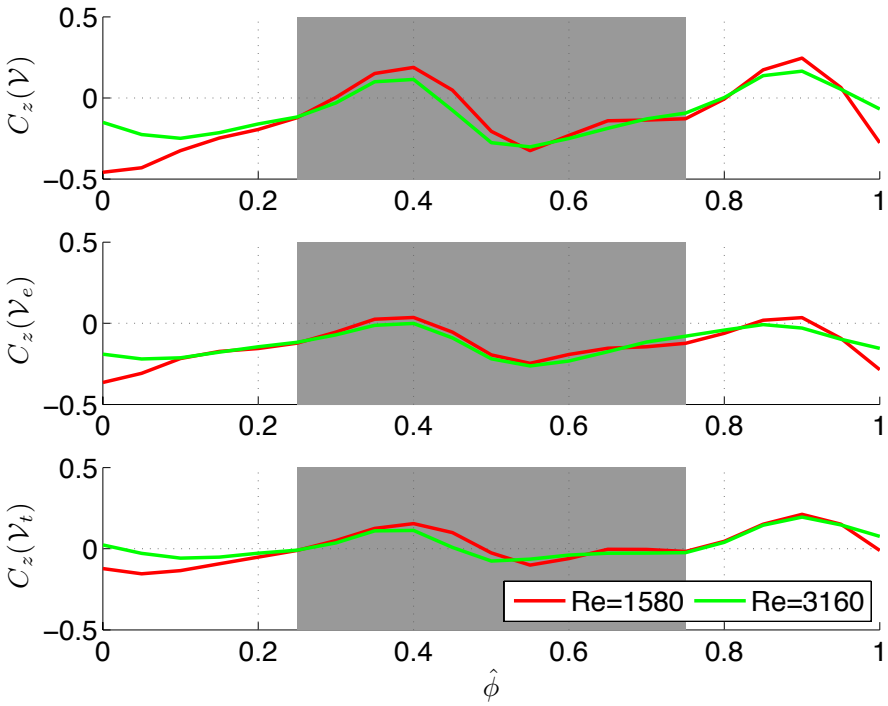

Figure 5.18: C_z at $z/c = 0.5$ calculated with $\mathcal{V}$ and decomposed into $\mathcal{V}_e$ and $\mathcal{V}_t$.

Table 5.3: Time-averaged C_x at $z/c = 0.5$ calculated with $\mathcal{V}$, $\mathcal{V}_e$ and $\mathcal{V}_t$.

	$\mathcal{V}$	$\mathcal{V}_e$	$\mathcal{V}_t$
Re=1580	0.0062	-0.0232	0.0281
Re=3160	-0.0164	-0.0348	0.0163

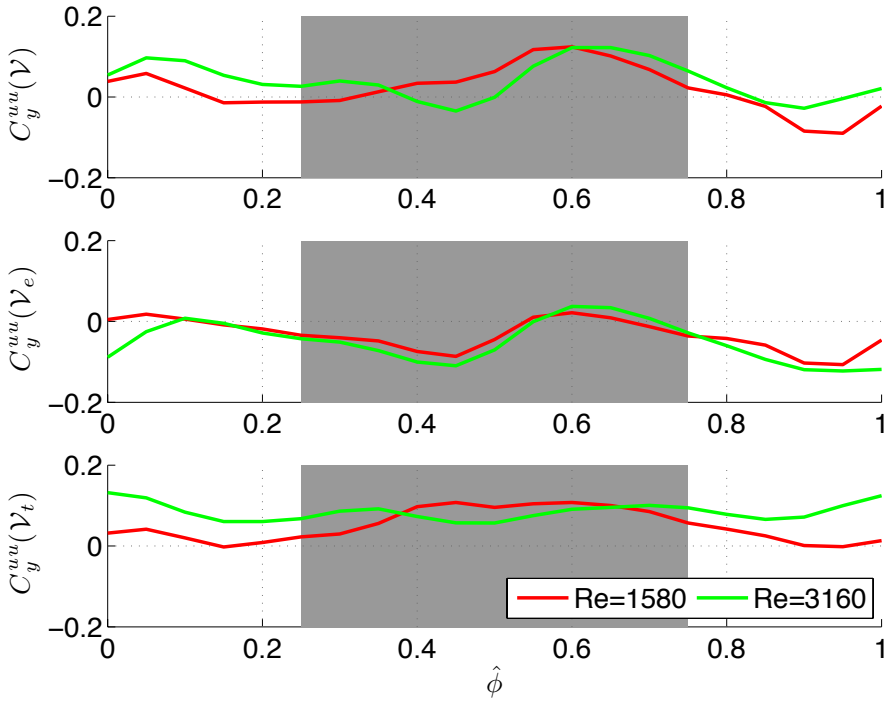

Figure 5.19: C_y^{uu} at $z/c = 0.5$ calculated with $\mathcal{V}$ and decomposed into $\mathcal{V}_e$ and $\mathcal{V}_t$.

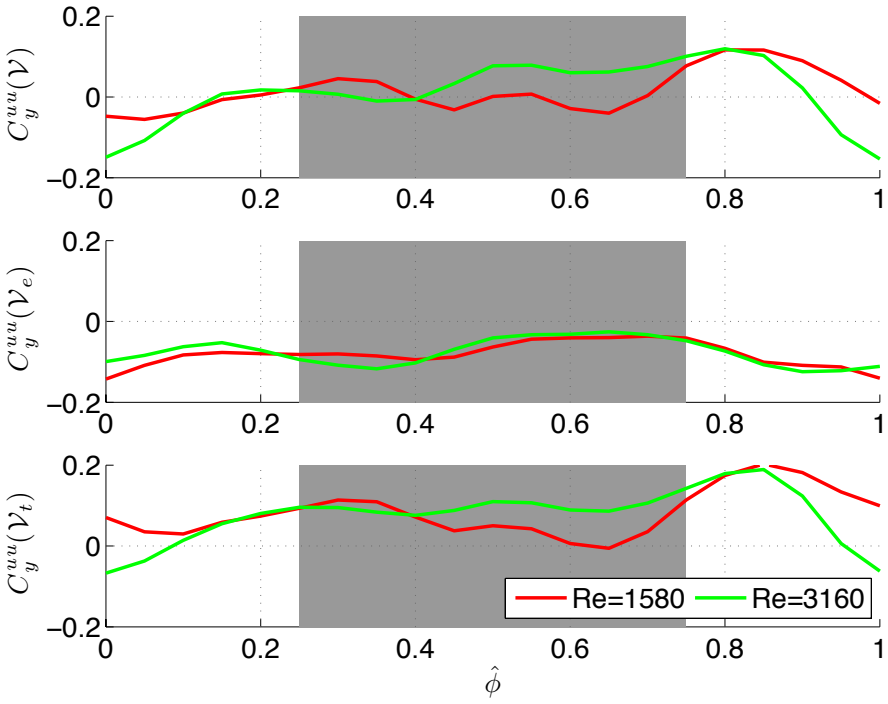

Figure 5.20: C_y^{uu} at $z/c = 0.5$ calculated with $\mathcal{V}$ and decomposed into $\mathcal{V}_e$ and $\mathcal{V}_t$.

5.6 Concluding remarks

Quantitative flow visualization and the evaluation of force of a control volume were applied to the phase-averaged velocity field and time-averaged velocity generated by the periodic motion of a rigid plate. Velocity field were measured with stereo PIV in the region surrounding the tip of the plate.

The calculation of the second invariance of the deformation tensor, $\langle Q \rangle$, depicts the three-dimensional structure of the vortex around the plate but does not visualize the dynamics of the structure. Additional information was visualized with streamlines for the regions with $\langle Q \rangle < 0$.

The selection of control volume size for the force analysis enables the investigation of selected parts of the phase-averaged velocity field, which provides better understanding of the vortex structures that influence force generation. By properly selecting the size of the control volume, acceleration, and convection of the flow can be explained using their respective terms in the integral equation of fluid motion.

Force calculated by control volume analysis of the phase-averaged velocity field shows that the vortex attached to the surface of the plate plays a dominant role in the generation of force. Delays in reaching the maxima of the force magnitude are caused by the existence of the vortex structure of the previous stroke obstructing the motion of the plate. Increases in the extremes of the force due to the Reynolds number only appear in the unsteady term near the edge of the plate.

This study demonstrates the flexibility of the proposed control volume analysis in analyzing features of the flow around a flapping plate. The lack of spatial resolution in the z-direction results in an underdetermined vortex size. However, comparison with qualitative visualization shows reasonable similarities and enables the study of vortex structures produced by the motion.

Chapter 6

The pressure field around the flapping plate

The estimation of the pressure field of the flow generated by a flapping rigid plate is given in this chapter. The facility setup is given in Chapter 4. Measurements were done with two measurement plane configurations as explained in §6.1. The validation of measurement data and the measurement uncertainty were quantified in §6.2. The numerical methods to solve the Poisson equation in the *xy* planes and *xz* planes are explained in §6.3 and §6.4, respectively. The pressure field as the result of integrating the Poisson equation is presented in §6.5 and final remarks are given in §6.6.

6.1 Measurement setup

For the surface pressure integration, at least three planes were required to solve the three dimensional Poisson equation of each slice of the flow for each phase angle and each Reynolds number. Two positions of the plate were investigated: at the mid-chord section, three planes were measured at $z = (-2, 0, 2)$mm, and at the leading-edge section, three planes were measured at $z = (8, 10, 12)$mm, as shown in Fig. 6.1. A similar setup was used to record the leading edge vortices along the spanwise with measurement planes parallel to the *xz* planes; the flow on three planes were measured at $y = (-12, -10, -8)$mm and at $y = (-2, 0, 2)$mm as shown in Fig. 6.2.

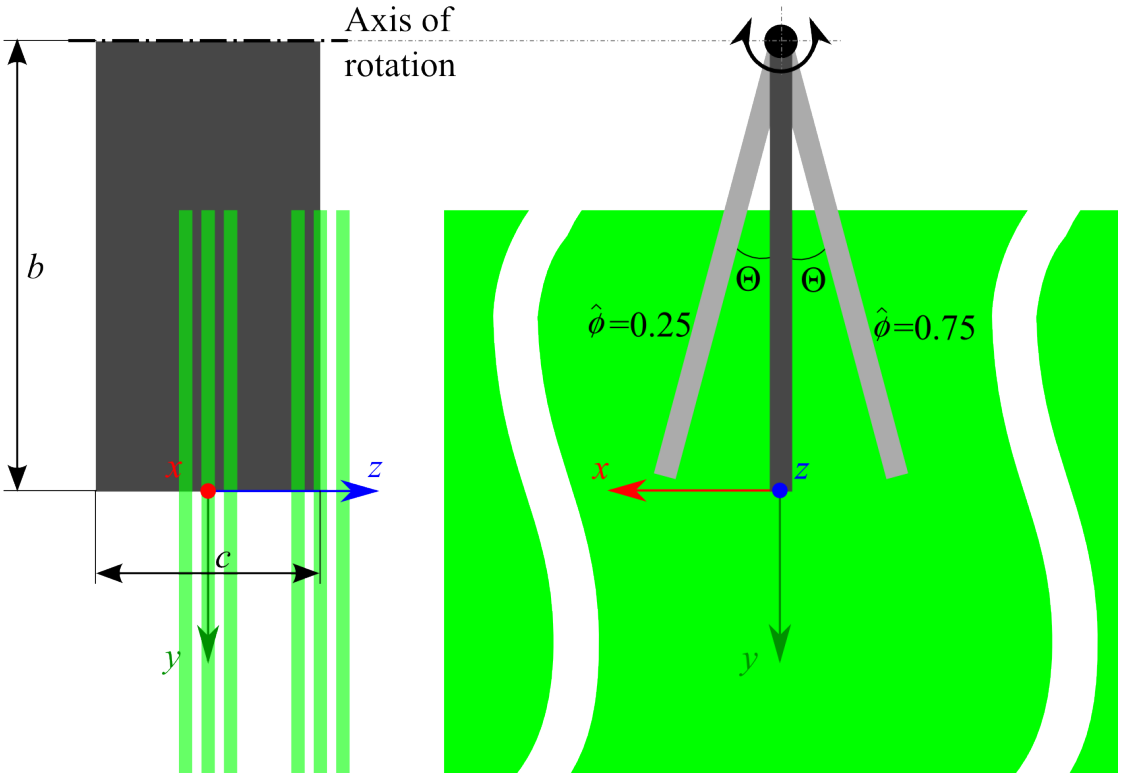

Figure 6.1: Position of measurement planes parallel to *xy*-plane used for the integration of surface pressure. The plate is illustrated in *dark gray*.

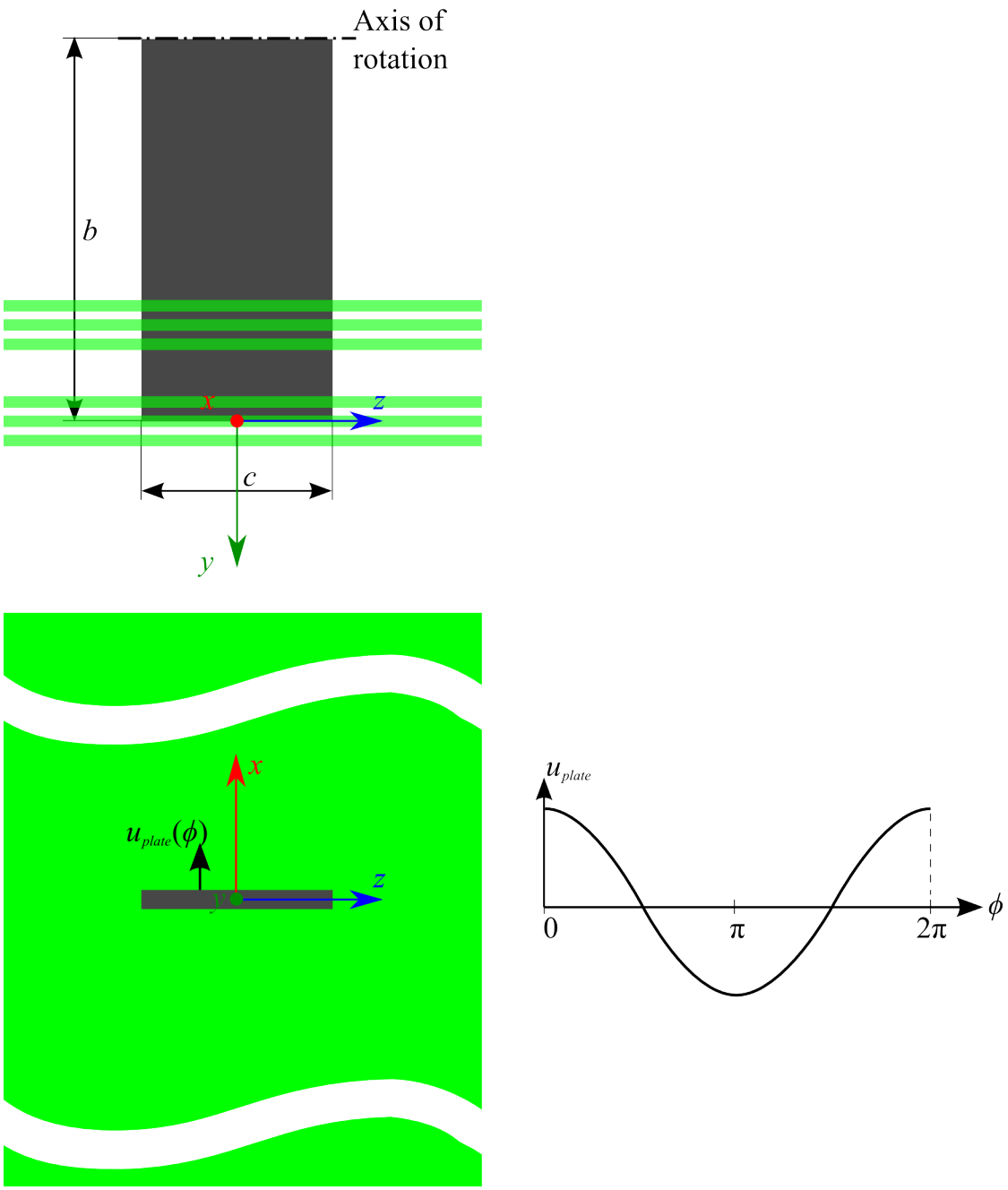

Figure 6.2: Position of measurement planes parallel to *xz*-plane used for the integration of surface pressure. The plate is illustrated in *dark gray*.

6.2 Data validation and measurement uncertainty

Classification of the cause of the velocity fluctuation of a measured field needs careful treatment because it will affect the estimation of flow properties. The fluctuation may be caused by measurement uncertainty, which has random behavior and the other cause of fluctuation is small-scale turbulence structures. The first source is inherent in any measurement and the second one, if it exist at all, will be superposed with the first. In this study, PIV was used to measure the flow near a flapping wing and a complex flow is expected due to three dimensionality. Therefore, the fitness of sample was evaluated for the entire sampling points. Statistics test for normality can be applied, because the first source produces a normal distribution of the probability distribution function of the instantaneous velocity and the second one causes a departure from normality. For PIV, the result of the statistics test can be presented using a boolean map of the flow field.

In this paper, Shapiro-Wilk test was used to validate the uncertainty. Shapiro-Wilk test examines the *null hypothesis* that a sample comes from a normally distributed population (Shapiro and Wilk, 1965). The Shapiro-Wilk test was chosen because it is suited to process a large number of sample. The result of the test is an acceptance of the null hypothesis. The rejection will come when small scale turbulent structures are stronger than the inherent measurement uncertainty.

The Shapiro-Wilk test is formulated as

$$W = \frac{(\sum_{i=1}^{n} a_i x_{(i)})^2}{\sum_{i=1}^{n} (x_i - \bar{x})} \tag{6.1}$$

where a_i is

$$(a_1, \cdots, a_n) = \frac{m^T V^{-1}}{(m^T V^{-1} V^{-1} m)^{1/2}} \tag{6.2}$$

and $m^T = m_1, \cdots, m_n$ are the expected values of the order statistics of independent and identically-distributed random variables sampled from the standard normal distribution, and V is the covariance matrix of those order statistics.

The criteria to reject the null hypothesis can be found from the W–p value table (Shapiro and Wilk, 1965). if $p(\alpha) < W$, the null hypothesis is rejected. α is called the *level of significance*. In the above explanation of statistics test, the result may have *type*

I errors at a rate of α. Namely, there is an α chance that the result is accepted when it should be rejected (type I error is also known as, false positive).

A normally distributed sample has zero skewness and kurtosis. Skewness represents the asymmetry of the probability of density function of a real valued random variable from the mean value. Positive skewness shows that the tail of the right side of the probability density function is longer than the left side. The skewness is formulated as

$$g_1 = \frac{m_3}{m_2^{3/2}} = \frac{\frac{1}{n}\sum_{i=1}^{n}(x_i - \bar{x})^3}{(\frac{1}{n}\sum_{i=1}^{n}(x_i - \bar{x})^2)^{3/2}} \tag{6.3}$$

Kurtosis represents the flatness of the probability distribution function of a real-valued random sample. A sample with positive kurtosis will have a more acute peak around the mean. The kurtosis is formulated as

$$g_2 = \frac{m_4}{m_2^2} - 3 = \frac{\frac{1}{n}\sum_{i=1}^{n}(x_i - \bar{x})^4}{(\frac{1}{n}\sum_{i=1}^{n}(x_i - \bar{x})^2)^2} - 3 \tag{6.4}$$

Departure of normality will show a departure of zero skewness and kurtosis.

In the evaluation of the periodic velocity field measured by PIV, the sample x_i is the cycle-to-cycle velocity distribution of each flapping phase. Therefore, $x_i = u_i(x, y, z, \hat{\phi})$ for all measured cycles.

The Boolean map in Fig. 6.3(a) shows the points where the sample departs from normality as evaluated by the Shapiro-Wilk test. The Boolean map shows the acceptance (red) or rejection (blue) of the null hypothesis that the sample comes from a normal distribution. The points that departed from normality was observed to be correlated with the excess of kurtosis and skewness, as shown in Fig. 6.3(c) and (b). The departure from normality shows that the sample consists of fluctuations by flow structures instead of only by measurement uncertainties. This non-normality is taken into account by introducing the Reynolds decomposition of the governing equations. The measurement uncertainties were calculated as described in Coleman and Steele (1995) and their spatial average are $\sigma_{\langle u \rangle}, \sigma_{\langle v \rangle}, \sigma_{\langle w \rangle} = (3\%, 3\%, 5\%)$ of the maximum tip velocity of the plate. The repeatability of the flow is evident from Fig. 6.4. In this figure, the velocity profile along the x-axis at $z = 0$ and $y = -c/2$ from measurements taken on the xy-plane and xz-plane are plotted together. The vertical bars in these figures indicate the measurement uncertainties. These figures show that the velocity profiles of different

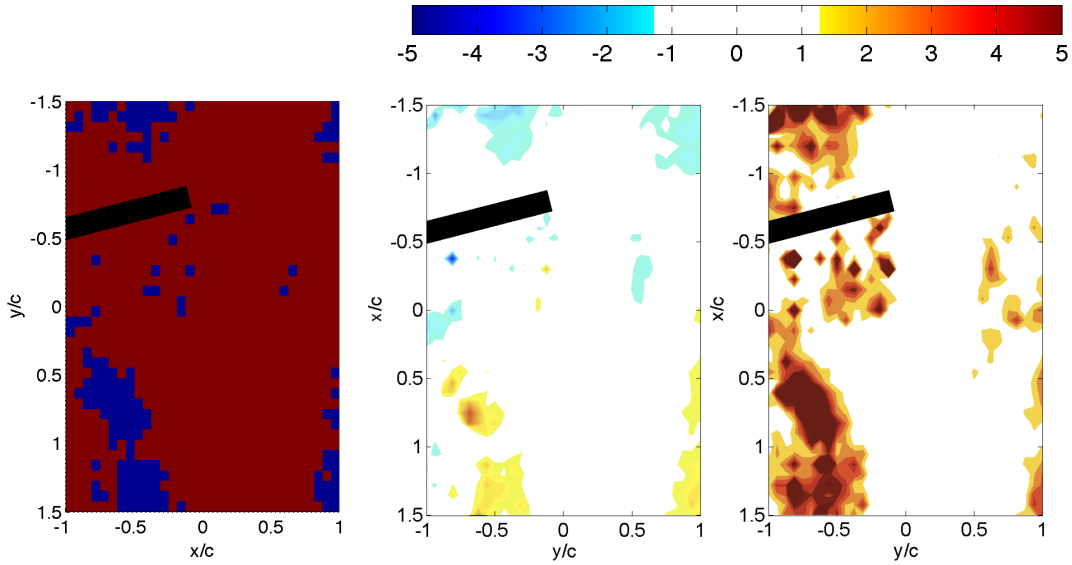

(a) Shapiro-Wilk test, $\hat{\phi} = 0.35$, $z = 0$

(b) Skewness, Eq. (6.3)

(c) Kurtosis, Eq. (6.4)

Figure 6.3: Statistical evaluation of the velocity field by (a) the Shapiro-Wilk test, (b) Skewness, and (c) Kurtosis for the flow at $\hat{\phi} = 0.35$. For (a), *red* indicates normally distributed sample and *blue* indicates a sample that deviated the normal distribution.

measurement plane orientation are within the measurement uncertainties. Especially for $\langle w \rangle$, its profile varies around zero.

The symmetry of the flow can be seen in Fig. 6.5 for both low and high reynolds number. The magnitude of the circulation of $z < 0$ and $z > 0$ are compared with each other. The circulation was calculated from the velocity distribution on the xz-plane at $y = -c/2$. The vertical bars are the ambiguity of the circulation due to measurement uncertainty. This figure shows that the circulation around the two parts of the flow are within the margin of uncertainty and the flow can be assumed to be symmetric along the xy-plane.

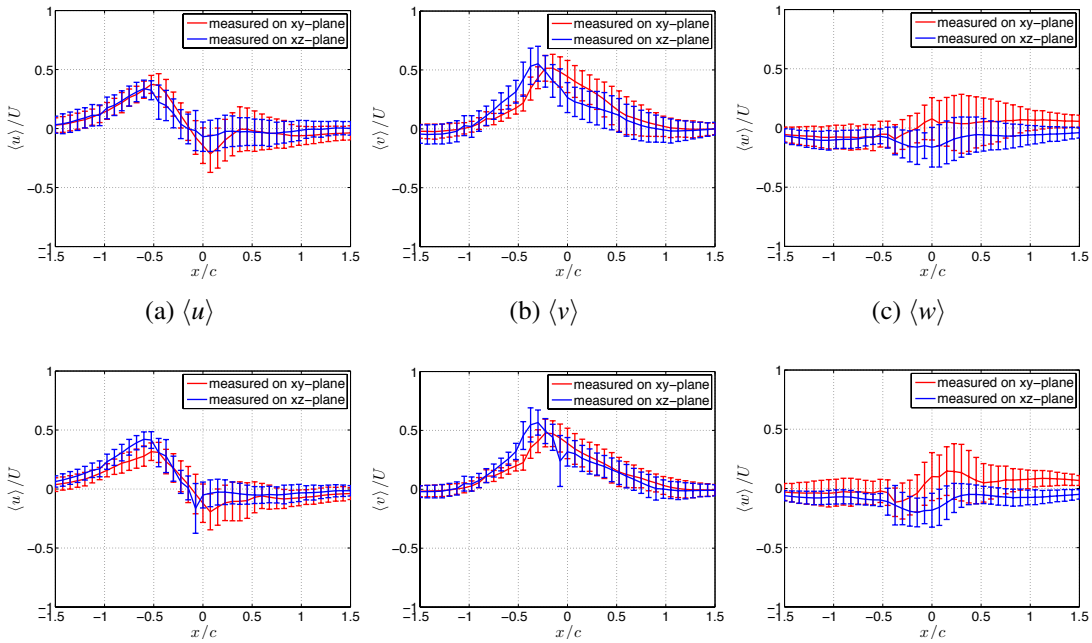

(a) $\langle u \rangle$ (b) $\langle v \rangle$ (c) $\langle w \rangle$

(d) $\langle u \rangle$ (e) $\langle v \rangle$ (f) $\langle w \rangle$

Figure 6.4: Repeatability of velocity measurements as shown by the velocity profiles at $z = 0$ and $y = -c/2$ of $\langle u \rangle$, $\langle v \rangle$, $\langle w \rangle$ normalized by the maximum velocity of the tip, U, for (a)–(c) Re=1580 and (d)–(f) Re=3160. The red line represents the velocity measurements on xz-plane orientation, Fig. 6.1, and the blue line represents the measurement on xz-plane orientation, Fig. 6.2.

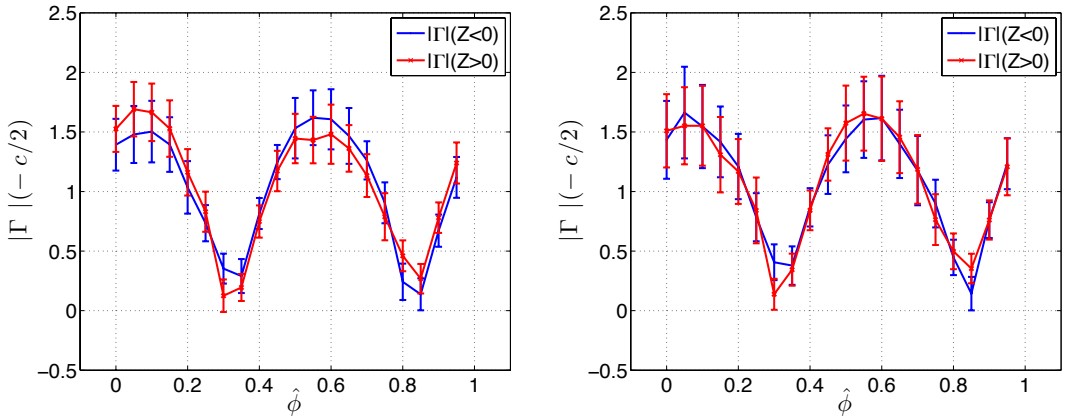

(a) $|\Gamma(\mathrm{Re} = 1580)|$ (b) $|\Gamma(\mathrm{Re} = 3160)|$

Figure 6.5: Symmetricity of the circulation ($\Gamma(Ub\Theta) = \int_A \omega \cdot d\mathbf{A}$) profile at $Y = -c/2$ along the Z-axis for (a) Re= 1580 and (b) Re= 3160.

6.3 Numerical method for solving the Poisson equation in the xy planes

The method to estimate the pressure field around a flapping plate was derived in Chapter 3. The global mesh was applied on the measured velocity field and the local mesh was applied attached to the flapping plate. Because the plate is moving, the velocity field of the local mesh was relative to the non-inertial reference frame.

6.3.1 In the global mesh

The pressure equation in global mesh is formulated as

$$\frac{\partial^2\langle p\rangle}{\partial x_i^2} = \frac{\partial\langle u_i\rangle}{\partial x_j}\frac{\partial\langle u_j\rangle}{\partial x_i} + \frac{\partial^2}{\partial x_i \partial x_j}\langle u_i' u_j'\rangle \tag{6.5}$$

and the global mesh is shown in Fig. 6.6.

Expanding the tensorial indices, where $x_i = (x, y, z)$ and $\langle u_i\rangle = (\langle u\rangle, \langle v\rangle, \langle w\rangle)$, Eq. (6.5) becomes

$$\begin{aligned}
&\frac{\partial^2\langle p\rangle}{\partial x^2} + \frac{\partial^2\langle p\rangle}{\partial y^2} + \frac{\partial^2\langle p\rangle}{\partial z^2} = \\
&\quad -\rho\left[\left(\frac{\partial\langle u\rangle}{\partial x}\right)^2 + \left(\frac{\partial\langle v\rangle}{\partial y}\right)^2 + \left(\frac{\partial\langle w\rangle}{\partial z}\right)^2 + 2\left(\frac{\partial\langle u\rangle}{\partial y}\frac{\partial\langle v\rangle}{\partial x} + \frac{\partial\langle u\rangle}{\partial z}\frac{\partial\langle w\rangle}{\partial x} + \frac{\partial\langle v\rangle}{\partial z}\frac{\partial\langle w\rangle}{\partial y}\right)\right. \\
&\qquad \left. + \left(\frac{\partial^2\langle u'u'\rangle}{\partial x^2} + \frac{\partial^2\langle v'v'\rangle}{\partial y^2} + \frac{\partial^2\langle w'w'\rangle}{\partial z^2}\right) + 2\left(\frac{\partial^2\langle u'v'\rangle}{\partial y\partial x} + \frac{\partial^2\langle u'w'\rangle}{\partial z\partial x} + \frac{\partial^2\langle v'w'\rangle}{\partial z\partial y}\right)\right]
\end{aligned} \tag{6.6}$$

The derivation of Eq. (6.6) to the finite difference expression is discussed next in two section: the right hand side, which will be denoted by a short-hand, ψ, and the left hand side, $\nabla^2 p$.

Finite differentiation of ψ

The PIV velocity field is located on the corner faces of the numerical mesh. We want to solve the pressure on the center node. The coordinates of the corners are given as (x, y, z)

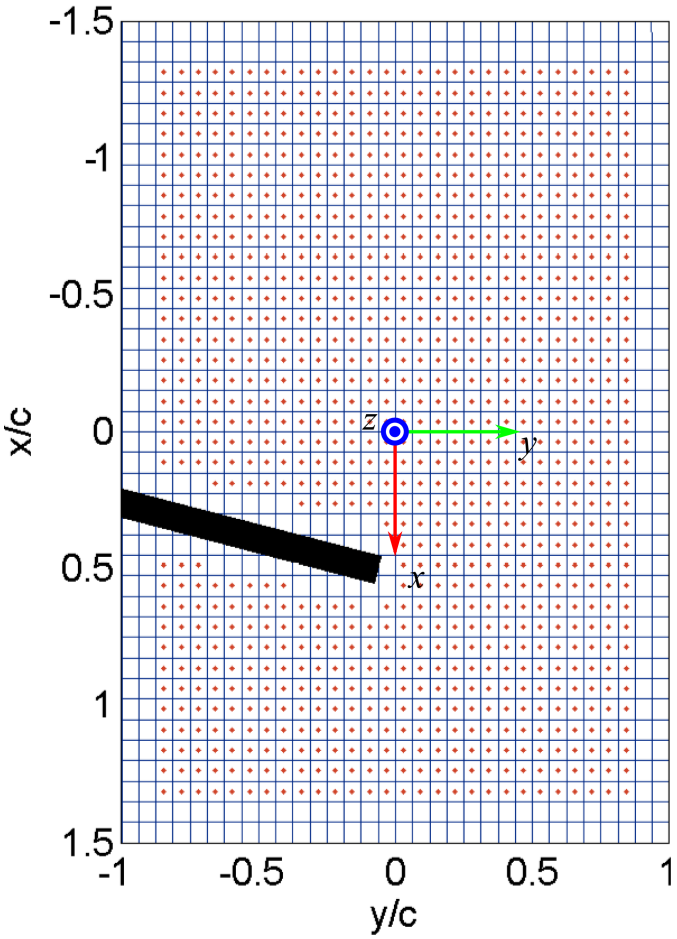

Figure 6.6: The definition of global mesh. The phase-averaged velocity field is on the blue grid and the pressure was estimated on the red dots. The black line represents the plate.

and the center nodes as (x^c, y^c, z). The velocity field on the center nodes are obtained by interpolating the PIV velocity field, linearly, and are given as $(\langle u\rangle^c, \langle v\rangle^c, \langle w\rangle^c)$.

The coordinates of the center nodes are given as

$$x^c = \frac{(x)+(x+\Delta x)}{2} \tag{6.7}$$

$$y^c = \frac{(y)+(y+\Delta y)}{2} \tag{6.8}$$

as shown in Fig. 6.7 and the velocity $u_i(x^c, y^c, z)$ is given as

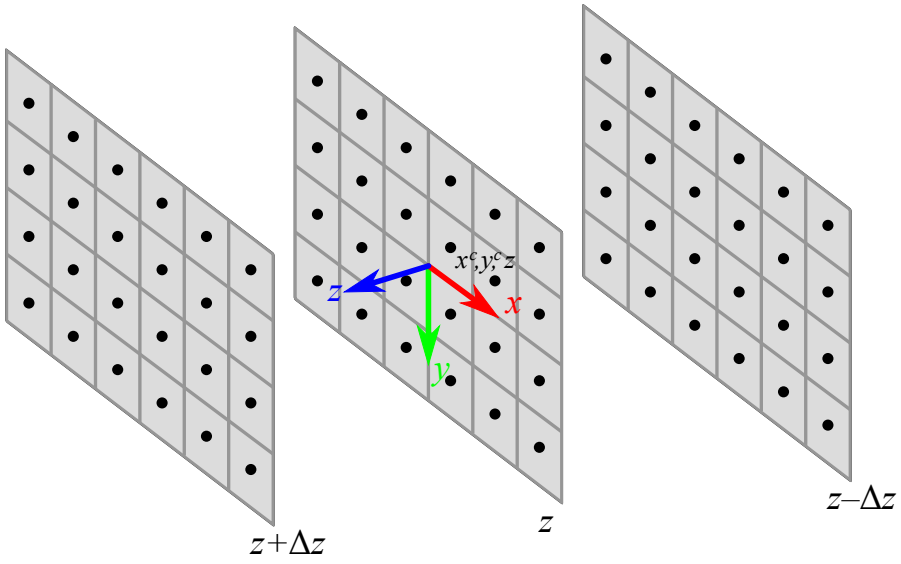

Figure 6.7: Definition of the position of the center nodes: x^c, y^c.

$$\begin{aligned}\langle u\rangle^c &= \langle u\rangle(x^c,y^c,z)\\ &= \frac{1}{4}\Big(u(x,y,z)+u(x+\Delta x,y,z)+u(x,y+\Delta y,z)+u(x+\Delta x,y+\Delta y,z)\Big)\end{aligned} \tag{6.9}$$

$$\begin{aligned}\langle v\rangle^c &= \langle v\rangle(x^c,y^c,z)\\ &= \frac{1}{4}\Big(v(x,y,z)+v(x+\Delta x,y,z)+v(x,y+\Delta y,z)+v(x+\Delta x,y+\Delta y,z)\Big)\end{aligned} \tag{6.10}$$

$$\begin{aligned}\langle w\rangle^c &= \langle w\rangle(x^c,y^c,z)\\ &= \frac{1}{4}\Big(w(x,y,z)+w(x+\Delta x,y,z)+w(x,y+\Delta y,z)+w(x+\Delta x,y+\Delta y,z)\Big)\end{aligned} \tag{6.11}$$

The spatial derivatives are evaluated for the center nodes as shown in the finite differentiation scheme,

$$\begin{aligned}\frac{\partial f}{\partial x} &\approx \frac{\Delta f}{\Delta x}\\ &\approx \frac{f(x+\Delta x,y+\Delta y,z)+f(x+\Delta x,y,z)-f(x,y+\Delta y,z)-f(x,y,z)}{2\Delta x}\end{aligned} \tag{6.12}$$

$$\begin{aligned}\frac{\partial f}{\partial y} &\approx \frac{\Delta f}{\Delta y}\\ &\approx \frac{f(x+\Delta x,y+\Delta y,z)+f(x,y+\Delta y,z)-f(x+\Delta x,y,z)-f(x,y,z)}{2\Delta y}\end{aligned} \tag{6.13}$$

special treatment is required for the derivatives with respect to z because of the length of data available in that direction and the need to evaluate the derivative on the measurement plane.

$$\begin{aligned}\frac{\partial f}{\partial z} &\approx \frac{\Delta f}{\Delta z} \\ &\approx \frac{1}{2\Delta z}\Bigg[\frac{1}{4}\Big(f(x+\Delta x,y+\Delta y,z+\Delta z)+f(x+\Delta x,y,z+\Delta z) \\ &\qquad +f(x,y+\Delta y,z+\Delta z)+f(x,y,z+\Delta z)\Big) \\ &\quad -\frac{1}{4}\Big(f(x+\Delta x,y+\Delta y,z-\Delta z)+f(x+\Delta x,y,z-\Delta z) \\ &\qquad +f(x,y+\Delta y,z-\Delta z)+f(x,y,z-\Delta z)\Big)\Bigg]\end{aligned} \tag{6.14}$$

at the ends of the length of data, the one-sided finite difference formula for the derivative with respect to z was used,

$$\begin{aligned}\frac{\partial f}{\partial z} = \frac{1}{2\Delta z}\frac{1}{4}\Bigg[&-3\Big(f(x+\Delta x,y+\Delta y,z)+f(x+\Delta x,y,z)+f(x,y+\Delta y,z)+f(x,y,z)\Big) \\ &+4\Big(f(x+\Delta x,y+\Delta y,z+\Delta z)+f(x+\Delta x,y,z+\Delta z) \\ &\qquad +f(x,y+\Delta y,z+\Delta z)+f(x,y,z+\Delta z)\Big) \\ &-\Big(f(x+\Delta x,y+\Delta y,z+2\Delta z)+f(x+\Delta x,y,z+2\Delta z) \\ &\qquad +f(x,y+\Delta y,z+2\Delta z)+f(x,y,z+2\Delta z)\Big)\Bigg]\end{aligned} \tag{6.15}$$

where $\Delta z = \Delta z$ or $\Delta z = -\Delta z$ depending on the orientation of the boundary.

The second order derivatives were approximated as

$$\frac{\partial^2 f}{\partial x^2} \approx \frac{\Delta^2 f}{\Delta x^2} = \frac{f(x^c+\Delta x,y^c,z)+2f(x^c,y^c,z)-f(x^c-\Delta x,y^c,z)}{\Delta x^2} \tag{6.16}$$

$$\frac{\partial^2 f}{\partial y^2} \approx \frac{\Delta^2 f}{\Delta y^2} = \frac{f(x^c,y^c+\Delta y,z)+2f(x^c,y^c,z)-f(x^c,y^c-\Delta y,z)}{\Delta x^2} \tag{6.17}$$

$$\frac{\partial^2 f}{\partial z^2} \approx \frac{\Delta^2 f}{\Delta z^2} = \frac{f(x^c,y^c,z+\Delta z)+2f(x^c,y^c,z)-f(x^c,y^c,z-\Delta z)}{\Delta z^2} \tag{6.18}$$

where one-sided finite difference formula was used at the ends of the data. For $z = z_0$,

$$\frac{\partial^2 f}{\partial z^2}_0 \approx \frac{\Delta^2 f}{\Delta z^2}_0 = \frac{f(x^c,y^c,z_0)+2f(x^c,y^c,z_0+\Delta z)-f(x^c,y^c,z_0+2\Delta z)}{\Delta z^2} \tag{6.19}$$

and for $z = z_M$,

$$\frac{\partial^2 f}{\partial z^2}_M \approx \frac{\Delta^2 f}{\Delta z^2}_M = \frac{f(x^c, y^c, z_M) + 2f(x^c, y^c, z_M - \Delta z) - f(x^c, y^c, z_M - 2\Delta z)}{\Delta z^2} \tag{6.20}$$

And the mixed derivatives are approximated as

$$\begin{aligned}\frac{\partial^2 f}{\partial x \partial y} &\approx \frac{\Delta^2 f}{\Delta x \Delta y} \\ &\approx \frac{1}{\Delta x \Delta y}\Big[f(x+\Delta x, y+\Delta y, z) + f(x,y,z) \\ &\qquad - f(x, y+\Delta y, z) - f(x+\Delta x, y, z)\Big]\end{aligned} \tag{6.21}$$

$$\begin{aligned}\frac{\partial^2 f}{\partial x \partial z} &\approx \frac{\Delta^2 f}{\Delta x \Delta z} \\ &\approx \frac{1}{4\Delta x \Delta y}\Big[f(x+\Delta x, y, z+\Delta z) + f(x+\Delta x, y+\Delta y, z+\Delta z) \\ &\qquad - f(x, y, z+\Delta z) - f(x, y+\Delta y, z+\Delta z) \\ &\qquad - f(x+\Delta x, y, z-\Delta z) - f(x+\Delta x, y+\Delta y, z-\Delta z) \\ &\qquad + f(x, y, z-\Delta z) + f(x, y+\Delta y, z-\Delta z)\Big]\end{aligned} \tag{6.22}$$

$$\begin{aligned}\frac{\partial^2 f}{\partial y \partial z} &\approx \frac{\Delta^2 f}{\Delta y \Delta z} \\ &\approx \frac{1}{4\Delta y \Delta z}\Big[f(x+\Delta x, y+\Delta y, z+\Delta z) + f(x, y+\Delta y, z+\Delta z) \\ &\qquad - f(x+\Delta x, y, z+\Delta z) - f(x, y, z+\Delta z) \\ &\qquad - f(x+\Delta x, y+\Delta y, z-\Delta z) - f(x, y+\Delta y, z-\Delta z) \\ &\qquad + f(x+\Delta x, y, z-\Delta z) + f(x, y, z-\Delta z)\Big]\end{aligned} \tag{6.23}$$

The acceleration is formulated as

$$\begin{aligned}\frac{\partial f}{\partial t} &\approx \frac{\Delta f}{\Delta t} \\ &\approx \frac{1}{\Delta t}\frac{1}{4}\Big[\Big(f(x+\Delta x,y+\Delta y,z,t+\Delta t)+f(x+\Delta x,y,z,t+\Delta t) \\ &\qquad +f(x,y+\Delta y,z,t+\Delta t)+f(x,y,z,t+\Delta t)\Big) \\ &\qquad \Big(f(x+\Delta x,y+\Delta y,z,t)+f(x+\Delta x,y,z,t) \\ &\qquad +f(x,y+\Delta y,z,t)+f(x,y,z,t)\Big)\Big]\end{aligned} \tag{6.24}$$

Finite differentiation of $\nabla^2\langle p\rangle$

The right hand side was approximated by the finite difference formulation explained above and will be represented as ψ for the rest of the discussion. The Poisson equation in the global mesh is

$$\frac{\partial^2\langle p\rangle}{\partial x^2}+\frac{\partial^2\langle p\rangle}{\partial y^2}+\frac{\partial^2\langle p\rangle}{\partial z^2}=\psi \tag{6.25}$$

and it was discretized as

$$\begin{aligned}&\frac{\langle p\rangle(x^c-\Delta x^c,y^c,z)-2\langle p\rangle(x^c,y^c,z)+\langle p\rangle(x^c+\Delta x^c,y^c,z)}{\Delta x^2} \\ &+\frac{\langle p\rangle(x^c,y^c-\Delta y^c,z)-2\langle p\rangle(x^c,y^c,z)+\langle p\rangle(x^c,y^c+\Delta y^c,z)}{\Delta y^2} \\ &+\frac{\langle p\rangle(x^c,y^c,z-\Delta z)-2\langle p\rangle(x^c,y^c,z)+\langle p\rangle(x^c,y^c,z+\Delta z)}{\Delta z^2}=\psi\end{aligned} \tag{6.26}$$

in vector form,

$$\begin{bmatrix}\frac{1}{\Delta z^2} & \cdots & \frac{1}{\Delta y^2} & \cdots & \frac{1}{\Delta x^2} & \frac{-2}{\Delta x^2}-\frac{2}{\Delta y^2}-\frac{2}{\Delta z^2} & \frac{1}{\Delta x^2} & \cdots & \frac{1}{\Delta y^2} & \cdots & \frac{1}{\Delta z^2}\end{bmatrix}\begin{bmatrix}p(x^c,y^c,z-\Delta z)\\ \cdots \\ p(x^c,y^c-\Delta y,z)\\ \cdots \\ p(x^c-\Delta x,y^c,z)\\ p(x^c,y^c,z)\\ p(x^c+\Delta x,y^c,z)\\ \cdots \\ p(x^c,y^c+\Delta y,z)\\ \cdots \\ p(x^c,y^c,z+\Delta z)\end{bmatrix}=\psi \tag{6.27}$$

The boundary condition was given as

$$\begin{aligned}\frac{\Delta\langle p\rangle}{\Delta x} =-\rho\Bigg(&\frac{\Delta u}{\Delta t}+\langle u\rangle^c\frac{\Delta u}{\Delta x}+\langle v\rangle^c\frac{\Delta u}{\Delta y}+\langle w\rangle^c\frac{\Delta u}{\Delta z} \\ &+\frac{\Delta}{\Delta x}\langle u'u'\rangle+\frac{\Delta}{\Delta y}\langle u'v'\rangle+\frac{\Delta}{\Delta z}\langle u'w'\rangle\Bigg)\end{aligned} \tag{6.28}$$

$$\frac{\Delta\langle p\rangle}{\Delta y} = -\rho\left(\frac{\Delta v}{\Delta t} + \langle u\rangle^c\frac{\Delta v}{\Delta x} + \langle v\rangle^c\frac{\Delta v}{\Delta y} + \langle w\rangle^c\frac{\Delta v}{\Delta z} + \frac{\Delta}{\Delta x}\langle u'v'\rangle + \frac{\Delta}{\Delta y}\langle v'v'\rangle + \frac{\Delta}{\Delta z}\langle v'w'\rangle\right) \tag{6.29}$$

$$\frac{\Delta\langle p\rangle}{\Delta z} = -\rho\left(\frac{\Delta w}{\Delta t} + \langle u\rangle^c\frac{\Delta w}{\Delta x} + \langle v\rangle^c\frac{\Delta w}{\Delta y} + \langle w\rangle^c\frac{\Delta w}{\Delta z} + \frac{\Delta}{\Delta x}\langle u'w'\rangle + \frac{\Delta}{\Delta y}\langle v'w'\rangle + \frac{\Delta}{\Delta z}\langle w'w'\rangle\right) \tag{6.30}$$

The discrete governing equation, Eq. 6.26, near the boundary was treated to include the boundary condition, Eqs. 6.28–6.30. The forward finite differentiation scheme was applied to the boundary of global mesh as shown in Fig. 6.8 at $x^c = x_2^c$ and $x^c = x_{l+1}^c$, marked by blue dots. The finite difference formulation in Eq. (6.31) is given for $x^c = x_2^c$,

$$\begin{aligned}\frac{1}{\Delta x^2}&\left(-\frac{2}{3}\langle p\rangle(x_2^c,y^c,z) + \frac{2}{3}\langle p\rangle(x_3^c,y^c,z)\right)\\ &+\frac{1}{\Delta y^2}\left(\langle p\rangle(x_2^c,y^c+\Delta y,z) - 2\langle p\rangle(x_2^c,y^c,z) + \langle p\rangle(x_2^c,y^c-\Delta y,z)\right)\\ &+\frac{1}{\Delta z^2}\left(\langle p\rangle(x_2^c,y^c,z+\Delta z) - 2\langle p\rangle(x_2^c,y^c,z) + \langle p\rangle(x_2^c,y^c,z-\Delta z)\right)\\ &= \psi(x_2^c,y^c,z) + \frac{2}{3\Delta x}\frac{\Delta\langle p\rangle}{\Delta x}\bigg|_1\end{aligned} \tag{6.31}$$

and along the other axis, the forward scheme was applied at $y^c = y_2^c$ and $y^c = y_{k+1}^c$ as shown in Fig. 6.9. The finite differentiation on this boundary is formulated in Eq. (6.32),

$$\begin{aligned}\frac{1}{\Delta x^2}&\left(\langle p\rangle(x^c+\Delta x,y_2^c,z) - 2\langle p\rangle(x^c,y_2^c,z) + \langle p\rangle(x^c-\Delta x,y_2^c,z)\right)\\ &+\frac{1}{\Delta y^2}\left(-\frac{2}{3}\langle p\rangle(x^c,y_2^c,z) + \frac{2}{3}\langle p\rangle(x^c,y_3^c,z)\right)\\ &+\frac{1}{\Delta z^2}\left(\langle p\rangle(x^c,y_2^c,z+\Delta z) - 2\langle p\rangle(x^c,y_2^c,z) + \langle p\rangle(x^c,y_2^c,z-\Delta z)\right)\\ &= \psi(x^c,y_2^c,z) + \frac{2}{3\Delta y^c}\frac{\Delta\langle p\rangle}{\Delta y}\bigg|_1\end{aligned} \tag{6.32}$$

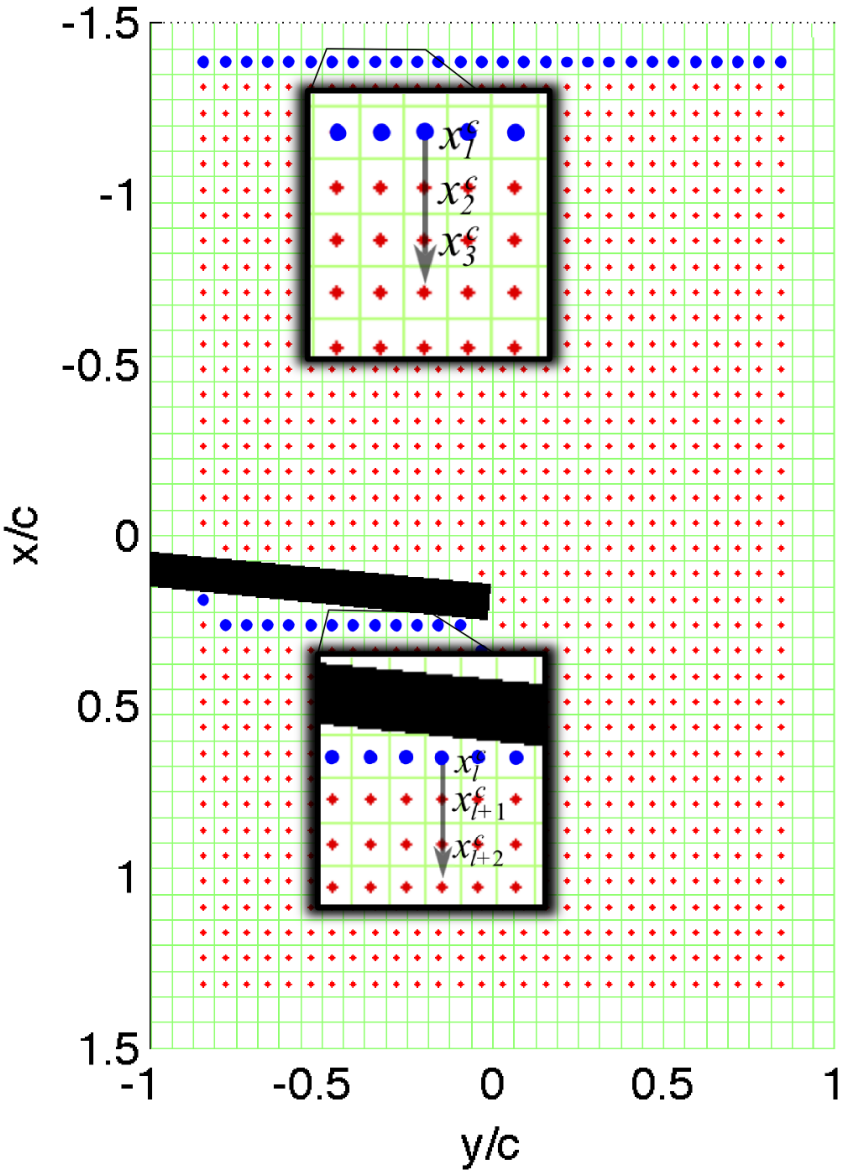

Figure 6.8: Application of the forward scheme on the boundary of global mesh. The boundary is marked by blue dots and indices are shown in the insets.

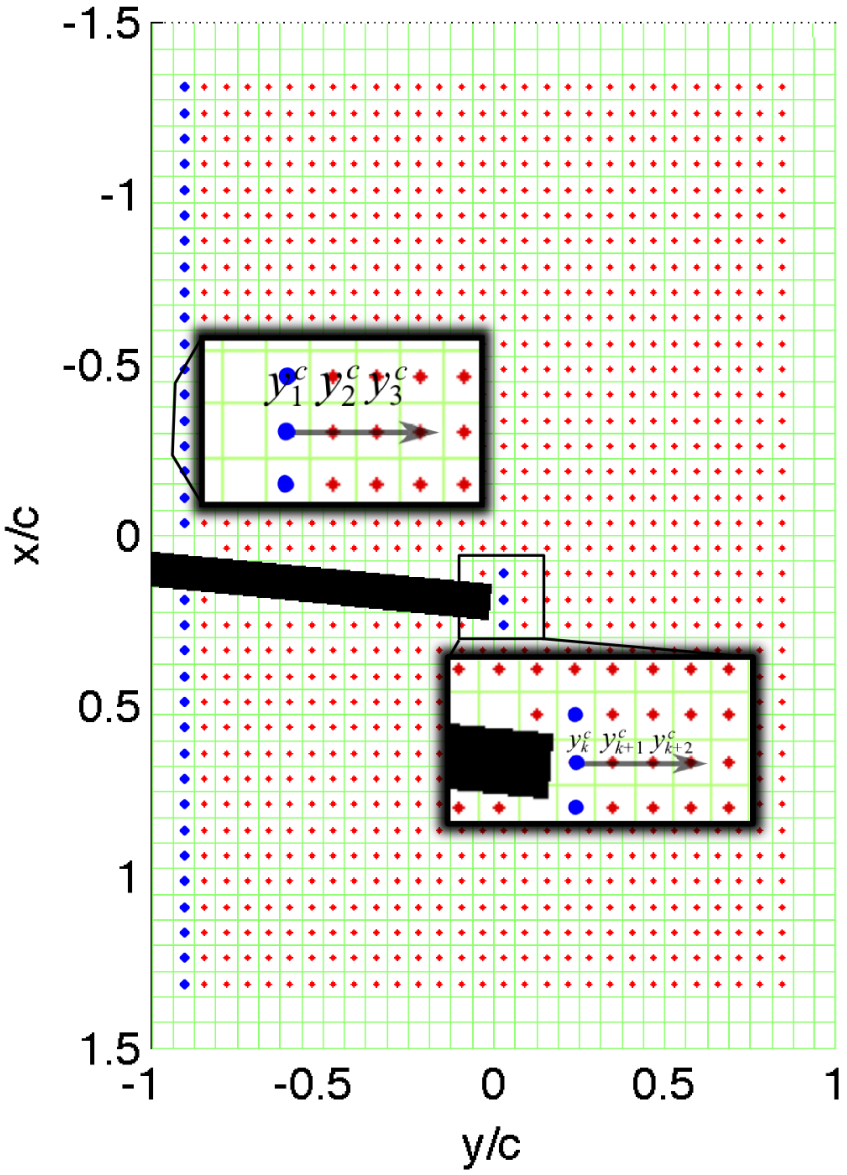

Figure 6.9: Application of the forward scheme on the boundary of global mesh. The boundary is marked by blue dots and indices are shown in the insets.

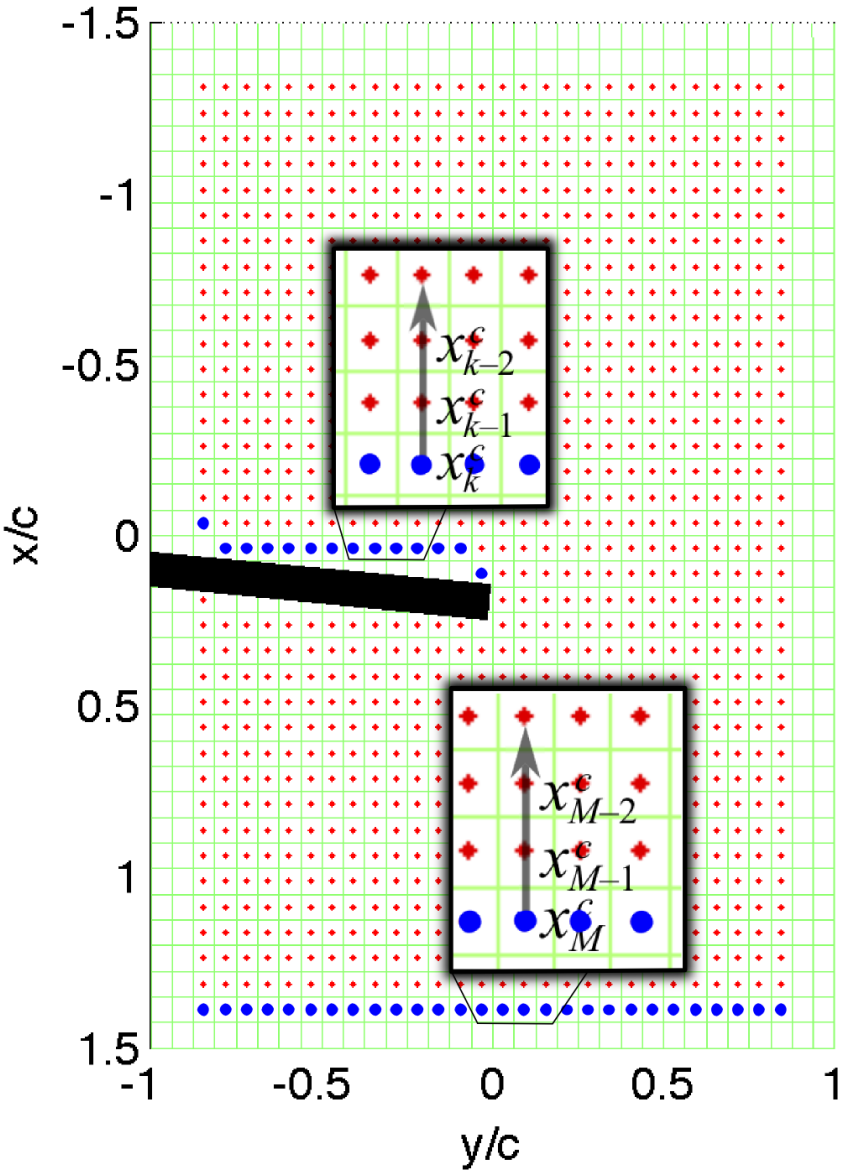

Figure 6.10: Application of the backward scheme on the boundary of global mesh. The boundary is marked by blue dots and indices are shown in the insets.

For the other side of the boundary of the global mesh, the backward finite differentiation was applied at positions as shown in Fig. 6.10 at $x^c = x^c_{M-1}$ and $x^c = x^c_{k-1}$. The finite difference formulation is shown for $x^c = x^c_{M-1}$,

$$\begin{aligned}
&\frac{1}{\Delta x^2}\left(\frac{2}{3}\langle p\rangle(x^c_{M-2},y^c,z)-\frac{2}{3}\langle p\rangle(x^c_{M-1},y^c,z)\right)\\
&\quad+\frac{1}{\Delta y^2}\left(\langle p\rangle(x^c_{M-1},y^c+\Delta y,z)-2\langle p\rangle(x^c_{M-1},y^c,z)+\langle p\rangle(x^c_{M-1},y^c-\Delta y,z)\right)\\
&\quad\quad+\frac{1}{\Delta z^2}\left(\langle p\rangle(x^c_{M-1},y^c,z+\Delta z)-2\langle p\rangle(x^c_{M-1},y^c,z)+\langle p\rangle(x^c_{M-1},y^c,z-\Delta z)\right)\\
&\quad\quad\quad=\psi(x^c_{M-1},y^c,z)-\frac{2}{3\Delta x}\frac{\Delta\langle p\rangle}{\Delta x}\bigg|_M
\end{aligned} \tag{6.33}$$

and similary the backward finite differentiation scheme was applied at positions as shown in Fig. 6.11 at $y^c = y^c_{N-1}$,

$$\begin{aligned}
&\frac{1}{\Delta x^2}\left(\langle p\rangle(x^c+\Delta x,y^c_{N-1},z)-2\langle p\rangle(x^c,y^c_{N-1},z)+\langle p\rangle(x^c-\Delta x,y^c_{N-1},z)\right)\\
&\quad+\frac{1}{\Delta y^2}\left(\frac{2}{3}\langle p\rangle(x^c,y^c_{N-2},z)-\frac{2}{3}\langle p\rangle(x^c,y^c_{N-1},z)\right)\\
&\quad\quad+\frac{1}{\Delta z^2}\left(\langle p\rangle(x^c,y^c_{N-1},z+\Delta z)-2\langle p\rangle(x^c,y^c_{N-1},z)+\langle p\rangle(x^c,y^c_{N-1},z-\Delta z)\right)\\
&\quad\quad\quad=\psi(x^c,y^c_{N-1},z)-\frac{2}{3\Delta y}\frac{\Delta\langle p\rangle}{\Delta y}\bigg|_N
\end{aligned} \tag{6.34}$$

The pressure equation along the z-axis was treated with the forward difference scheme on $z = z_1$, where the location of z_1 is indicated in Fig. 6.12,

$$\begin{aligned}
&\frac{1}{\Delta x^2}\left(\langle p\rangle(x^c+\Delta x,y^c,z_1)-2\langle p\rangle(x^c,y^c,z_1)+\langle p\rangle(x^c-\Delta x,y^c,z_1)\right)\\
&\quad+\frac{1}{\Delta y^2}\left(\langle p\rangle(x^c,y^c+\Delta y,z_1)-2\langle p\rangle(x^c,y^c,z_1)+\langle p\rangle(x^c,y^c-\Delta y,z_1)\right)\\
&\quad\quad+\frac{1}{\Delta z^2}\left(-2\langle p\rangle(x^c,y^c,z_1)+2\langle p\rangle(x^c,y^c,z_2)\right)\\
&\quad\quad\quad=\psi(x^c,y^c,z_1)+\frac{2}{\Delta z}\frac{\Delta\langle p\rangle}{\Delta z}\bigg|_1
\end{aligned} \tag{6.35}$$

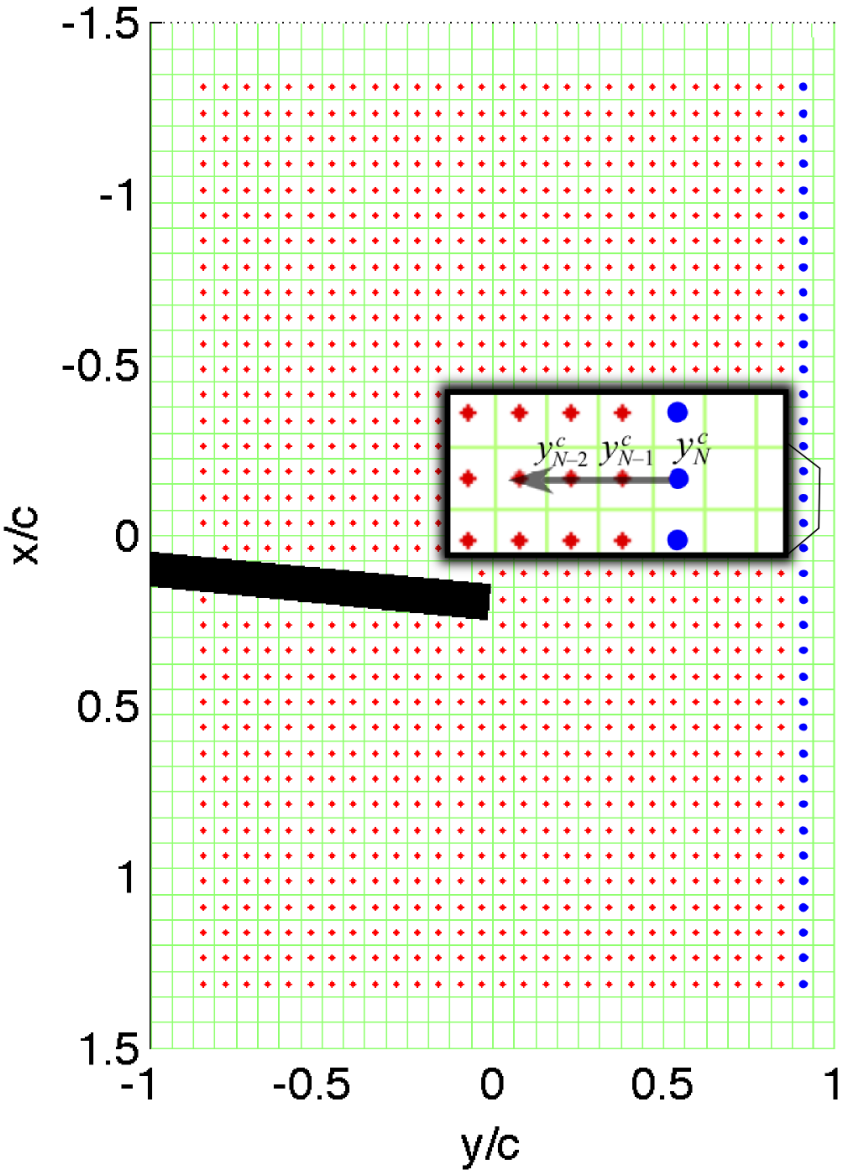

Figure 6.11: Application of the backward scheme on the boundary of global mesh. The boundary is marked by blue dots and indices are shown in the insets.

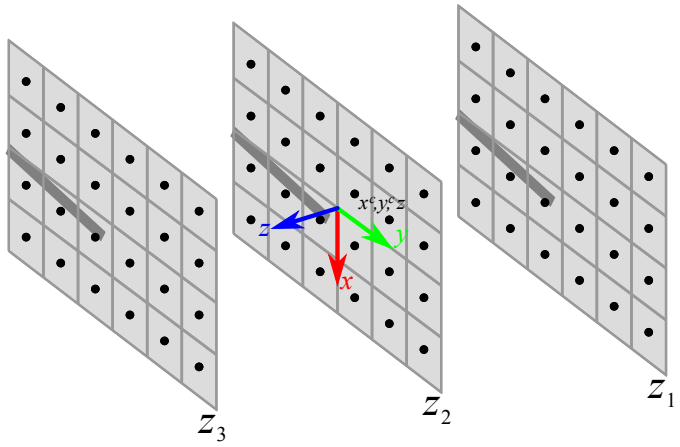

Figure 6.12: The numerical meshes along the z-axis: z_1 and z_3 are the numerical boundaries along the z-axis.

and the treatment of the pressure equation from the boundary condition on $z = z_3$ was

$$\begin{aligned}
&\frac{1}{\Delta x^2}\Big(\langle p\rangle(x^c+\Delta x,y^c,z_3)-2\langle p\rangle(x^c,y^c,z_3)+\langle p\rangle(x^c-\Delta x,y^c,z_3)\Big)\\
&\quad+\frac{1}{\Delta y^2}\Big(\langle p\rangle(x^c,y^c+\Delta y,z_3)-2\langle p\rangle(x^c,y^c,z_3)+\langle p\rangle(x^c,y^c-\Delta y,z_3)\Big)\\
&\quad+\frac{1}{\Delta z^2}\Big(2\langle p\rangle(x^c,y^c,z_2)-2\langle p\rangle(x^c,y^c,z_3)\Big)\\
&\quad=\psi(x^c,y^c,z_3)-\frac{2}{\Delta z}\frac{\Delta\langle p\rangle}{\Delta z}_3
\end{aligned} \tag{6.36}$$

6.3.2 In the local mesh

The pressure equation in the local mesh is

$$\frac{\partial^2\langle p\rangle}{\partial\xi_i^2}=\frac{\partial\langle\upsilon_i\rangle}{\partial\xi_j}\frac{\partial\langle\upsilon_j\rangle}{\partial\xi_i}+\frac{\partial^2}{\partial\xi_i\partial\xi_j}\langle\upsilon_i'\upsilon_j'\rangle+2\frac{\partial}{\partial\xi_k}(\Omega_i\upsilon_j\varepsilon_{ijk}) \tag{6.37}$$

where the local mesh is illustrated in Fig. 6.13. Expanding Eq. (6.37) with $\upsilon_i = (u_\xi, u_\eta, u_\zeta)$ and $\xi_i = (\xi,\eta,\zeta)$,

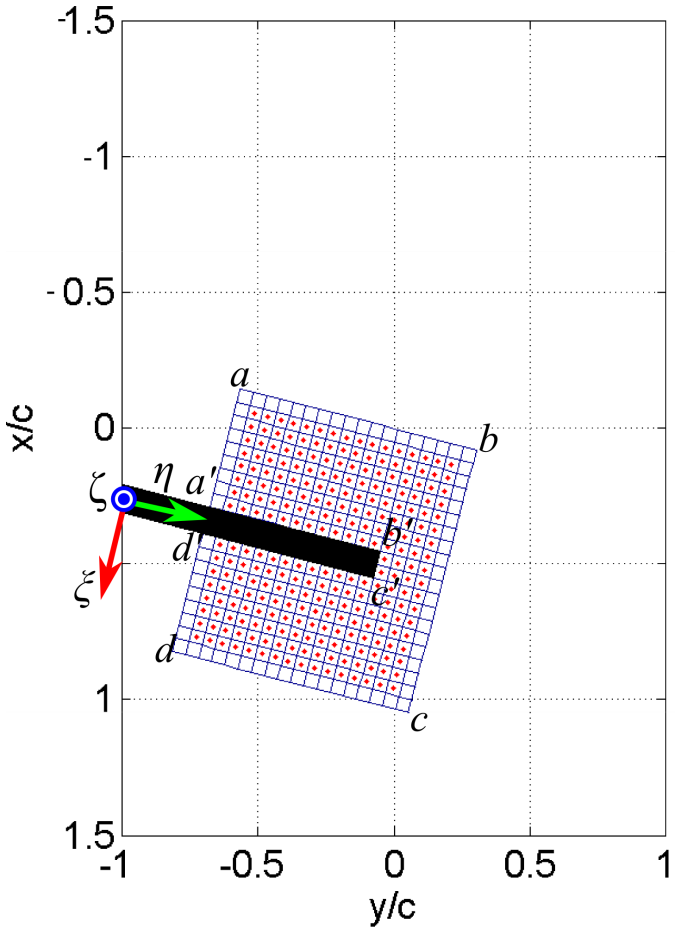

Figure 6.13: The definition of local mesh. The phase-averaged velocity field is on the blue grid and the pressure was estimated on the red dots. The black line represents the plate.

$$
\begin{aligned}
\frac{\partial^2\langle p\rangle}{\partial\xi^2}+\frac{\partial^2\langle p\rangle}{\partial\eta^2}+\frac{\partial^2\langle p\rangle}{\partial\zeta^2} \approx & \frac{\Delta^2\langle p\rangle}{\Delta\xi^2}+\frac{\Delta^2\langle p\rangle}{\Delta\eta^2}+\frac{\Delta^2\langle p\rangle}{\Delta\zeta^2} \\
\approx & -\rho\Bigg[\left(\frac{\Delta\langle u_\xi\rangle}{\Delta\xi}\right)^2+\left(\frac{\Delta\langle u_\eta\rangle}{\Delta\eta}\right)^2+\left(\frac{\Delta\langle u_\zeta\rangle}{\Delta\zeta}\right)^2 \\
& +2\left(\frac{\Delta\langle u_\xi\rangle}{\Delta\eta}\frac{\Delta\langle u_\eta\rangle}{\Delta\xi}+\frac{\Delta\langle u_\eta\rangle}{\Delta\zeta}\frac{\Delta\langle u_\zeta\rangle}{\Delta\xi}+\frac{\Delta\langle u_\zeta\rangle}{\Delta\zeta}\frac{\Delta\langle u_\zeta\rangle}{\Delta\eta}\right) \\
& +\left(\frac{\Delta^2\langle u'_\xi u'_\xi\rangle}{\Delta\xi^2}+\frac{\Delta^2\langle u'_\eta u'_\eta\rangle}{\Delta\eta^2}+\frac{\Delta^2\langle u'_\zeta u'_\zeta\rangle}{\Delta\zeta^2}\right) \\
& +2\left(\frac{\Delta^2\langle u'_\xi u'_\eta\rangle}{\Delta\xi\Delta\eta}+\frac{\Delta^2\langle u'_\xi u'_\zeta\rangle}{\Delta\xi\Delta\zeta}+\frac{\Delta^2\langle u'_\eta u'_\zeta\rangle}{\Delta\eta\Delta\zeta}\right) \\
& +2\Omega_\zeta\left(\frac{\Delta u_\xi}{\Delta\eta}-\frac{\Delta u_\eta}{\Delta\xi}\right)\Bigg]
\end{aligned}
\tag{6.38}
$$

The finite differentiation of Eq. (6.38) is discussed in the next two section: the right hand side, ψ_{local}, and the left hand side $\nabla^2 p$.

Finite differentiation of ψ_{local}

The spatial derivatives for the local mesh (ξ,η,ζ) are

$$\frac{\partial f}{\partial\xi_i}=\left(\frac{\partial f}{\partial\xi},\frac{\partial f}{\partial\eta},\frac{\partial f}{\partial\zeta}\right) \tag{6.39}$$

$$\frac{\partial^2 f}{\partial\xi_i^2}=\left(\frac{\partial^2 f}{\partial\xi^2},\frac{\partial^2 f}{\partial\eta^2},\frac{\partial^2 f}{\partial\zeta^2}\right) \tag{6.40}$$

$$\frac{\partial^2 f}{\partial\xi_i\partial xi_j}=\left(\frac{\partial^2 f}{\partial\xi\partial\eta},\frac{\partial^2 f}{\partial\xi\partial\zeta},\frac{\partial^2 f}{\partial\eta\partial\zeta}\right) \tag{6.41}$$

where

$$
\begin{aligned}
\frac{\partial f}{\partial\xi} &\approx \frac{\Delta f}{\Delta\xi} \\
&\approx \frac{f(\xi+\Delta\xi,\eta+\Delta\eta,\zeta)+f(\xi+\Delta\xi,\eta,\zeta)-f(\xi,\eta+\Delta\eta,\zeta)+f(\xi,\eta,\zeta)}{2\Delta\xi}
\end{aligned}
\tag{6.42}
$$

$$
\begin{aligned}
\frac{\partial f}{\partial\eta} &= \frac{\Delta f}{\Delta\eta} \\
&= \frac{f(\xi+\Delta\xi,\eta+\Delta\eta,\zeta)+f(\xi,\eta+\Delta\eta,\zeta)-f(\xi+\Delta\xi,\eta,\zeta)+f(\xi,\eta,\zeta)}{2\Delta\eta}
\end{aligned}
\tag{6.43}
$$

where the ζ-derivative was approximated as

$$\begin{aligned}\frac{\partial f}{\partial \zeta} \approx & \frac{\Delta f}{\Delta \zeta} \\ \approx & \frac{1}{4}\frac{1}{2\Delta\zeta}\Big[\Big(f(\xi+\Delta\xi,\eta+\Delta\eta,\zeta+\Delta\zeta)+f(\xi+\Delta\xi,\eta,\zeta+\Delta\zeta) \\ & +f(\xi,\eta+\Delta\eta,\zeta+\Delta\zeta)+f(\xi,\eta,\zeta+\Delta\zeta)\Big) \\ & -\Big(f(\xi+\Delta\xi,\eta+\Delta\eta,\zeta-\Delta\zeta)+f(\xi+\Delta\xi,\eta,\zeta-\Delta\zeta) \\ & +f(\xi,\eta+\Delta\eta,\zeta-\Delta\zeta)+f(\xi,\eta,\zeta-\Delta\zeta)\Big)\Big]\end{aligned} \tag{6.44}$$

At the ends of the length of data, the one-sided finite difference formula for the derivative with respect to ζ was used,

$$\begin{aligned}\frac{\partial f}{\partial \zeta} \approx & \frac{\Delta f}{\Delta \zeta} \\ \approx & \frac{1}{2\Delta\zeta}\frac{1}{4}\Big[-3\Big(f(\xi+\Delta\xi,\eta+\Delta\eta,\zeta)+f(\xi+\Delta\xi,\eta,\zeta)+f(\xi,\eta+\Delta\eta,\zeta)+f(\xi,\eta,\zeta)\Big) \\ & +4\Big(f(\xi+\Delta\xi,\eta+\Delta\eta,\zeta+\Delta\zeta)+f(\xi+\Delta\xi,\eta,\zeta+\Delta\zeta) \\ & +f(\xi,\eta+\Delta\eta,\zeta+\Delta\zeta)+f(\xi,\eta,\zeta+\Delta\zeta)\Big) \\ & -\Big(f(\xi+\Delta\xi,\eta+\Delta\eta,\zeta+2\Delta\zeta)+f(\xi+\Delta\xi,\eta,\zeta+2\Delta\zeta) \\ & +f(\xi,\eta+\Delta\eta,\zeta+2\Delta\zeta)+f(\xi,\eta,\zeta+2\Delta\zeta)\Big)\Big]\end{aligned} \tag{6.45}$$

where $\Delta\zeta = \Delta\zeta$ or $\Delta\zeta = -\Delta\zeta$ depending on which end of the data.

The center nodes are defined as ξ^c, η^c, where the space between nodes remain the same $(\Delta\xi, \Delta\eta)$. The second derivatives were approximated as

$$\frac{\partial^2 f}{\partial \xi^2} \approx \frac{\Delta^2 f}{\Delta \xi^2} = \frac{f(\xi^c+\Delta\xi,\eta^c,\zeta)+2f(\xi^c,\eta^c,\zeta)-f(\xi^c-\Delta\xi,\eta^c,\zeta)}{\Delta\xi^2} \tag{6.46}$$

$$\frac{\partial^2 f}{\partial \eta^2} \approx \frac{\Delta^2 f}{\Delta \eta^2} = \frac{f(\xi^c,\eta^c+\Delta\eta,\zeta)+2f(\xi^c,\eta^c,\zeta)-f(\xi^c,\eta^c-\Delta\eta,\zeta)}{\Delta\eta^2} \tag{6.47}$$

$$\frac{\partial^2 f}{\partial \zeta^2} \approx \frac{\Delta^2 f}{\Delta \zeta^2} = \frac{f(\xi^c,\eta^c,\zeta+\Delta\zeta)+2f(\xi^c,\eta^c,\zeta)-f(\xi^c,\eta^c,\zeta-\Delta\zeta)}{\Delta\zeta^2} \tag{6.48}$$

where the one-sided finite difference formula was used along the boundary. For $\zeta = \zeta_0$,

$$\frac{\partial^2 f}{\partial z^2}_0 \approx \frac{\Delta^2 f}{\Delta\zeta^2} = \frac{f(\xi^c,\eta^c,\zeta_0) + 2f(\xi^c,\eta^c,\zeta_0+\Delta\zeta) - f(\xi^c,\eta^c,\zeta_0+2\Delta\zeta)}{\Delta\zeta^2} \tag{6.49}$$

and for $\zeta = \zeta_M$,

$$\frac{\partial^2 f}{\partial z^2}_M \approx \frac{\Delta^2 f}{\Delta\zeta^2} = \frac{f(\xi^c,\eta^c,\zeta_M) + 2f(\xi^c,\eta^c,\zeta_M-\Delta\zeta) - f(\xi^c,\eta^c,\zeta_M-2\Delta\zeta)}{\Delta\zeta^2} \tag{6.50}$$

And the mixed derivatives were approximated as

$$\begin{aligned}\frac{\partial^2 f}{\partial\xi\partial\eta} \approx& \frac{\Delta^2 f}{\Delta\xi\Delta\eta} \\ \approx& \frac{1}{\Delta\xi\Delta\eta}\left[f(\xi+\Delta\xi,\eta+\Delta\eta,\zeta) + f(\xi,\eta,\zeta) - f(\xi,\eta+\Delta\eta,\zeta) - f(\xi+\Delta\xi,\eta,\zeta)\right]\end{aligned} \tag{6.51}$$

$$\begin{aligned}\frac{\partial^2 f}{\partial\xi\partial\zeta} \approx& \frac{\Delta^2 f}{\Delta\xi\Delta\zeta} \\ \approx& \frac{1}{4\Delta\xi\Delta\zeta}\Big[\Big(f(\xi+\Delta\xi,\eta,\zeta+\Delta\zeta) + f(\xi+\Delta\xi,\eta+\Delta\eta,\zeta+\Delta\zeta) \\ & - f(\xi,\eta,\zeta+\Delta\zeta) - f(\xi,\eta+\Delta\eta,\zeta+\Delta\zeta)\Big) \\ & - \Big(+f(\xi+\Delta\xi,\eta,\zeta-\Delta\zeta) + f(\xi+\Delta\xi,\eta+\Delta\eta,\zeta-\Delta\zeta) \\ & - f(\xi,\eta,\zeta-\Delta\zeta) - f(\xi,\eta+\Delta\eta,\zeta-\Delta\zeta)\Big)\Big]\end{aligned} \tag{6.52}$$

$$\begin{aligned}\frac{\partial^2 f}{\partial\eta\partial\zeta} \approx& \frac{\Delta^2 f}{\Delta\eta\Delta\zeta} \\ \approx& \frac{1}{4\Delta\eta\Delta\zeta}\Big[\Big(f(\xi+\Delta\xi,\eta+\Delta\eta,\zeta+\Delta\zeta) + f(\xi,\eta+\Delta\eta,\zeta+\Delta\zeta) \\ & - f(\xi+\Delta\xi,\eta,\zeta+\Delta\zeta) - f(\xi,\eta,\zeta+\Delta\zeta)\Big) \\ & - \Big(f(\xi+\Delta\xi,\eta+\Delta\eta,\zeta-\Delta\zeta) + f(\xi,\eta+\Delta\eta,\zeta-\Delta\zeta) \\ & - f(\xi+\Delta\xi,\eta,\zeta-\Delta\zeta) - f(\xi,\eta,\zeta-\Delta\zeta)\Big)\Big]\end{aligned} \tag{6.53}$$

The one sided formulations with respect to ζ were given as

$$\begin{aligned}
\frac{\partial^2 f}{\partial\xi\partial\zeta} \approx & \frac{\Delta^2 f}{\Delta\xi\Delta\zeta} \\
\approx & \frac{1}{4\Delta\xi\Delta\zeta}\frac{1}{2}\Big[-3\Big(f(\xi+\Delta\xi,\eta,\zeta)+f(\xi+\Delta\xi,\eta+\Delta\eta,\zeta) \\
& -f(\xi,\eta,\zeta)-f(\xi,\eta+\Delta\eta,\zeta)\Big) \\
& +4\Big(+f(\xi+\Delta\xi,\eta,\zeta+\Delta\zeta)+f(\xi+\Delta\xi,\eta+\Delta\eta,\zeta+\Delta\zeta) \\
& -f(\xi,\eta,\zeta+\Delta\zeta)-f(\xi,\eta+\Delta\eta,\zeta+\Delta\zeta)\Big)\Big] \\
& -\Big(+f(\xi+\Delta\xi,\eta,\zeta+2\Delta\zeta)+f(\xi+\Delta\xi,\eta+\Delta\eta,\zeta+2\Delta\zeta) \\
& -f(\xi,\eta,\zeta+2\Delta\zeta)-f(\xi,\eta+\Delta\eta,\zeta+2\Delta\zeta)\Big)\Big]
\end{aligned} \tag{6.54}$$

$$\begin{aligned}
\frac{\partial^2 f}{\partial\eta\partial\zeta} \approx & \frac{\Delta^2 f}{\Delta\eta\Delta\zeta} \\
\approx & \frac{1}{4\Delta\eta\Delta\zeta}\frac{1}{2}\Big[-3\Big(f(\xi+\Delta\xi,\eta+\Delta\eta,\zeta)+f(\xi,\eta+\Delta\eta,\zeta) \\
& -f(\xi+\Delta\xi,\eta,\zeta)-f(\xi,\eta,\zeta)\Big) \\
& +4\Big(f(\xi+\Delta\xi,\eta+\Delta\eta,\zeta+\Delta\zeta)+f(\xi,\eta+\Delta\eta,\zeta+\Delta\zeta) \\
& -f(\xi+\Delta\xi,\eta,\zeta+\Delta\zeta)-f(\xi,\eta,\zeta+\Delta\zeta)\Big)\Big] \\
& -\Big(f(\xi+\Delta\xi,\eta+\Delta\eta,\zeta+2\Delta\zeta)+f(\xi,\eta+\Delta\eta,\zeta+2\Delta\zeta) \\
& -f(\xi+\Delta\xi,\eta,\zeta+2\Delta\zeta)-f(\xi,\eta,\zeta+2\Delta\zeta)\Big)\Big]
\end{aligned} \tag{6.55}$$

The one sided formulation of ${}^{\Delta^2 f}/_{\Delta\eta\Delta\zeta}$ was not required because Eq. (6.38) was not solved along the boundaries as Eq. (6.38) was treated for the boundary condition.

Finite differentiation of $\nabla^2 p$

The finite difference approximation of the left hand side of Eq. (6.38) is expanded as

$$\frac{\Delta^2\langle p\rangle}{\Delta\xi^2}+\frac{\Delta^2\langle p\rangle}{\Delta\eta^2}+\frac{\Delta^2\langle p\rangle}{\Delta\zeta^2}=\psi_{local} \tag{6.56}$$

and is discretized as

$$\begin{aligned}
&\frac{\langle p\rangle(\xi^c-\Delta\xi,\eta^c,\zeta)-2\langle p\rangle(\xi^c,\eta^c,\zeta)+\langle p\rangle(\xi^c+\Delta\xi,\eta^c,\zeta)}{\Delta\xi^2}\\
&\quad+\frac{\langle p\rangle(\xi^c,\eta^c-\Delta\eta,\zeta)-2\langle p\rangle(\xi^c,\eta^c,\zeta)+\langle p\rangle(\xi^c,\eta^c+\Delta\eta,\zeta)}{\Delta\eta^2}\\
&\quad+\frac{\langle p\rangle(\xi^c,\eta^c,\zeta-\Delta\zeta)-2\langle p\rangle(\xi^c,\eta^c,\zeta)+\langle p\rangle(\xi^c,\eta^c,\zeta+\Delta\zeta)}{\Delta\zeta^2}=\psi_{local}
\end{aligned}\tag{6.57}$$

In the local mesh (cf. Fig. 6.13), the Dirichlet boundary condition, $\langle p\rangle$, was applied on the numerical boundary, ab, bc, and cd. The Dirichlet boundary condition, $\langle p\rangle$, was obtained by interpolating the pressure field from the global mesh to the local mesh,

$$\begin{aligned}
\langle p\rangle(\xi^c,\eta^c,\zeta)\approx&\frac{\langle p\rangle(x^c,y^c,z)}{\Delta x\Delta y}(x^c+\Delta x-x_l)(y^c+\Delta y-y_{local})\\
&+\frac{\langle p\rangle(x^c+\Delta x,y^c,z)}{\Delta x\Delta y}(x_{local}-x^c)(y^c+\Delta y-y_{local})\\
&+\frac{\langle p\rangle(x^c,y^c+\Delta y,z)}{\Delta x\Delta y}(x^c+\Delta x-x_{local})(y_{local}-y^c)\\
&+\frac{\langle p\rangle(x^c+\Delta x,y^c+\Delta y,z)}{\Delta x\Delta y}(x_{local}-x^c)(y_{local}-y^c)
\end{aligned}\tag{6.58}$$

where the coordinates of the local mesh on the cartesian coordinate was given as

$$\begin{pmatrix}x_{local}\\y_{local}\\z_{local}\end{pmatrix}=\begin{bmatrix}\cos(\theta)&-\sin(\theta)&0\\\sin(\theta)&\cos(\theta)&0\\0&0&1\end{bmatrix}^{-1}\begin{pmatrix}\xi^c\\\eta^c\\\zeta\end{pmatrix}\tag{6.59}$$

The Neumann boundary condition was applied on aa' and dd',

$$\begin{aligned}
\frac{\partial\langle p\rangle}{\partial\eta}\approx\frac{\Delta\langle p\rangle}{\Delta\eta}=-\rho\Bigg(&\frac{\Delta\langle u_\eta\rangle}{\Delta t}+\langle u_\xi\rangle\frac{\Delta\langle u_\eta\rangle}{\Delta\xi}+\langle u_\eta\rangle\frac{\Delta\langle u_\eta\rangle}{\Delta\eta}+\langle u_\zeta\rangle\frac{\Delta\langle u_\eta\rangle}{\Delta\zeta}\\
&+\frac{\Delta}{\Delta\xi}\langle u'_\eta u'_\xi\rangle+\frac{\Delta}{\Delta\eta}\langle u'_\eta u'_\eta\rangle+\frac{\Delta}{\Delta\zeta}\langle u'_\eta u'_\zeta\rangle\\
&+(\ddot{\theta}_\zeta\xi)+(-\dot{\theta}_\zeta^2\eta)+2(\dot{\theta}_\zeta\langle u_\xi\rangle)\Bigg)
\end{aligned}\tag{6.60}$$

On the surface of the plate, $a'b'c'd'$, the Neumann boundary condition was also applied. The boundary condition on the surface of the plate, $a'b'$ and $c'd'$, was

$$\frac{\partial\langle p\rangle}{\partial\xi}=\rho(\ddot{\theta}\eta+\dot{\theta}^2\xi)\tag{6.61}$$

and on $b'c'$, the following boundary condition was applied,

$$\frac{\partial p}{\partial \eta} = \rho(-\ddot{\theta}\xi + \dot{\theta}^2\eta) \tag{6.62}$$

The pressure on the surface was extrapolated using the Lagrangian extrapolation. For the upper surface of the plate,

$$\langle p\rangle_{surface} = \frac{15}{8}\langle p\rangle(\xi_k,\eta,\zeta) - \frac{10}{8}\langle p\rangle(\xi_{k-1},\eta,\zeta) + \frac{3}{8}\langle p\rangle(\xi_{k-2},\eta,\zeta) \tag{6.63}$$

and for the lower surface of the plate,

$$\langle p\rangle_{surface} = \frac{15}{8}\langle p\rangle(\xi_l,\eta,\zeta) - \frac{10}{8}\langle p\rangle(\xi_{l+1},\eta,\zeta) + \frac{3}{8}\langle p\rangle(\xi_{l+2},\eta,\zeta) \tag{6.64}$$

The one-sided finite difference formulation of the Poisson equation of the local mesh at the boundaries are,

1. The forward finite differentiation scheme was applied next to the boundaries as shown in Fig. 6.14 at $\xi^c = \xi_2^c$ and $\xi^c = \xi_{l+1}^c$, where the boundaries are marked by red dots. The Dirichlet boundary condition was applied at $\xi^c = \xi_2^c$ and the finite differentiation formulation is shown as Eq. (6.65) and the Neumann boundary condition was applied at $\xi^c = \xi_{l+1}^c$ and the finite differentiation formulation is shown as Eq. (6.66)

$$\begin{aligned}
&\frac{-2\langle p\rangle(\xi_2^c,\eta^c,\zeta) + \langle p\rangle(\xi_3^c,\eta^c,\zeta)}{\Delta\xi^2} \\
&\quad + \frac{\langle p\rangle(\xi_2^c,\eta^c-\Delta\eta,\zeta) - 2\langle p\rangle(\xi_2^c,\eta^c,\zeta) + \langle p\rangle(\xi_2^c,\eta^c+\Delta\eta,\zeta)}{\Delta\eta^2} \\
&\quad + \frac{\langle p\rangle(\xi_2^c,\eta^c,\zeta-\Delta\zeta) - 2\langle p\rangle(\xi_2^c,\eta^c,\zeta) + \langle p\rangle(\xi_2^c,\eta^c,\zeta+\Delta\zeta)}{\Delta\zeta^2} \\
&\qquad = \psi_{local} - \langle p\rangle(\xi_1^c,\eta^c,\zeta)
\end{aligned} \tag{6.65}$$

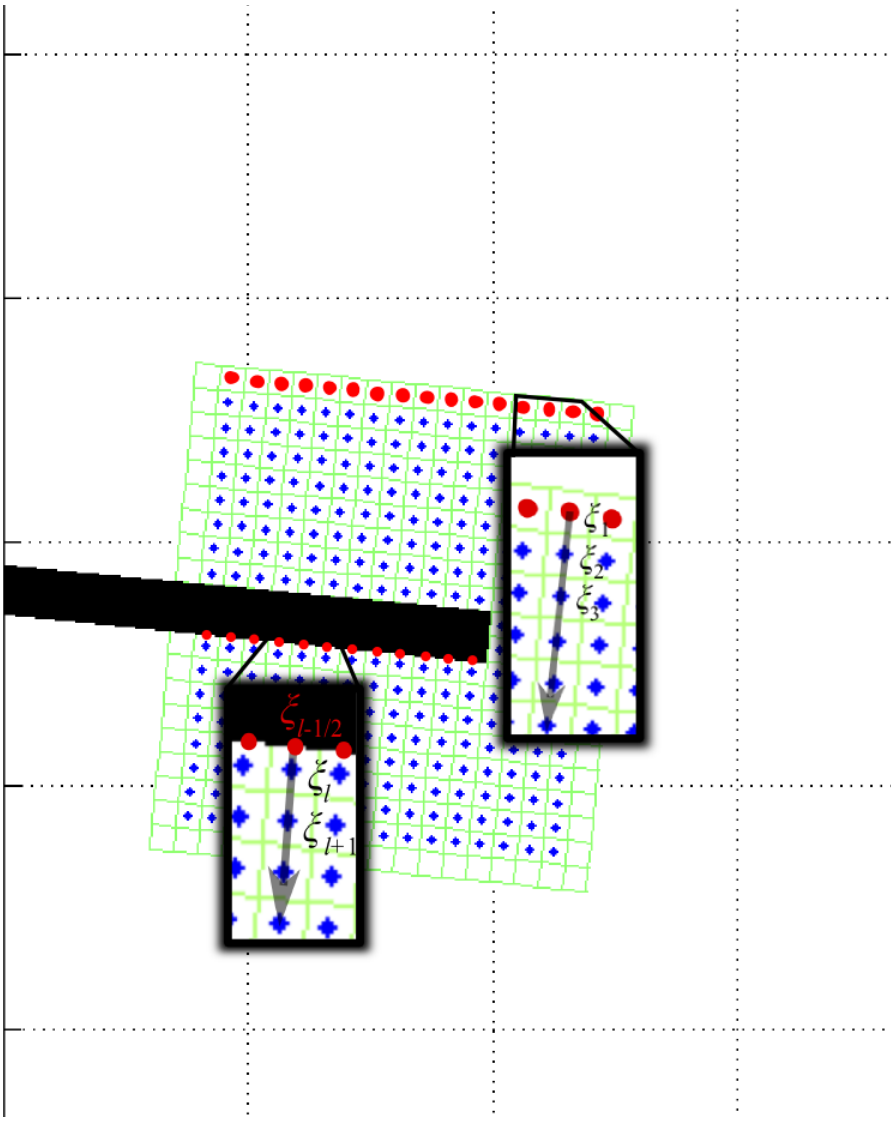

Figure 6.14: Application of the forward scheme on the boundary of local mesh. The boundary is marked by red dots and indices are shown in the insets.

and

$$
\begin{aligned}
&-\frac{\langle p\rangle(\xi_l^c,\eta^c,\zeta)-\langle p\rangle(\xi_{l+1}^c,\eta^c,\zeta)}{\Delta\xi^2}\\
&\quad+\frac{\langle p\rangle(\xi_{l+1}^c,\eta^c-\Delta\eta,\zeta)2\langle p\rangle(\xi_{l+1}^c,\eta^c,\zeta)+\langle p\rangle(\xi_{l+1}^c,\eta^c+\Delta\eta,\zeta)}{\Delta\eta^2}\\
&\quad+\frac{\langle p\rangle(\xi_{l+1}^c,\eta^c,\zeta-\Delta\zeta)-2\langle p\rangle(\xi_{l+1}^c,\eta^c,\zeta)+\langle p\rangle(\xi_{l+1}^c,\eta^c,\zeta+\Delta\zeta)}{\Delta\zeta^2}\\
&=\psi_{local}-\frac{1}{\Delta\xi}\frac{\Delta\langle p\rangle}{\Delta\xi}\bigg|_{l-1/2}
\end{aligned}
\tag{6.66}
$$

2. The backward finite differentiation scheme was applied on the other side of the boundary as shown in Fig. 6.15 at $\xi^c=\xi_{M-1}^c$ and $\xi^c=\xi_{k-1}^c$. The Dirichlet boundary condition was applied to solve the pressure equation at $\xi^c=\xi_{M-1}^c$; it is formulated Eq. (6.67). The Neumann boundary condition was applied to solve the pressure equation at $\xi^c=\xi_{k-1}^c$; the formulation of the pressure equation is shown in Eq. (6.68).

$$
\begin{aligned}
&\frac{\langle p\rangle(\xi_{M-2}^c,\eta^c,\zeta)-2\langle p\rangle(\xi_{M-1}^c,\eta^c,\zeta)}{\Delta\xi^2}\\
&\quad+\frac{\langle p\rangle(\xi_{M-1}^c,\eta^c-\Delta\eta,\zeta)-2\langle p\rangle(\xi_{M-1}^c,\eta^c,\zeta)+\langle p\rangle(\xi_{M-1}^c,\eta^c+\Delta\eta,\zeta)}{\Delta\eta^2}\\
&\quad+\frac{\langle p\rangle(\xi_{M-1}^c,\eta^c,\zeta-\Delta\zeta)-2\langle p\rangle(\xi_{M-1}^c,\eta^c,\zeta)+\langle p\rangle(\xi_{M-1}^c,\eta^c,\zeta+\Delta\zeta)}{\Delta\zeta^2}\\
&=\psi_{local}-\langle p\rangle(\xi_M^c,\eta^c,\zeta)
\end{aligned}
\tag{6.67}
$$

and

$$
\begin{aligned}
&\frac{\langle p\rangle(\xi_{k-1}^c,\eta^c,\zeta)-\langle p\rangle(\xi_k^c,\eta^c,\zeta)}{\Delta\xi^2}\\
&\quad+\frac{\langle p\rangle(\xi_{k-1}^c,\eta^c-\Delta\eta,\zeta)2\langle p\rangle(\xi_{k-1}^c,\eta^c,\zeta)+\langle p\rangle(\xi_{k-1}^c,\eta^c+\Delta\eta,\zeta)}{\Delta\eta^2}\\
&\quad+\frac{\langle p\rangle(\xi_{k-1}^c,\eta^c,\zeta-\Delta\zeta)-2\langle p\rangle(\xi_{k-1}^c,\eta^c,\zeta)+\langle p\rangle(\xi_{k-1}^c,\eta^c,\zeta+\Delta\zeta)}{\Delta\zeta^2}\\
&=\psi_{local}+\frac{1}{\Delta\xi}\frac{\Delta\langle p\rangle}{\Delta\xi}\bigg|_{k+1/2}
\end{aligned}
\tag{6.68}
$$

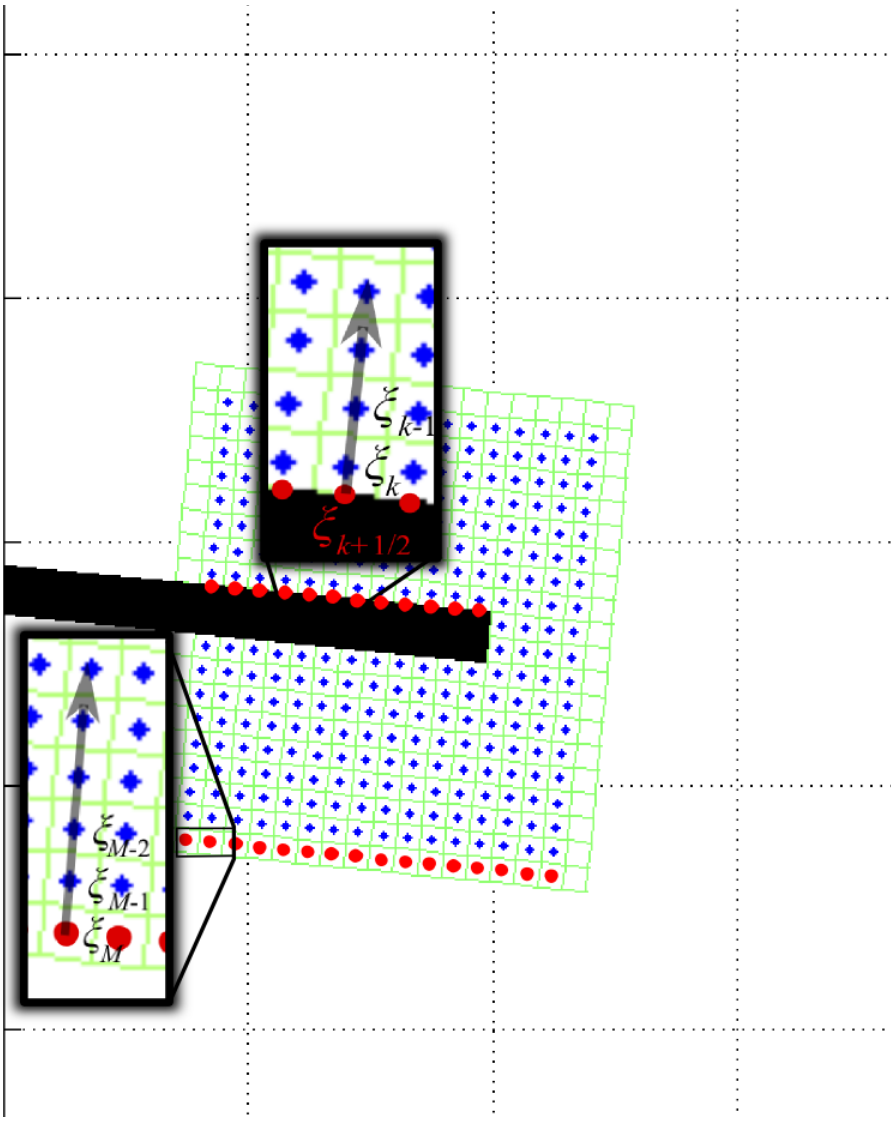

Figure 6.15: Application of the backward scheme on the boundary of local mesh. The boundary is marked by red dots and indices are shown in the insets.

3. Similarly to the treatment of boundaries along ξ, the forward difference scheme was applied to the pressure equation at $\eta^c = \eta_2^c$ and $\eta^c = \eta_{k+1}^c$ as shown in Fig. 6.16. At $\eta^c = \eta_2^c$, the Dirichlet boundary condition was applied to the pressure equation and at $\eta^c = \eta_{k+1}^c$, the Neumann boundary condition was applied.

$$\begin{aligned}
&\frac{\langle p\rangle(\xi^c-\Delta\xi,\eta_2^c,\zeta)-2\langle p\rangle(\xi^c,\eta_2^c,\zeta)+\langle p\rangle(\xi^c+\Delta\xi,\eta_2^c,\zeta)}{\Delta\xi^2}\\
&\quad+\frac{-2\langle p\rangle(\xi^c,\eta_2^c,\zeta)+\langle p\rangle(\xi^c,\eta_3^c,\zeta)}{\Delta\eta^2}\\
&\quad+\frac{\langle p\rangle(\xi^c,\eta_2^c,\zeta-\Delta\zeta)-2\langle p\rangle(\xi^c,\eta_2^c,\zeta)+\langle p\rangle(\xi^c,\eta_2^c,\zeta+\Delta\zeta)}{\Delta\zeta^2}\\
&=\psi_{local}-\langle p\rangle(\xi^c,\eta^c-\Delta\eta,\zeta)
\end{aligned} \tag{6.69}$$

and

$$\begin{aligned}
&\frac{\langle p\rangle(\xi^c-\Delta\xi,\eta_{l+1}^c,\zeta)-2\langle p\rangle(\xi^c,\eta_{l+1}^c,\zeta)+\langle p\rangle(\xi^c+\Delta\xi,\eta_{l+1}^c,\zeta)}{\Delta\xi^2}\\
&\quad-\frac{\langle p\rangle(\xi^c,\eta_l^c,\zeta)-\langle p\rangle(\xi^c,\eta_{l+1}^c,\zeta)}{\Delta\eta^2}\\
&\quad+\frac{\langle p\rangle(\xi^c,\eta_{l+1}^c,\zeta-\Delta\zeta)-2\langle p\rangle(\xi^c,\eta_{l+1}^c,\zeta)+\langle p\rangle(\xi^c,\eta_{l+1}^c,\zeta+\Delta\zeta)}{\Delta\zeta^2}\\
&=\psi_{local}-\frac{1}{\Delta\eta}\frac{\Delta\langle p\rangle}{\Delta\eta}\bigg|_{l-1/2}
\end{aligned} \tag{6.70}$$

4. The backward difference scheme was applied to the pressure equation at $\eta^c = \eta_{N-1}^c$ as shown in Fig. 6.17. The Dirichlet boundary condition was applied at $\eta^c = \eta_N^c - 1$.

$$\begin{aligned}
&\frac{\langle p\rangle(\xi^c-\Delta\xi,\eta_{N-1}^c,\zeta)-2\langle p\rangle(\xi^c,\eta_{N-1}^c,\zeta)+\langle p\rangle(\xi^c+\Delta\xi,\eta_{N-1}^c,\zeta)}{\Delta\xi^2}\\
&\quad+\frac{\langle p\rangle(\xi^c,\eta_{N-2}^c,\zeta)-2\langle p\rangle(\xi^c,\eta_{N-1}^c,\zeta)}{\Delta\eta^2}\\
&\quad+\frac{\langle p\rangle(\xi^c,\eta_{N-1}^c,\zeta-\Delta\zeta)-2\langle p\rangle(\xi^c,\eta_{N-1}^c,\zeta)+\langle p\rangle(\xi^c,\eta_{N-1}^c,\zeta+\Delta\zeta)}{\Delta\zeta^2}\\
&=\psi_{local}-\langle p\rangle(\xi^c,\eta_N^c,\zeta)
\end{aligned} \tag{6.71}$$

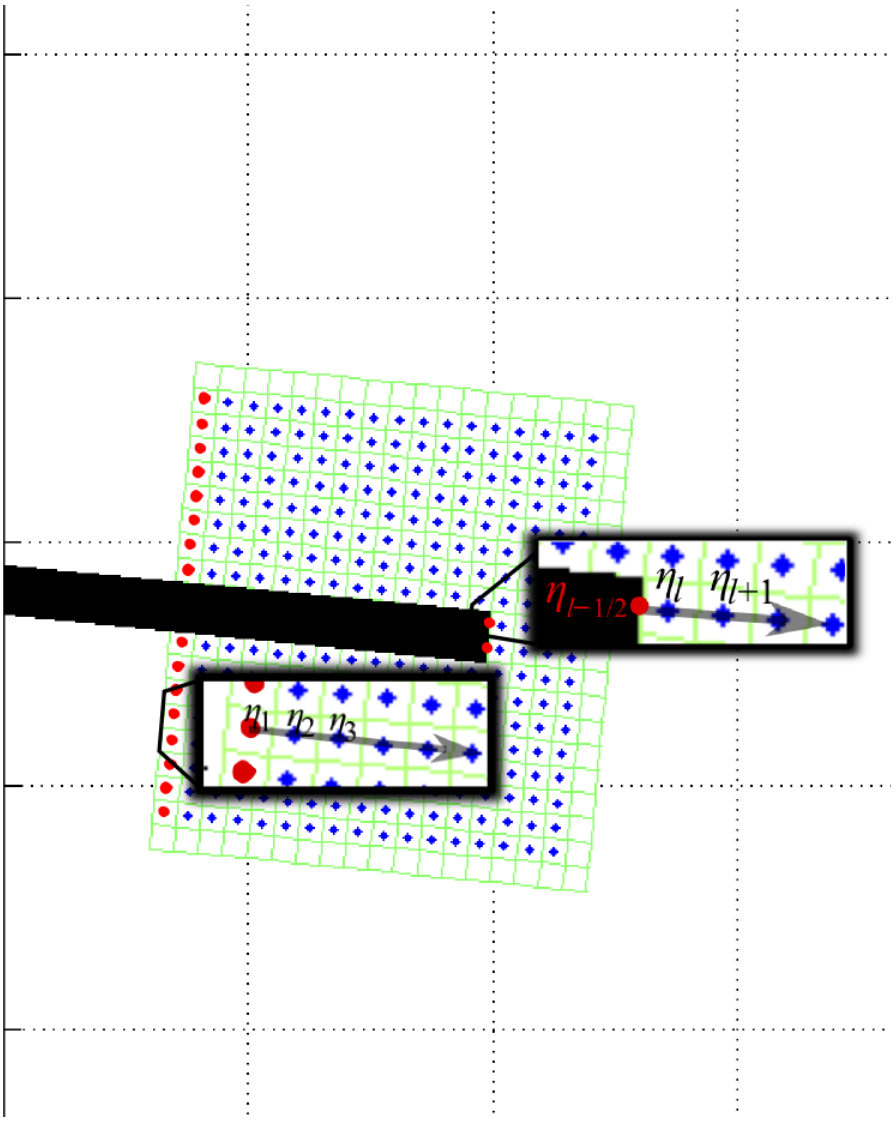

Figure 6.16: Application of the forward scheme on the boundary of local mesh. The boundary is marked by red dots and indices are shown in the insets.

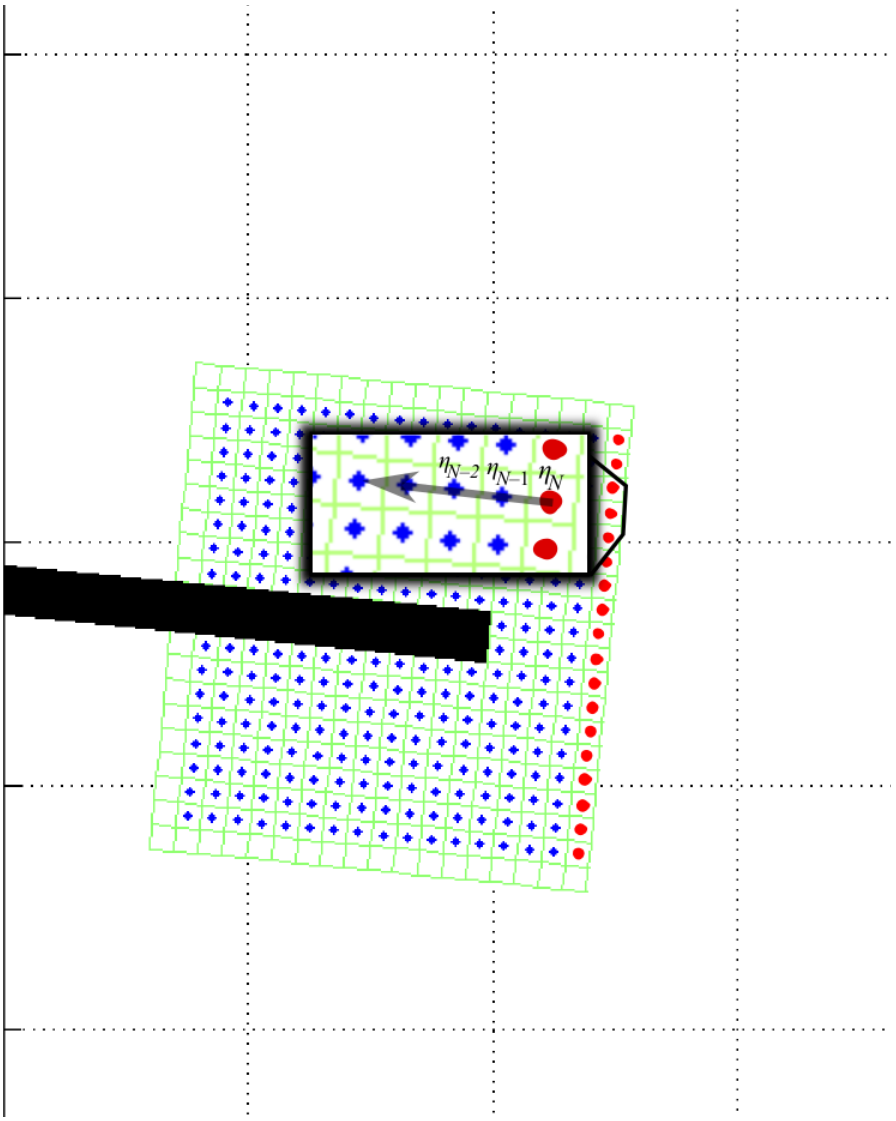

Figure 6.17: Application of the backward scheme on the boundary of local mesh. The boundary is marked by red dots and indices are shown in the insets.

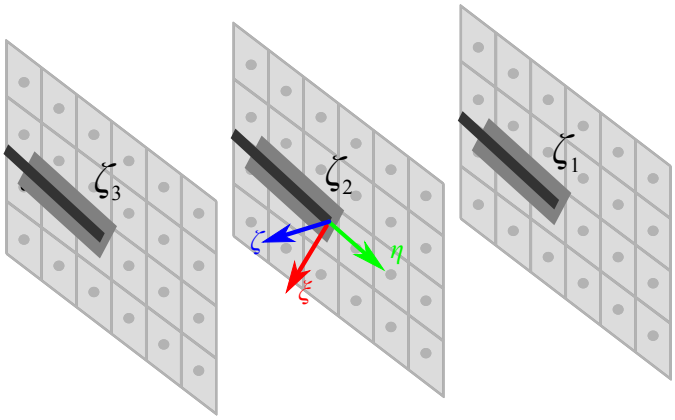

Figure 6.18: The numerical meshes along the ζ-axis: ζ_1 and ζ_3 are the numerical boundaries along the ζ-axis.

5. For boundary at $\zeta = \zeta_1$

$$\begin{aligned}
&\frac{\langle p\rangle(\xi^c-\Delta\xi,\eta^c,\zeta)-2\langle p\rangle(\xi^c,\eta^c,\zeta)+\langle p\rangle(\xi^c+\Delta\xi,\eta^c,\zeta)}{\Delta\xi^2}\\
&\quad+\frac{\langle p\rangle(\xi^c,\eta^c-\Delta\eta,\zeta)-2\langle p\rangle(\xi^c,\eta^c,\zeta)+\langle p\rangle(\xi^c,\eta^c+\Delta\eta,\zeta)}{\Delta\eta^2}\\
&\quad+\frac{-2\langle p\rangle(\xi^c,\eta^c,\zeta_1)+2\langle p\rangle(\xi^c,\eta^c,\zeta_2)}{\Delta\zeta^2}=\psi_{local}+\frac{2}{\Delta\zeta}\frac{\Delta\langle p\rangle}{\Delta\zeta}\bigg|_{\zeta_1}
\end{aligned}\tag{6.72}$$

6. For boundary at $\zeta = \zeta_3$

$$\begin{aligned}
&\frac{\langle p\rangle(\xi^c-\Delta\xi,\eta^c,\zeta)-2\langle p\rangle(\xi^c,\eta^c,\zeta)+\langle p\rangle(\xi^c+\Delta\xi,\eta^c,\zeta)}{\Delta\xi^2}\\
&\quad+\frac{\langle p\rangle(\xi^c,\eta^c-\Delta\eta,\zeta)-2\langle p\rangle(\xi^c,\eta^c,\zeta)+\langle p\rangle(\xi^c,\eta^c+\Delta\eta,\zeta)}{\Delta\eta^2}\\
&\quad+\frac{2\langle p\rangle(\xi^c,\eta^c,\zeta_2)-2\langle p\rangle(\xi^c,\eta^c,\zeta_3)}{\Delta\zeta^2}=\psi_{local}-\frac{2}{\Delta\zeta}\frac{\Delta\langle p\rangle}{\Delta\zeta}\bigg|_{\zeta_3}
\end{aligned}\tag{6.73}$$

where ζ_1 and ζ_3 are indicated by the illustration of the numerical mesh in Fig. 6.18.

6.4 Numerical method for solving the Poisson equation in the xz planes

The poisson equation for pressure was solved on the grids parallel to the xz plane. In total 3 grids are needed to solve the three-dimensional Poisson equation on the plane at $y = -c/2$ and another 3 grids to solve the same equation at $y = 0$. The pressure solution here is given for the cartesian coordinate system in the global mesh. Because of the orientation of the measurement plane relative to the flapping plate, at phase angles $\hat{\phi} \neq 0$ and $\hat{\phi} \neq 0.5$ the surface of the flapping plate is not orthogonal to the measurement plane making it impossible to set the boundary condition on the surface. Therefore, the calculation was not extended for the local mesh.

The frame of reference for the numerical mesh parallel to the xz planes is given in Fig. 6.19 and the finite difference Poisson equation to be solved within that domain is

$$\begin{aligned}\frac{\partial^2\langle p\rangle}{\partial x^2}+\frac{\partial^2\langle p\rangle}{\partial y^2}+\frac{\partial^2\langle p\rangle}{\partial z^2} = \\ -\rho\left[\left(\frac{\partial u}{\partial x}\right)^2+\left(\frac{\partial v}{\partial y}\right)^2+\left(\frac{\partial w}{\partial z}\right)^2+2\left(\frac{\partial u}{\partial y}\frac{\partial v}{\partial x}+\frac{\partial u}{\partial z}\frac{\partial w}{\partial x}+\frac{\partial v}{\partial z}\frac{\partial w}{\partial y}\right)\right. \\ \left.+\left(\frac{\partial^2\langle u'u'\rangle}{\partial x^2}+\frac{\partial^2\langle v'v'\rangle}{\partial y^2}+\frac{\partial^2\langle w'w'\rangle}{\partial z^2}\right)+2\left(\frac{\partial^2\langle u'v'\rangle}{\partial y\partial x}+\frac{\partial^2\langle u'w'\rangle}{\partial z\partial x}+\frac{\partial^2\langle v'w'\rangle}{\partial z\partial y}\right)\right]\end{aligned} \tag{6.74}$$

The boundary conditions are given as the pressure gradient normal to the respective boundaries. Because the global mesh is in x, y, and z directions, the boundary conditions are,

$$\frac{\Delta\langle p\rangle}{\Delta x} = -\rho\left[\frac{\Delta\langle u\rangle}{\Delta t}+\langle u\rangle\frac{\Delta\langle u\rangle}{\Delta x}+\langle v\rangle\frac{\Delta\langle u\rangle}{\Delta y}+\langle w\rangle\frac{\Delta\langle u\rangle}{\Delta z}+\frac{\Delta\langle u'u'\rangle}{\Delta x}+\frac{\Delta\langle u'v'\rangle}{\Delta y}+\frac{\Delta\langle u'w'\rangle}{\Delta z}\right] \tag{6.75}$$

for the boundaries orthogonal to the x-direction,

$$\frac{\Delta\langle p\rangle}{\Delta y} = -\rho\left[\frac{\Delta\langle v\rangle}{\Delta t}+\langle u\rangle\frac{\Delta\langle v\rangle}{\Delta x}+\langle v\rangle\frac{\Delta\langle v\rangle}{\Delta y}+\langle w\rangle\frac{\Delta\langle v\rangle}{\Delta z}+\frac{\Delta\langle u'v'\rangle}{\Delta x}+\frac{\Delta\langle v'v'\rangle}{\Delta y}+\frac{\Delta\langle v'w'\rangle}{\Delta z}\right] \tag{6.76}$$

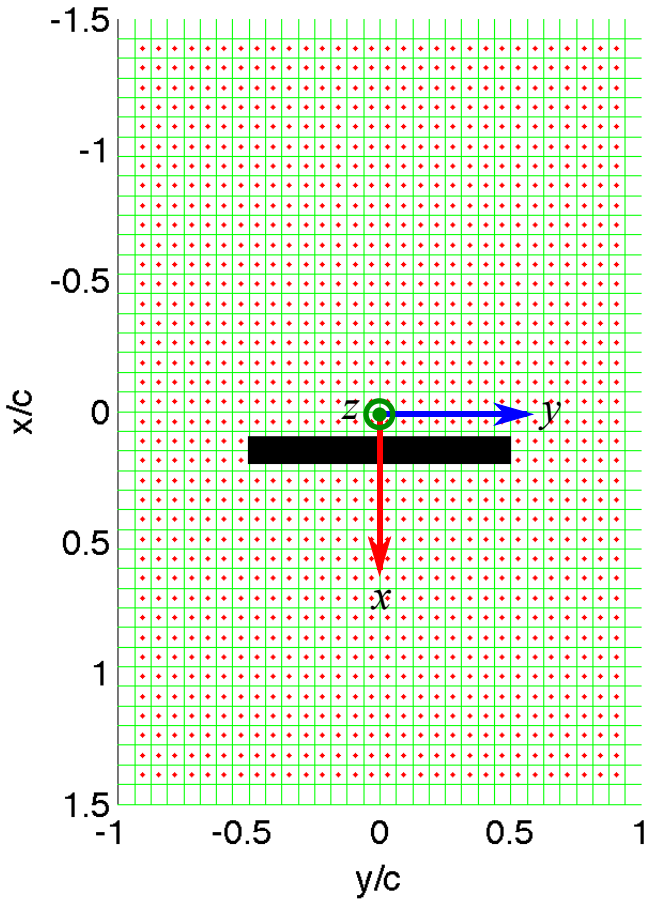

Figure 6.19: Definition of reference frame for the numerical mesh parallel to the xz plane. Pressure is solved on the red nodes at the center of each surface mesh.

for the boundaries orthogonal to the y-direction, and

$$\frac{\Delta\langle p\rangle}{\Delta z} = -\rho\left[\frac{\Delta\langle w\rangle}{\Delta t} + \langle u\rangle\frac{\Delta\langle w\rangle}{\Delta x} + \langle v\rangle\frac{\Delta\langle w\rangle}{\Delta y} + \langle w\rangle\frac{\Delta\langle w\rangle}{\Delta z} + \frac{\Delta\langle u'w'\rangle}{\Delta x} + \frac{\Delta\langle v'w'\rangle}{\Delta y} + \frac{\Delta\langle w'w'\rangle}{\Delta z}\right] \tag{6.77}$$

for the boundaries orthogonal to the z-direction

Adjacent to the numerical boundary, Eq. (6.74) was treated to include the given Neumann boundary condition. The forward finite difference scheme in x-direction was applied adjacent to the boundaries given in Fig. 6.20. Substituting Eq. (6.74) with the

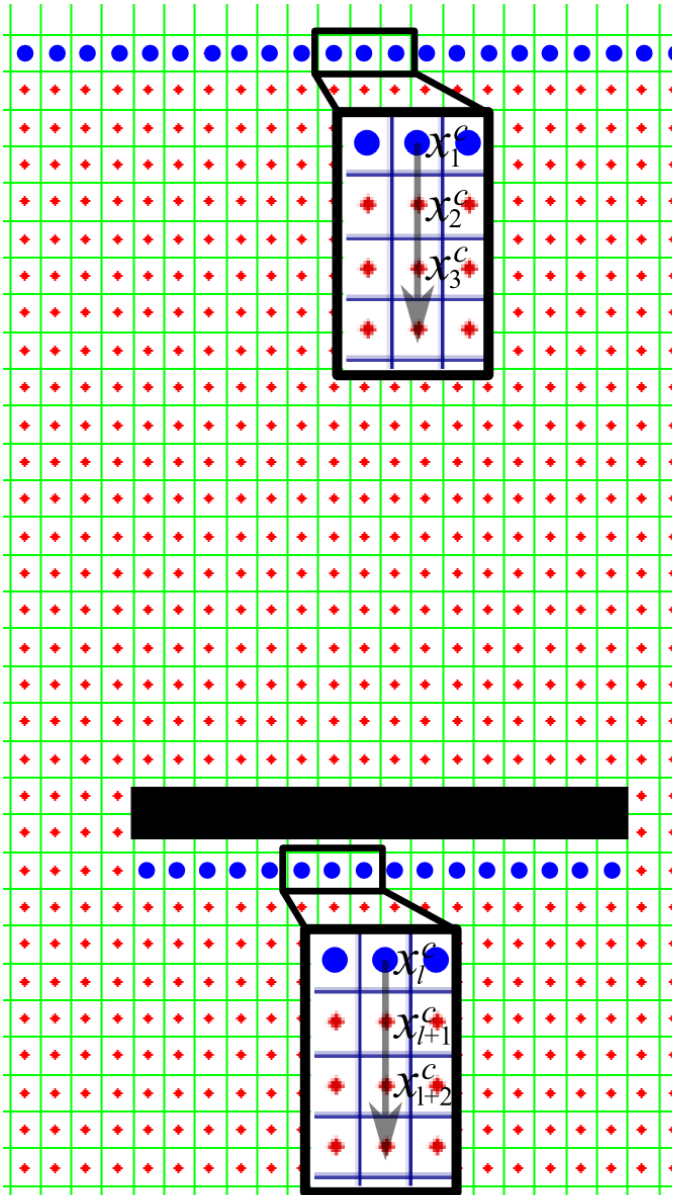

Figure 6.20: Forward finite difference scheme in x-direction. The boundary is marked by blue nodes and indices are shown in the insets.

necessary boundary condition,

$$\begin{aligned}
&\frac{1}{\Delta x^2}\left(-\frac{2}{3}\langle p\rangle(x_2^c,y^c,z)+\frac{2}{3}\langle p\rangle(x_3^c,y^c,z)\right)\\
&\quad+\frac{1}{\Delta y^2}\left(\langle p\rangle(x_2^c,y^c+\Delta y,z)-2\langle p\rangle(x_2^c,y^c,z)+\langle p\rangle(x_2^c,y^c-\Delta y,z)\right)\\
&\quad+\frac{1}{\Delta z^2}\left(\langle p\rangle(x_2^c,y^c,z+\Delta z)-2\langle p\rangle(x_2^c,y^c,z)+\langle p\rangle(x_2^c,y^c,z-\Delta z)\right)\\
&=\psi(x_2^c,y^c,z)+\frac{2}{3\Delta x}\frac{\Delta\langle p\rangle}{\Delta x}\bigg|_1
\end{aligned} \tag{6.78}$$

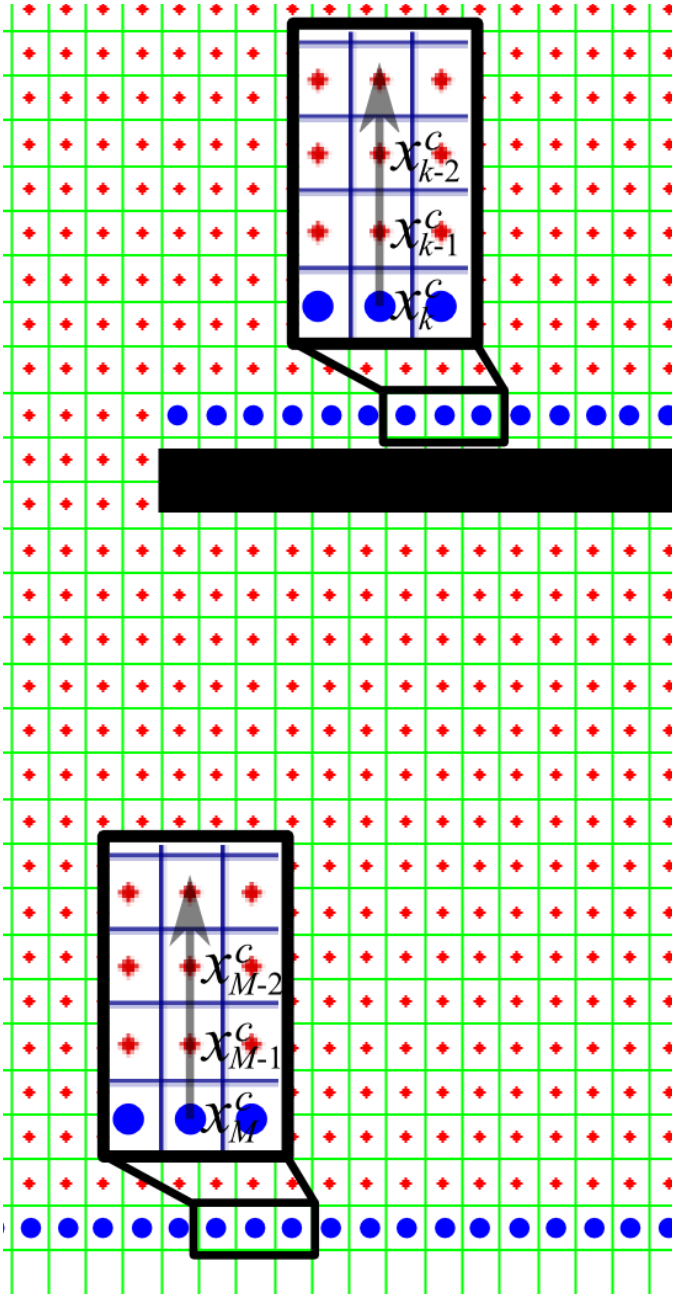

Figure 6.21: Backward finite difference scheme in x-direction. The boundary is marked by blue nodes and indices are shown in the insets.

The backward finite difference in x-direction was applied adjacent to the boundaries given in Fig. 6.21 Substituting Eq. (6.74) with the necessary boundary condition,

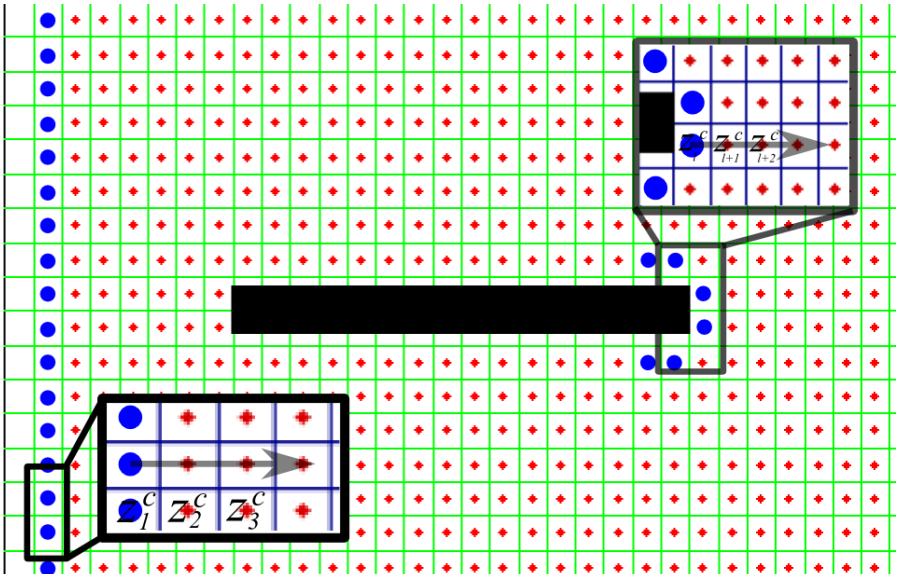

Figure 6.22: Forward finite difference scheme in z-direction. The boundary is marked by blue nodes and indices are shown in the insets.

$$\begin{aligned}
&\frac{1}{\Delta x^2}\left(\frac{2}{3}\langle p\rangle(x^c_{M-2},y^c,z)-\frac{2}{3}\langle p\rangle(x^c_{M-1},y^c,z)\right)\\
&\quad+\frac{1}{\Delta y^2}\left(\langle p\rangle(x^c_{M-1},y^c+\Delta y,z)-2\langle p\rangle(x^c_{M-1},y^c,z)+\langle p\rangle(x^c_{M-1},y^c-\Delta y,z)\right)\\
&\quad+\frac{1}{\Delta z^2}\left(\langle p\rangle(x^c_{M-1},y^c,z+\Delta z)-2\langle p\rangle(x^c_{M-1},y^c,z)+\langle p\rangle(x^c_{M-1},y^c,z-\Delta z)\right)\\
&=\psi(x^c_{M-1},y^c,z)-\frac{2}{3\Delta x}\frac{\Delta\langle p\rangle}{\Delta x}\bigg|_M
\end{aligned} \tag{6.79}$$

The forward finite difference in z-direction was applied adjacent to the boundaries given in Fig. 6.22 Substituting Eq. (6.74) with the necessary boundary condition,

$$\begin{aligned}
&\frac{1}{\Delta x^2}\left(\langle p\rangle(x^c+\Delta x,y^c,z_2)-2\langle p\rangle(x^c,y^c,z_2)+\langle p\rangle(x^c-\Delta x,y^c,z_2)\right)\\
&\quad+\frac{1}{\Delta y^2}\left(\langle p\rangle(x^c,y^c-\Delta y,z_2)-2\langle p\rangle(x^c,y^c,z_2)+\langle p\rangle(x^c,y^c-\Delta y,z_2)\right)\\
&\quad+\frac{1}{\Delta z^2}\left(-\frac{2}{3}\langle p\rangle(x^c,y^c,z_2)+\frac{2}{3}\langle p\rangle(x^c,y^c,z_3)\right)\\
&=\psi(x^c,y^c,z_2)+\frac{2}{3\Delta z}\frac{\Delta\langle p\rangle}{\Delta z}\bigg|_1
\end{aligned} \tag{6.80}$$

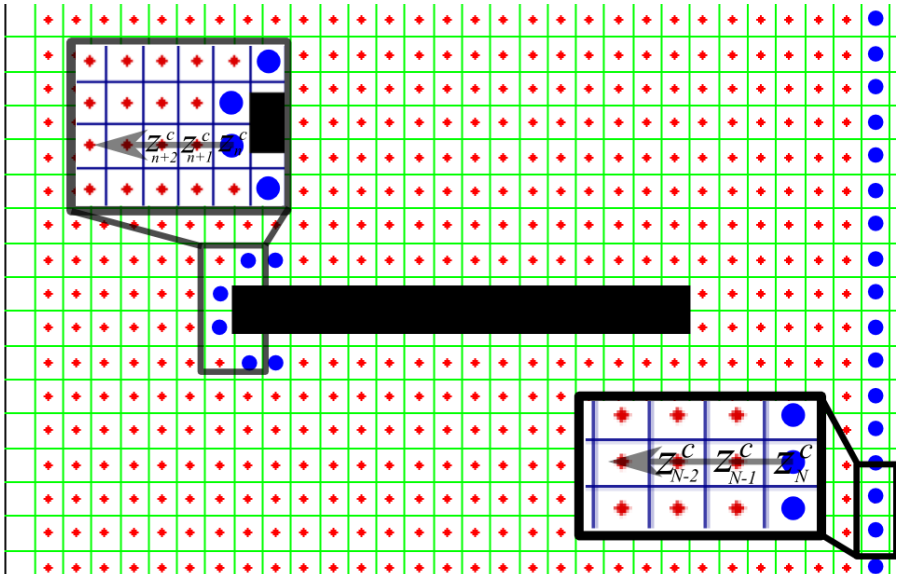

Figure 6.23: Backward finite difference scheme in z-direction. The boundary is marked by blue nodes and indices are shown in the insets.

The backward finite difference scheme in z-direction was applied adjacent to the boundaries given in Fig. 6.23 Substituting Eq. (6.74) with the necessary boundary condition,

$$\begin{aligned}
&\frac{1}{\Delta x^2}\Big(\langle p\rangle(x^c+\Delta x,y^c,z_{N-1})-2\langle p\rangle(x^c,y^c,z_{N-1})+\langle p\rangle(x^c-\Delta x,y^c,z_{N-1})\Big)\\
&\quad+\frac{1}{\Delta y^2}\Big(\langle p\rangle(x^c,y^c+\Delta y,z_{N-1})-2\langle p\rangle(x^c,y^c,z_{N-1})+\langle p\rangle(x^c,y^c-\Delta z,z_{N-1})\Big)\\
&\quad+\frac{1}{\Delta z^2}\Big(\frac{2}{3}\langle p\rangle(x^c,y^c,z_{N-2})-\frac{2}{3}\langle p\rangle(x^c,y^c,z_{N-1})\Big)\\
&=\psi(x^c,y^c,z_{N-1})-\frac{2}{3\Delta z}\frac{\Delta\langle p\rangle}{\Delta z}\bigg|_N
\end{aligned} \tag{6.81}$$

The numerical mesh along the y-direction is depicted in Fig. 6.24 for the mesh around $y=y_2$. Substituting Eq. (6.82) with the necessary boundary condition. The

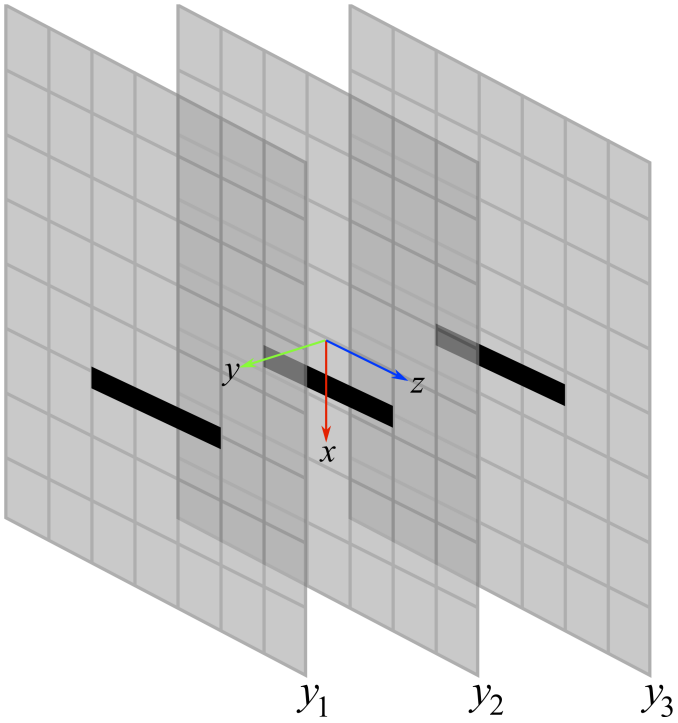

Figure 6.24: Illustration of the numerical mesh along the y-direction. Two adjacent mesh is shown around $y = y_0$ to solve the three-dimensional Poisson equation on $y = y_0$.

.

forward finite difference scheme along the y-direction is

$$\begin{aligned}
&\frac{1}{\Delta x^2}\Big(\langle p\rangle(x^c+\Delta x, y_1, z^c) - 2\langle p\rangle(x^c, y_1, z^c) + \langle p\rangle(x^c-\Delta x, y, z^c)\Big) \\
&\quad + \frac{1}{\Delta y^2}\Big(-2\langle p\rangle(x^c, y_1, z^c) + 2\langle p\rangle(x^c, y_2, z^c)\Big) \\
&\quad + \frac{1}{\Delta z^2}\Big(\langle p\rangle(x^c, y_1, z^c-\Delta z) - 2\langle p\rangle(x^c, y_1, z^c) + \langle p\rangle(x^c, y_1, z^c-\Delta z)\Big) \\
&= \psi(x^c, y_1, z^c) + \frac{2}{\Delta y}\frac{\Delta\langle p\rangle}{\Delta y}\bigg|_1
\end{aligned} \tag{6.82}$$

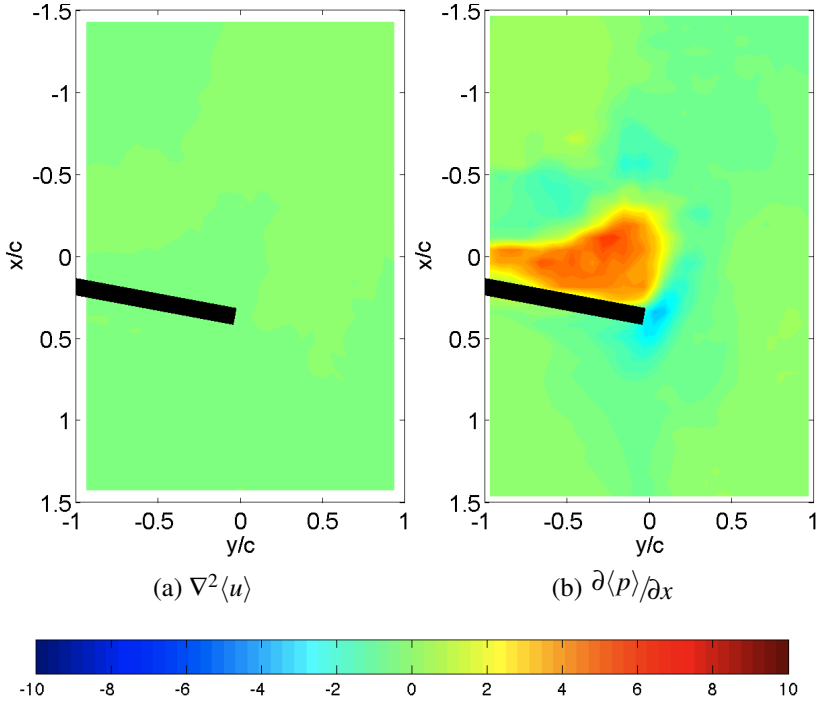

(a) $\nabla^2\langle u\rangle$ (b) $\partial\langle p\rangle/\partial x$

Figure 6.25: Comparison of (a) $\mu\nabla^2\langle u\rangle$ and (b) $\partial\langle p\rangle/\partial x$ at $\hat{\phi} = 0.6$. The former is considered negligible in the governing equation.

and the backward finite difference scheme along the y-direction is

$$\begin{aligned}
&\frac{1}{\Delta x^2}\Big(\langle p\rangle(x^c+\Delta x, y_3, z^c) - 2\langle p\rangle(x^c, y_3, z^c) + \langle p\rangle(x^c-\Delta x, y_3, z^c)\Big) \\
&\quad + \frac{1}{\Delta y^2}\Big(2\langle p\rangle(x^c, y_2, z^c) - 2\langle p\rangle(x^c, y_3, z^c)\Big) \\
&\quad + \frac{1}{\Delta z^2}\Big(\langle p\rangle(x^c, y_3, z^c+\Delta z) - 2\langle p\rangle(x^c, y_3, z^c) + \langle p\rangle(x^c, y_3, z^c-\Delta z)\Big) \\
&= \psi(x^c, y_3, z^c) - \frac{2}{\Delta y}\frac{\Delta\langle p\rangle}{\Delta y}_3
\end{aligned} \tag{6.83}$$

6.5 The estimated pressure field

The governing equations and boundary conditions were derived from the assumption that the flow is inviscid. The viscous term calculated from the phase-averaged velocity field as shown in Fig. 6.25, shows that the viscous term $\mu\nabla^2\langle u\rangle$ has negligible effect

compared to $\partial\langle p\rangle/\partial x$, which is a direct consequence of the similarities of the velocity profile in Fig. 6.4. This substantiate the inviscid flow assumption.

6.5.1 Pressure field on the xy-planes

The estimated pressure fields, as evaluated using Eq. (6.6), are shown in Fig. 6.26 at the mid-chord, $z = 0$, and at the leading-edge, $z = c/2$, for (a)–(b) $\hat{\phi} = 0.25$ and (c)–(d) $\hat{\phi} = 0.45$. The pressure field is presented as the non-dimensional pressure coefficient $C_p = \langle p\rangle/(\frac{1}{2}\rho U^2)$.

The Poisson equation consists of only spatial derivatives and by using the Neumann boundary condition, the pressure fields in Fig. 6.26 are independent from each other and not to be mistaken as a representation of the time evolution of the pressure. However, it should be noted that the pressure difference on the surface of the plate can represent the time evolution of the force acting on that surface. Strong discontinuities of the pressure field between the global and the local mesh can be observed in Fig. 6.26(d). This discontinuity is caused by the mixed Dirichlet-Neumann boundary condition that was used for the local mesh. The Neumann boundary condition was applied on the boundary immediate to the surface of the plate.

The proposed method estimated the pressure field reasonably well on the mid-chord and poorly on the leading edge as shown in Figs. 6.26(a)–(b). This may be because around the leading edge, the Neumann boundary condition on the surface of the plate was insufficient to properly solve the Poisson equation because the measurement plane is located around the bend of the edge of the plate. The spatial resolution of the out-of-plane velocity component was evaluated by comparing the finite derivative of that component,

$$\frac{\partial\langle w\rangle}{\partial z} = \frac{\langle w\rangle\big|_{(z+\Delta z)} - \langle w\rangle\big|_{(z-\Delta z)}}{2\Delta z} - \frac{1}{6}(\Delta z)^2\frac{\partial^3\langle w\rangle}{\partial z^3}(\varepsilon) \tag{6.84}$$

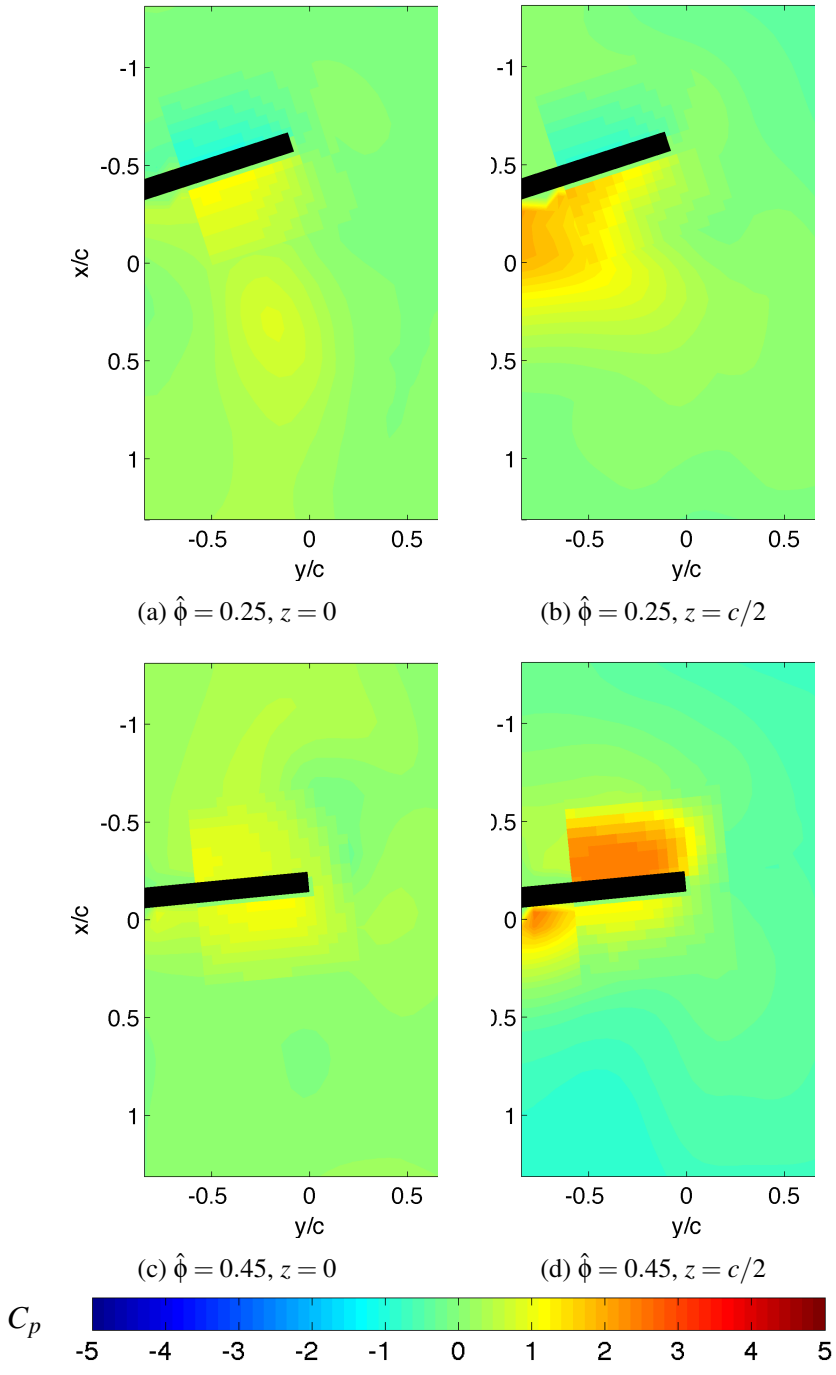

(a) $\hat{\phi} = 0.25, z = 0$ (b) $\hat{\phi} = 0.25, z = c/2$

(c) $\hat{\phi} = 0.45, z = 0$ (d) $\hat{\phi} = 0.45, z = c/2$

Figure 6.26: Pressure distribution on the xy-planes. Contour indicates C_p.

with the one calculated with the assumption that the continuity condition is fulfillled,

$$\begin{aligned}\frac{\partial\langle u\rangle}{\partial x}+\frac{\partial\langle v\rangle}{\partial y}+\frac{\partial\langle w\rangle}{\partial z}&=0\\ \frac{\partial\langle w\rangle}{\partial z}&=-\left(\frac{\partial\langle u\rangle}{\partial x}+\frac{\partial\langle v\rangle}{\partial y}\right)\\ \frac{\partial\langle w\rangle}{\partial z}&=-\left(\frac{\Delta\langle u\rangle}{\Delta x}+\frac{\Delta\langle v\rangle}{\Delta y}\right)+\left(\frac{1}{6}(\Delta x)^2\frac{\partial^3\langle u\rangle}{\partial x}(\varepsilon)+\frac{1}{6}(\Delta y)^2\frac{\partial^3\langle v\rangle}{\partial y}(\varepsilon)\right)\end{aligned} \tag{6.85}$$

In this study, the velocity gradients were calculated with a second order finite difference scheme. The comparison is shown in Fig. 6.27, where it shows an underestimation of the out-of-plane velocity gradient on the leading-edge.

The comparison of the out-of-plane velocity gradient on the mid-chord is shown in Fig. 6.28. On the mid-chord of the plate, the out-of-plane gradient was also underestimated. However, the gradients in Fig. 6.28 is qualitatively more agreeable with each other than the ones in Fig. 6.27. Therefore, the flow around the leading edge, which is highly three-dimensional, requires a proper volumetric PIV measurement to resolve the boundary condition and the spatial resolution. The result of the pressure estimation in Fig. 6.26 suggests that with the current measurement configuration it is safe to estimate the pressure field along $-c/2 < z < c/2$.

6.5.2 Pressure field on the xz-planes

The estimated pressure fields on the xz-planes were evaluated using Eq. (6.74) with the boundary conditions of Eqs. (6.78)–(6.83). A sample of this pressure field is shown in Fig. 6.29 for $y = -c/2$ and $y = 0$ at $\hat{\phi} = 0.25$.

The pressure fields in Fig. 6.29 show the cross-section of the flapping plate with the measurement plane. for the plane at $y = -c/2$, the cross-section is represented by the black square and at $y = 0$, a projection of the flapping plate on the measurement plane is represented by the empty square as an indicator of the location of the flapping plate relative to the flow.

The calculation of these pressure fields are more straightforward because they were done only on the global mesh. This is due to the configuration that was used to measure

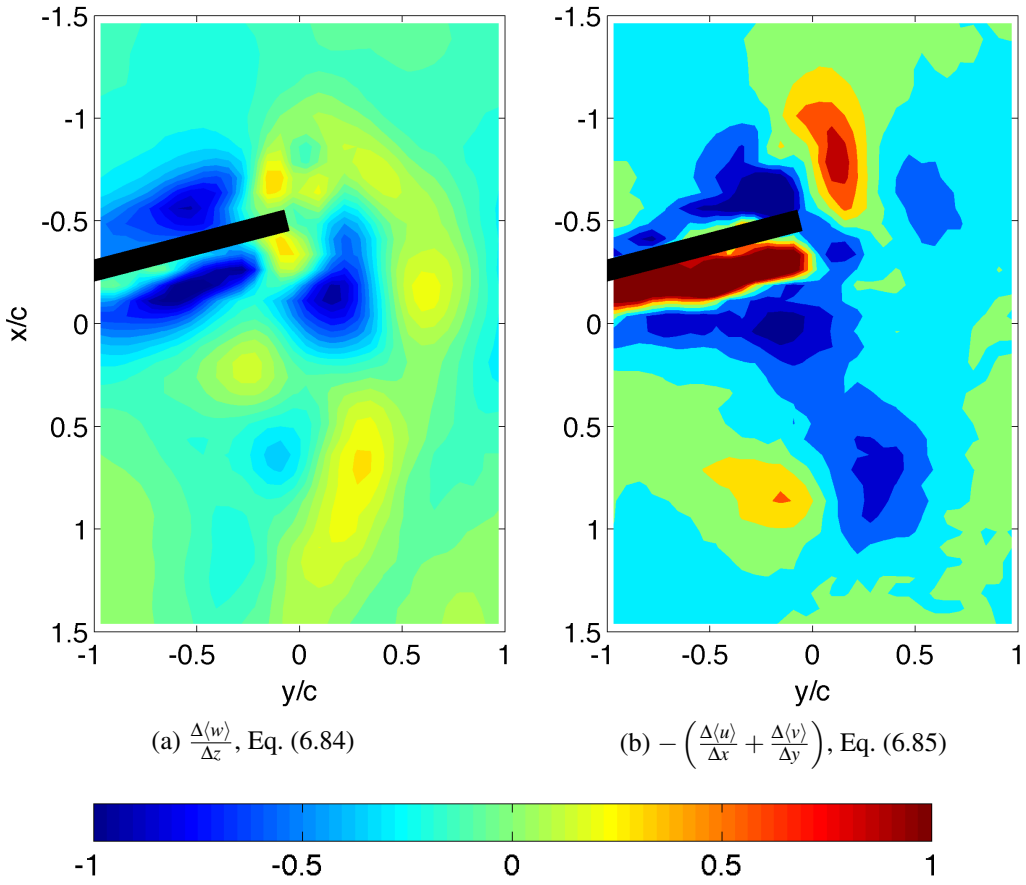

(a) $\frac{\Delta\langle w\rangle}{\Delta z}$, Eq. (6.84)

(b) $-\left(\frac{\Delta\langle u\rangle}{\Delta x}+\frac{\Delta\langle v\rangle}{\Delta y}\right)$, Eq. (6.85)

Figure 6.27: Comparison of the out-of-plane gradient on the leading-edge, $z = c/2$, at $\hat{\phi} = 0.35$.

the velocity on xz-planes. At $\hat{\phi} \neq 0$ and $\hat{\phi} \neq 0.5$, the measurement plane is not orthogonal to the surface of the plate. Because the local mesh is a subset of the measurement plane, it is impossible to assign the pressure gradient normal to the surface of the plate as the boundary condition in the current configuration.

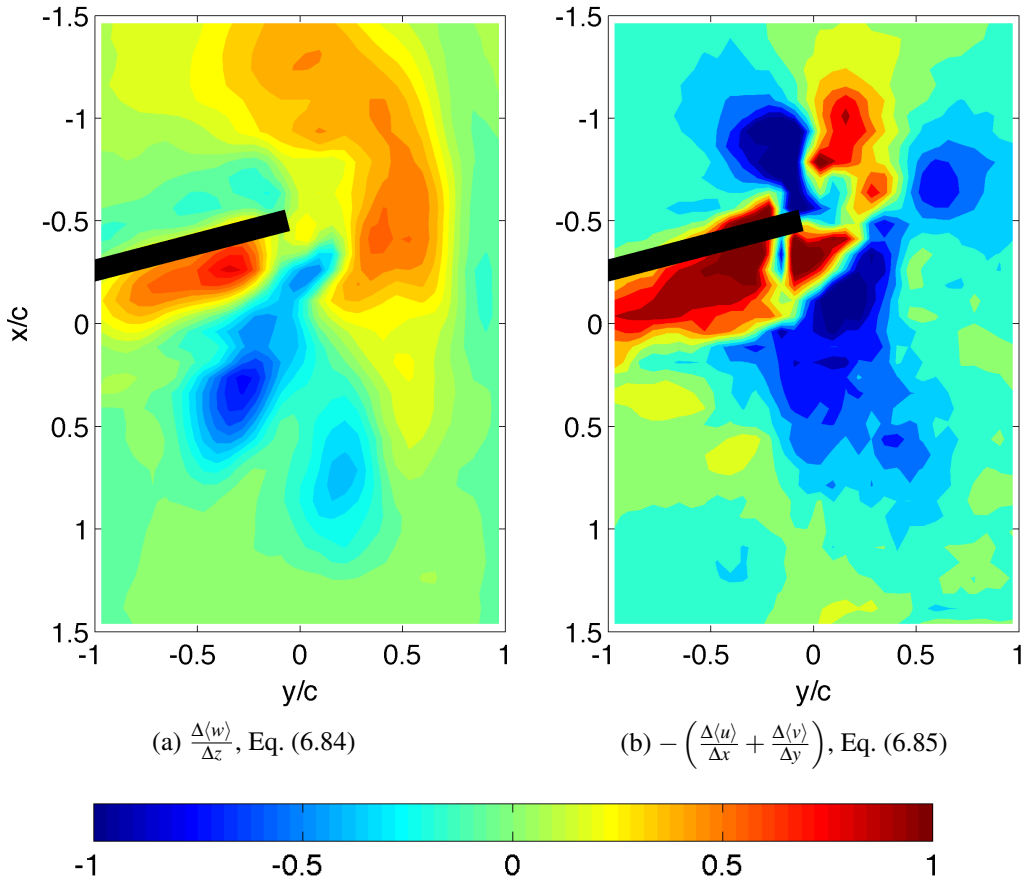

(a) $\frac{\Delta\langle w\rangle}{\Delta z}$, Eq. (6.84)

(b) $-\left(\frac{\Delta\langle u\rangle}{\Delta x}+\frac{\Delta\langle v\rangle}{\Delta y}\right)$, Eq. (6.85)

Figure 6.28: Comparison of the out-of-plane gradient on the mid-chord, $z=0$, at $\hat{\phi}=0.35$.

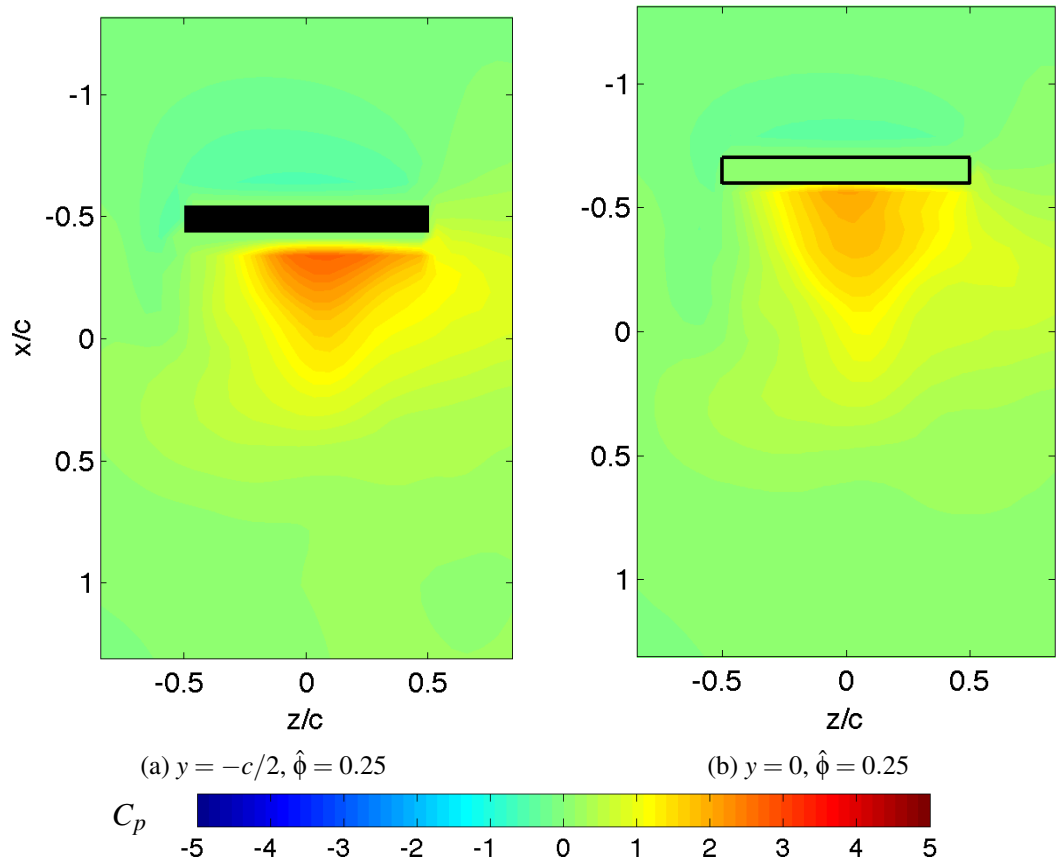

Figure 6.29: Pressure distribution on the xz-planes. Contour indicates C_p.

6.6 Concluding remarks

This chapter demonstrates the visualization of pressure generated during flapping motion down to the surface of the flapping plate. The pressure field was obtained by solving the Poisson equation for pressure, where the Laplacian of pressure was approximated by the velocity field as obtained using stereo PIV.

An overlapping mesh system was proposed to estimate the pressure on the surface of the plate. In this study, two meshes were used: global mesh, in the inertial frame of reference, and local mesh, constrained to the motion of the flapping plate. Large discontinuity in the leading edge section of the plate, $z = c/2$, is caused by improper boundary condition and low spatial resolution of the measured plane. Because of its location on the edge of the plate, the pressure gradient boundary condition normal to the surface of the plate was not enough to obtain continuous pressure distribution because the measurement plane was at the edge of the plate and it included the bend of the plate's surface.

The pressure estimation on *xz*-planes was done for only the global mesh due to the measurement configuration where the measurement plane was not orthogonal to the surface of plate except for $\hat{\phi} = 0$ and $\hat{\phi} = 0.5$. Because of this configuration, the assignment of the pressure gradient normal to the surface of the body was impossible to be done.

Chapter 7

The estimation of flapping torque

This chapter presents the estimation of the flapping torque from the integration of the surface pressure distribution. The flapping torque is the product of the force of the wing. So, the estimation assesses the force acting on the wing as well. The flapping torque is compared with the strain gauge measurement. The integral equation and the result is presented in §7.1 and final remarks are given in §7.2.

7.1 Pressure integration

The estimation of torque was calculated by integrating the pressure along a set of lines, which are the intersections of the local meshes with the surface of the plate. The integration was evaluated with the control surface, *pqrs*, as illustrated in Fig. 7.1. The torque is presented as the non-dimensional torque coefficient,

$$C_T = \frac{T}{{}^1\!/_2\rho(2\pi f b\Theta)^2 b(bc)} \tag{7.1}$$

The torque acting on the axis of the flapping motion is shown in Fig. 7.2 which is

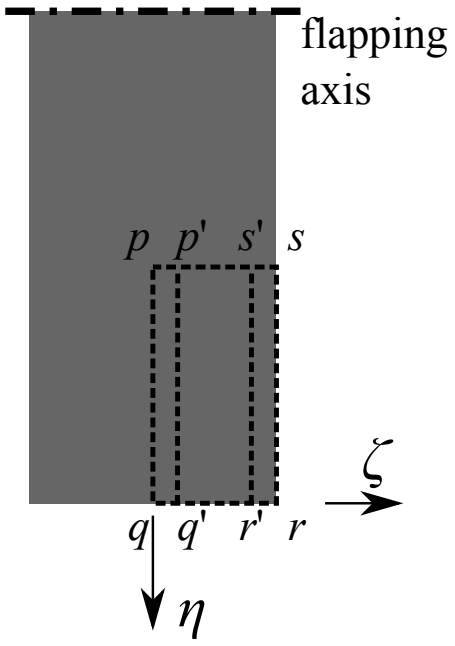

Figure 7.1: Definition of the control surface for the integration of pressure on the plate.

the integration of the estimated pressure as evaluated by

$$T = 2\left[\int_p^q \int_p^{q'} \left(\eta\langle p\rangle\hat{n}_\xi + \xi\langle p\rangle\hat{n}_\eta\right) d\zeta d\eta \right. \tag{7.2}$$

$$\int_{p'}^{q'} \int_{p'}^{s'} \left(\eta\langle p\rangle\hat{n}_\xi + \xi\langle p\rangle\hat{n}_\eta\right) d\zeta d\eta \tag{7.3}$$

$$\left. \int_{s'}^{r'} \int_{s'}^{s} \left(\eta\langle p\rangle\hat{n}_\xi + \xi\langle p\rangle\hat{n}_\eta\right) d\zeta d\eta \right] \tag{7.4}$$

Where on the right hand side, the first and third term were evaluated directly and the second term was interpolated on $p'q'$ from that on pq and on $s'r'$ from that on sr.

In Fig. 7.2 the estimated torque is compared with the torque directly measured by strain gauges. With the information available from the pressure field for estimating the torque, reasonable qualitative agreement is observed for the amplitudes of both torque curves. However, the similarity ends there because a phase difference is observed between them.

As discussed in the previous chapter, the pressure estimation on *rs* is inaccurate because of the lack of spatial resolution and improper boundary condition because of

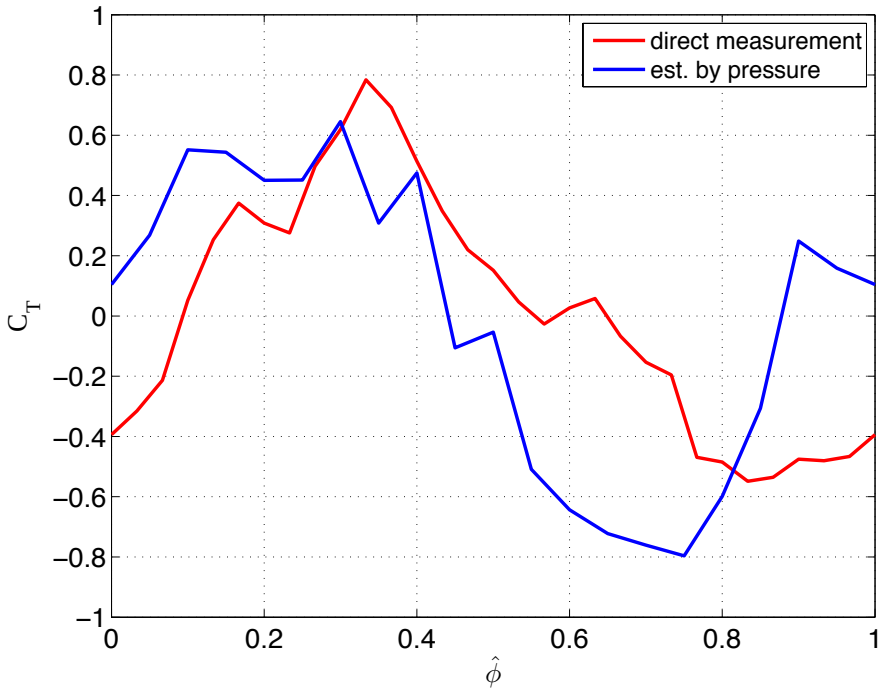

Figure 7.2: Comparison of torque coefficients estimated ("est") by pressure and torque directly measured by strain gauges for flapping rigid plate at Re=3160.

the complicated surface. The integrations of surface pressure along pq and rs are given in Fig. 7.3.

In Fig. 7.3 the infinitesimal surface of the plate is discretized as $(qq')(d\eta)$, where $qq' = rr' = h$ is the distance between two laser sheet and the pressure distribution along this length is assumed to be constant. Because of this, the magnitude in Fig. 7.3 is one order less than in Fig. 7.2. The torque around pq is

$$T(z) = \int_{p-h/2}^{p+h/2} \int_{p}^{q} \left(\eta \langle p \rangle \hat{n}_\xi + \xi \langle p \rangle \hat{n}_\eta \right) d\eta d\zeta \tag{7.5}$$

and the torque around the leading-edge is

$$T(z) = \int_{s-h/2}^{s} \int_{s}^{r} \left(\eta \langle p \rangle \hat{n}_\xi + \xi \langle p \rangle \hat{n}_\eta \right) d\eta d\zeta \tag{7.6}$$

With the current measurement configuration, a sinusoidal form of the torque curves at $z = 0$ and $z = c/2$ are observed in Fig. 7.3. An increase in torque is observed from

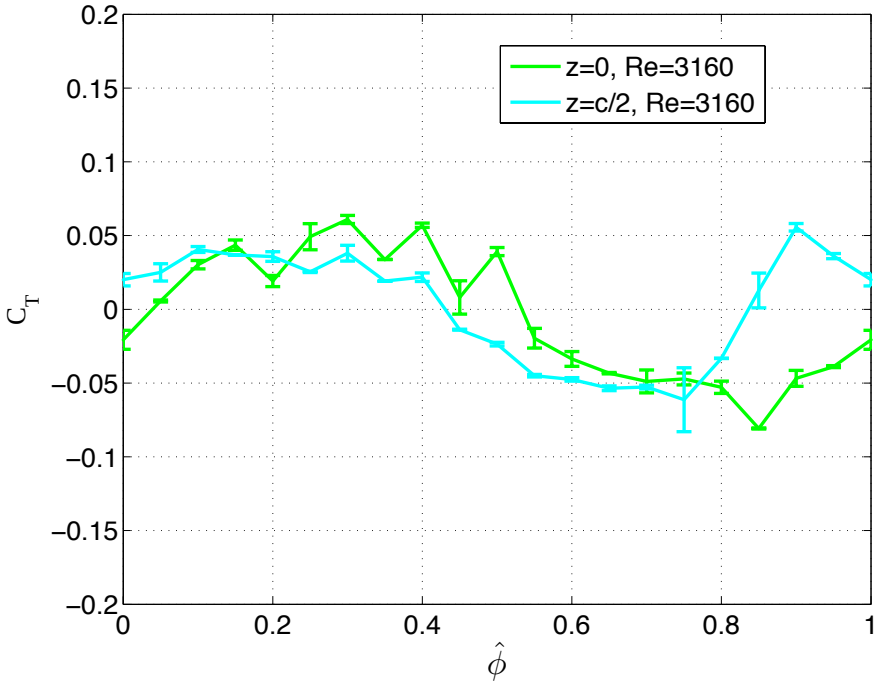

Figure 7.3: Comparison of torque coefficients estimated by pressure integrated on the mid-chord plane and on the leading-edge plane for flapping rigid plate at Re=3160.

$\hat{\phi} = 0.25$ at $z = 0$ despite the plate is moving at low velocity. The torque at $\hat{\phi} = 0.30$ is caused by the high pressure region on the forward facing surface of the plate as shown in Fig. 7.4(a). The pressure difference between the forward and rear facing surface of the plate decreases at $\hat{\phi} = 0.50$ as shown in Fig. 7.5(a). Proportionally, the torque at $\hat{\phi} = 0.50$ is smaller than that at $\hat{\phi} = 0.3$. During the next flapping stroke, ie. at $\hat{\phi} = 0.85$, the pressure difference increases because of the high pressure region on the front facing surface of the plate (cf. Fig. 7.6(a)) similar to that described in Fig. 7.4(a).

In Fig. 7.3 the torque curves at $z = c/2$ shows a phase difference compared with the torque curves at $z = 0$ and the torque curves measured by strain gauges. The increase of the torque curve at $z = c/2$ starts $\hat{\phi} = 0.9$ and positive torque observed until $\hat{\phi} = 0.4$. The pressure field distribution at $z = c/2$ and $\hat{\phi} = 0.30$ in Fig. 7.4(b) shows large pressure difference between the front and rear facing surface of the plate similar to the pressure distribution at $z = 0$ of the same phase angle. At $\hat{\phi} = 0.50$ (cf. Fig. 7.5(b)) high pressure region is on the rear surface of the plate, which is the opposite of the pressure field

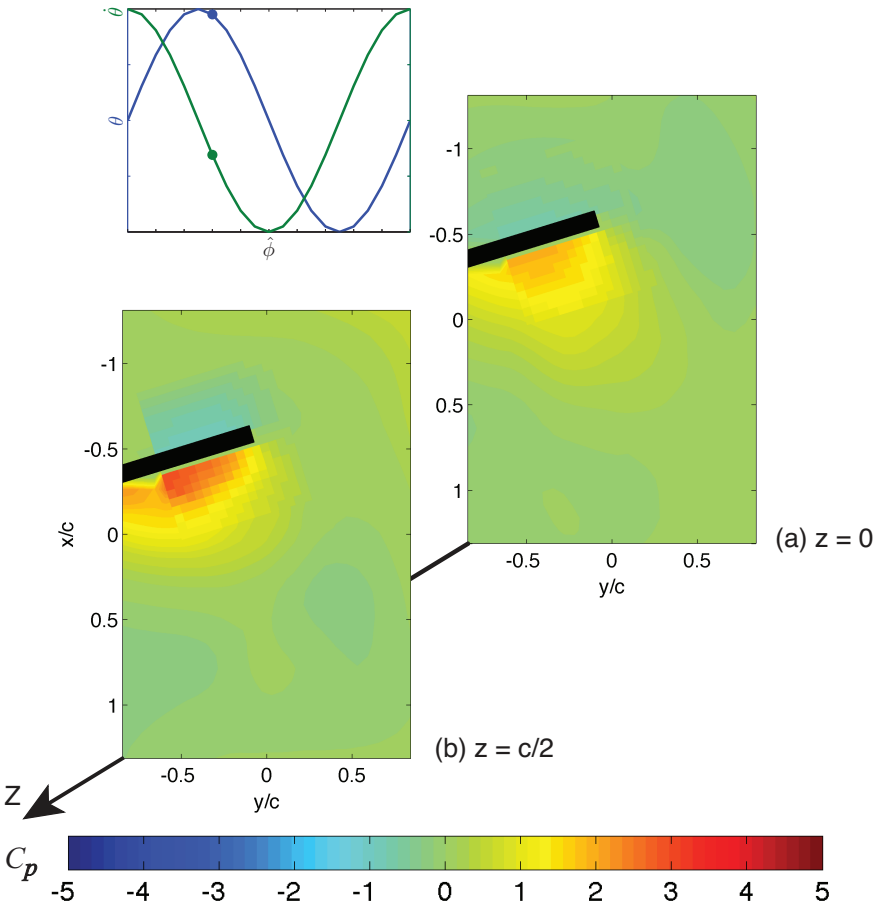

Figure 7.4: Estimated pressure distribution on xy-planes at $\hat{\phi} = 0.30$.

at $z = 0$, Fig. 7.4(b). The high pressure region is caused by the leading edge vortex moving towards the rear facing surface of the plate. The flow behind this surface acts like stagnated flow. In Fig. 7.6(b), the pressure distribution at $\hat{\phi} = 0.85$ around the surfaces of the plate shows discontinuity especially on the left edge of the local mesh. This result in a sharp drop of torque in Fig. 7.3.

Figure 7.3 shows that the qualitative comparison of the torque estimated by pressure on the mid-chord agrees well with the directly measured one and the shift in the flapping phase angle is due to the estimation of the surface pressure on the leading-edge. With these regards, the flow at $-c/2 < z < c/2$ can be used to estimate the pressure field and its derived products.

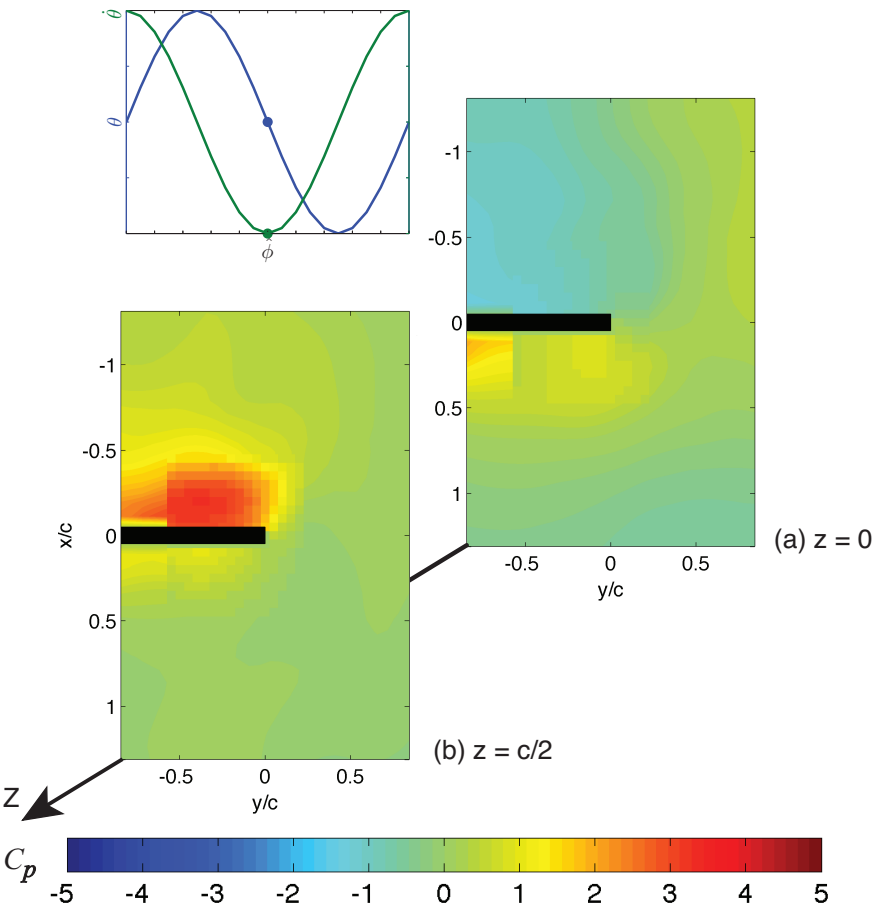

Figure 7.5: Estimated pressure distribution on xy-planes at $\hat{\phi} = 0.50$.

The mechanics of the increased torque is explained by the production of the vortex flow behind the flapping plate. Slices of the pressure and vorticity distribution on the xz-planes are shown in Figs. 7.7 – 7.12 and the pressure difference is compared with the torque curve measured by strain gauges in Fig. 7.2.

The start of the flapping down stroke, $\hat{\phi} = 0.25$, is shown in Fig. 7.7, where the flapping velocity is at minimum. In Fig. 7.7(a), the leading edge vortices produced in the up stroke is shown on the rear surface of the plate. The diameter of each of the leading edge vortex is about half of the plate's chord length. These vortices interact with the rear surface of the plate and produce secondary vortices on the surface of the plate. Two counter rotating vortices induce the fluid to flow towards the rear surface of

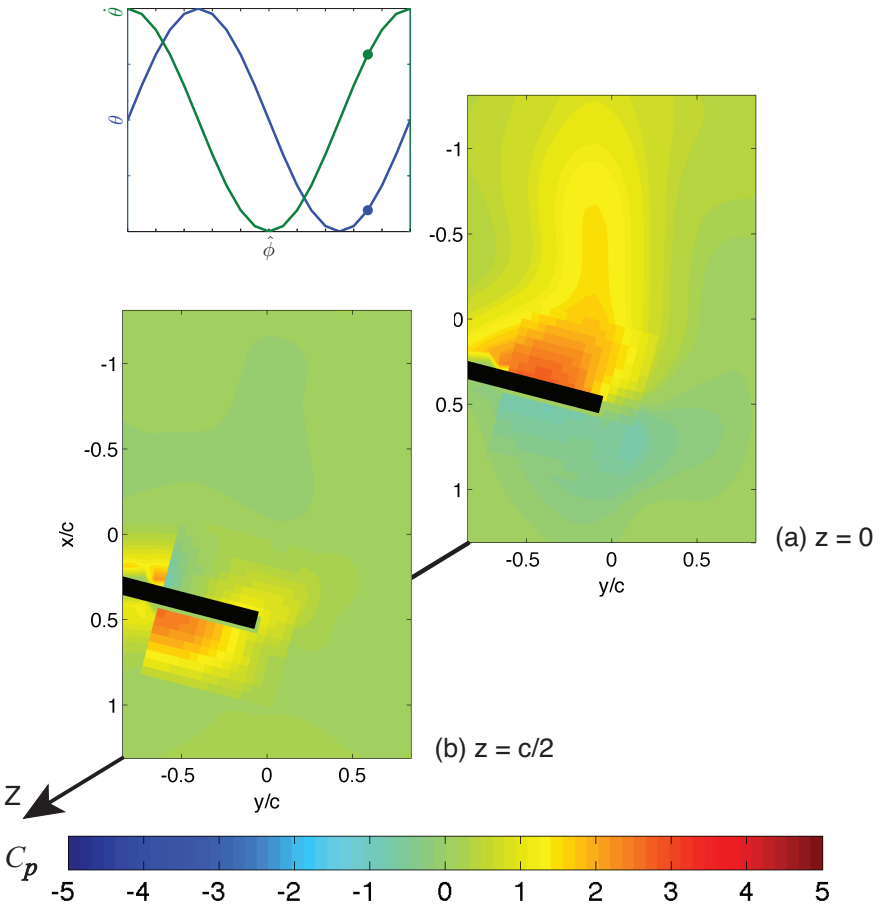

Figure 7.6: Estimated pressure distribution on *xy*-planes at $\hat{\phi} = 0.85$.

the plate called *inter-vortex stream*. The interaction of the inter-vortex stream with the plate stagnates the flow and creates a region of high pressure. At minimum velocity, the pressure distribution on the front surface of the plate is equal to the surrounding fluid.

The outer span of the plate is shown in Fig. 7.7(b). The leading edge vortices are smaller, positioned away from the plate, and are asymmetrical. The asymmetry of the leading edge vortex suggests a break down of the tip vortex as indicated by the control volume analysis in Chapter. 5. These vortices still show flow stagnation near the plate's tip as marked by the high pressure region on the bottom surface of the plate. The pressure difference on both sections of the plate at $\hat{\phi} = 0.25$ produces an increase of torque even though the plate is at minimum velocity. However the maximum torque is reached

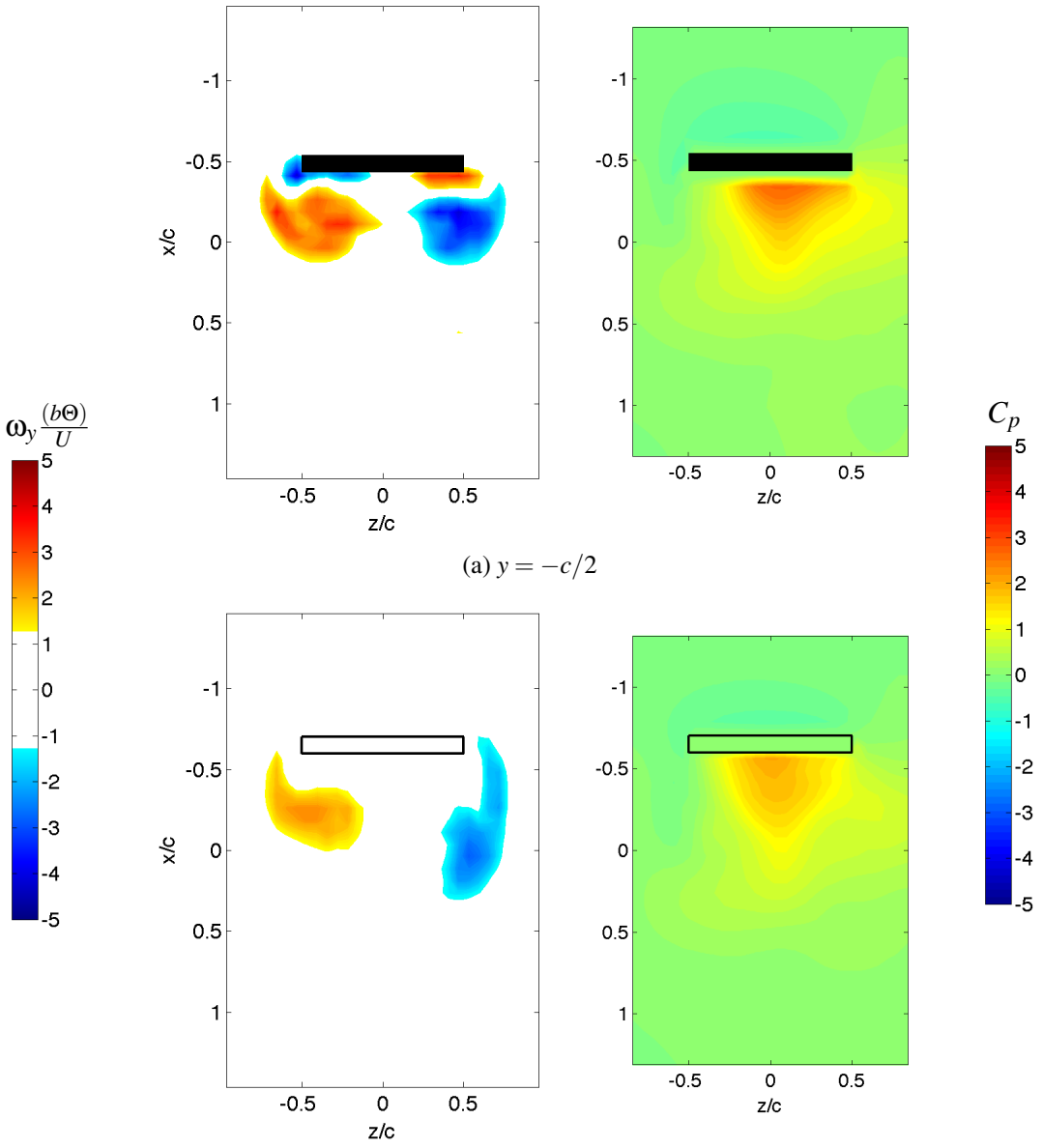

(a) $y = -c/2$

(b) $y = 0$

Figure 7.7: Vorticity ($\omega_y {}^{(b\Theta)}/_{U}$) and pressure ($C_p$) distribution at $\hat{\phi} = 0.25$.

at $\hat{\phi} = 0.35$.

At $\hat{\phi} = 0.35$, the plate is accelerating and the leading edge vortices are convected around the edge of the plate as shown in Fig. 7.8(a). The vortex from the up stroke

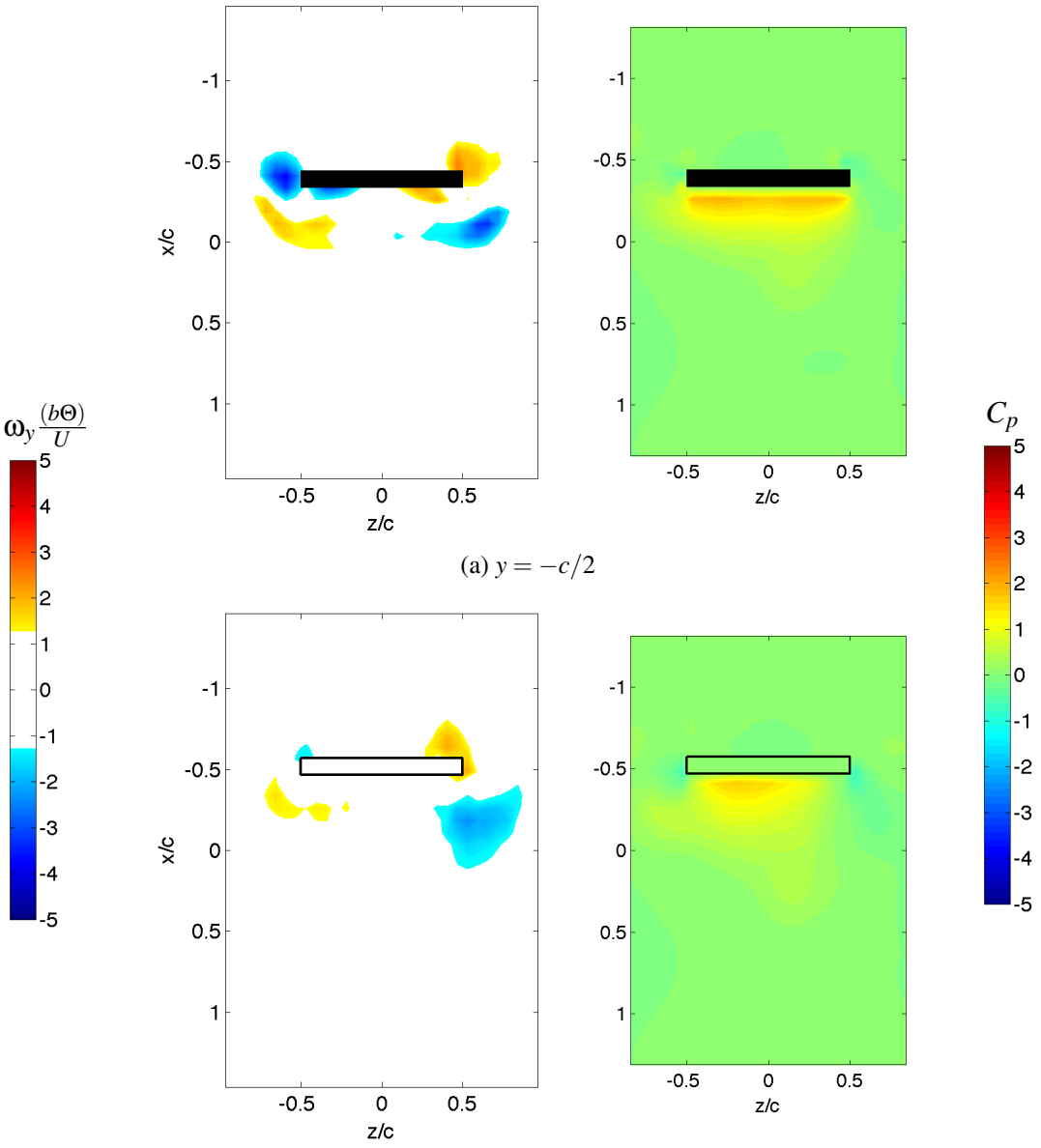

(a) $y = -c/2$

(b) $y = 0$

Figure 7.8: Vorticity ($\omega_y {}^{(b\Theta)}/_U$) and pressure ($C_p$) distribution at $\hat{\phi} = 0.35$.

is diffused and the secondary vortex is expanding rearward. At this phase angle, high pressure is distributed on the front facing surface of the plate for the full chord length of the plate. Because the vortices are being diffused the pressure distribution on the front

facing surface is largely due to flow stagnation because of the plate's motion. On the rear surface there is no difference with the ambient pressure due to weak vortices and how far apart they are positioned. These conditions create a large pressure difference between the surfaces of the plate, which increase the flapping torque.

Similar distribution of the vorticity with Fig. 7.8(a) at the outer span of the plate is produced as shown in Fig. 7.8(b). The leading edge vortices from the up stroke still exist on this section because they were located farther from the plate. The interaction of the vortices and the plate produces, on the front surface of the plate, pressure distribution that is smaller than the one in the inner span. The pressure difference on the surface of the plate at $\hat{\phi} = 0.35$ produces the maximum torque at the same phase angle in Fig. 7.2.

The vorticity distribution in Fig. 7.9(a) shows the growth of the leading edge vortices toward the rear of the plate. These vortices produce a pressure drop inside the core and two stagnation pressure points appear on the inside of the plate. A high pressure region on the front surface of the plate is also observed. The outer span of the plate in Fig. 7.9(b) shows the leading edge vortices growing simultaneously with the inner span of the plate. The pressure distribution also shows the pressure drop in the vortex core, two stagnation points, and large stagnation region on the front surface of the plate.

The high pressure region on the front facing surface of the plate is caused by flow stagnation related to the flapping motion as the plate's velocity increases. The two pressure stagnation points on the rear surface of the plate show how the surrounding fluid is induced by the vortices but, has not produced a single stream. The strength of the vortices and their position about one chord length apart produce two stagnation points on the surface of the plate. Because of the increase of pressure on the rear facing surface of the plate, the pressure difference on the plate's surfaces decreases and is depicted by the decrease of torque at $\hat{\phi} = 0.40$ in Fig. 7.2.

At the mid-point of the down stroke, $\hat{\phi} = 0.5$, where the acceleration is minimum and the plate is at maximum velocity, the leading edge vortices in Fig. 7.10(a) are stretched to the rear of the plate. These vortices are stronger and closer together than in Fig. 7.9(a). These conditions cause the stagnation point to converge about the center of the rear surface of the plate. The pressure distribution on the front surface of the plate remains unchanged. In Fig. 7.10(b), the vorticity distribution of the leading edge vortices con-

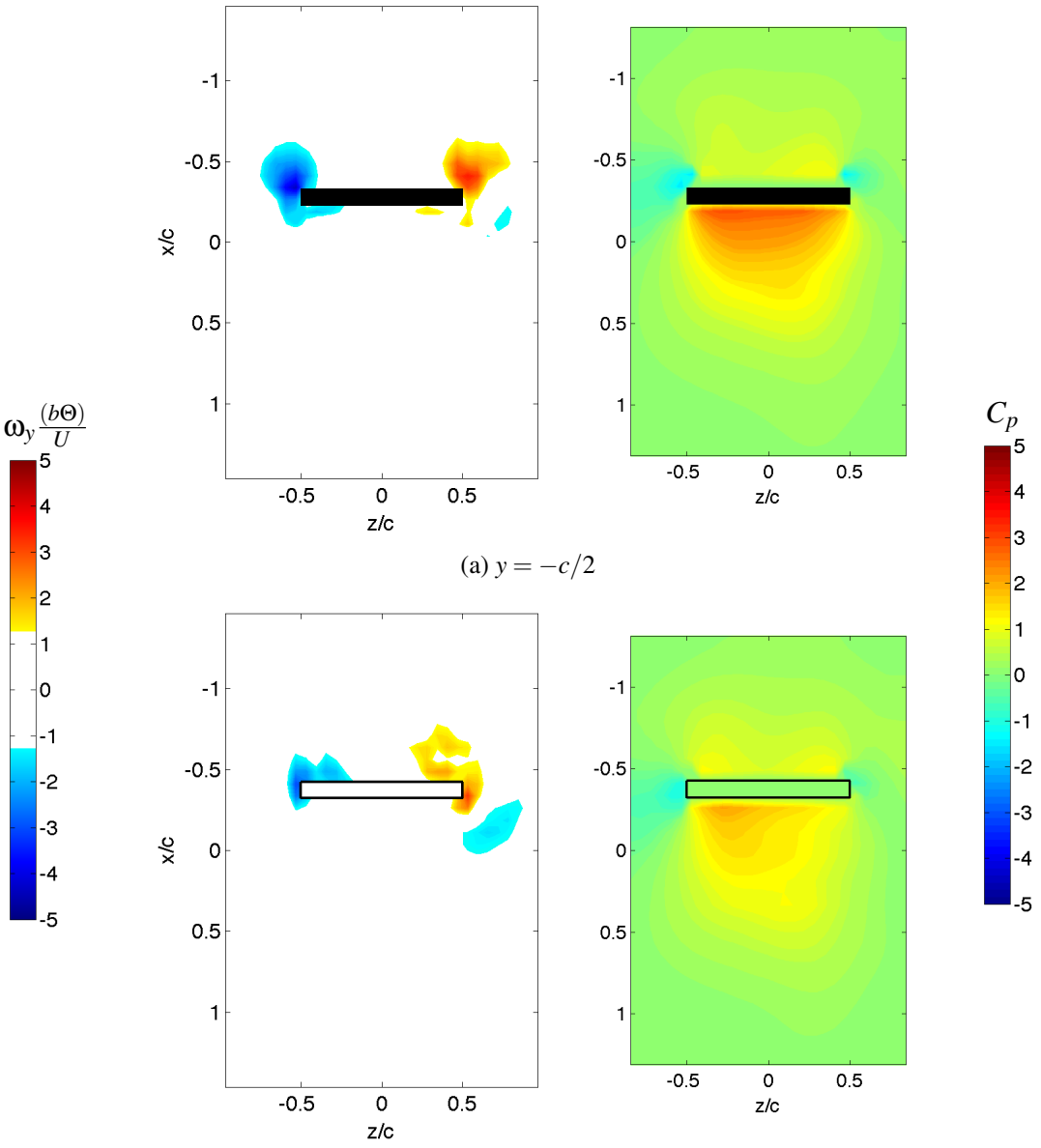

(a) $y = -c/2$

(b) $y = 0$

Figure 7.9: Vorticity ($\omega_y {}^{(b\Theta)}/_U$) and pressure ($C_p$) distribution at $\hat{\phi} = 0.40$.

verges at the center of the plate. These vortices are stretched rearward and show an approximately symmetrical structure. This vorticity distribution depicts the extension of the leading edge vortices to the tip vortex. The pressure distribution of this section

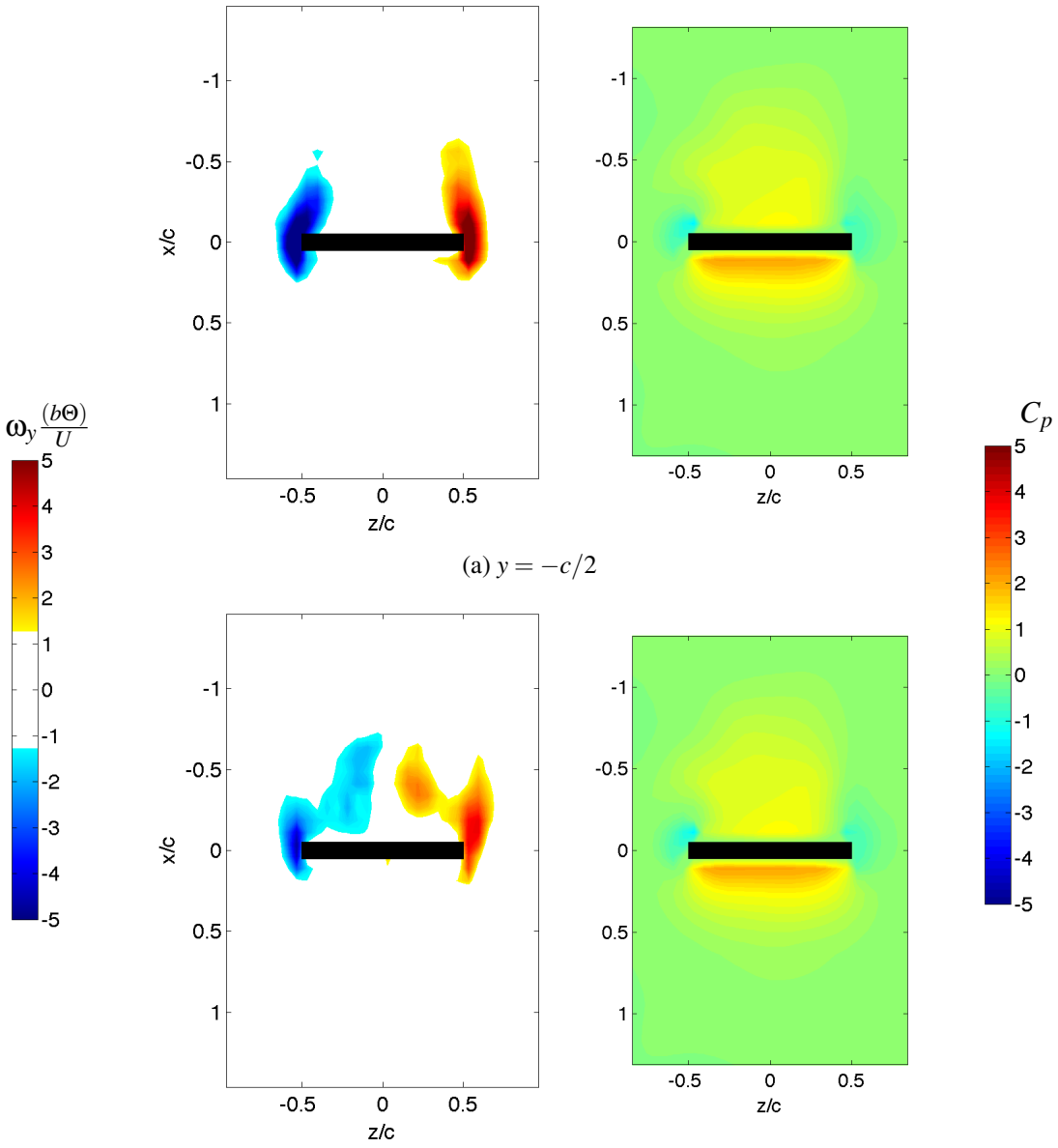

(a) $y = -c/2$

(b) $y = 0$

Figure 7.10: Vorticity ($\omega_y {}^{(b\Theta)}/_U$) and pressure ($C_p$) distribution at $\hat{\phi} = 0.50$.

is approximately similar to the inner section of the plate. The decrease of the pressure difference of the surface of the plate further decreases the torque at $\hat{\phi} = 0.50$ in Fig. 7.2.

The vorticity distribution during the deceleration of the plate in Fig. 7.11(a) shows

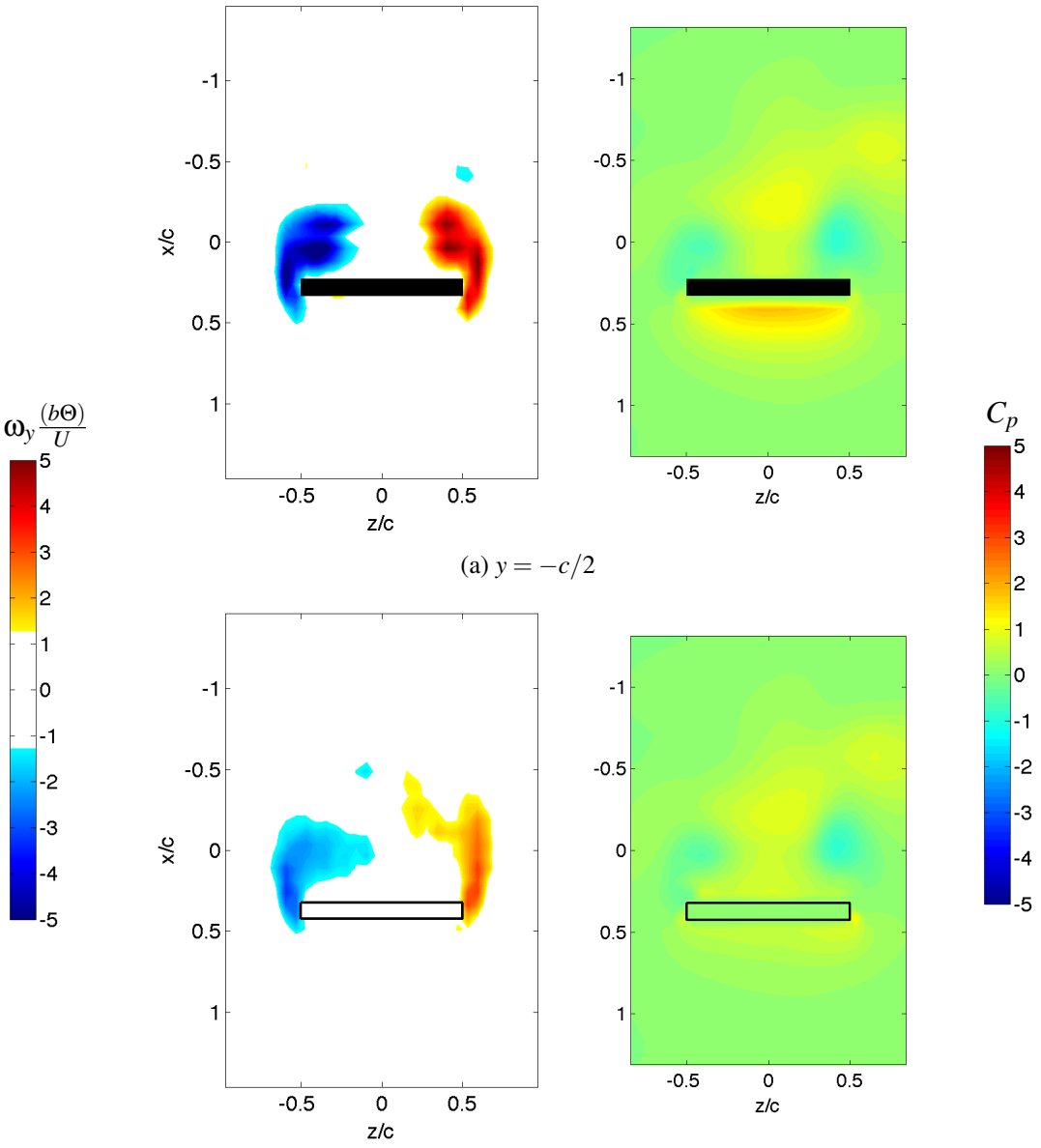

(a) $y = -c/2$

(b) $y = 0$

Figure 7.11: Vorticity ($\omega_y {}^{(b\Theta)}/_U$) and pressure ($C_p$) distribution at $\hat{\phi} = 0.60$.

an increase of the size of the leading edge vortices. These vortices are also located closer together. The pressure distribution still shows the stagnation on the front surface of the plate and a stagnation pressure region above the rear surface of the plate. Two regions

of lower pressure in the vortex cores are also observed on that surface.

At the outer span of the plate, the vorticity distribution in Fig. 7.11(b) shows the leading edge vortices develop into an asymmetric structure. The pressure distribution on this section shows a considerably small pressure difference between the front and rear surfaces. The stagnation pressure above the top surface also appears similar on the inner section. The conditions of the two sections of the flow at this phase angle shows a decrease in the pressure difference between the plate's surfaces. This translates into further decrease of the torque of the flapping axis at $\hat{\phi} = 0.60$ in Fig. 7.2.

The end of the down stroke in Fig. 7.12(a), $\hat{\phi} = 0.75$, the leading edge vortices separate from the plate. These vortices are about half a chord length in diameter. The interaction of the separated vortices with the plate induces the production of new vortices on the rear surface of the plate. The pressure distribution at this phase angle shows a stagnation region at the center of the rear surface of the plate and does not cover the full chord length of the plate. The pressure distribution on the front surface of the plate is equal to the surrounding fluid.

The outer span of the plate in Fig. 7.12(b) shows an asymmetric vortical structure and above the rear surface of the plate and the high pressure distribution is on the rear surface of the plate. The conditions on both sections are similar to the start of the downstroke shown in Fig. 7.12(a). Indeed Fig. 7.12 approximately mirrors Fig. 7.7.

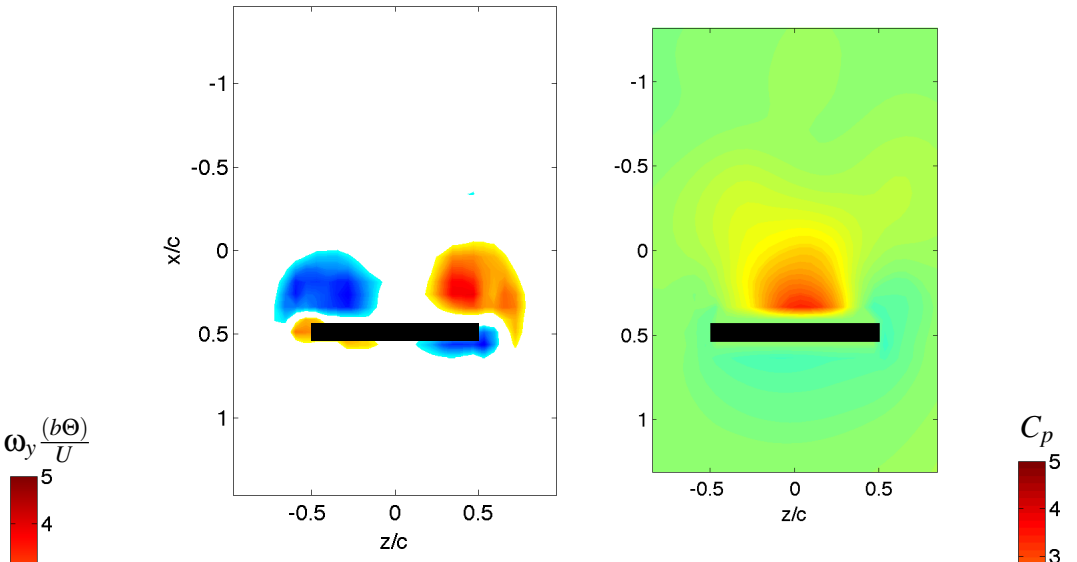

(a) $y = -c/2$

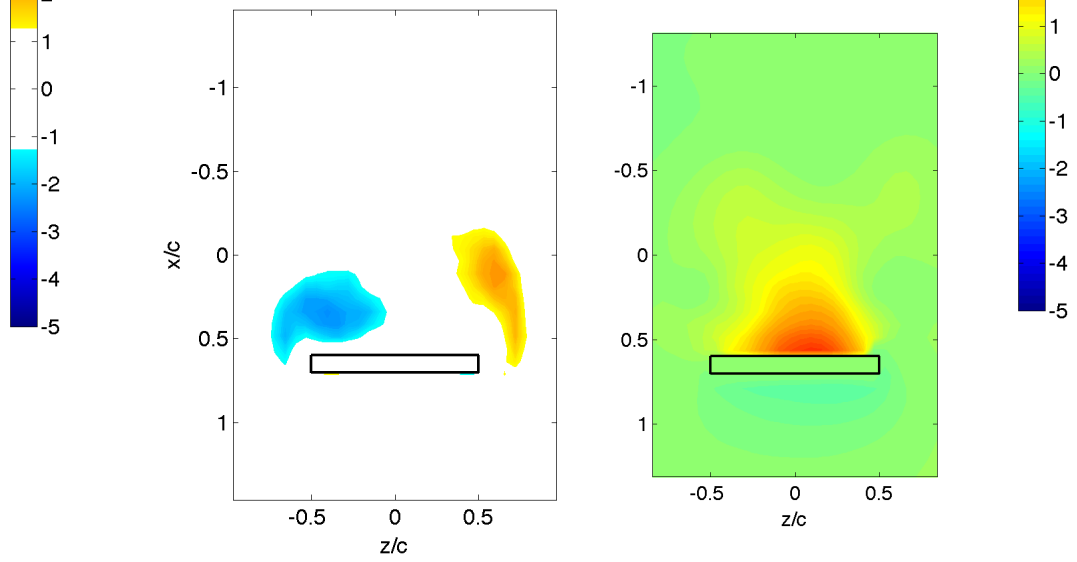

(b) $y = 0$

Figure 7.12: Vorticity ($\omega_y {}^{(b\Theta)}/_{U}$) and pressure ($C_p$) distribution at $\hat{\phi} = 0.75$.

7.2 Concluding remarks

Comparison of the estimation of torque by surface pressure integration and the torque measured by strain gauges show reasonable qualitative agreement with each other. The comparison shows similar amplitude but different phase between the two curves. The cause of the phase difference is the inaccuracy of the pressure distribution on the leading-edge of the plate due to the pressure estimation on the plane intersecting the leading-edge. This inaccuracy is due to the large discontinuity of the pressure field between the global and local mesh because of the improper boundary condition and spatial resolution to resolve the vortex flow. However, the torque calculated from the estimated pressure on the mid-chord plane shows no phase difference with the measured torque. This suggests that the torque can be estimated well by measuring the entire surface of the plate without intersecting the edge of the plate and with special attention taken to resolve the spatial resolution near the leading-edge.

The relation of the torque of the flapping axis with vorticity was investigated through several slices of the vorticity distribution and pressure distribution. It was found that the leading-edge vortices induce the surrounding fluid called the inter-vortex stream, which in this study produces flow moving towards the plate. The presence of rigid plate stagnates the inter-vortex stream and creates a region of high pressure on one side of the plate's surface. This condition dominates when the plate is at low velocity notably at the start of every new stroke.

After the initial start of the stroke flow stagnation appears on the front facing surface of the plate. The flow stagnates because of the plate moving through a quiescent fluid. The aerodynamic efficiency may be improved by setting the flapping wing at an acute angle of attack. In that configuration, the leading-edge vortex is diffused to middle of the rear facing surface of the plate limiting the stagnation pressure on that surface. Thereby, giving the pressure difference that benefits to the vertical component of the aerodynamic force.

Chapter 8

Conclusions

8.1 Concluding Remarks

The study investigates the relation of vorticity and pressure distribution in the case of flapping wing and the method to investigate the force of an actual micro-air vehicle. The flapping wing was simplified as a flapping plate with a sinusoidal motion with the flapping axis in the chordwise direction. Measurements were done using stereo PIV with multiple measurement planes offset along the out-of-plane direction of the measurement planes. Phase averaging of the velocity field of each discrete phase angles was used to present the evolution of the flow in one flapping cycle, one downstroke and one upstroke. The governing equations were decomposed into the averaged component and fluctuating component.

The flow was visualized by calculating the second invariance of the deformation tensor, $\langle Q \rangle$, which depicts the three dimensional structure of the vortex around the plate but does not visualize the dynamics of that structure. Additional information were visualized with streamlines for the regions where $\langle Q \rangle < 0$.

The control volume analysis provides the investigation tool to study the dynamics of vortex and structure interaction. The selection of control volume size for the force analysis enables the investigation of selected parts of the phase-averaged velocity field, which provides better understanding of the vortex structures that influences force generation. By properly selecting the size of the control volume, acceleration and convection

of the flow can be explained using their respective terms in the integral equation of fluid motion.

Force calculated by control volume analysis of the phase-averaged velocity field shows that the vortex attached to the surface of the plate plays a dominant role in the generation of the force. Delays reaching the maxima of the force magnitude are caused by the existence of the vortex structure of the previous stroke obstructing the motion of the plate. Increases in the extremes of the force due to the Reynolds number only appear in the unsteady term of the leading edge of the plate.

To estimate the pressure distribution on the surface of the plate, the Poisson equation was integrated in an overlapping mesh system. For the flapping plate, two meshes were used: global mesh in the inertial frame and local mesh constrained to the motion of the flapping plate. In the mid-chord of the plate, continuous pressure distribution with the global mesh was achieved along the boundaries of the local mesh. However on the edge of the plate, discontinuity of the pressure distribution is observed which may arise from the lack of spatial resolution in the out-of-plane distribution and the improper boundary condition because of the bend on the edge of the surface of the plate.

The pressure field on the xz-plane shows the spanwise sections of the flow generated by a flapping plate. The pressure field was solved only for the global mesh because the measurement planes are not orthogonal to the surface of the plate for all phase angles except for $\hat{\phi} = 0$ and $\hat{\phi} = 0.5$.

Comparison of the estimation of the torque by surface pressure integration and the torque measured by strain gauges shows reasonable qualitative agreement of each other. The two torques have similar amplitudes but different phases. The phase difference is due to the pressure distribution on the leading edge of the plate, which is inaccurate due to improper boundary condition and lack of spatial resolution in the measurement of the vortex flow. However, the torque calculated from the estimated pressure on the mid-chord plane shows no phase difference with the measured torque. This suggest that the torque can be estimated well by measuring the entire surface of the plate without intersecting the edge of the plate and by improving the spatial accuracy along the out-of-plane direction.

The relation of the torque of the flapping axis with vorticity was investigated through

several slices of the vorticity distribution and pressure distribution. It was found that the leading edge vortices induce the surrounding fluid which produces a part of the flow moving between the vortices called inter-vortex stream. In this study the inter-vortex stream moves toward the plate. The presence of rigid plate stagnates the inter-vortex stream and creates a region of high pressure on one side of the plate's surface. This condition dominates when the plate is at low velocity notably at the start of every new stroke.

8.2 Recommendations

Measurements were done by manually traversing the measurement plane along the out-of-plane direction of the measurement plane or the chordwise direction of the plate. For control volume analysis, the high spatial resolution of the plate is not important because the integral equation is not a function of the velocity spatial gradient. In the estimation of pressure field, the spatial resolution must be resolved adequately. The estimation of pressure field can benefit from the volumetric measurement using more advanced PIV measurement methods such as tomographic or holographic PIV.

Qualitative agreement between the torque curves as estimated by surface pressure integration and strain gauge measurements shows that the pressure estimation method can be used to estimate the forces of a small mechanical device such as an MAV. In this study, further improvements of the estimation of the force of the flapping plate can be done by measuring for the full surface of the plate without intersecting the edge of the plate.

After the initial start of the stroke flow stagnation appears on the front surface of the plate. The flow stagnates because of the plate moving through a quiescent fluid. Aerodynamic efficiency may be improved by setting the flapping wing at an acute angle of attack. In that configuration, the leading-edge vortex is diffused to the middle of the rear surface of the plate limiting the stagnation pressure on that surface.

The author recognizes that certain aspects of this study are not perfect but hopes that the results can help the understanding of the dynamics of flow generated by a flapping wing.

Bibliography

Ansari SA, Phillips N, Stabler G, Wilkins PC, Zbikowski R, Knowles K (2009) Experimental investigation of some aspects of insect-like flapping flight aerodynamics for application to micro air vehicles. Experiments in Fluids 46:777 – 798

Azuma A (1992) The biokinetics of flying and swimming. American Institute of Aeronautics and Astronautics, Springer-Verlag New York

Azuma A, Azuma S, Watanabe I, Furuta T (1985) Flight mechanics of a dragonfly. Journal of Experimental Biology (116):79 – 107

Bandyoypadhyay PR (2009) Swimming and flying in nature – the route toward applications: the freeman scholar lecture. Journal of Fluids Engineering 131:031,801

Bendat JS, Piersol AG (2000) Random Data: Analysis and Measurement Procedures, 3rd edn. John Wiley & Sons, Inc.

van den Berg C, Ellington C (1997) The vortex wake of a'hovering'model hawkmoth. Philosophical Transactions of the Royal Society B: Biological Sciences 352(1351):317

Bernard P, Wallace J (2002) Turbulent flow: analysis, measurement, and prediction. John Wiley & Sons, Inc.

Betz A (1912) Ein Beitrag zur Erklaerung des Segelfluges. Zeitschrift fuer Flugtechnik und Motorluftschiffahrt 3:269–270

Bevington PR (1969) Data reduction and error analysis for the physical sciences. McGraw-Hill

Birch J, Dickinson M (2001) Spanwise flow and the attachment of the leading-edge vortex on insect wings. Nature 412(6848):729–733

Birch JM, Dickson WB, Dickinson MH (2004) Force production and flow structure of the leading edge vortex on flapping wings at high and low reynolds numbers. J Exp Biol 207(7):1063–1072

Bomphrey R, Lawson N, Harding N, Taylor G, Thomas A (2005) The aerodynamics of Manduca sexta: digital particle image velocimetry analysis of the leading-edge vortex. The Journal of experimental biology 208(Pt 6):1079

Coleman H, Steele W (1995) Engineering application of experimental uncertainty analysis. AIAA Journal 33:1888–1896

Cooper Instruments (2007) LQB 630 - Thin film load cell. URL http://cooperinst.thomasnet.com/Asset/LQB630.pdf

Coudert S, Schon J (2001) Back-projection algorithm with misalignment corrections for 2D3C stereoscopic PIV. Measurement science and technology 12(9):1371–1381

David L, Jardin T, Farcy A (2009) On the non-intrusive evaluation of fluid forces with the momentum equation approach. Measurement Science and Technology 20:095,401, DOI doi:10.1088/0957-0233/20/9/095401

Dickinson MH, Lehmann FO, Sane SP (1999) Wing rotation and the aerodynamic basis of insect flight. Science 284(5422):1954 – 1960

Ellington C (1984) The aerodynamics of hovering insect flight. Philosophical Transaction of the Royal Society of London Series B, Biological Sciences 305(1122):1 – 181

Ellington CP, Berg CVD, Willmott AP, Thomas AL (1996) Leading-edge vortices in insect flight. Nature (384):626 – 630

Foo L (2001) Nikon PC-Micro Nikkor 85mm f/2.8 D Special Perspective Control Close up application telephoto lens. URL http://www.mir.com.my/rb/photography/companies/nikon/nikkoresources/PC_Nikkor/index5.htm

Fujisawa N, Tanahashi S, Srivinas K (2005) Evaluation of pressure field and fluid forces on a circular cylinder with and without rotational oscillation using velocity data from PIV measurement. Measurement Science and Technology (16):989–996

Guglielmini L, Blondeaux P (2004) Propulsive efficiency of oscillating foils. European Journal of Mechanics-B/Fluids 23(2):255–278

Haddab Y, Chen Q, Lutz P (2009) Improvement of strain gauges micro-forces measurement using Kalman optimal filtering. Mechatronics 19(4):457–462

Heathcote S, Gursul I (2007) Jet switching phenomenon for a periodically plunging airfoil. Physics of Fluids 19:027,104

Heathcote S, Martin D, Gursul I (2004) Flexible flapping airfoil propulsion at zero freestream velocity. AIAA journal 42(11)

Heathcote S, Wang Z, Gursul I (2008) Effect of spanwise flexibility on flapping wing propulsion. Journal of Fluids and Structures 24(2):183–199

Ho S, Nassef H, Pornsinsirirak N, Tai Y, Ho C (2003) Unsteady aerodynamics and flow control for flapping wing flyers. Progress in Aerospace Sciences 39(8):635–681

Ishihara Sangyo Kaisha (2006) Titanium dioxide hollow microspheres, nst-b1. URL `www.iskweb.co.jp/eng/research/pdf/nst-b1_tf-4.pdf`

Jardin T, David L, Farcy A (2009) Characterization of vortical structures and loads based on time-resolved PIV for asymmetric hovering flapping flight. Experiments in Fluids 46(5):847 – 857, DOI 10.1007/s00348-009-0632-7

Jones K, Platzer M (1997) Numerical computation of flapping-wing propulsion and power extraction. AIAA paper pp 97–0826

Jones K, Dohring C, Platzer M (1998) Experimental and computational investigation of the knoller-betz effect. AIAA Journal 36(7):1240–1246

Jones KD, Platzer MF (2009) Design and development considerations for biologically inspired flapping-wing micro air vehicles. Experiments in Fluids 46:799 – 810

Jones KD, Duggan SJ, Platzer MF (2001) Flapping-wing propulsion for a micro air vehicle. AIAA Paper 126

de Kat R, Oudheusden BWV, Scarano F (2008) Instantaneous planar pressure field determination around a square-section cylinder based on time-resolved stereo-piv. In: 14th Int. Symp. on Application of Laser Techniques to Fluid Mechanics, pp 6–11

Keyence Corporation (2006) High-speed, high-accuracy CCD Laser Displacement Sensor LK-G Series User's Manual. Keyence Corporation, 1-3-14, Higashi-Nakajima, Higashi-Yodogawa-ku, Osaka, 533-8555, Japan.

Knoller R (1909) Die gesetze des luftwiderstandes. Flug-und Motortechnik (Wien) 3(21):1–7

Kyowa Electronic Instruments Co, Ltd (2004) DPM-700B series user manual. Kyowa Electronic Instruments Co., Ltd., 3-5-1, Chofugaoka, Chofu, Tokyo 182-8520, Japan

Kyowa Electronic Instruments Co, Ltd (2010a) How to form strain-gage bridges. http://www.kyowa-ei.co.jp/english/products/gages/index.htm, 3-5-1, Chofugaoka, Chofu, Tokyo 182-8520, Japan

Kyowa Electronic Instruments Co, Ltd (2010b) micro-strain measuring gages. http://www.kyowa-ei.co.jp/english/products/gages/mmg.htm, 3-5-1, Chofugaoka, Chofu, Tokyo 182-8520, Japan

Lai JC, Platzer MF (1999) Jet characteristics of a plunging airfoil. AIAA Journal 37(12):1529–1537

Lai JC, Platzer MF (2000) Characteristics of a plunging airfoil at zero freestream velocity. American Institute of Aeronautics and Astronautics 39(3):531–534

Lehmann F, Sane S, Dickinson M (2005) The aerodynamic effect of wing-wing interaction in flapping insect wings. Journal of Experimental Biology 208(16):3075

Mao S, Xin Y (2003) Flows around two airfoils performing fling and subsequent translation and translation and subsequent clap. Acta Mechanica Sinica 19(2):103–117

Masuda S (2006) Lecture notes in physical model of turbulence

McMichael JM, Francis MS (1997) Micro Air Vehicles – Toward A New Dimension In Flight. URL `http://www.fas.org/irp/program/collect/docs/mav_auvsi.htm`

Miller LA, Peskin CS (2005) A computational fluid dynamics of 'clap and fling' in the smallest insects. J Exp Biol 208(2):195–212, DOI 10.1242/jeb.01376

Mu-lin C, Wen-bo M, Chang-sheng Z (2006) Numerical simulation of insect flight. Applied Mathematics and Mechanics 27(5):601 – 606

National Instruments Co (1999) DAQ:6601/6602 User Manual. National Instruments Co., 11500 North Mopac ExpresswayAustin, Texas 78759-3504

National Instruments Co (2000) Data Acquisition Basics Manual. National Instruments Co., 11500 North Mopac ExpresswayAustin, Texas 78759-3504

National Instruments Co (2001) IMAQ PCI/PXI 1422 User Manual. National Instruments Co., 11500 North Mopac Expressway Austin, Texas 78759-3504

National Instruments Co (2006) Motion Control. National Instruments Co., 11500 North Mopac Expressway. Austin, Texas. 78759-3504. USA

National Instruments Co (2009) What is rtsi and how is it configured? URL `http://digital.ni.com/public.nsf/allkb/A120195AAAA9222A86256C69007C8B27`

National Instruments Co (2010) Universal Motion Interface (UMI)-7664. National Instruments Co., 11500 North Mopac Expressway Austin, Texas 78759-3504

New Wave Research (2003) Solo PIV Nd:YAG Laser System Operator's Manual. New Wave Research, 48660 Kato Road Freemont California 94538

Obi S, Tokai N (2006) The pressure–velocity correlation in oscillatory turbulent flow between a pair of bluff bodies. International Journal of Heat and Fluid Flow 27(5):768–776

Oriental Motor Co, Ltd (2002) RK Series Operating Manual. Oriental Motor Co., Ltd, 6-16-17 Ueno, Taito-ku, Tokyo, Japan

van Oudheusden B, Scarano F, Roosenboom E, Casimiri E, Souverein L (2007) Evaluation of integral forces and pressure fields from planer velocimetry data for incompressible and compressible flow. Experiments in Fluids 43(2):153–162

Platzer MF, Jones KD, Young J, Lai JC (2008) Flapping-wing aerodynamics: progress and challenges. AIAA Journal 46(9):2136–2159

Poelma C, Dickson W, Dickinson M (2006) Time-resolved reconstruction of the full velocity field around a dynamically-scaled flapping wing. Exp Fluids 41:213–225

Pope S (2000) Turbulent flows. Cambridge Univ Pr

Prasad AK (2000) Stereoscopic particle image velocimetry. Experiments in Fluids 29(2):103 – 116

Redlake MASD, Inc (2001) The Megaplus Model ES 1.0 Series Cameras User's Manual. Redlake MASD, Inc, Redlake MASD, Inc. 11633 Sorrento Valley Road San Diego, California 92121-1097

Ringuette M, Milano M, Gharib M (2007) Role of the tip vortex in the force generation of low-aspect-ratio normal flat plates. Journal of Fluid Mechanics 581:453–468

Sane SP, Dickinson MH (2001) The control of flight force by a flapping wing: lift and drag production. J Exp Biol 204:2607 – 2626

Sane SP, Dickinson MH (2002) The aerodynamic effects of wing rotation and a revised quasi-steady model of flapping flight. Journal of Experimental Biology 205(8):1087–1096

Sane SP, Jacobson NP (2006) Induced airflow in flying insects ii. measurement of induced flow. J Exp Biol 209(Pt 1):43–56, DOI 10.1242/jeb.01958

Shapiro S, Wilk M (1965) An analysis of variance test for normality (complete samples). Biometrika Trust 52(3 - 4):591 – 611

Shyy W, Berg M, Ljungqvist D (1999) Flapping and flexible wings for biological and micro air vehicles. Progress in Aerospace Sciences 35(5):455–505

Soloff S, Adrian R, Liu Z (1997) Distortion compensation for generalized stereoscopic particle image velocimetry. Measurement science and technology 8(12):1441 – 1454

Spedding GR, Hedenström A (2009) PIV-based investigations of animal flight. Experiments in Fluids 46(5):749–763, DOI 10.1007/s00348-008-0597-y

Srygley R, Thomas A (2002) Unconventional lift-generating mechanisms in free-flying butterflies. Nature 420(6916):660–664

Steltz E, Wood R, Avadhanula S, Fearing R (2006) Characterization of the micromechanical flying insect by optical position sensing. In: Robotics and Automation, 2005. ICRA 2005. Proceedings of the 2005 IEEE International Conference on, IEEE, pp 1252–1257

Sudhakar Y, Vengadesan S (2010) The Functional Significance of Delayed Stall in Insect Flight. Numerical Heat Transfer, Part A: Applications 58(1):65–83

Sun M, Lan SL (2004) A computational study of the aerodynamic forces and power requirement of dragonfly (aeschna juncea) hovering. J Exp Biol 207(11):1887 – 1901

Sun M, Tang J (2002) Unsteady aerodynamic force generation by a model fruit fly wing in flapping motion. Journal of experimental biology 205(1):55–70

Sunada S, Hatayama Y, Tokutake H (2010) Pitch, Roll, and Yaw Damping of a Flapping Wing. AIAA Journal 48(6):1261–1265

Tobalske BW (2009) Symmetry in turns. Science 324:190 – 191

Tsai B, Fu Y (2009) Design and aerodynamic analysis of a flapping-wing micro aerial vehicle. Aerospace Science and Technology 13(7):383–392

Unal M, Lin J, Rockwell D (1997) Force prediction by PIV imaging: a momentum-based approach. Journal of Fluids and Structures 11(8):965–971

Van Den Berg C, Ellington C (1997) The three-dimensional leading-edge vortex of a'hovering'model hawkmoth. Philosophical Transactions of the Royal Society B: Biological Sciences 352(1351):329

Wang ZJ (2000) Vortex shedding and frequency selection in flapping flight. J Fluid Mech 410:323–341

Wang ZJ (2001) Computation of insect hovering. Mathematical Methods In The Applied Sciences 24(17-18):1515–1521

Wang ZJ (2004) The role of drag in insect hovering. J Exp Biol 207(Pt 23):4147–4155, DOI 10.1242/jeb.01239

Westerweel J, Dabiri D, Gharib M (1997) The effect of a discrete window offset on the accuracy of cross-correlation analysis of digital PIV recording. Experiments in Fluids 23(1):20–28

Willert C (1997) Stereoscopic digital particle image velocimetry for application in wind tunnels. Measurement Science and Technology 8(12):1465 – 1479

Willert C, Gharib M (1991) Digital particle image velocimetry. Experiments in fluids 10(4):181–193

Willmott A, Ellington C, Thomas A (1997) Flow visualization and unsteady aerodynamics in the flight of the hawkmoth, Manduca sexta. Philosophical Transactions of the Royal Society B: Biological Sciences 352(1351):303

Wood R, Fearing R (2001) Flight force measurements for a micromechanical flying insect. In: Proceeding of the 2001 IEEE/RSJ, International Conference on Intelligent Robots and Systems

Wu JH, Sun M (2004) unsteady aerodynamics forces of a flapping wing. J Exp Biol 207(7):1137 – 1150

Zang W, Prasad A (1997) Performance evaluation of a Scheimpflug stereocamera for particle image velocimetry. Applied optics 36(33):8738–8744

Appendix A

Visualization Results

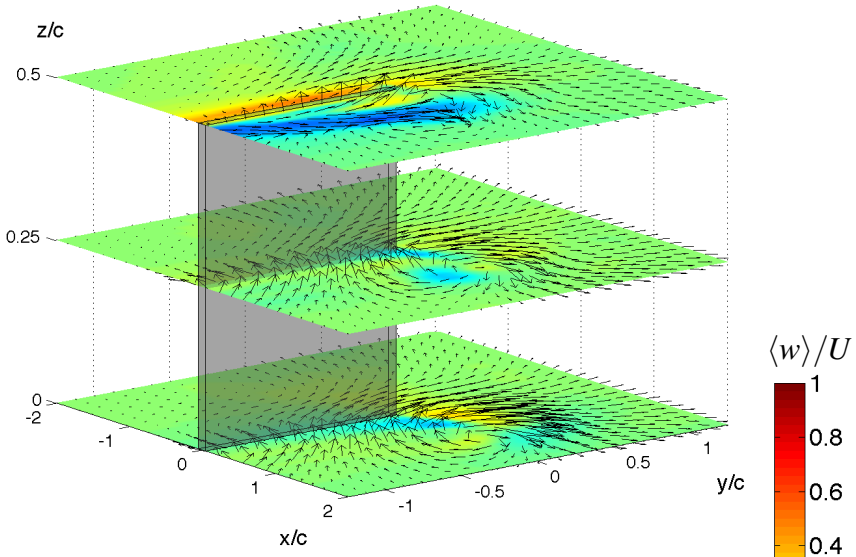

(a) $\hat{\phi} = 0$

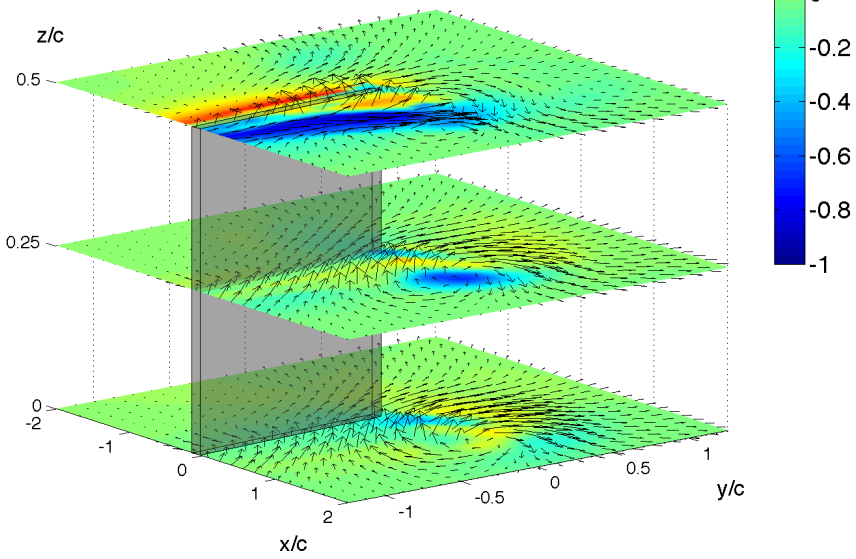

(b) $\hat{\phi} = 0.05$

Figure A.1: Velocity distributions on $z/c = [0, 0.25, 0.5]$, Re=1580. (*Continued*)

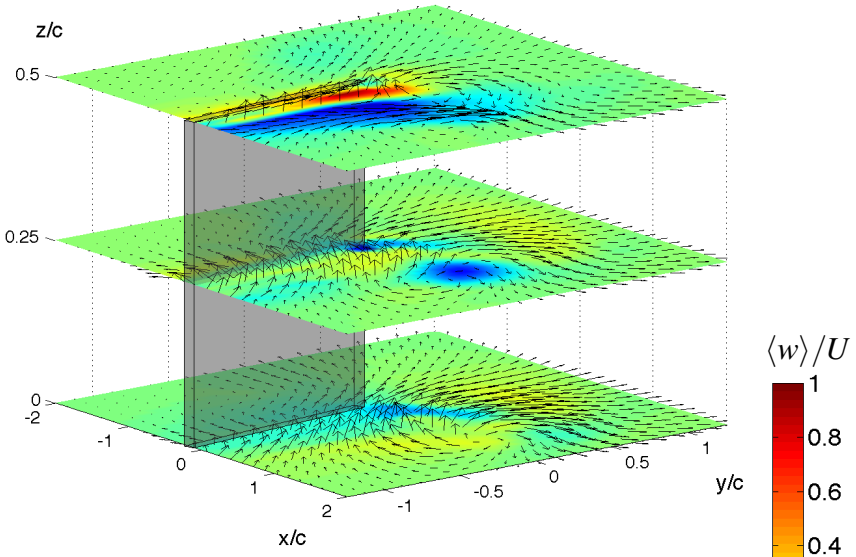

(c) $\hat{\phi} = 0.1$

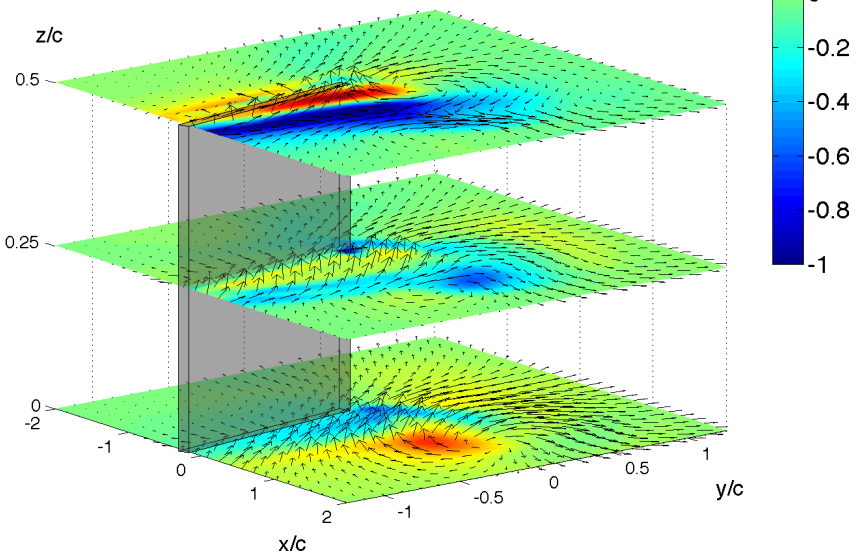

(d) $\hat{\phi} = 0.15$

Figure A.1: Velocity distributions on $z/c = [0, 0.25, 0.5]$, Re=1580. (*Continued*)

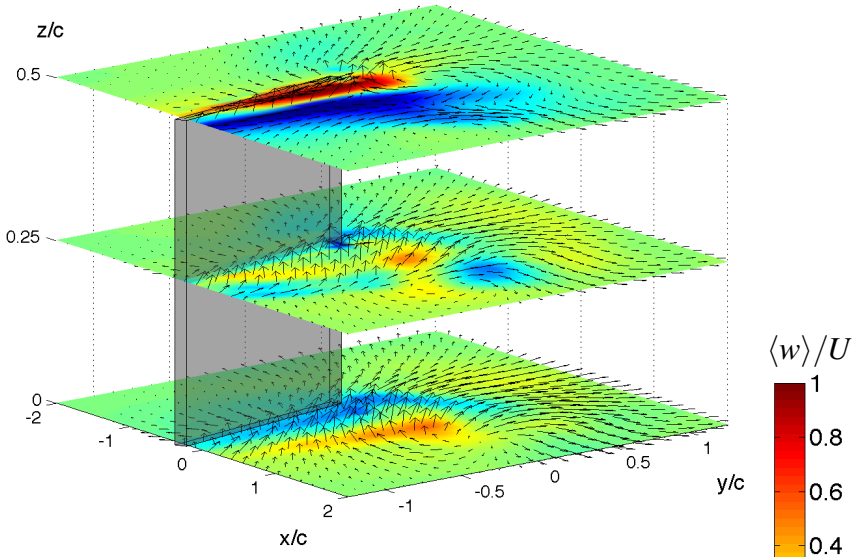

(e) $\hat{\phi} = 0.2$

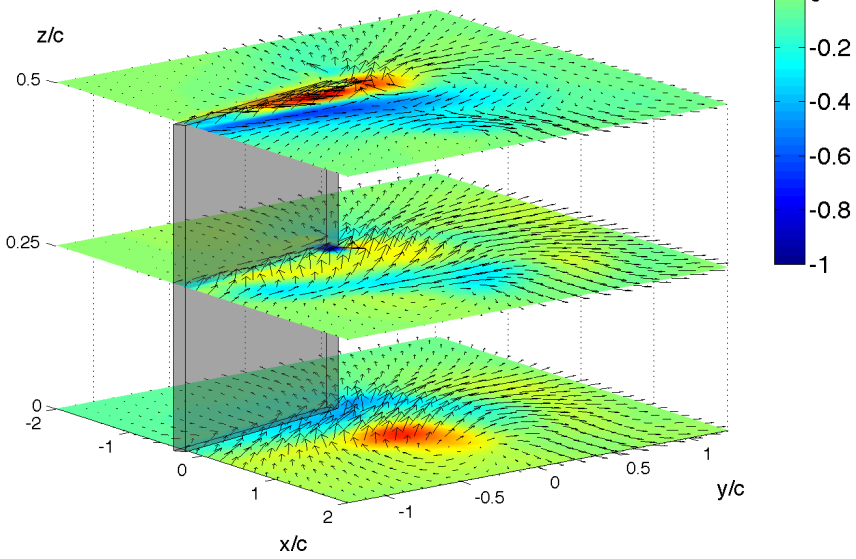

(f) $\hat{\phi} = 0.25$

Figure A.1: Velocity distributions on $z/c = [0, 0.25, 0.5]$, Re=1580. (*Continued*)

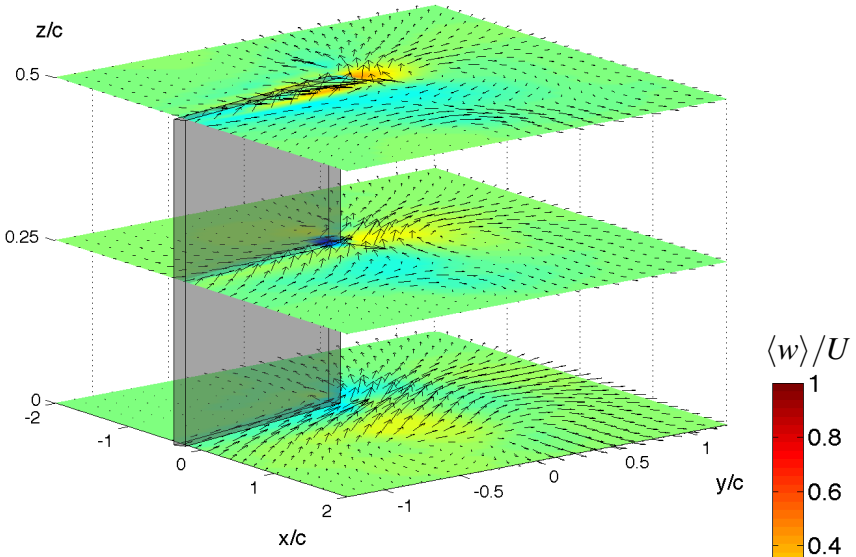

(g) $\hat{\phi} = 0.3$

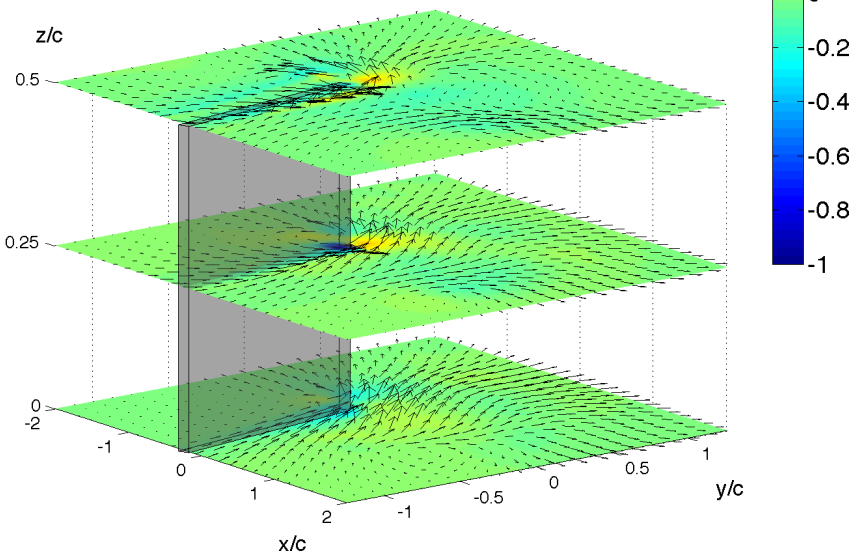

(h) $\hat{\phi} = 0.35$

Figure A.1: Velocity distributions on $z/c = [0, 0.25, 0.5]$, Re=1580. (*Continued*)

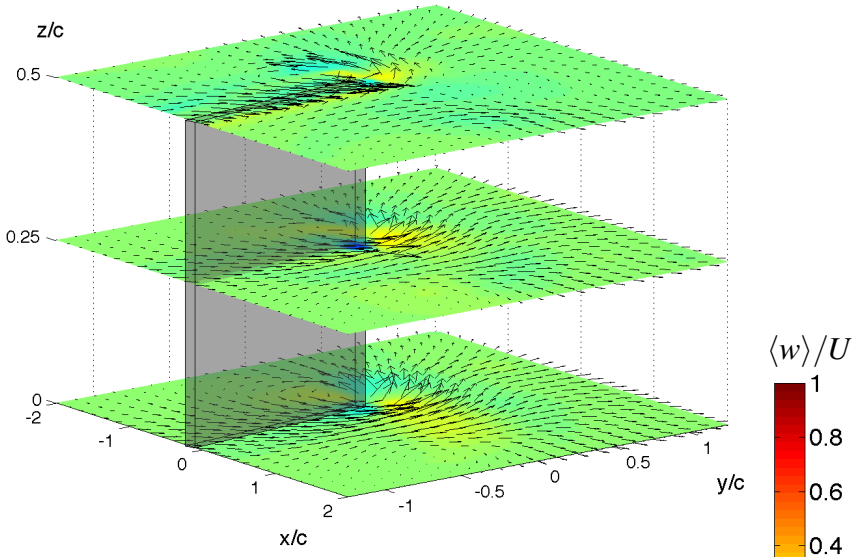

(i) $\hat{\phi} = 0.4$

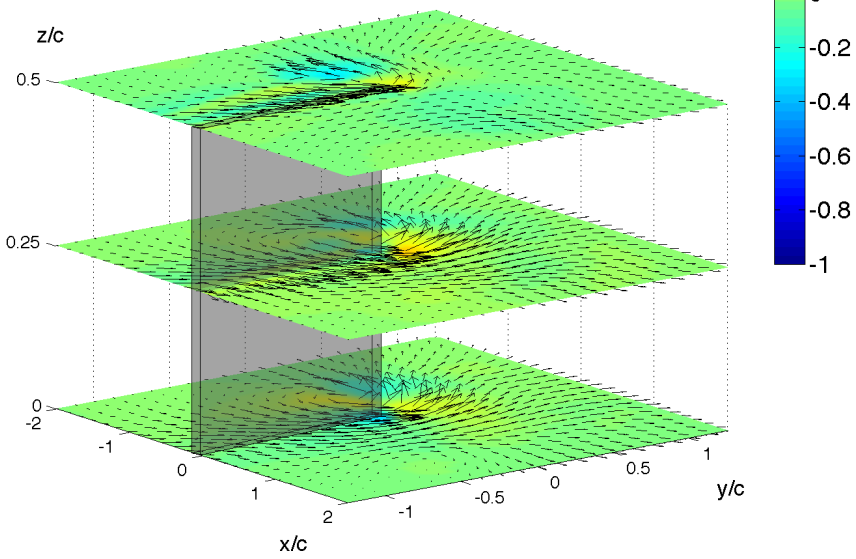

(j) $\hat{\phi} = 0.45$

Figure A.1: Velocity distributions on $z/c = [0, 0.25, 0.5]$, Re=1580. (*Continued*)

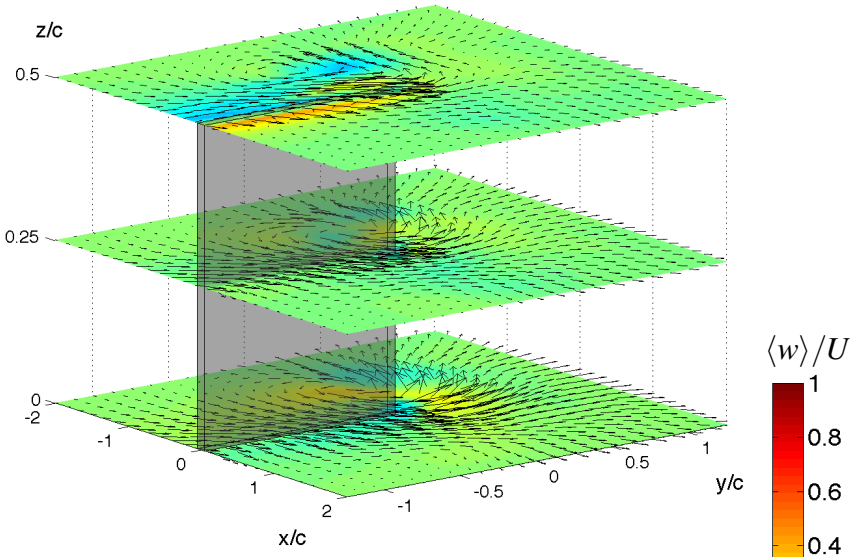

(k) $\hat{\phi} = 0.5$

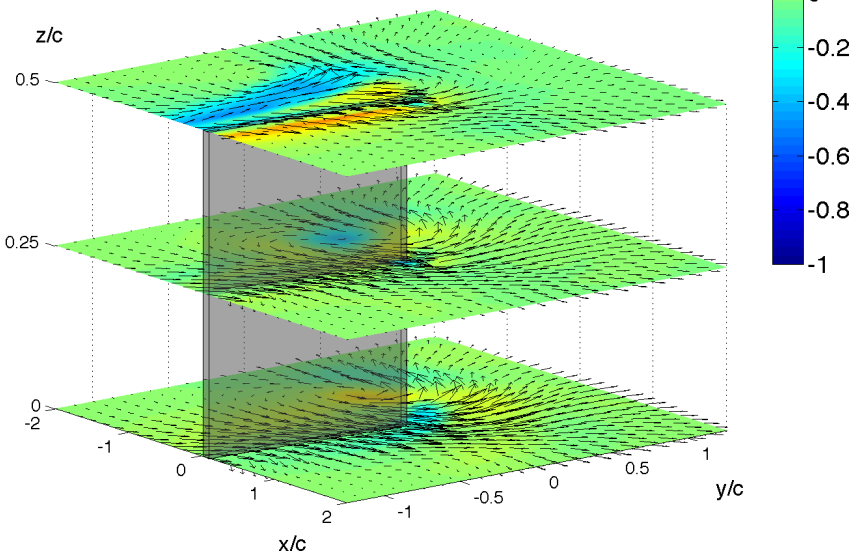

(l) $\hat{\phi} = 0.55$

Figure A.1: Velocity distributions on $z/c = [0, 0.25, 0.5]$, Re=1580. (*Continued*)

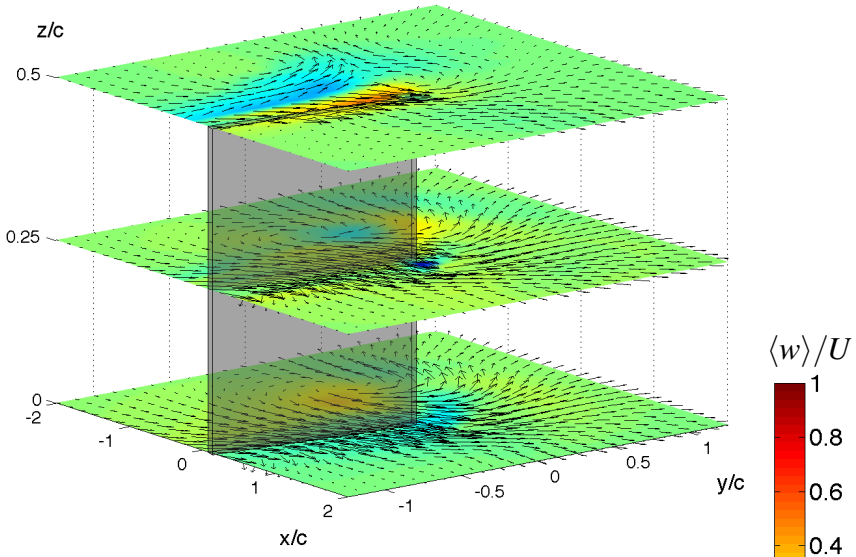

(m) $\hat{\phi} = 0.6$

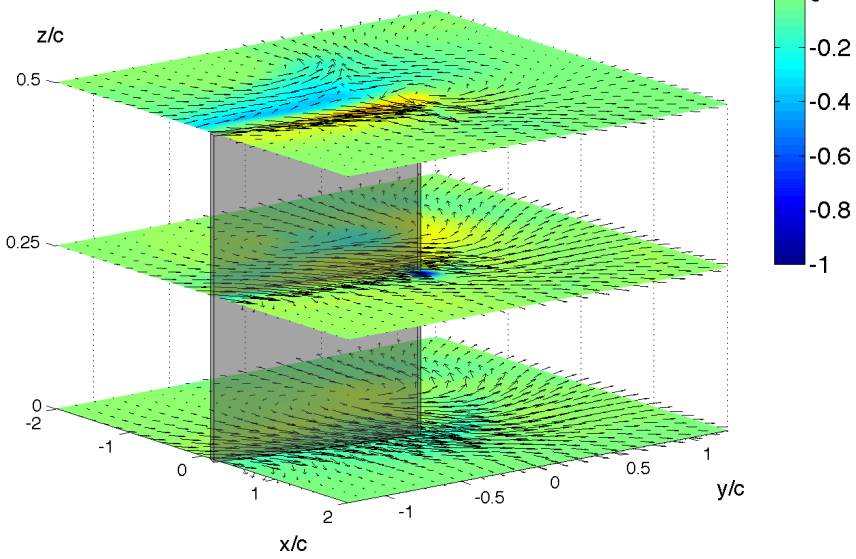

(n) $\hat{\phi} = 0.65$

Figure A.1: Velocity distributions on $z/c = [0, 0.25, 0.5]$, Re=1580. (*Continued*)

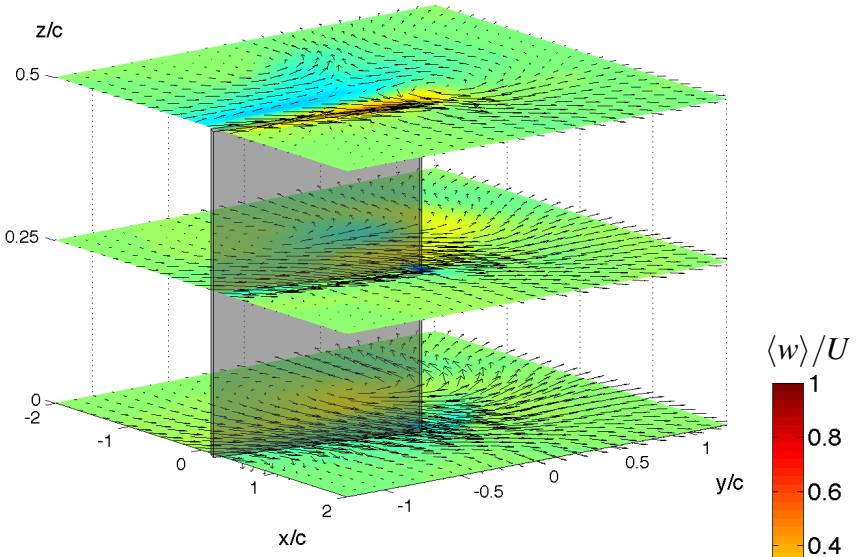

(o) $\hat{\phi} = 0.7$

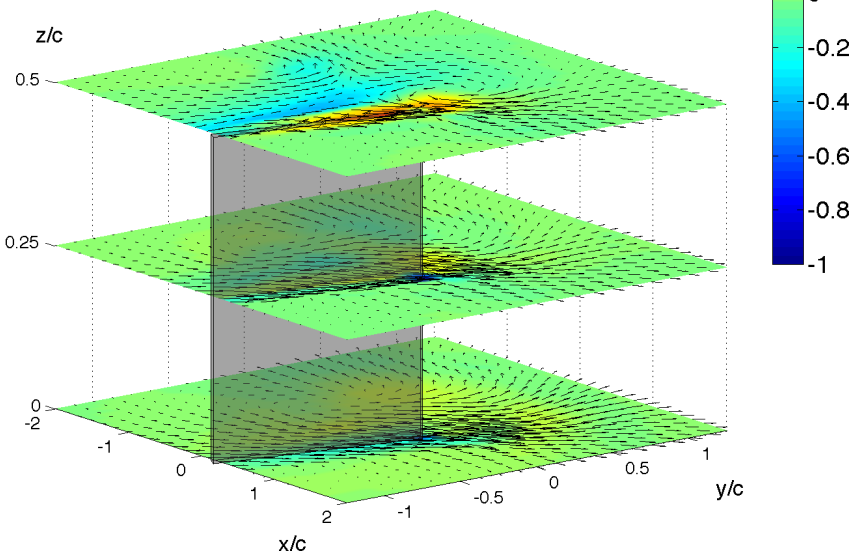

(p) $\hat{\phi} = 0.75$

Figure A.1: Velocity distributions on $z/c = [0, 0.25, 0.5]$, Re=1580. (*Continued*)

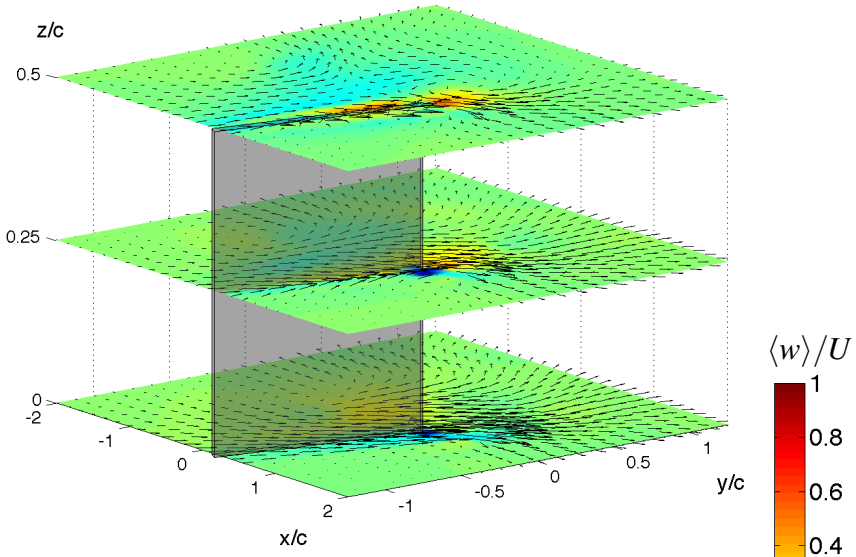

(q) $\hat{\phi} = 0.8$

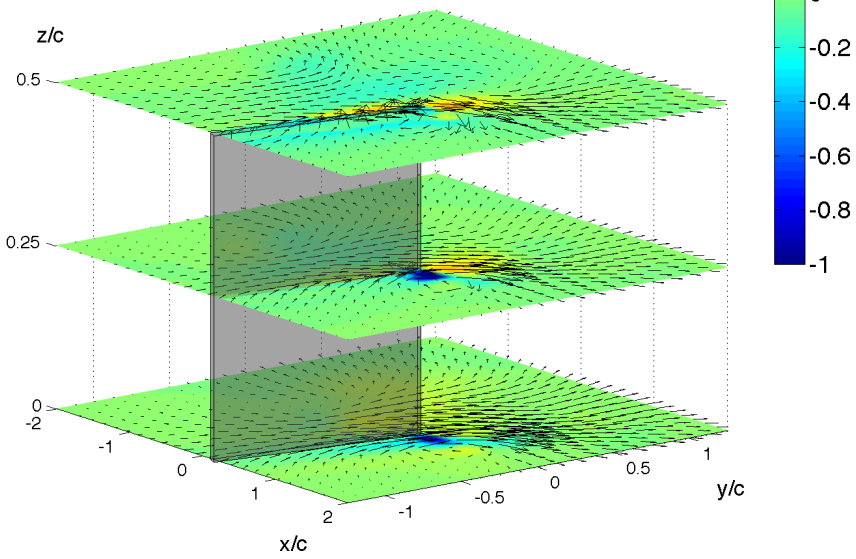

(r) $\hat{\phi} = 0.85$

Figure A.1: Velocity distributions on $z/c = [0, 0.25, 0.5]$, Re=1580. (*Continued*)

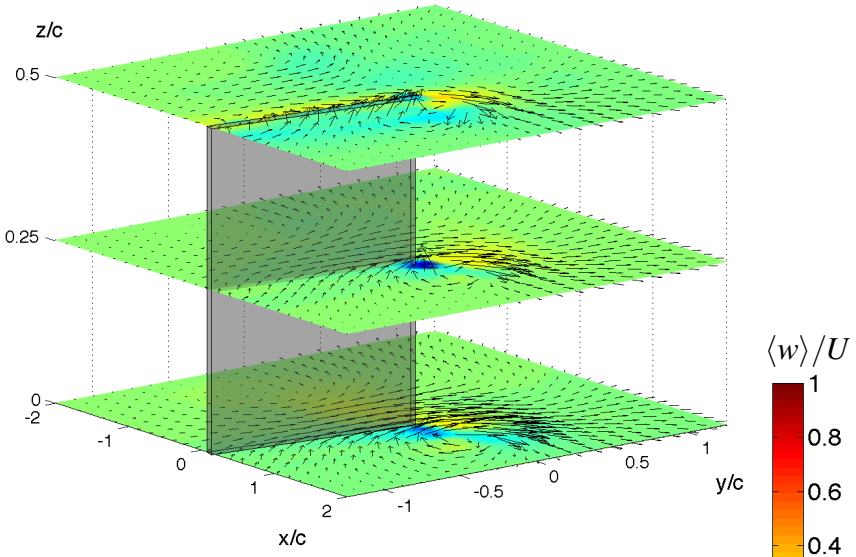

(s) $\hat{\phi} = 0.9$

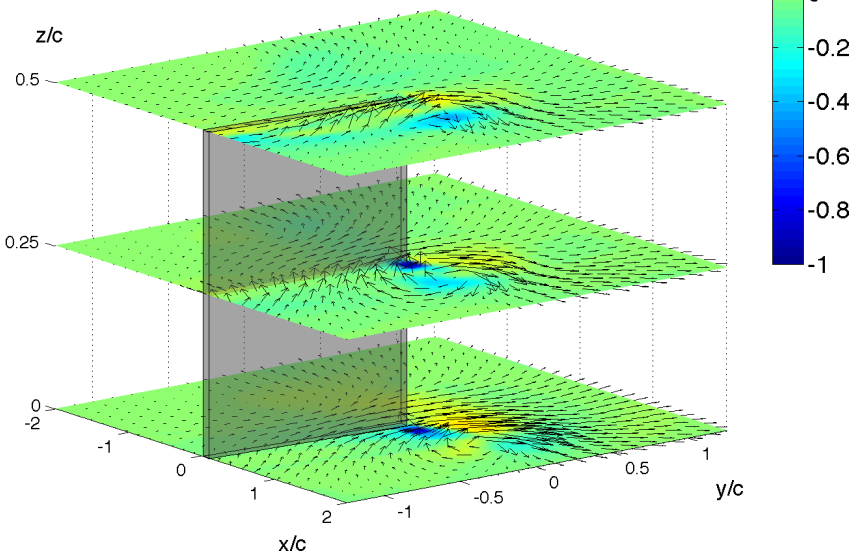

(t) $\hat{\phi} = 0.95$

Figure A.1: Velocity distributions on $z/c = [0, 0.25, 0.5]$, Re=1580.

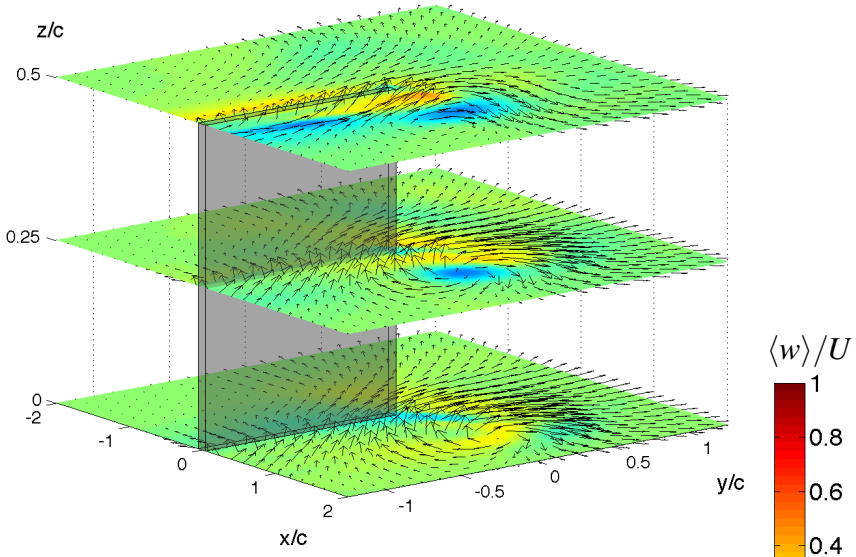

(a) $\hat{\phi} = 0$

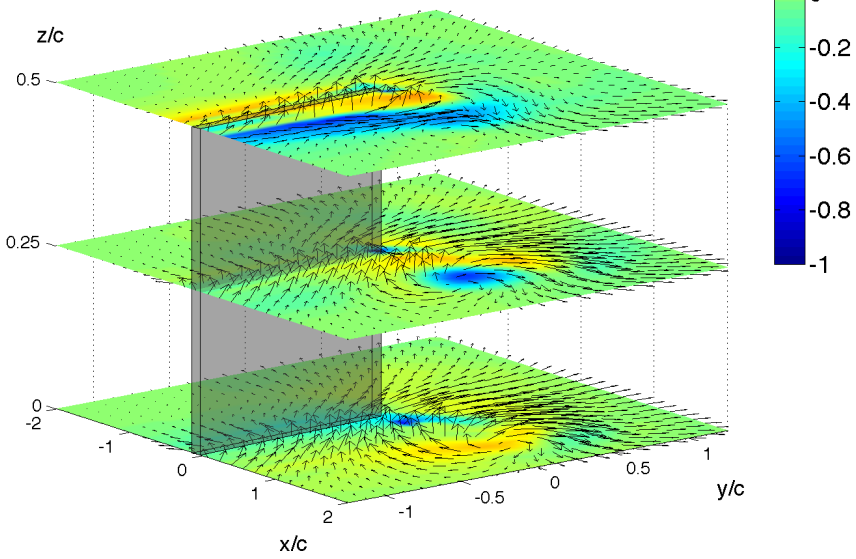

(b) $\hat{\phi} = 0.05$

Figure A.2: Velocity distributions on $z/c = [0, 0.25, 0.5]$, Re=3160. (*Continued*)

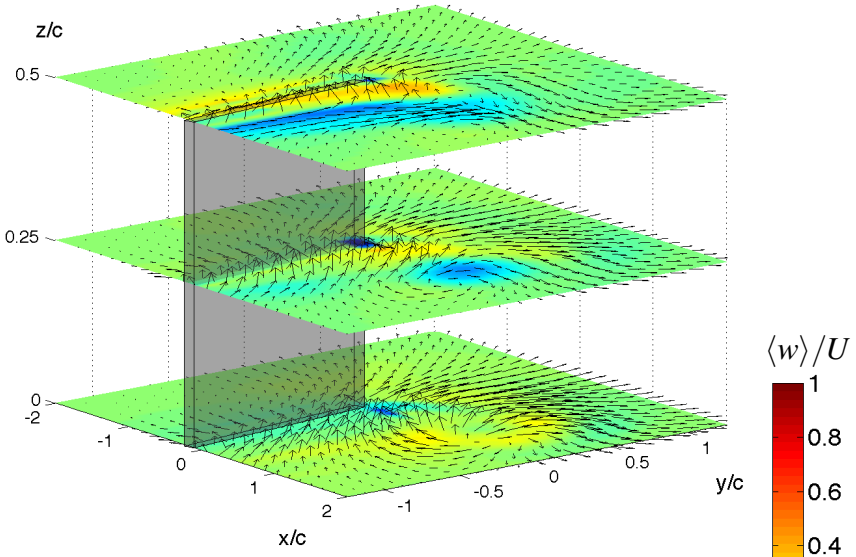

(c) $\hat{\phi} = 0.1$

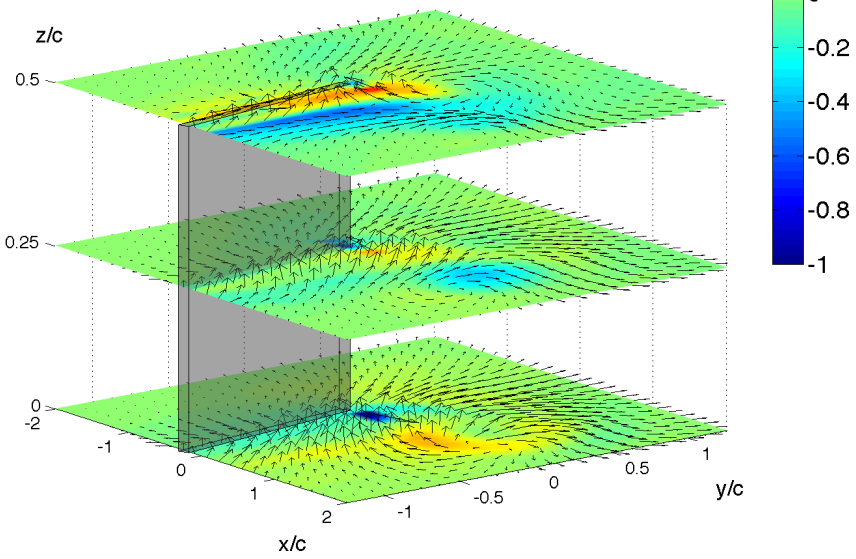

(d) $\hat{\phi} = 0.15$

Figure A.2: Velocity distributions on $z/c = [0, 0.25, 0.5]$, Re=3160. (*Continued*)

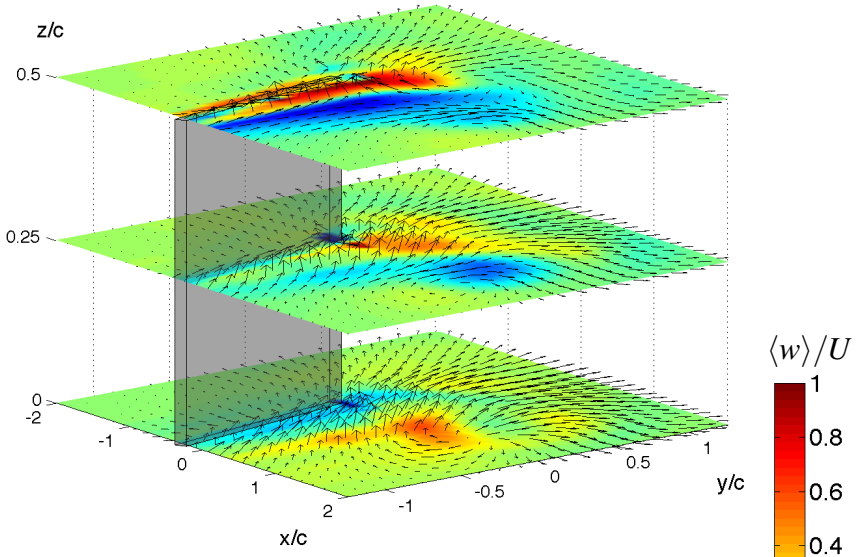

(e) $\hat{\phi} = 0.2$

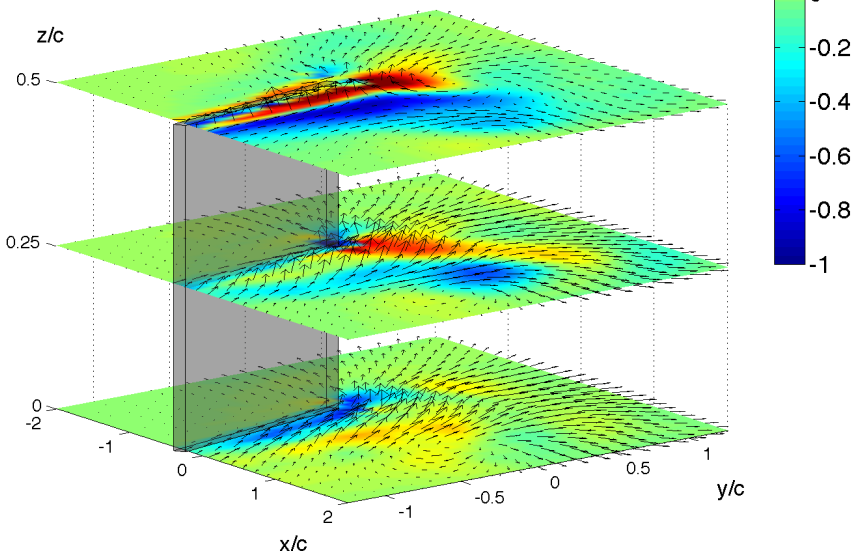

(f) $\hat{\phi} = 0.25$

Figure A.2: Velocity distributions on $z/c = [0, 0.25, 0.5]$, Re=3160. (*Continued*)

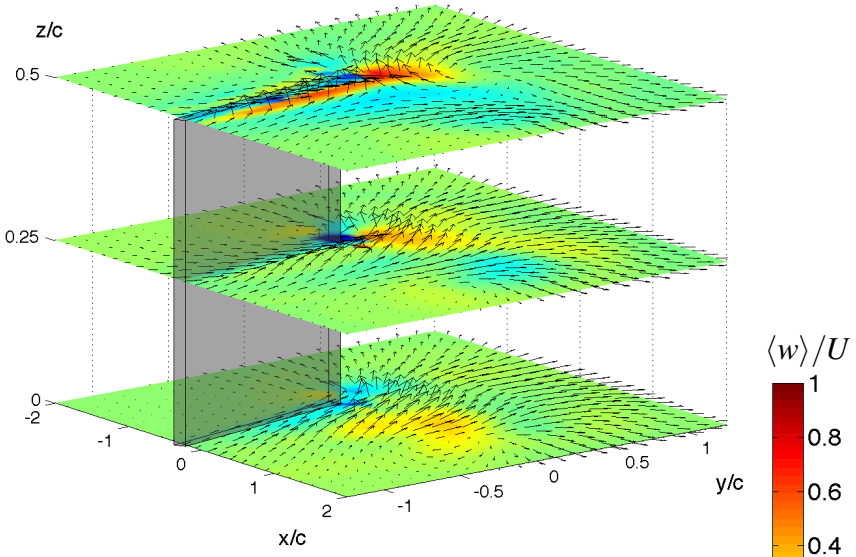

(g) $\hat{\phi} = 0.3$

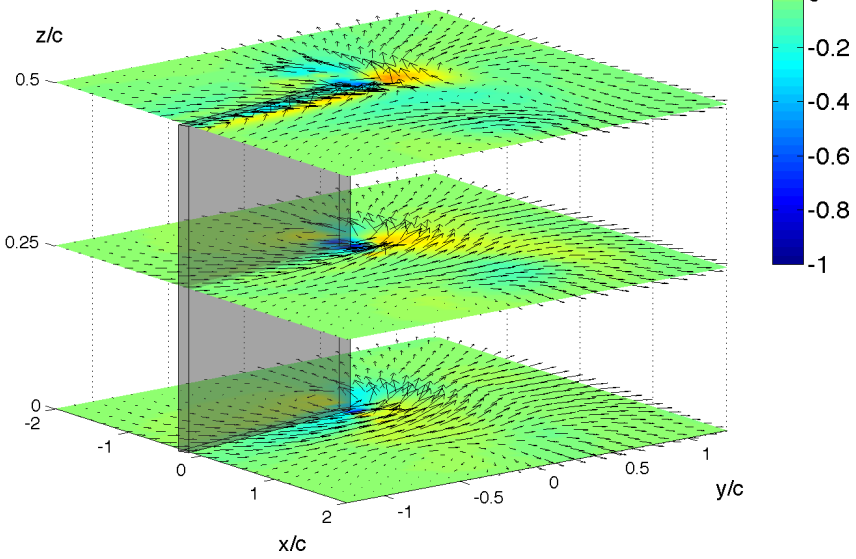

(h) $\hat{\phi} = 0.35$

Figure A.2: Velocity distributions on $z/c = [0, 0.25, 0.5]$, Re=3160. (*Continued*)

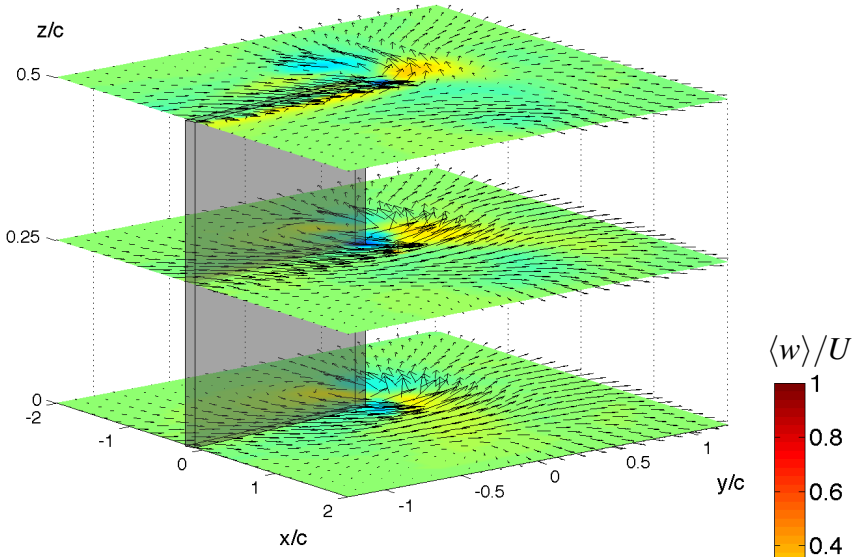

(i) $\hat{\phi} = 0.4$

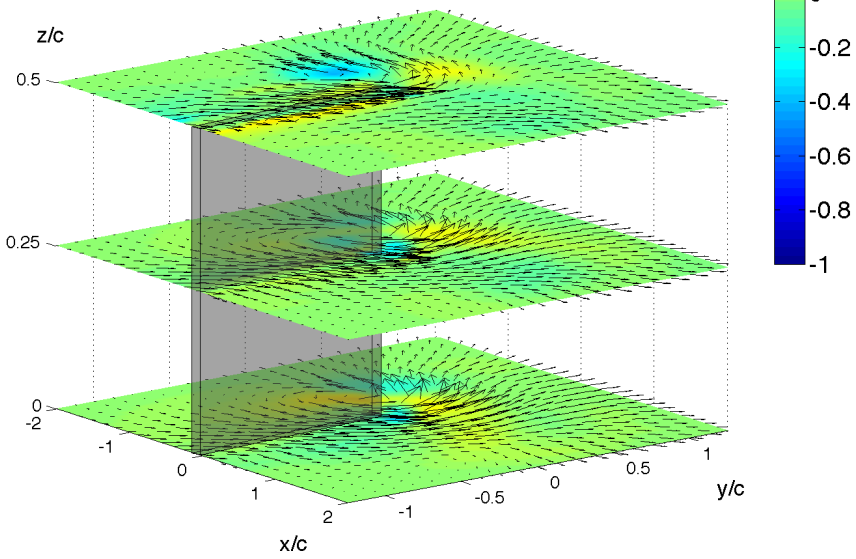

(j) $\hat{\phi} = 0.45$

Figure A.2: Velocity distributions on $z/c = [0, 0.25, 0.5]$, Re=3160. (*Continued*)

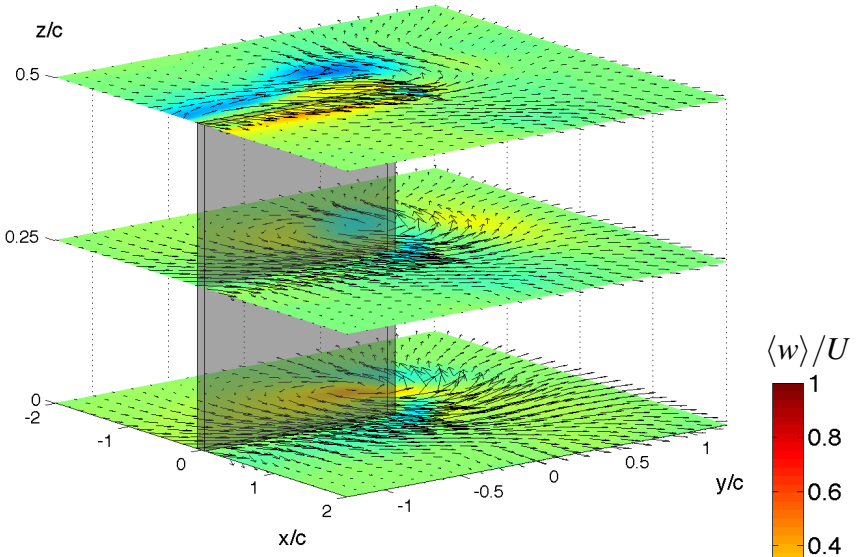

(k) $\hat{\phi} = 0.5$

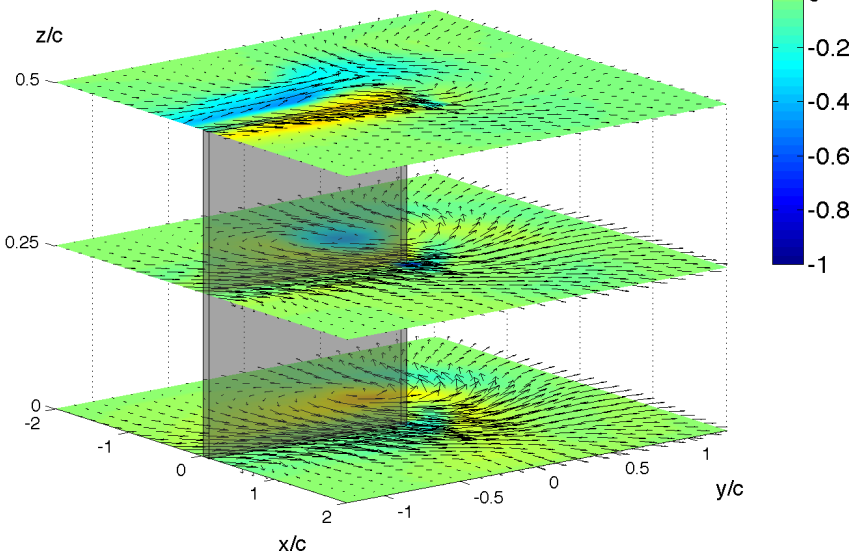

(l) $\hat{\phi} = 0.55$

Figure A.2: Velocity distributions on $z/c = [0, 0.25, 0.5]$, Re=3160. (*Continued*)

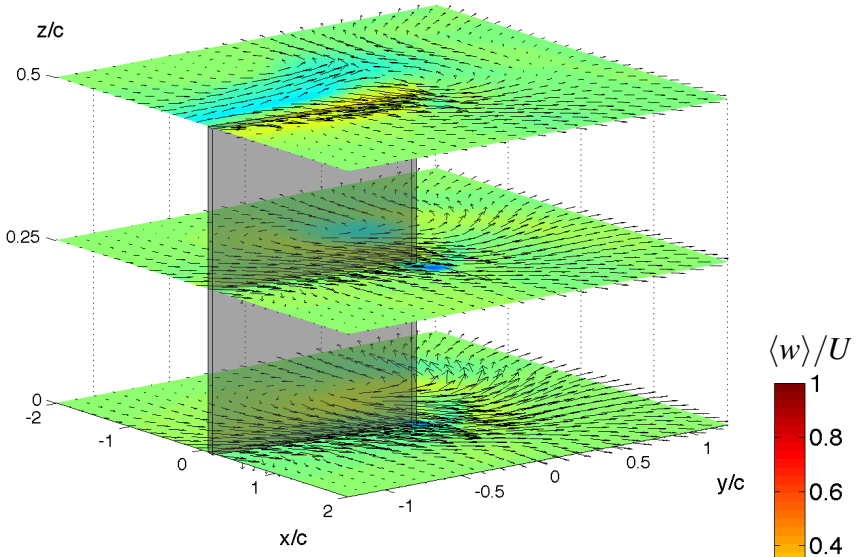

(m) $\hat{\phi} = 0.6$

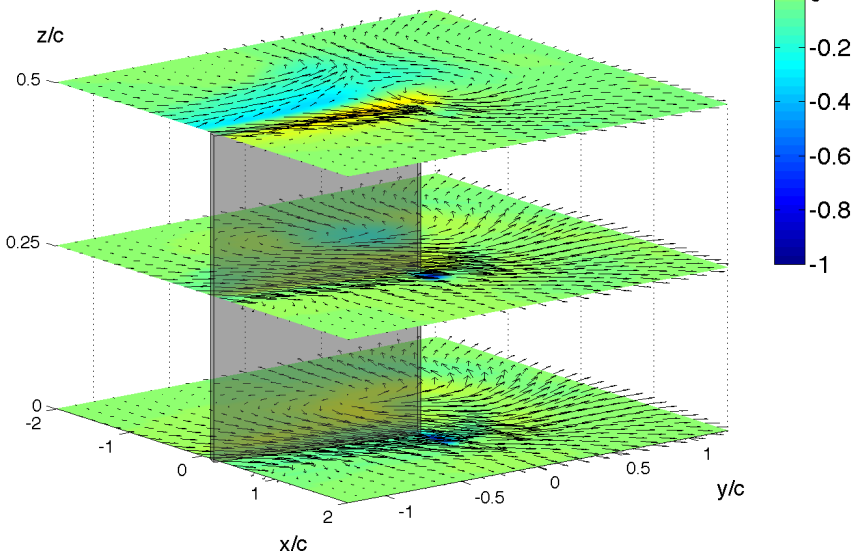

(n) $\hat{\phi} = 0.65$

Figure A.2: Velocity distributions on $z/c = [0, 0.25, 0.5]$, Re=3160. (*Continued*)

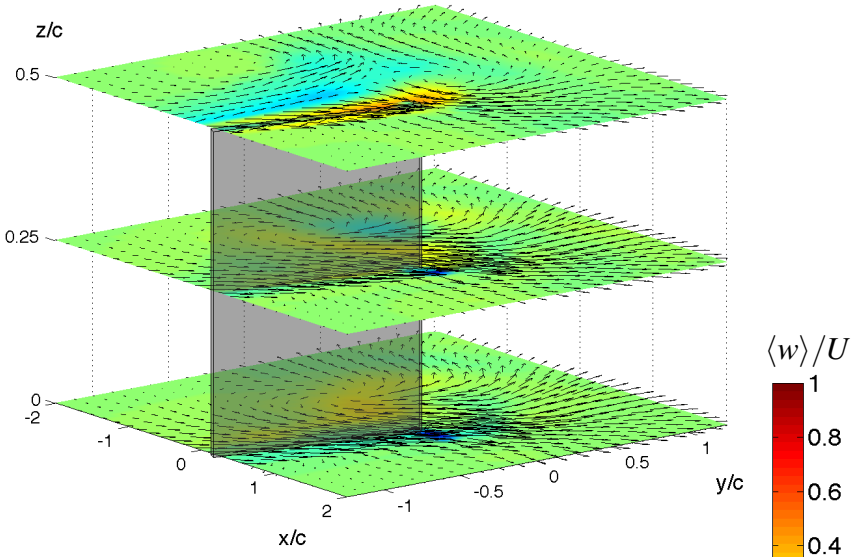

(o) $\hat{\phi} = 0.7$

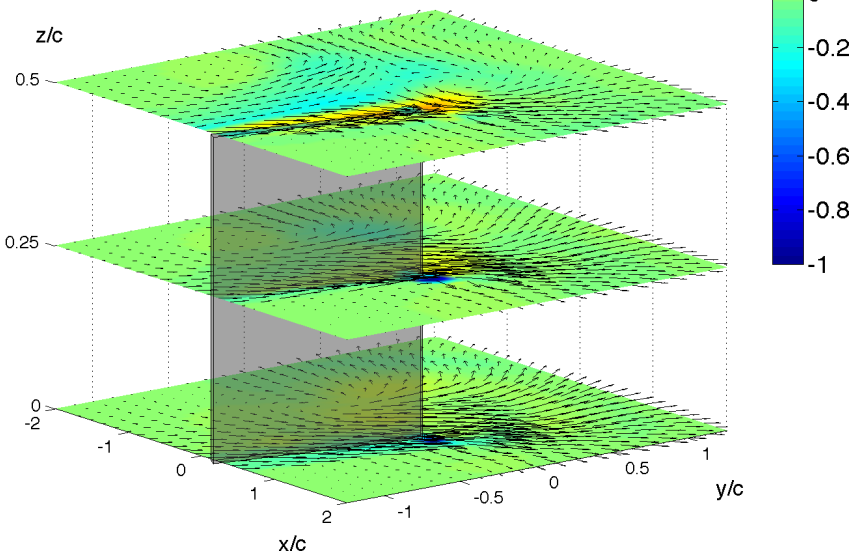

(p) $\hat{\phi} = 0.75$

Figure A.2: Velocity distributions on $z/c = [0, 0.25, 0.5]$, Re=3160. (*Continued*)

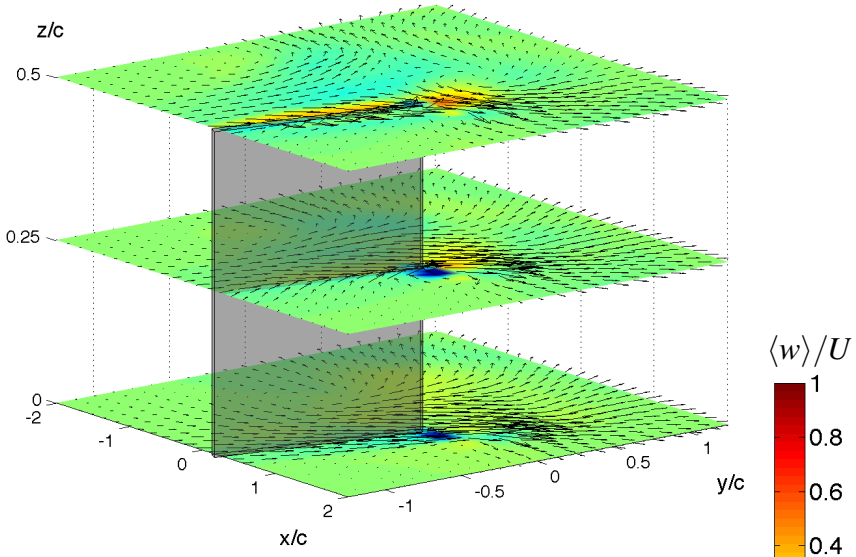

(q) $\hat{\phi} = 0.8$

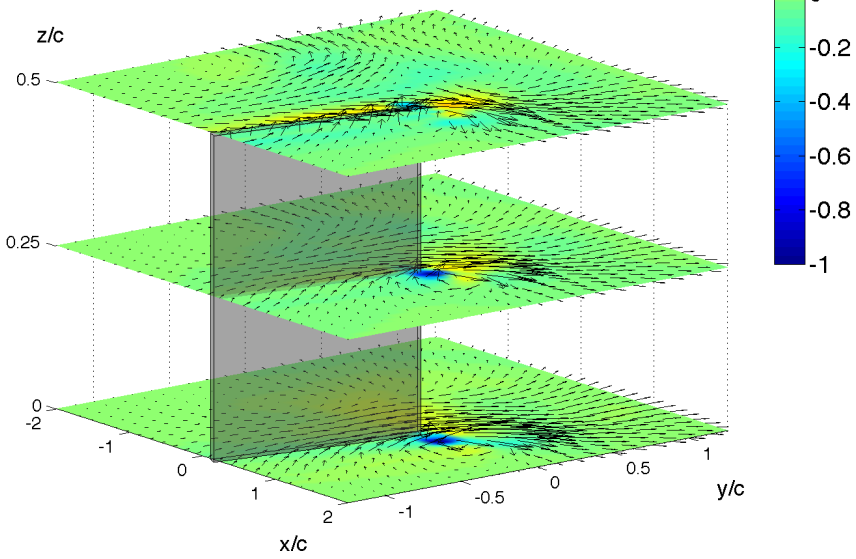

(r) $\hat{\phi} = 0.85$

Figure A.2: Velocity distributions on $z/c = [0, 0.25, 0.5]$, Re=3160. (*Continued*)

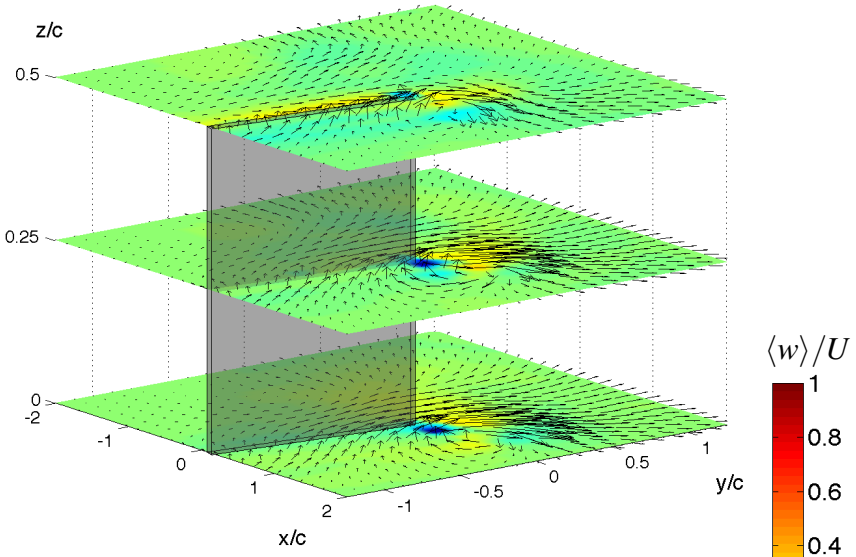

(s) $\hat{\phi} = 0.9$

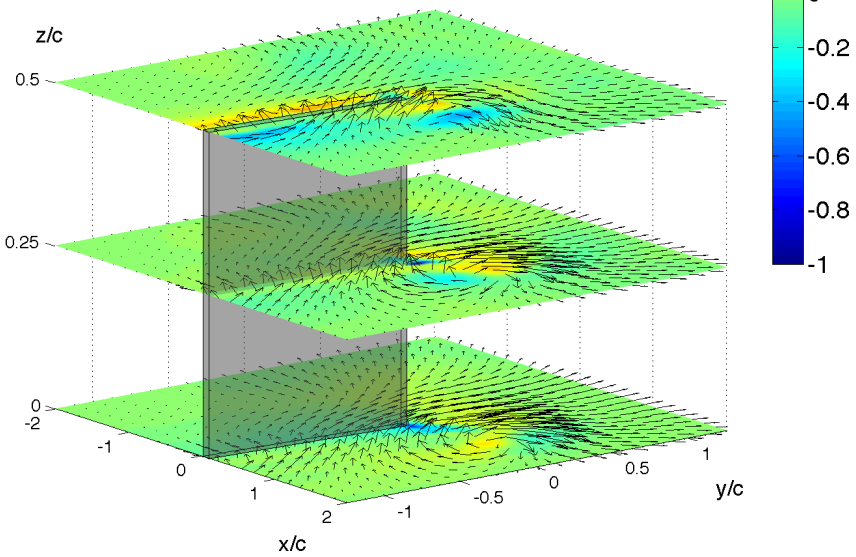

(t) $\hat{\phi} = 0.95$

Figure A.2: Velocity distributions on $z/c = [0, 0.25, 0.5]$, Re=3160.

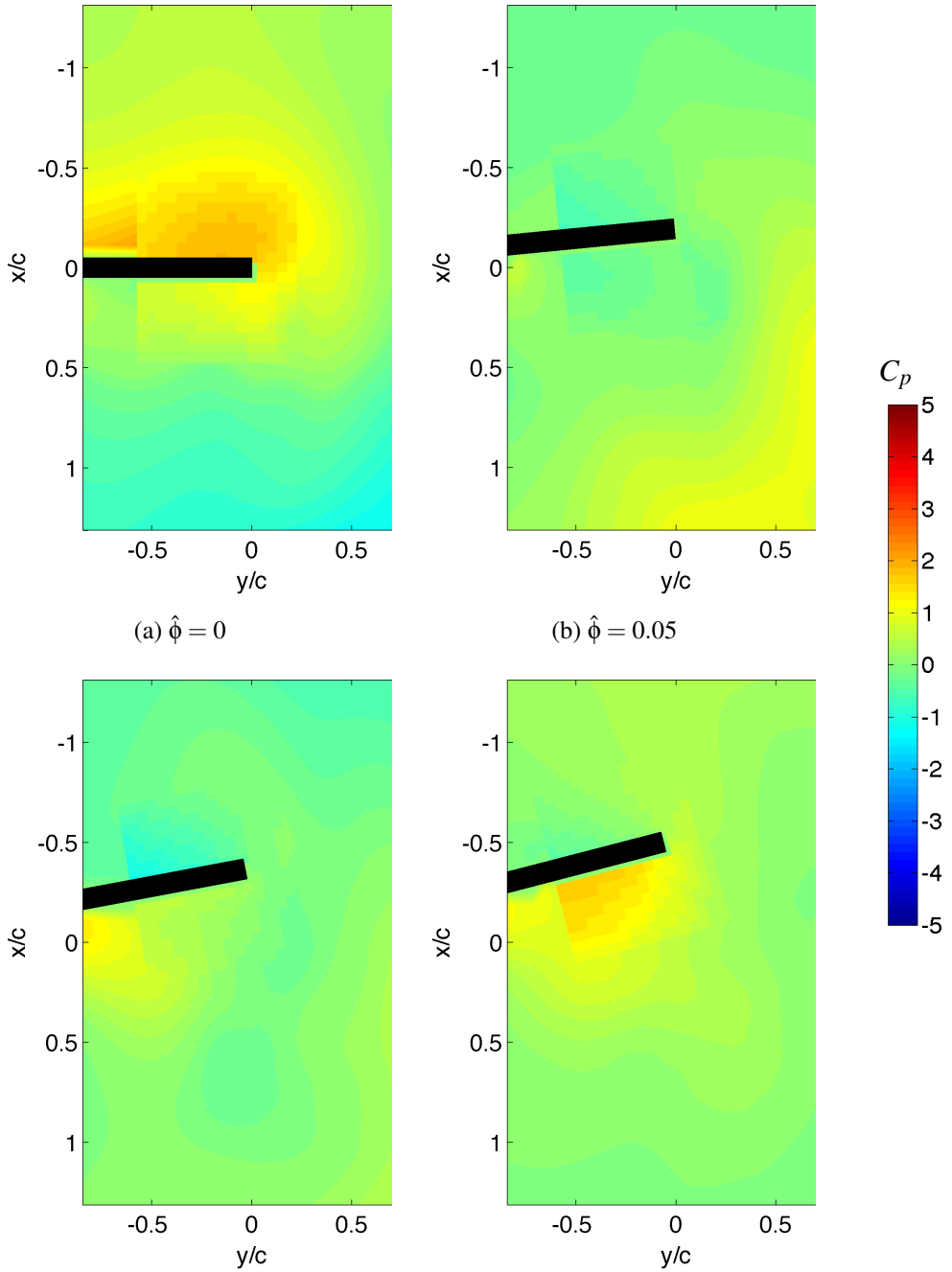

(a) $\hat{\phi} = 0$ (b) $\hat{\phi} = 0.05$

(c) $\hat{\phi} = 0.1$ (d) $\hat{\phi} = 0.15$

Figure A.3: Pressure distribution of Re=3160, $z = 0$. (*Continued*)

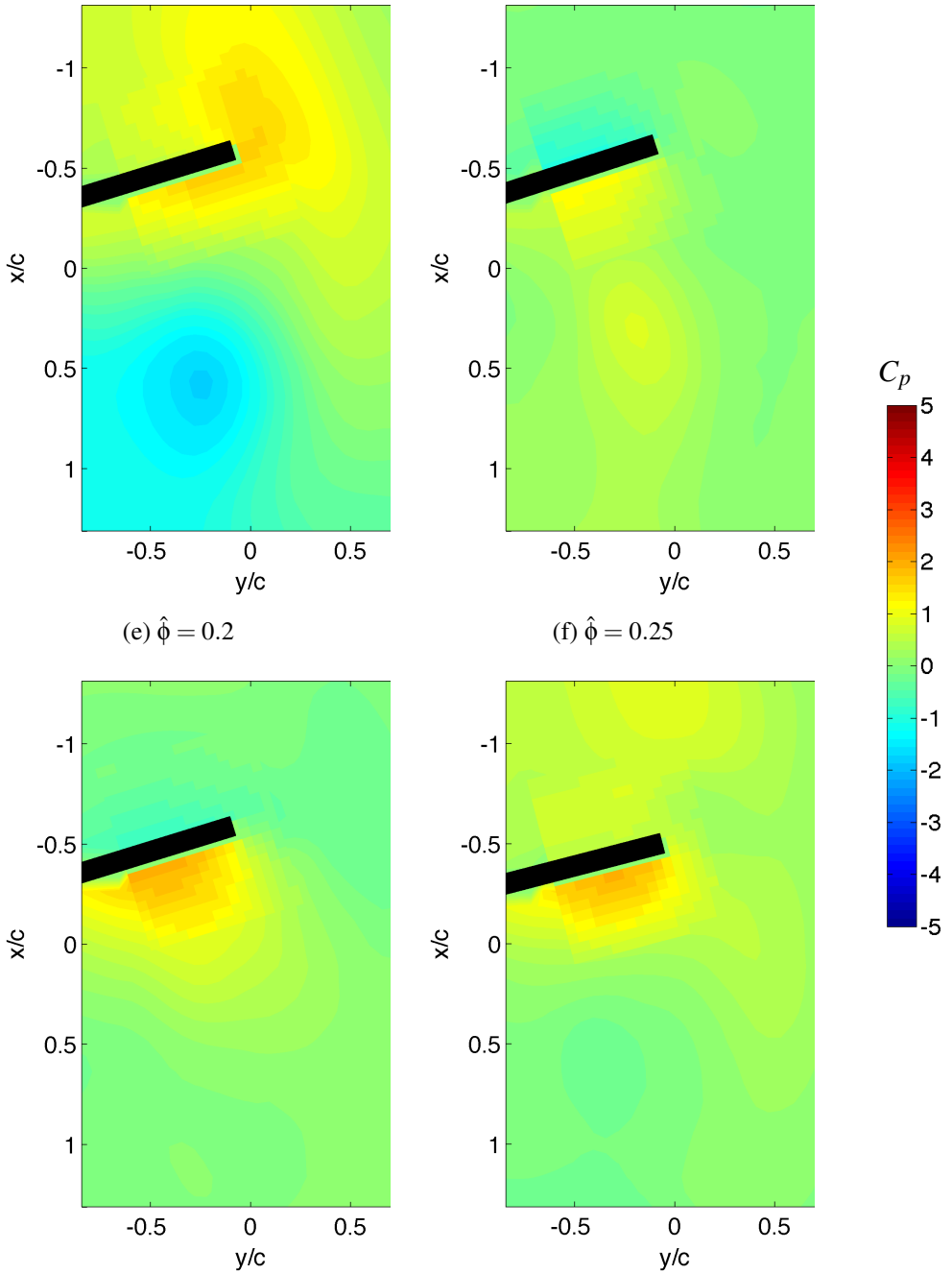

(e) $\hat{\phi} = 0.2$ (f) $\hat{\phi} = 0.25$

(g) $\hat{\phi} = 0.3$ (h) $\hat{\phi} = 0.35$

Figure A.3: Pressure distribution of Re=3160, $z = 0$. (*Continued*)

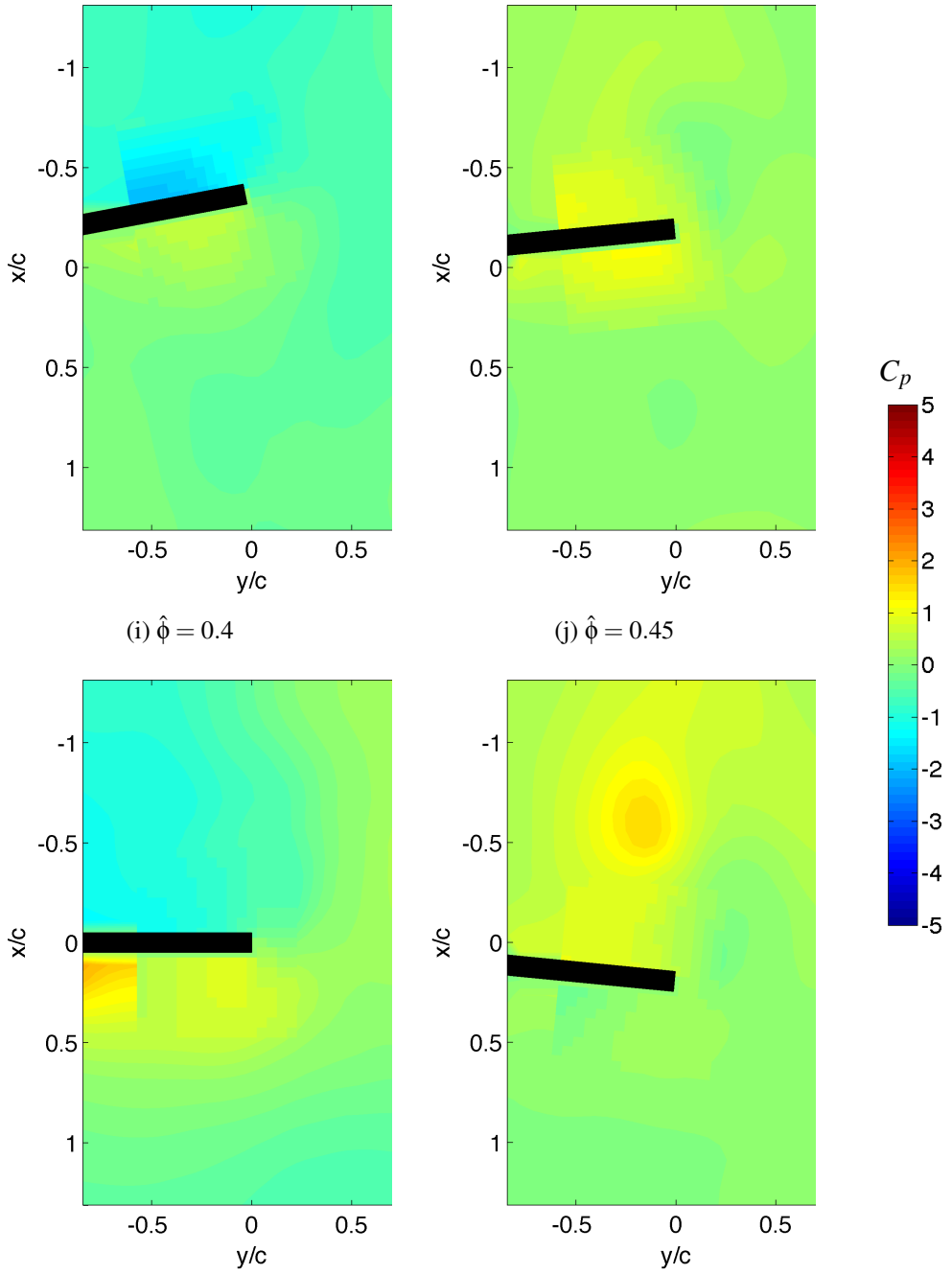

(i) $\hat{\phi} = 0.4$ (j) $\hat{\phi} = 0.45$

(k) $\hat{\phi} = 0.5$ (l) $\hat{\phi} = 0.55$

Figure A.3: Pressure distribution of Re=3160, $z = 0$. (*Continued*)

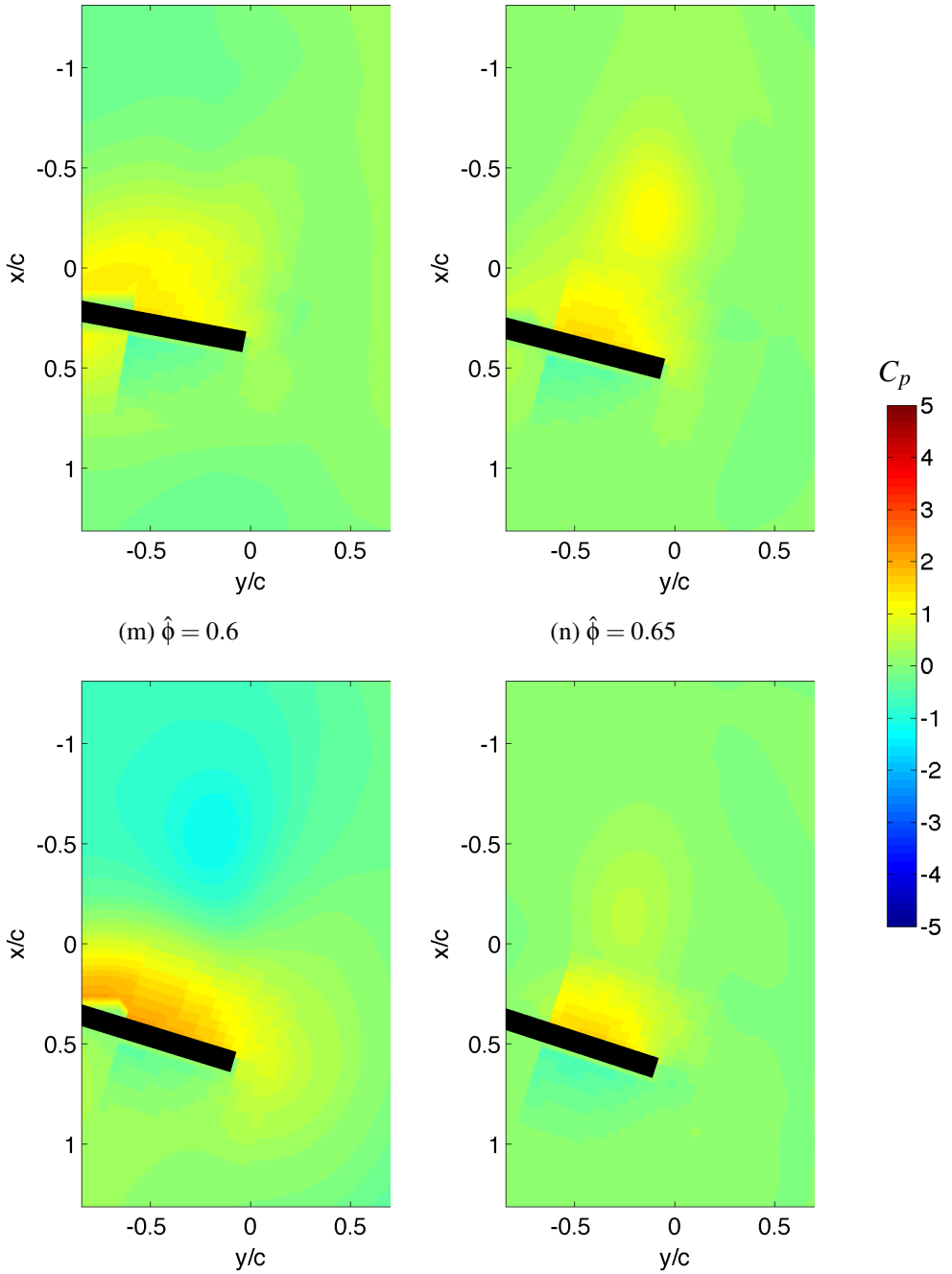

(m) $\hat{\phi} = 0.6$

(n) $\hat{\phi} = 0.65$

(o) $\hat{\phi} = 0.7$

(p) $\hat{\phi} = 0.75$

Figure A.3: Pressure distribution of Re=3160, $z = 0$. (*Continued*)

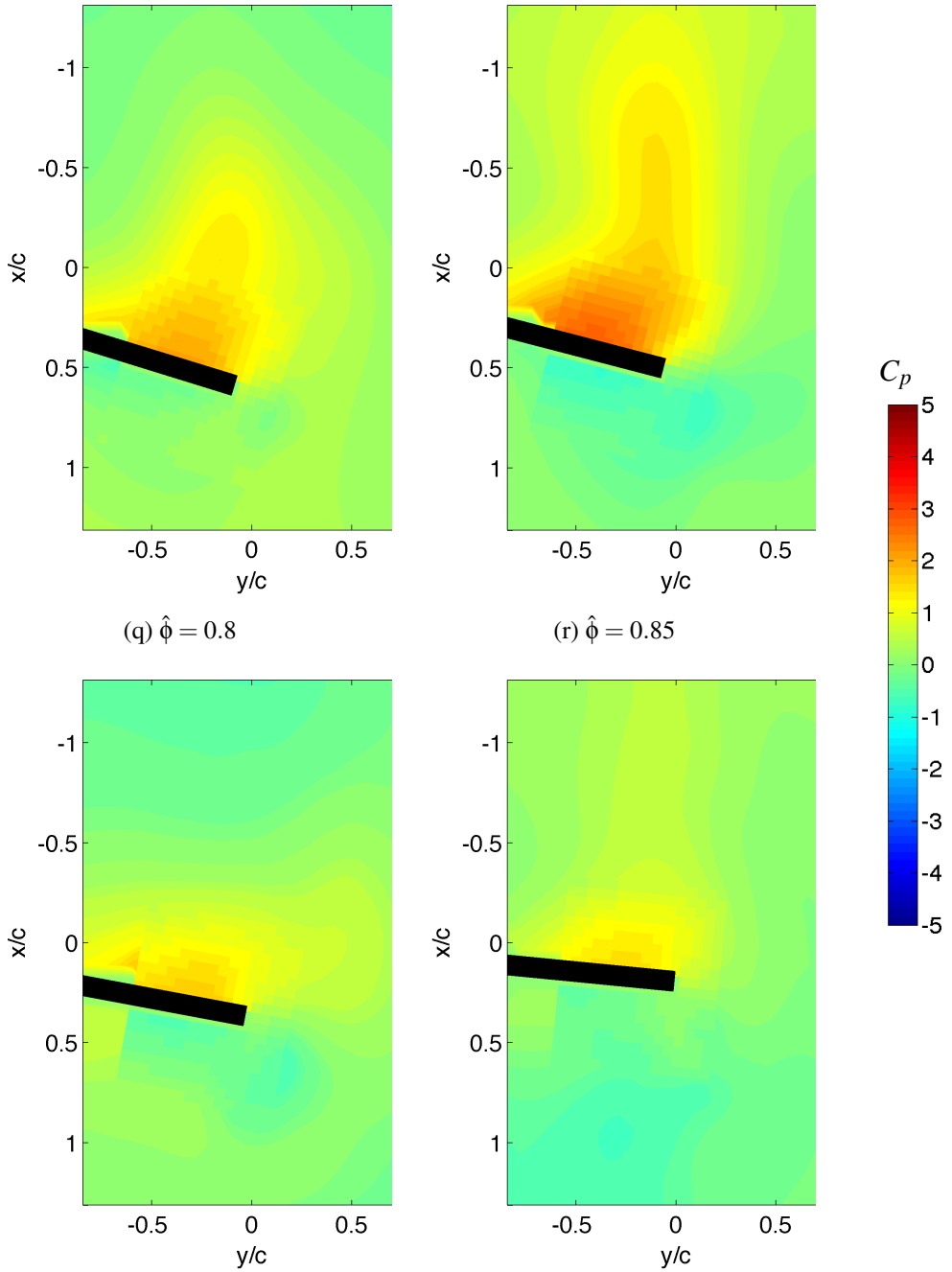

(q) $\hat{\phi} = 0.8$ (r) $\hat{\phi} = 0.85$

(s) $\hat{\phi} = 0.9$ (t) $\hat{\phi} = 0.95$

Figure A.3: Pressure distribution of Re=3160, $z = 0$.

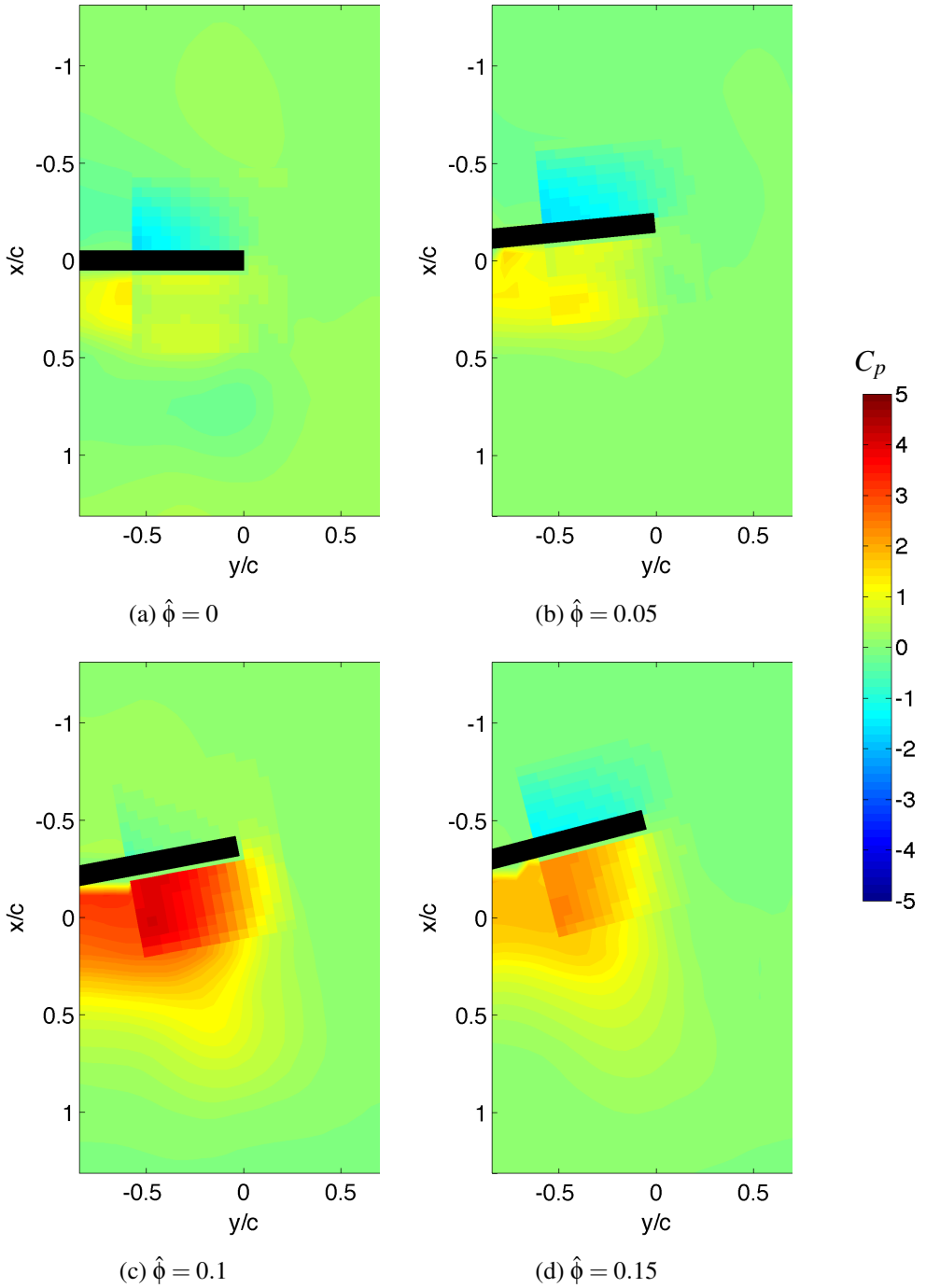

(a) $\hat{\phi} = 0$ (b) $\hat{\phi} = 0.05$

(c) $\hat{\phi} = 0.1$ (d) $\hat{\phi} = 0.15$

Figure A.4: Pressure distribution of Re=3160, $z = c/2$. (*Continued*)

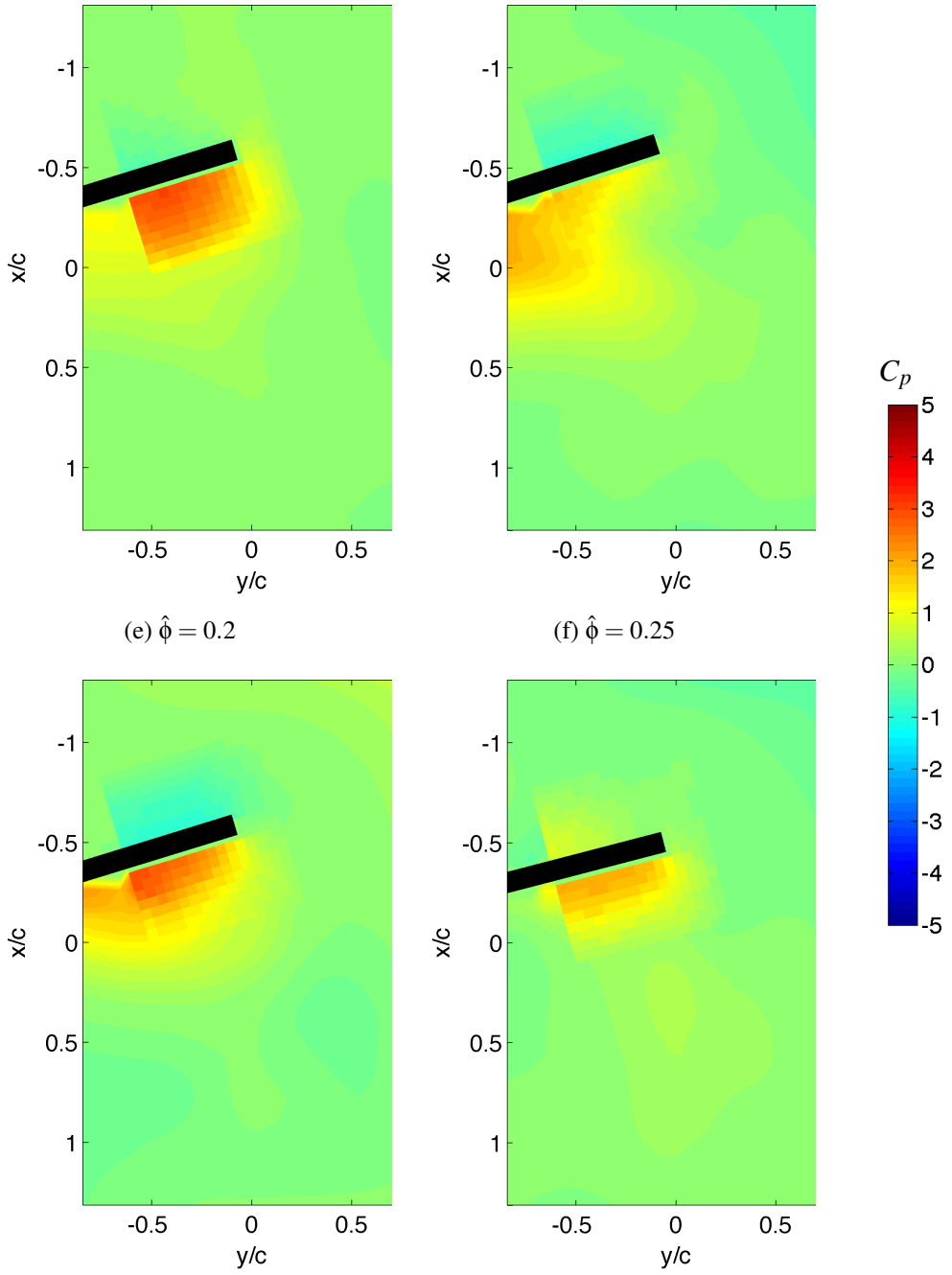

(e) $\hat{\phi} = 0.2$ (f) $\hat{\phi} = 0.25$

(g) $\hat{\phi} = 0.3$ (h) $\hat{\phi} = 0.35$

Figure A.4: Pressure distribution of Re=3160, $z = c/2$. (*Continued*)

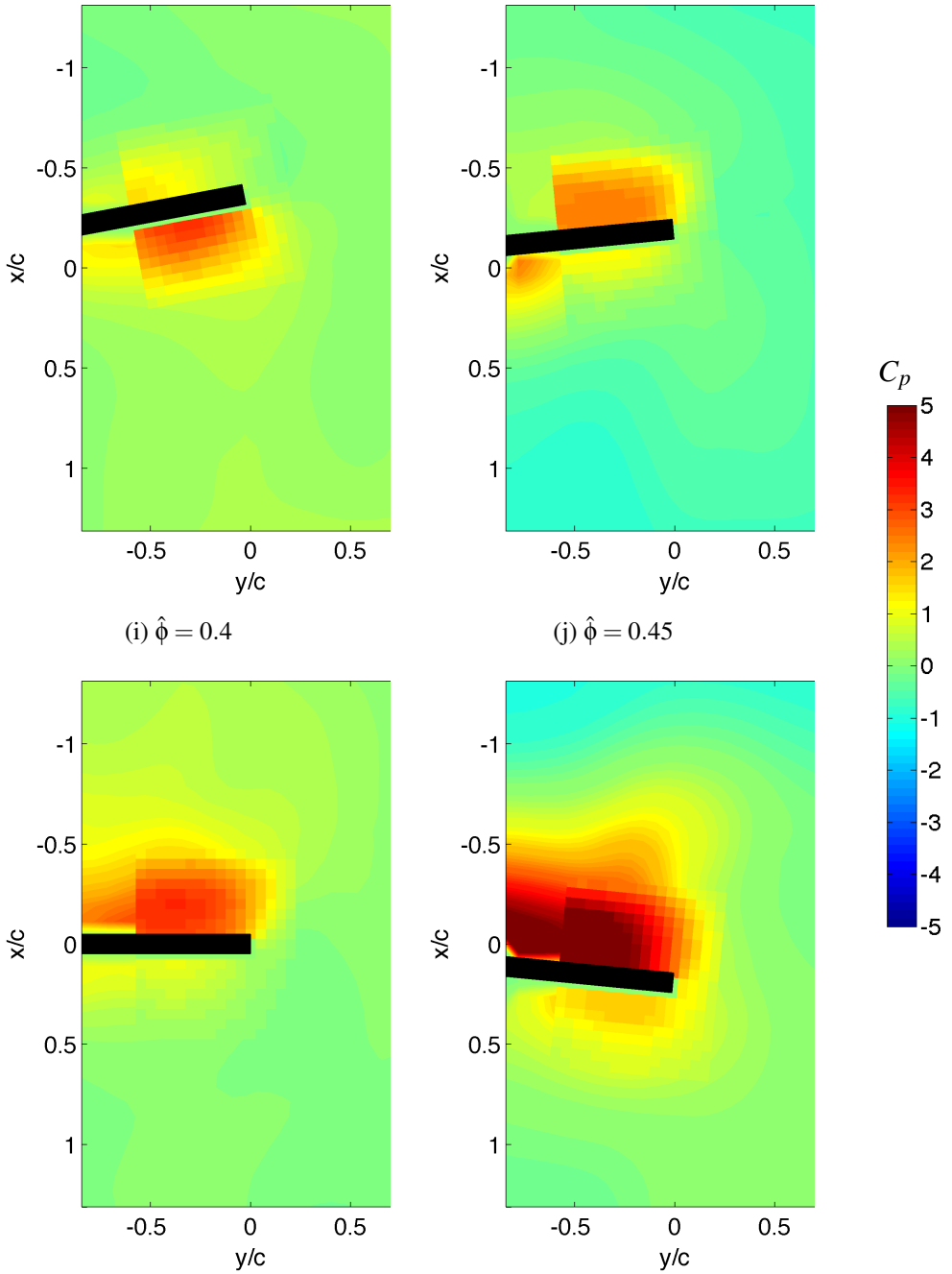

(i) $\hat{\phi} = 0.4$ (j) $\hat{\phi} = 0.45$

(k) $\hat{\phi} = 0.5$ (l) $\hat{\phi} = 0.55$

Figure A.4: Pressure distribution of Re=3160, $z = c/2$. (*Continued*)

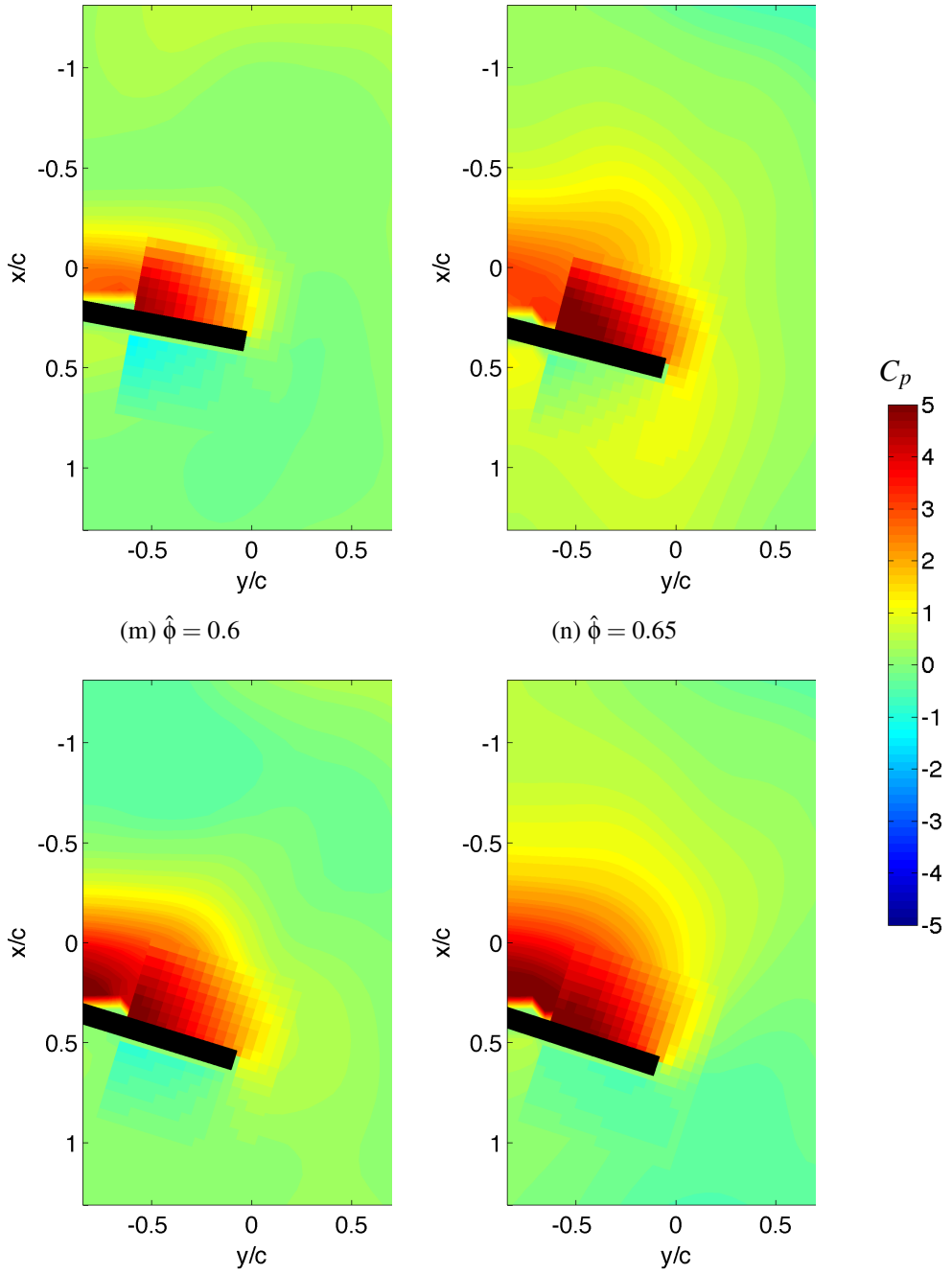

(m) $\hat{\phi} = 0.6$ (n) $\hat{\phi} = 0.65$

(o) $\hat{\phi} = 0.7$ (p) $\hat{\phi} = 0.75$

Figure A.4: Pressure distribution of Re=3160, $z = c/2$. (*Continued*)

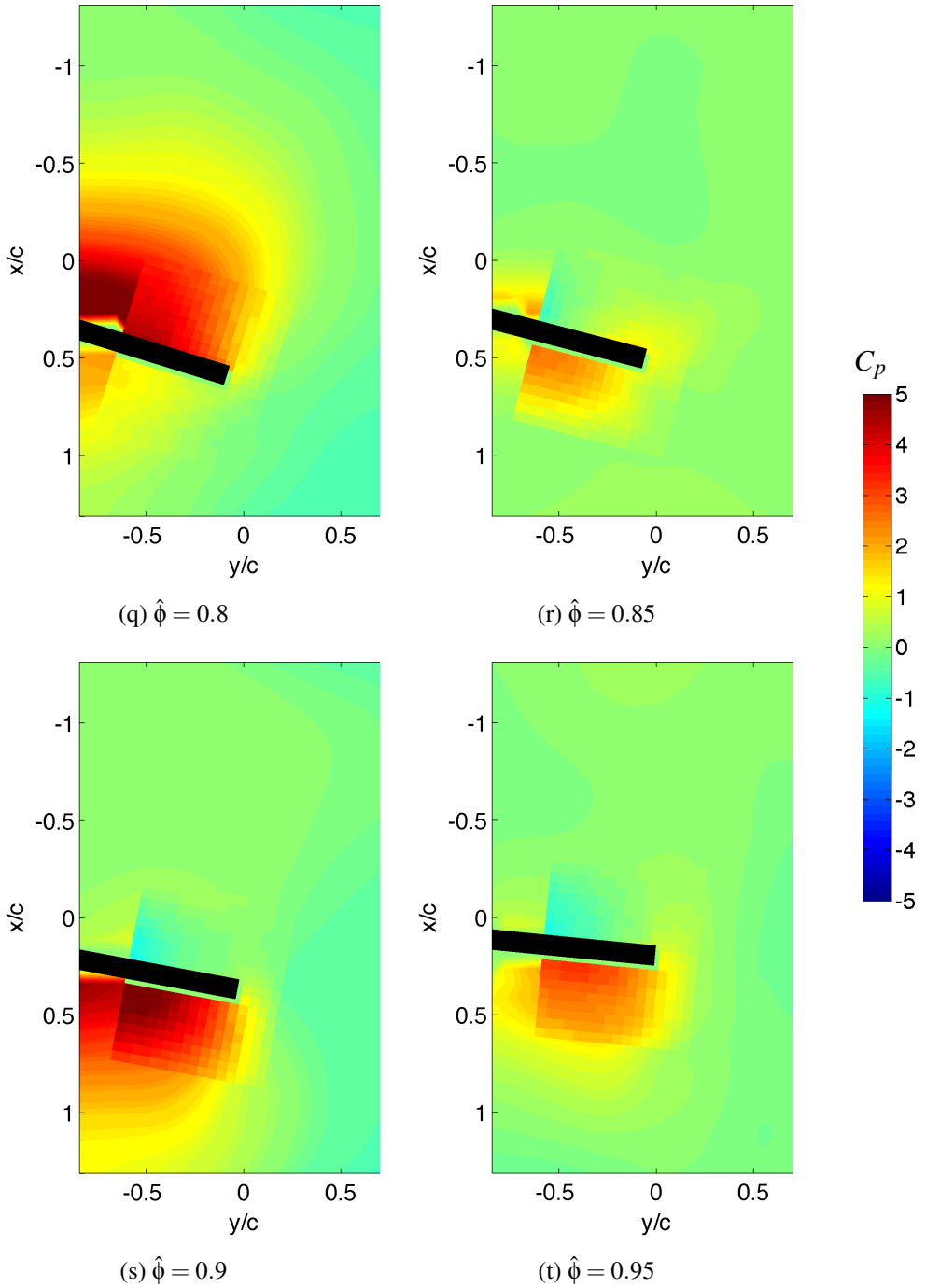

(q) $\hat{\phi} = 0.8$

(r) $\hat{\phi} = 0.85$

(s) $\hat{\phi} = 0.9$

(t) $\hat{\phi} = 0.95$

Figure A.4: Pressure distribution of Re=3160, $z = c/2$.

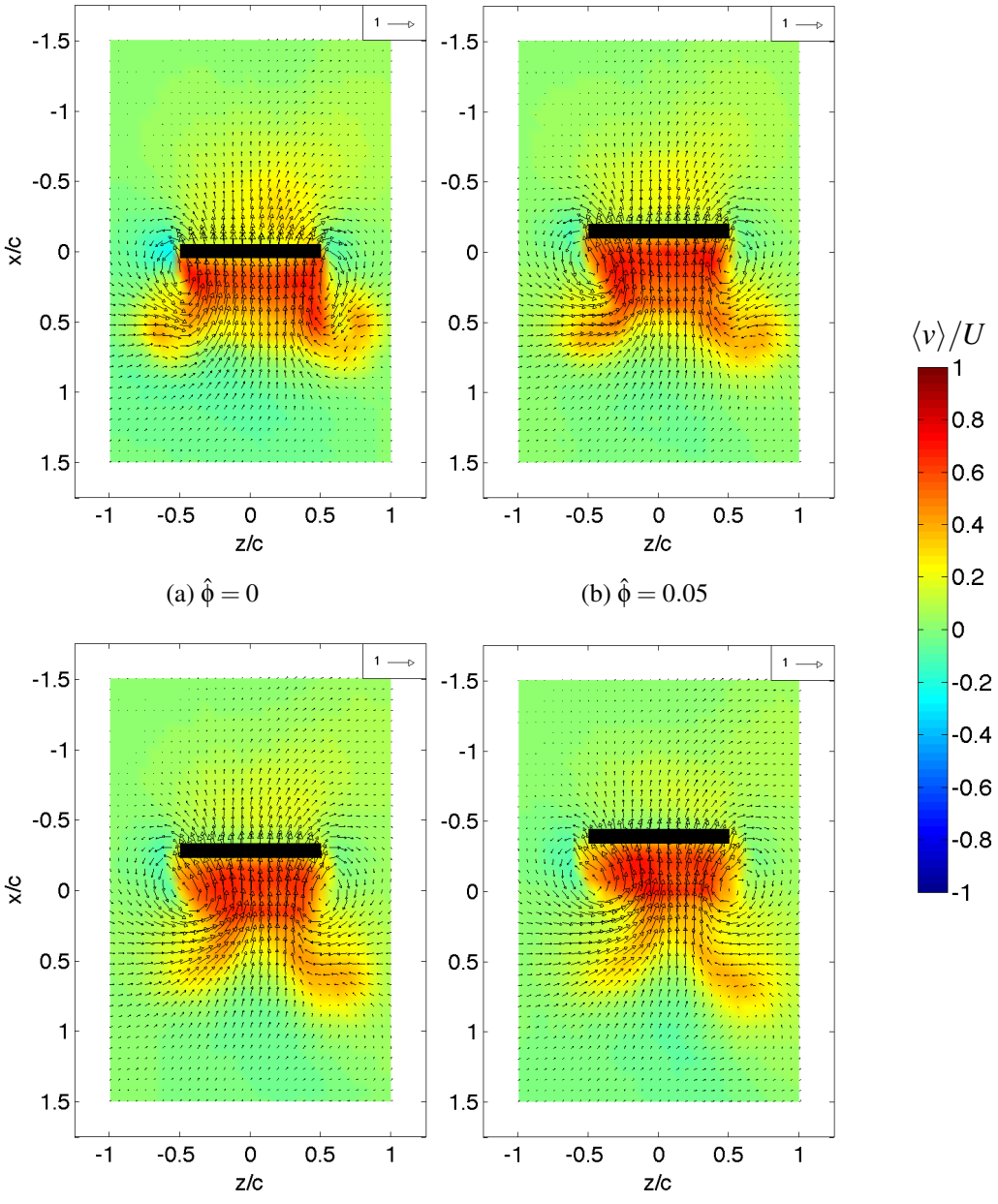

(a) $\hat{\phi} = 0$ (b) $\hat{\phi} = 0.05$

(c) $\hat{\phi} = 0.1$ (d) $\hat{\phi} = 0.15$

Figure A.5: Velocity distribution of Re=1580, $y = -c/2$. (*Continued*)

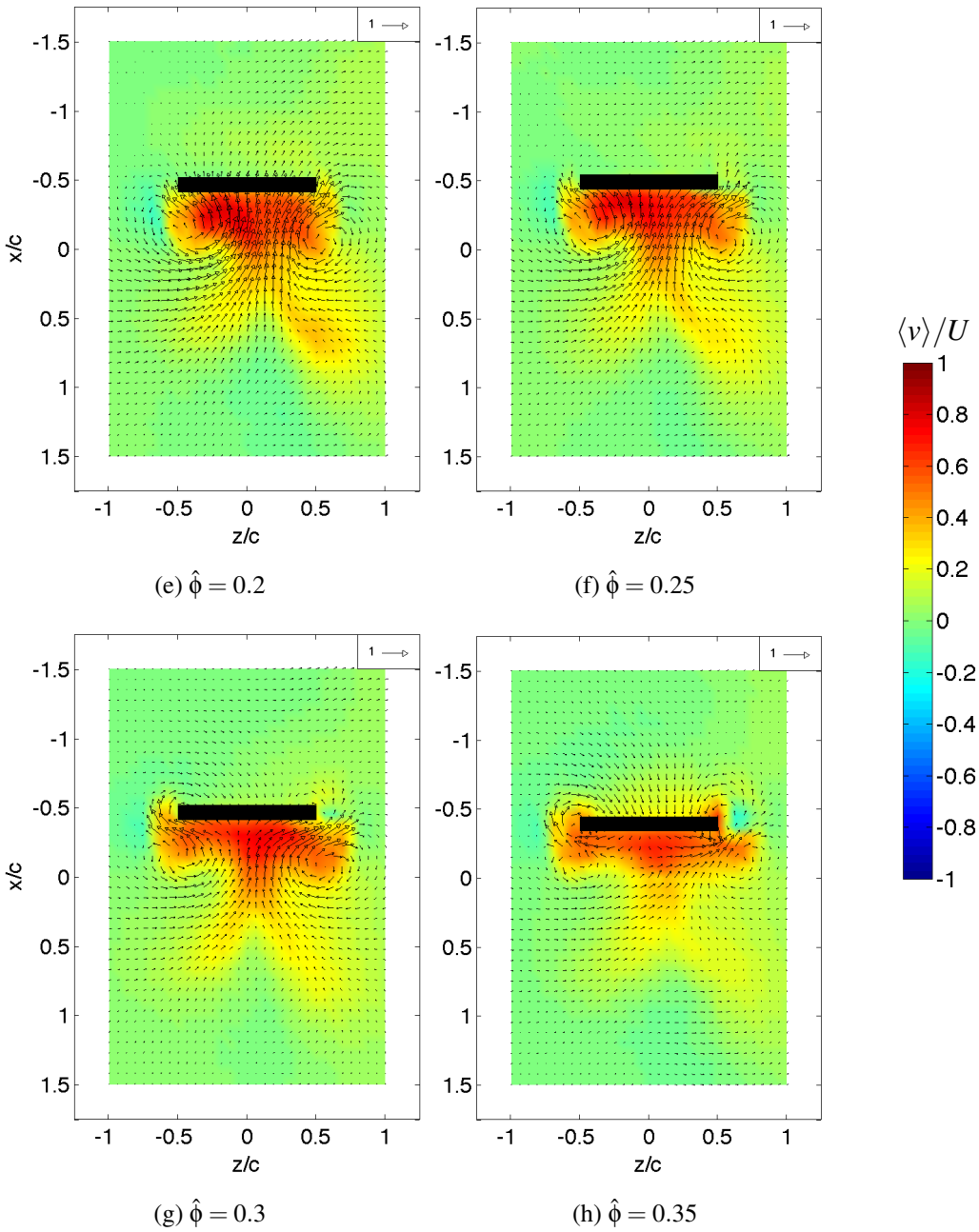

(e) $\hat{\phi} = 0.2$ (f) $\hat{\phi} = 0.25$

(g) $\hat{\phi} = 0.3$ (h) $\hat{\phi} = 0.35$

Figure A.5: Velocity distribution of Re=1580, $y = -c/2$. (*Continued*)

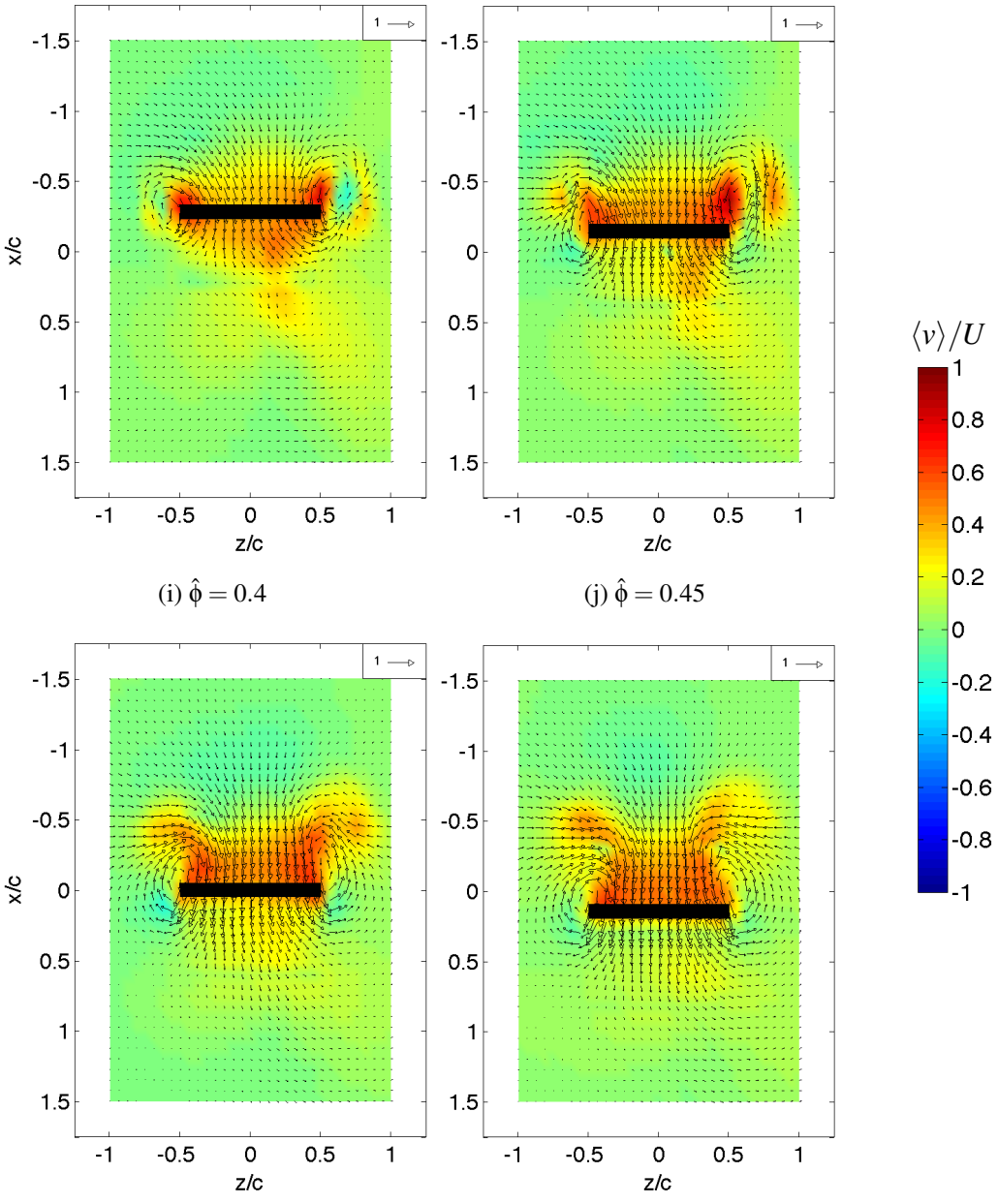

(i) $\hat{\phi} = 0.4$ (j) $\hat{\phi} = 0.45$

(k) $\hat{\phi} = 0.5$ (l) $\hat{\phi} = 0.55$

Figure A.5: Velocity distribution of Re=1580, $y = -c/2$. (*Continued*)

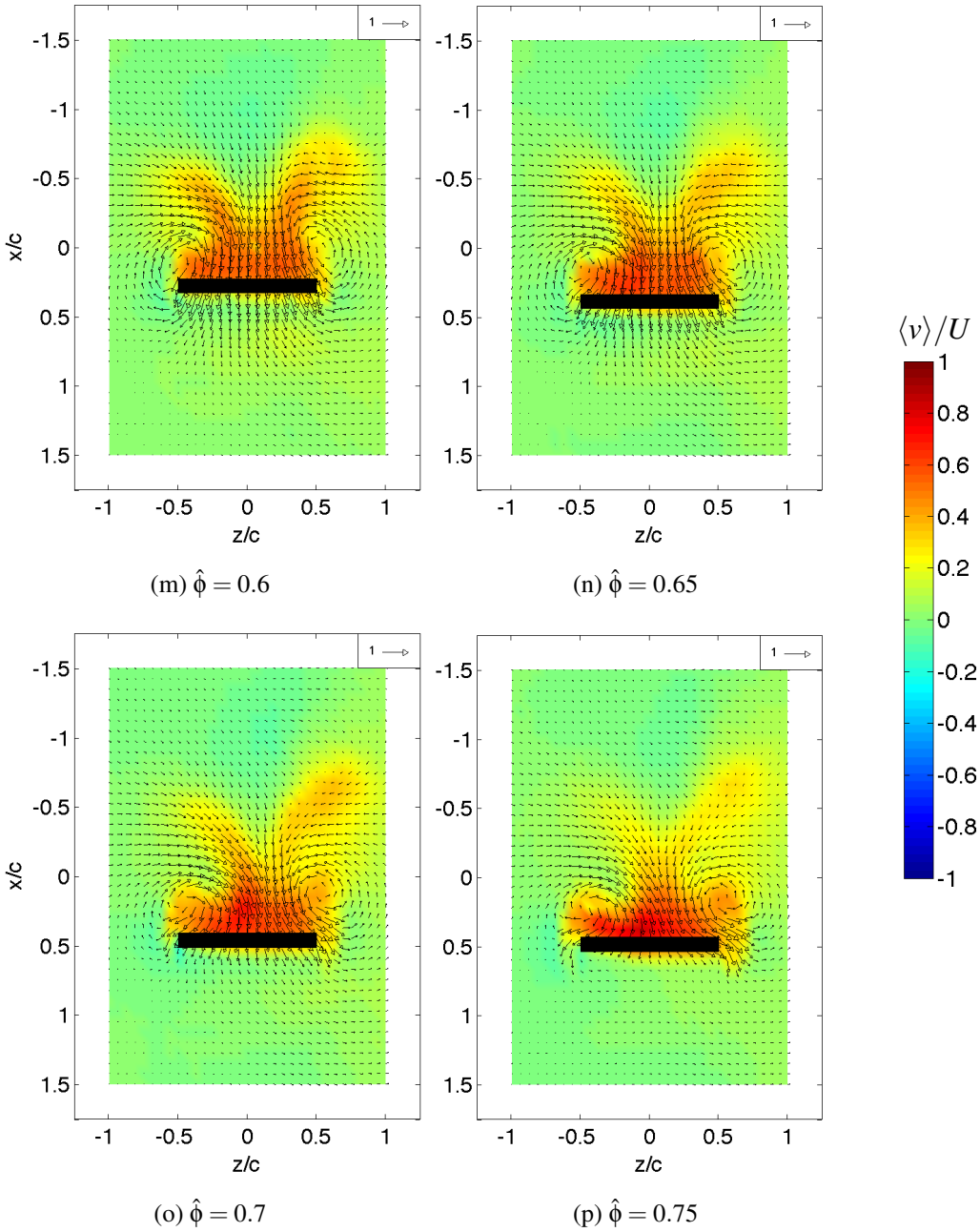

(m) $\hat{\phi} = 0.6$ (n) $\hat{\phi} = 0.65$

(o) $\hat{\phi} = 0.7$ (p) $\hat{\phi} = 0.75$

Figure A.5: Velocity distribution of Re=1580, $y = -c/2$. (*Continued*)

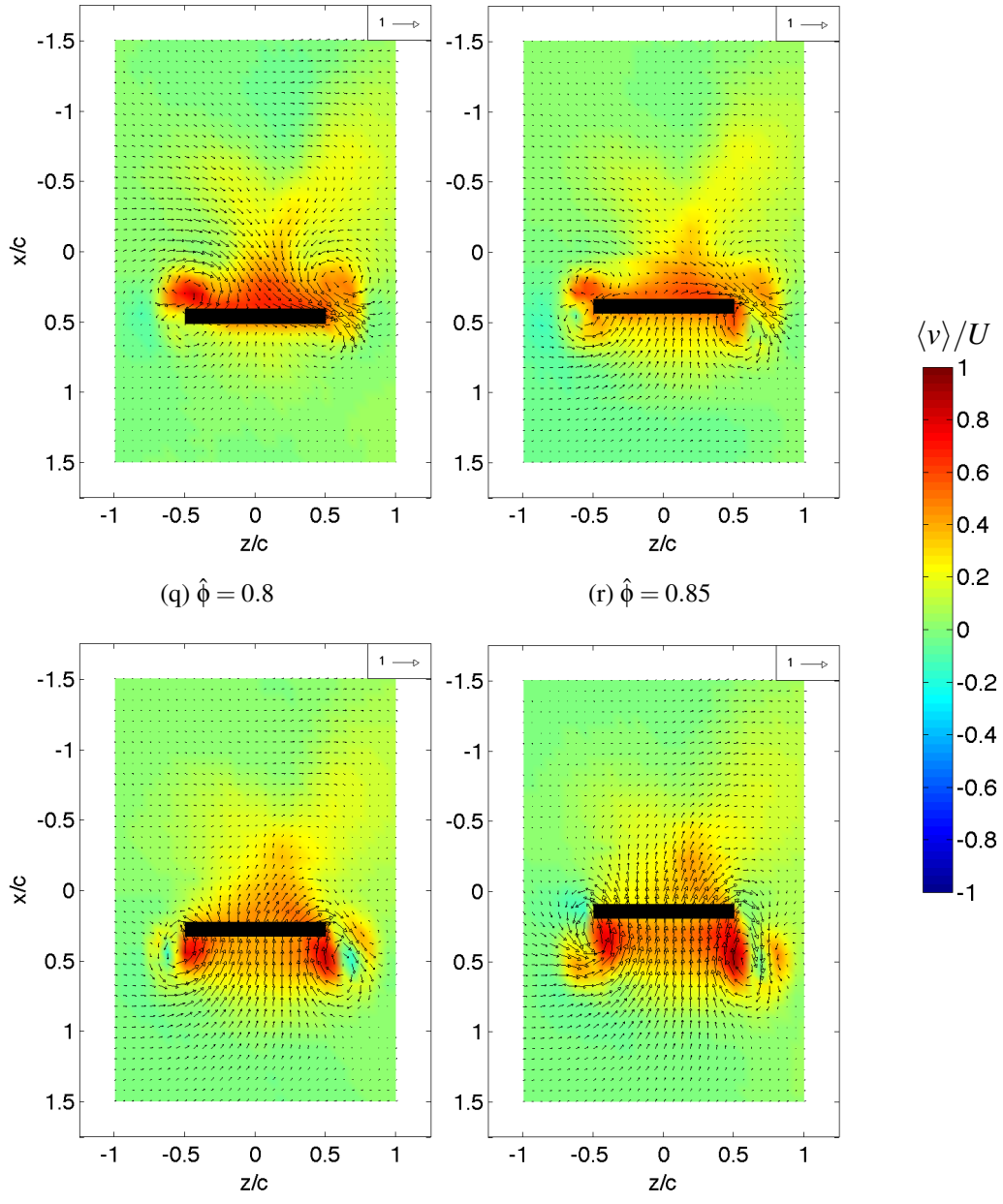

(q) $\hat{\phi} = 0.8$ (r) $\hat{\phi} = 0.85$

(s) $\hat{\phi} = 0.9$ (t) $\hat{\phi} = 0.95$

Figure A.5: Velocity distribution of Re=1580, $y = -c/2$.

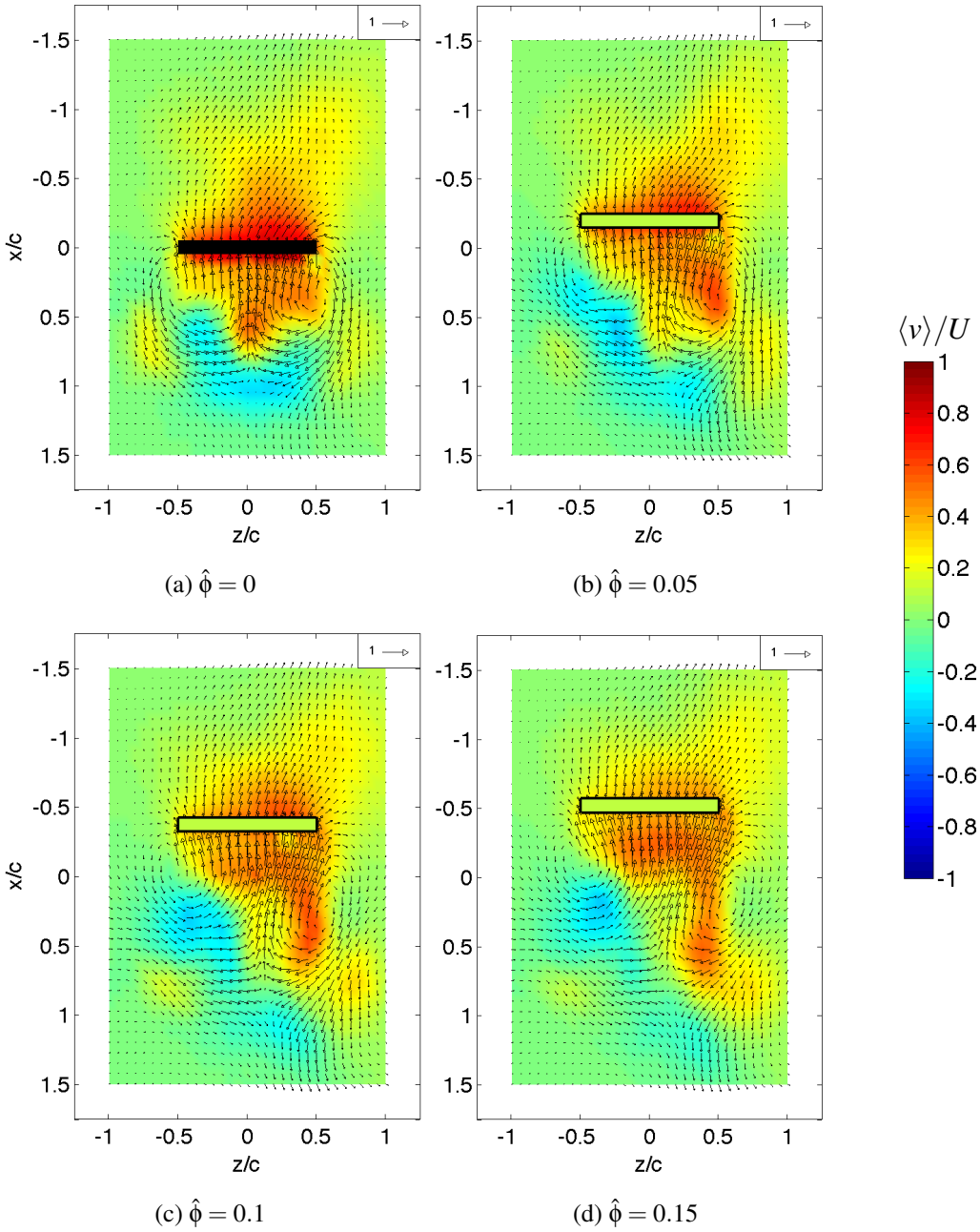

(a) $\hat{\phi} = 0$ (b) $\hat{\phi} = 0.05$

(c) $\hat{\phi} = 0.1$ (d) $\hat{\phi} = 0.15$

Figure A.6: Velocity distribution of Re=1580, $y = 0$. (*Continued*)

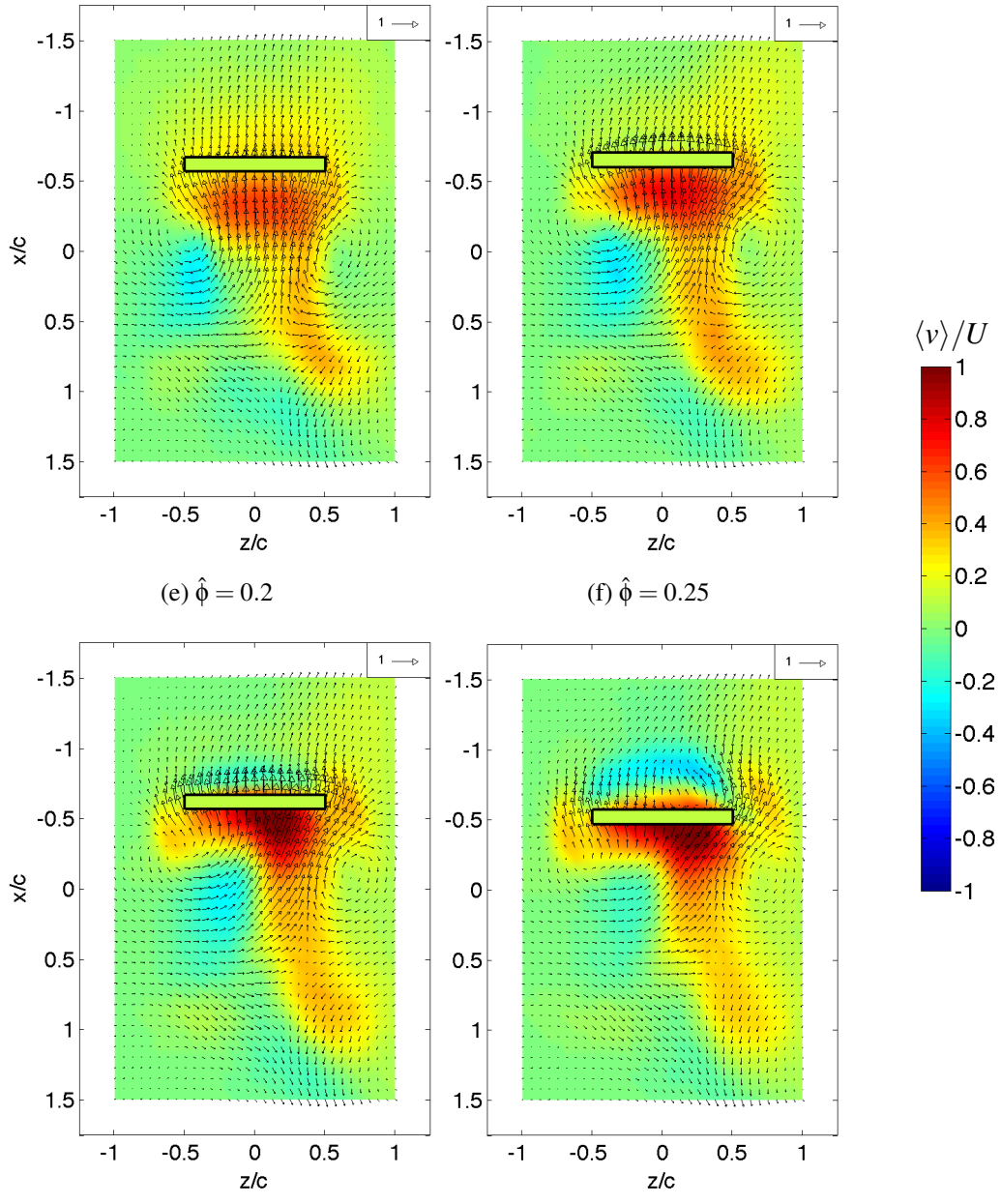

(e) $\hat{\phi} = 0.2$ (f) $\hat{\phi} = 0.25$

(g) $\hat{\phi} = 0.3$ (h) $\hat{\phi} = 0.35$

Figure A.6: Velocity distribution of Re=1580, $y = 0$. (*Continued*)

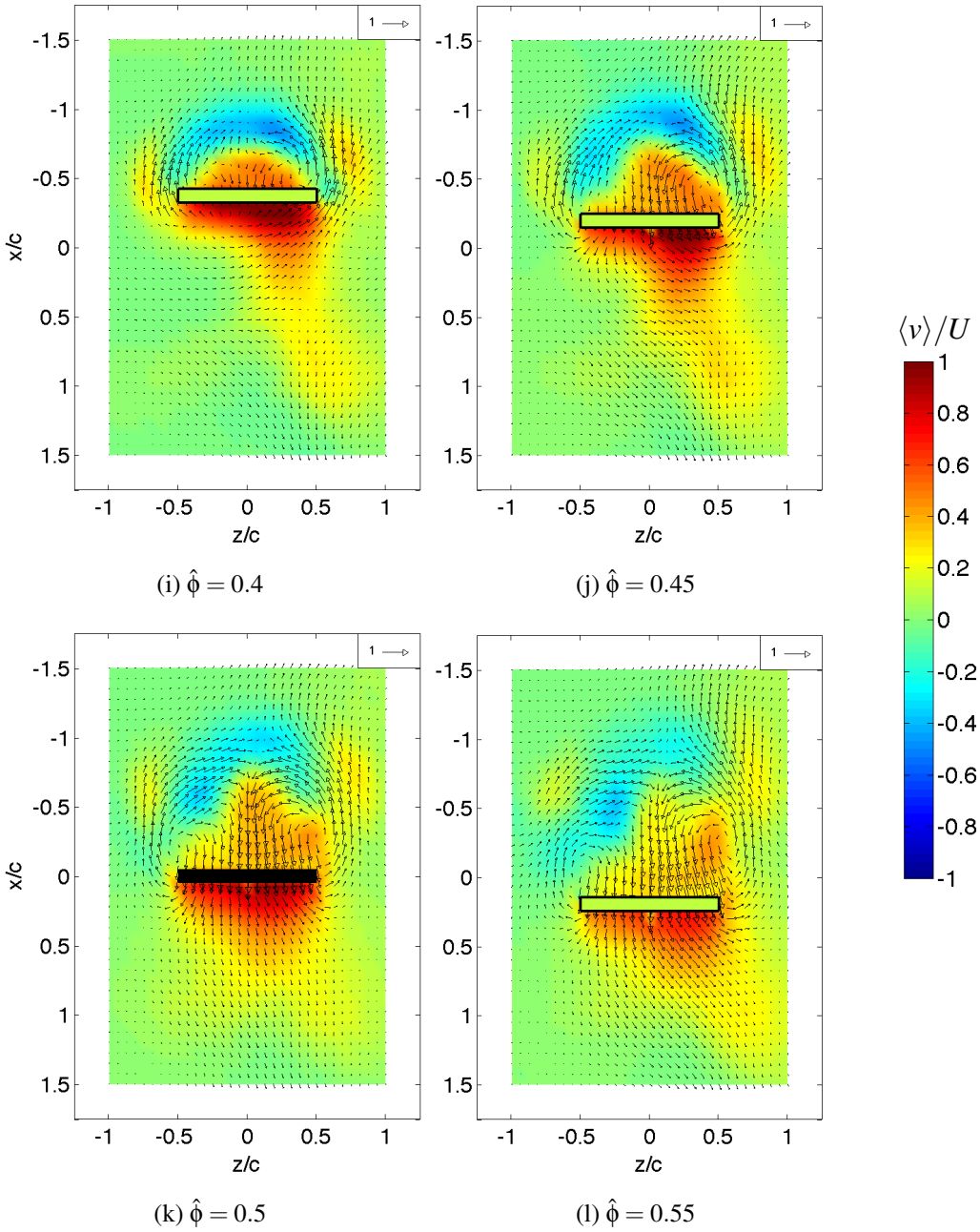

(i) $\hat{\phi} = 0.4$ (j) $\hat{\phi} = 0.45$

(k) $\hat{\phi} = 0.5$ (l) $\hat{\phi} = 0.55$

Figure A.6: Velocity distribution of Re=1580, $y = 0$. (*Continued*)

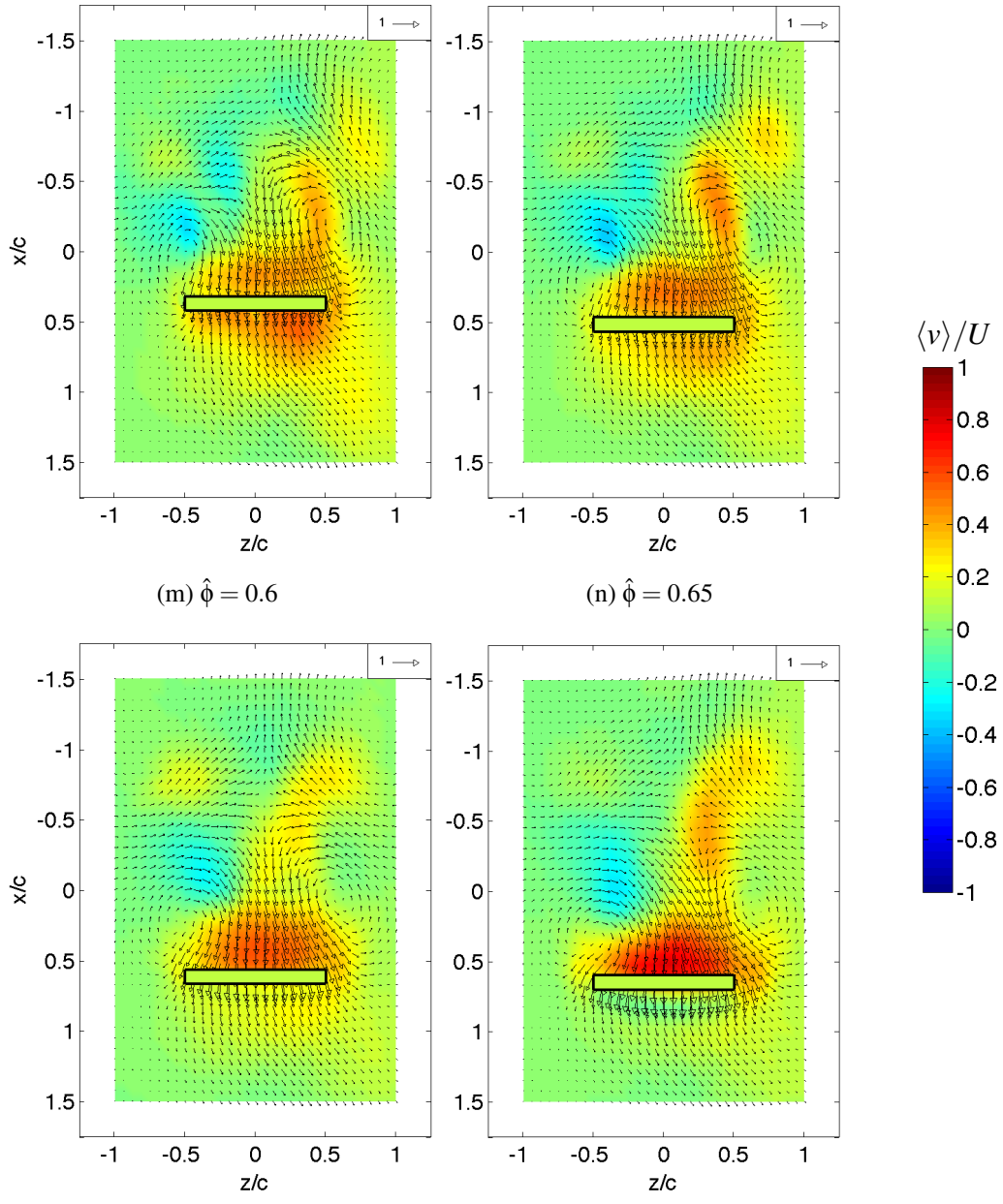

(m) $\hat{\phi} = 0.6$ (n) $\hat{\phi} = 0.65$

(o) $\hat{\phi} = 0.7$ (p) $\hat{\phi} = 0.75$

Figure A.6: Velocity distribution of Re=1580, $y = 0$. (*Continued*)

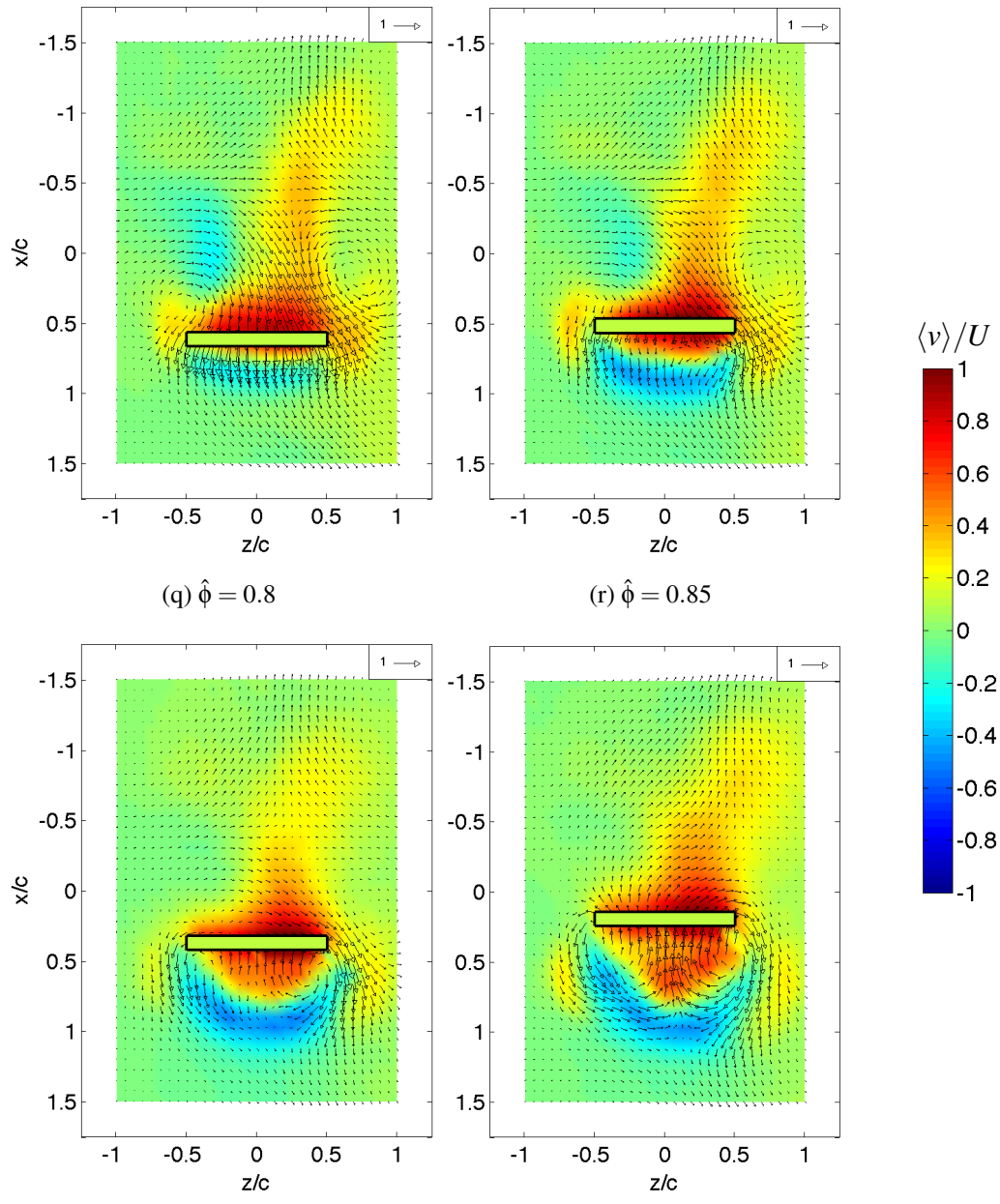

(q) $\hat{\phi} = 0.8$ (r) $\hat{\phi} = 0.85$

(s) $\hat{\phi} = 0.9$ (t) $\hat{\phi} = 0.95$

Figure A.6: Velocity distribution of Re=1580, $y = 0$.

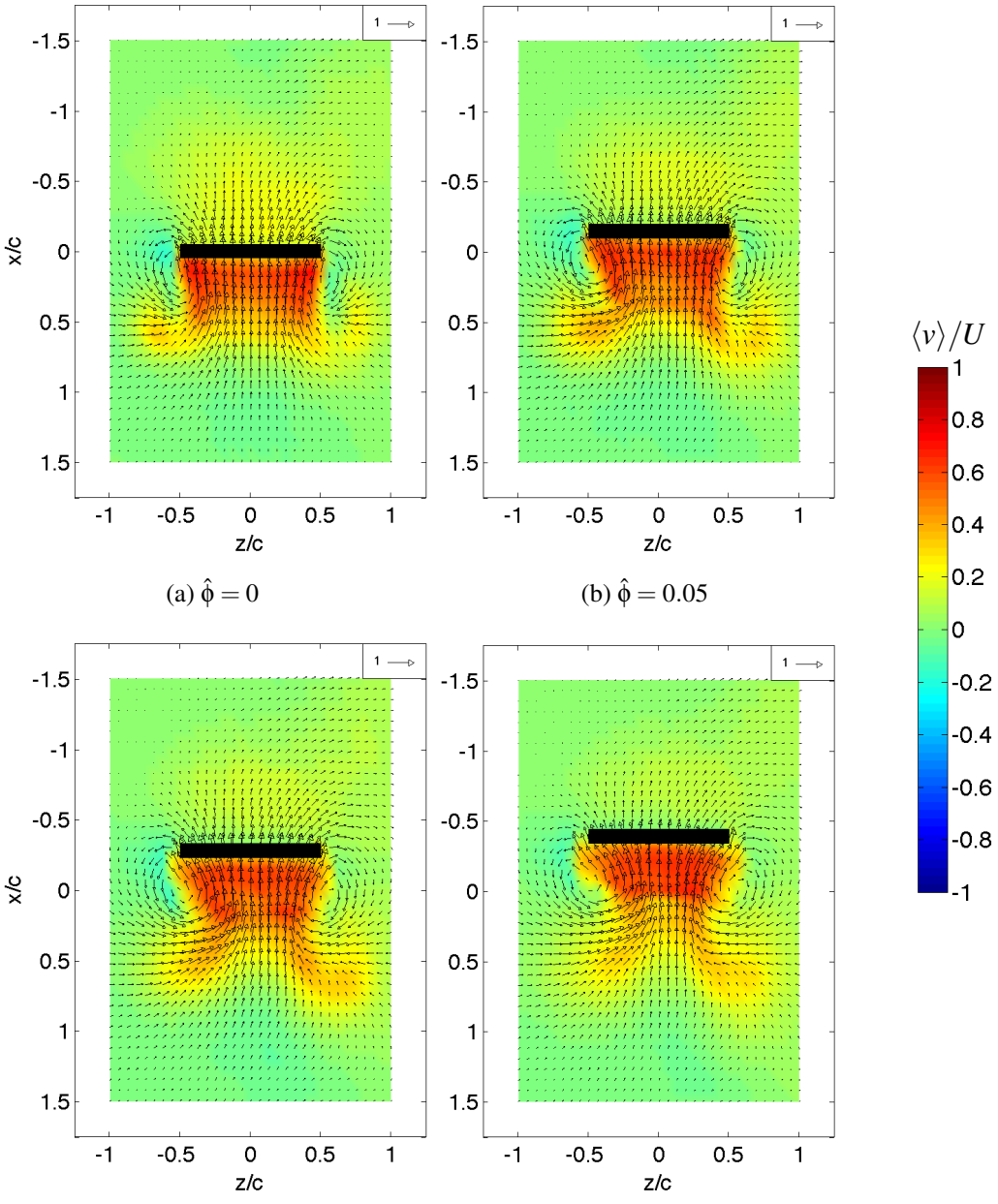

(a) $\hat{\phi} = 0$ (b) $\hat{\phi} = 0.05$

(c) $\hat{\phi} = 0.1$ (d) $\hat{\phi} = 0.15$

Figure A.7: Velocity distribution of Re=3160, $y = -c/2$. (*Continued*)

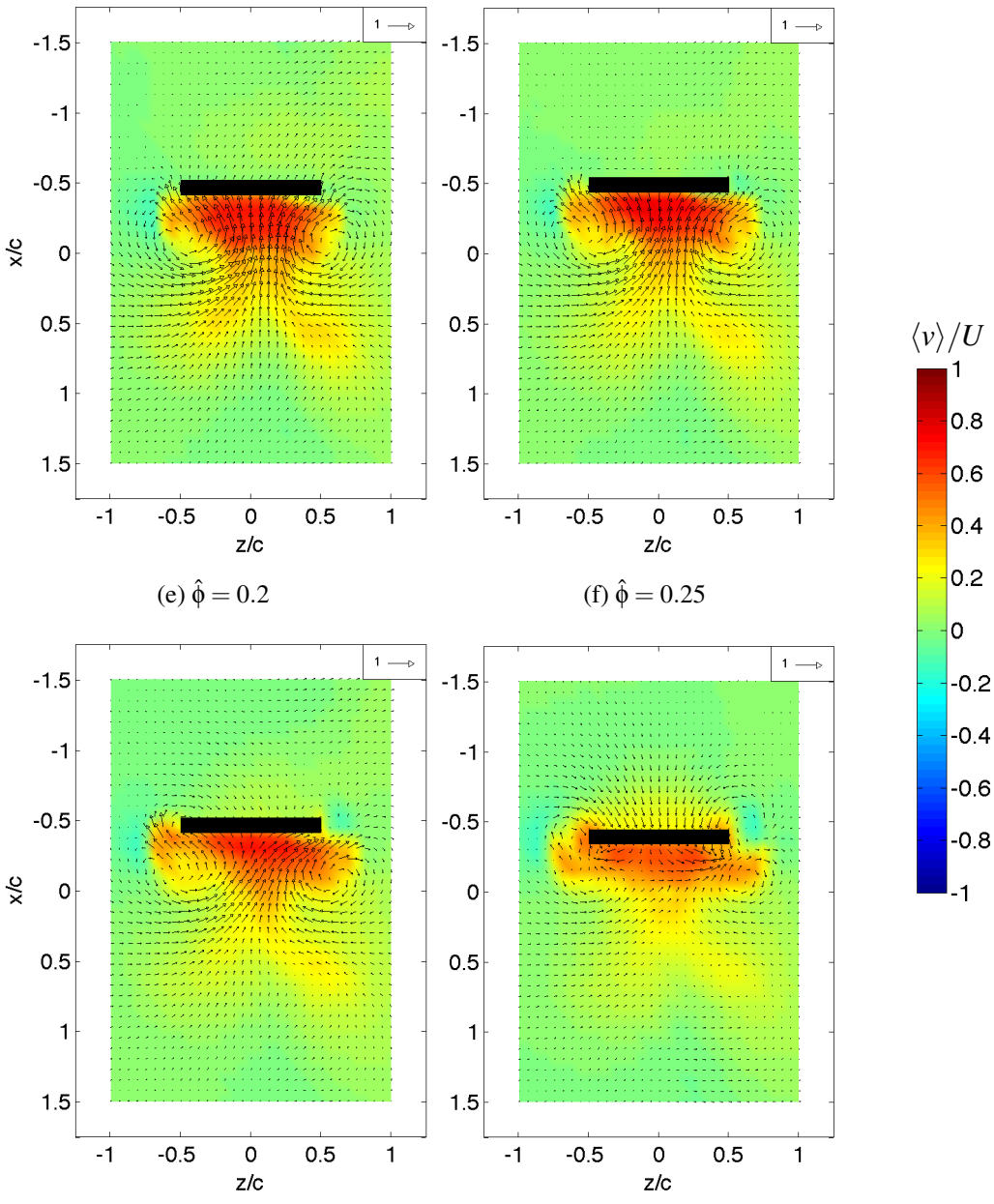

(e) $\hat{\phi} = 0.2$ (f) $\hat{\phi} = 0.25$

(g) $\hat{\phi} = 0.3$ (h) $\hat{\phi} = 0.35$

Figure A.7: Velocity distribution of Re=3160, $y = -c/2$. (*Continued*)

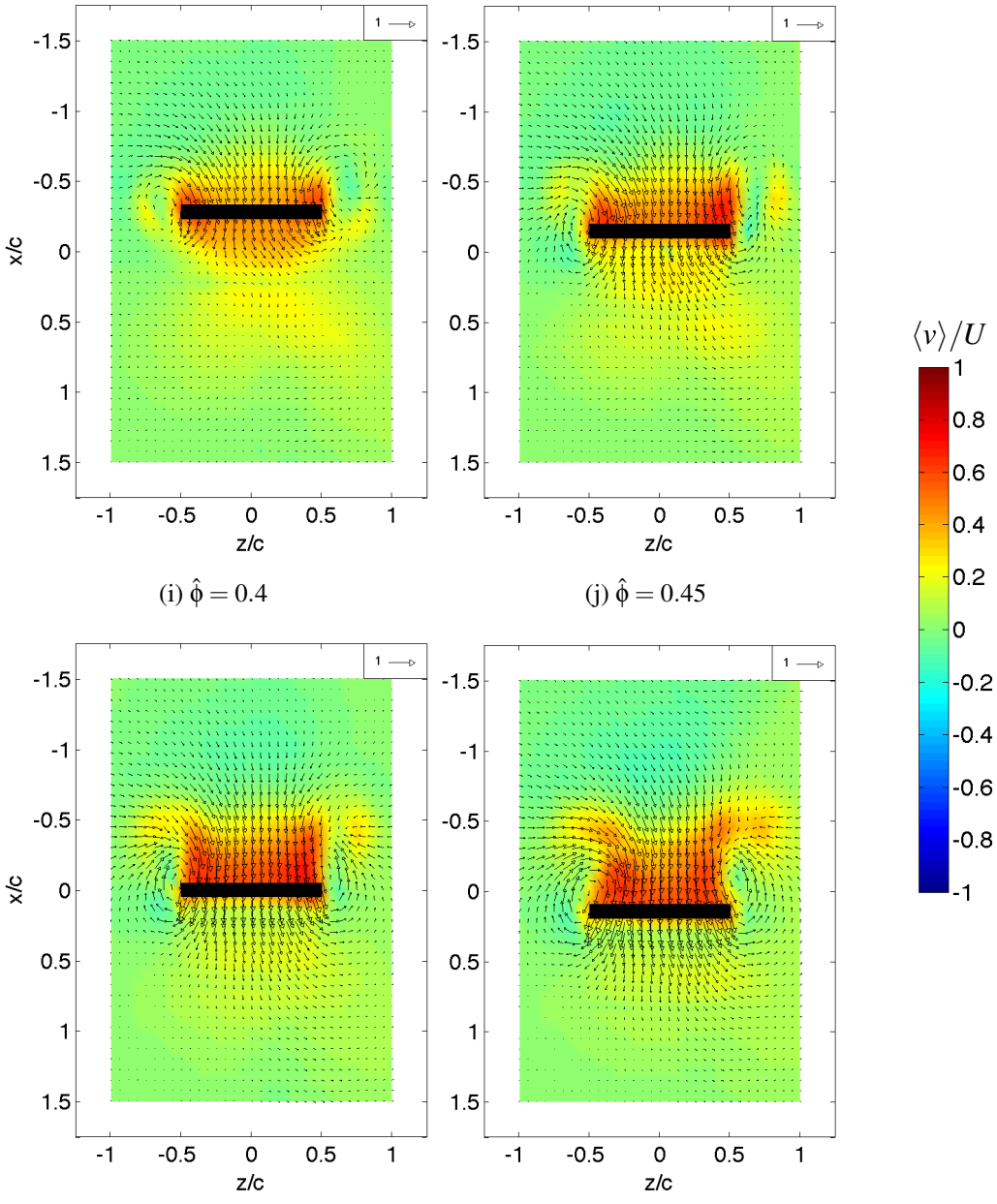

(i) $\hat{\phi} = 0.4$ (j) $\hat{\phi} = 0.45$

(k) $\hat{\phi} = 0.5$ (l) $\hat{\phi} = 0.55$

Figure A.7: Velocity distribution of Re=3160, $y = -c/2$. (*Continued*)

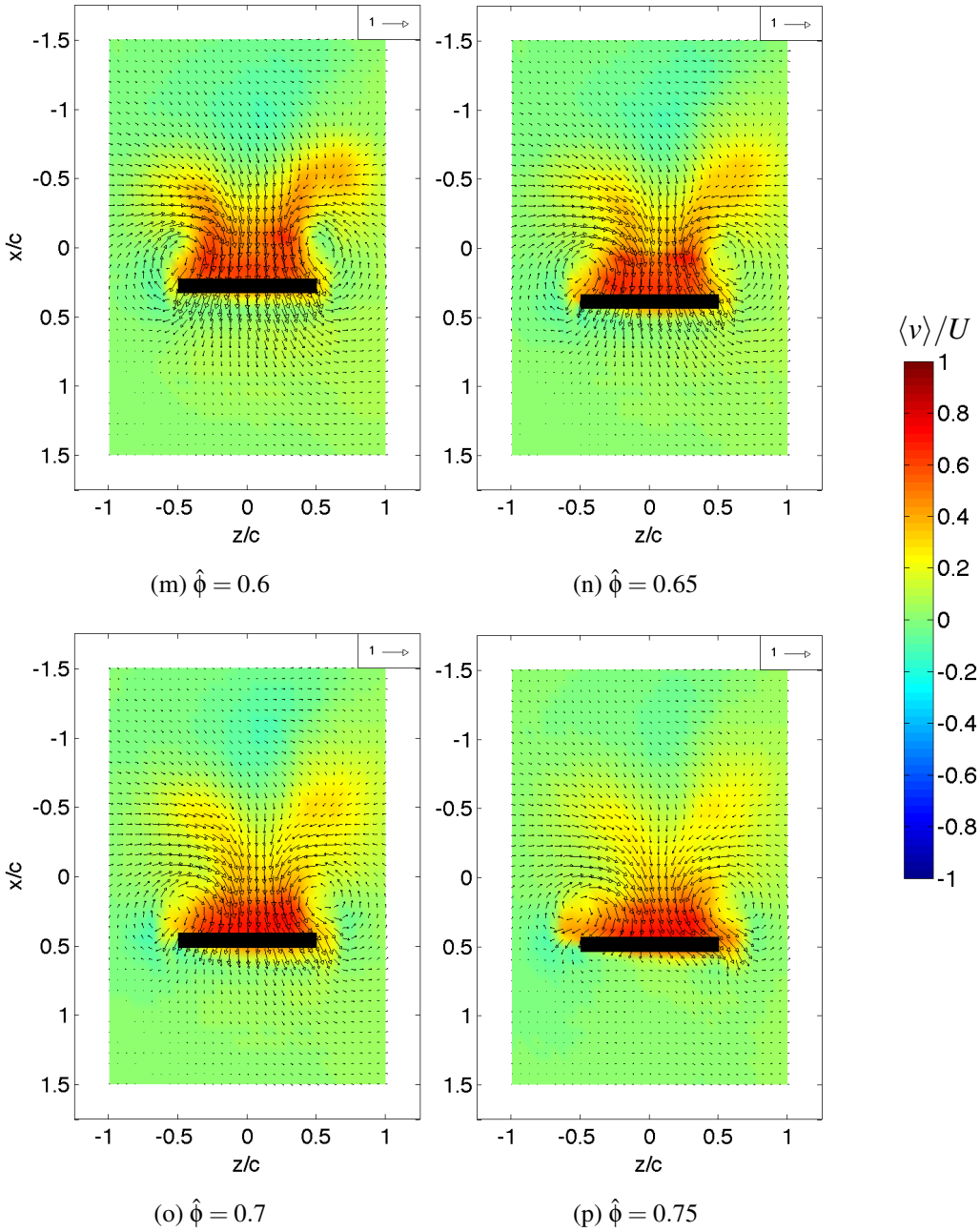

(m) $\hat{\phi} = 0.6$ (n) $\hat{\phi} = 0.65$

(o) $\hat{\phi} = 0.7$ (p) $\hat{\phi} = 0.75$

Figure A.7: Velocity distribution of Re=3160, $y = -c/2$. (*Continued*)

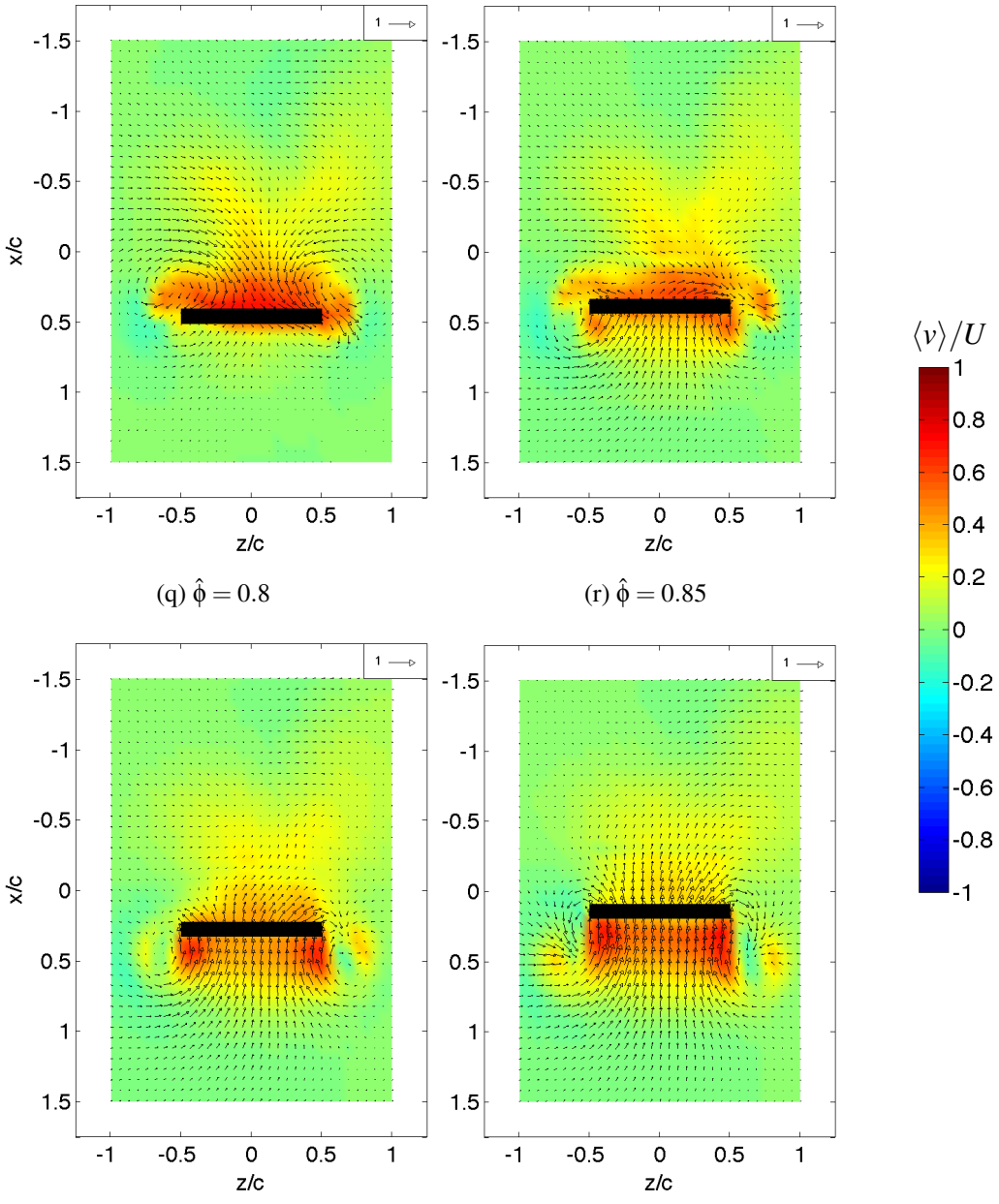

(q) $\hat{\phi} = 0.8$ (r) $\hat{\phi} = 0.85$

(s) $\hat{\phi} = 0.9$ (t) $\hat{\phi} = 0.95$

Figure A.7: Velocity distribution of Re=3160, $y = -c/2$.

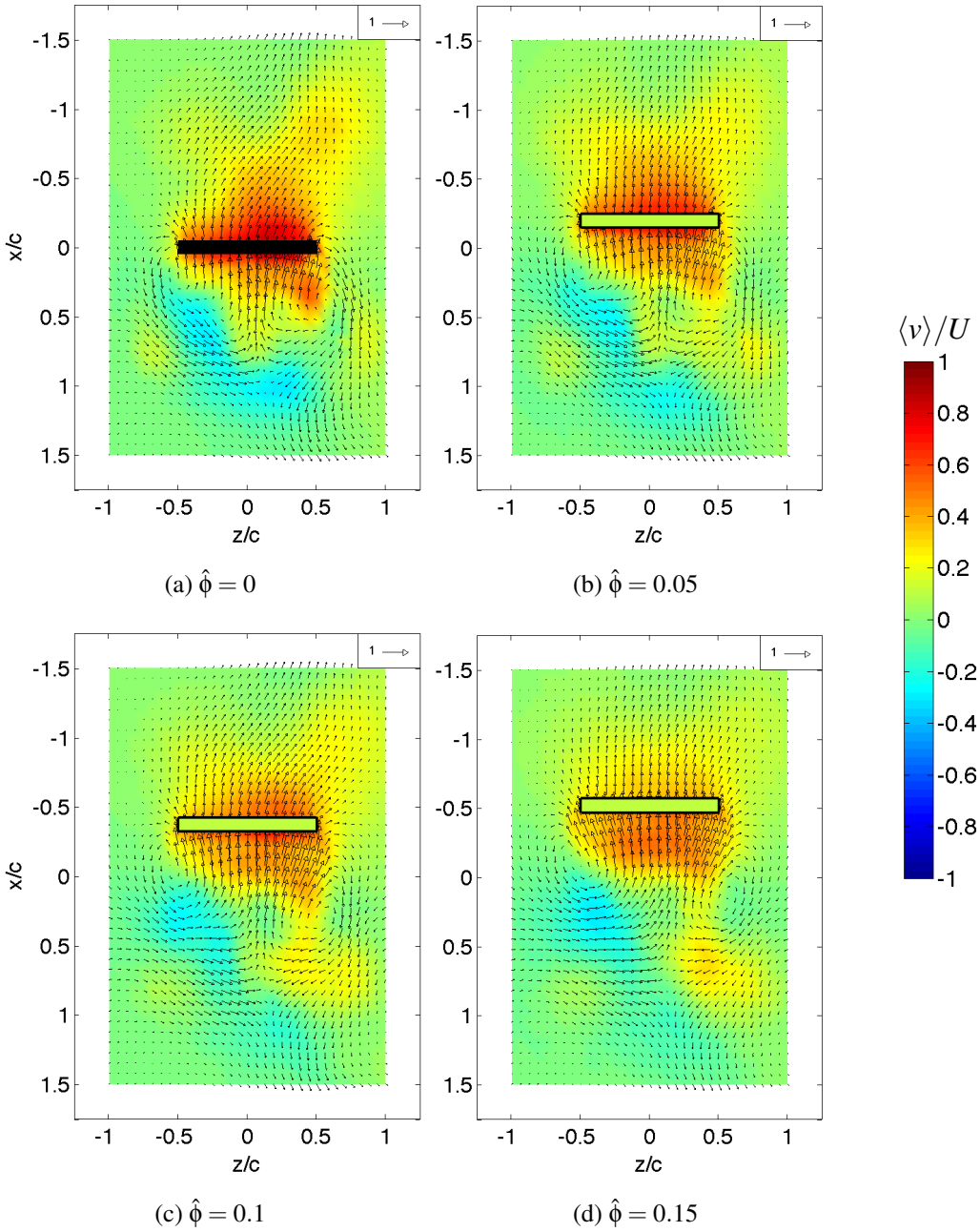

(a) $\hat{\phi} = 0$ (b) $\hat{\phi} = 0.05$

(c) $\hat{\phi} = 0.1$ (d) $\hat{\phi} = 0.15$

Figure A.8: Velocity distribution of Re=3160, $y = 0$. (*Continued*)

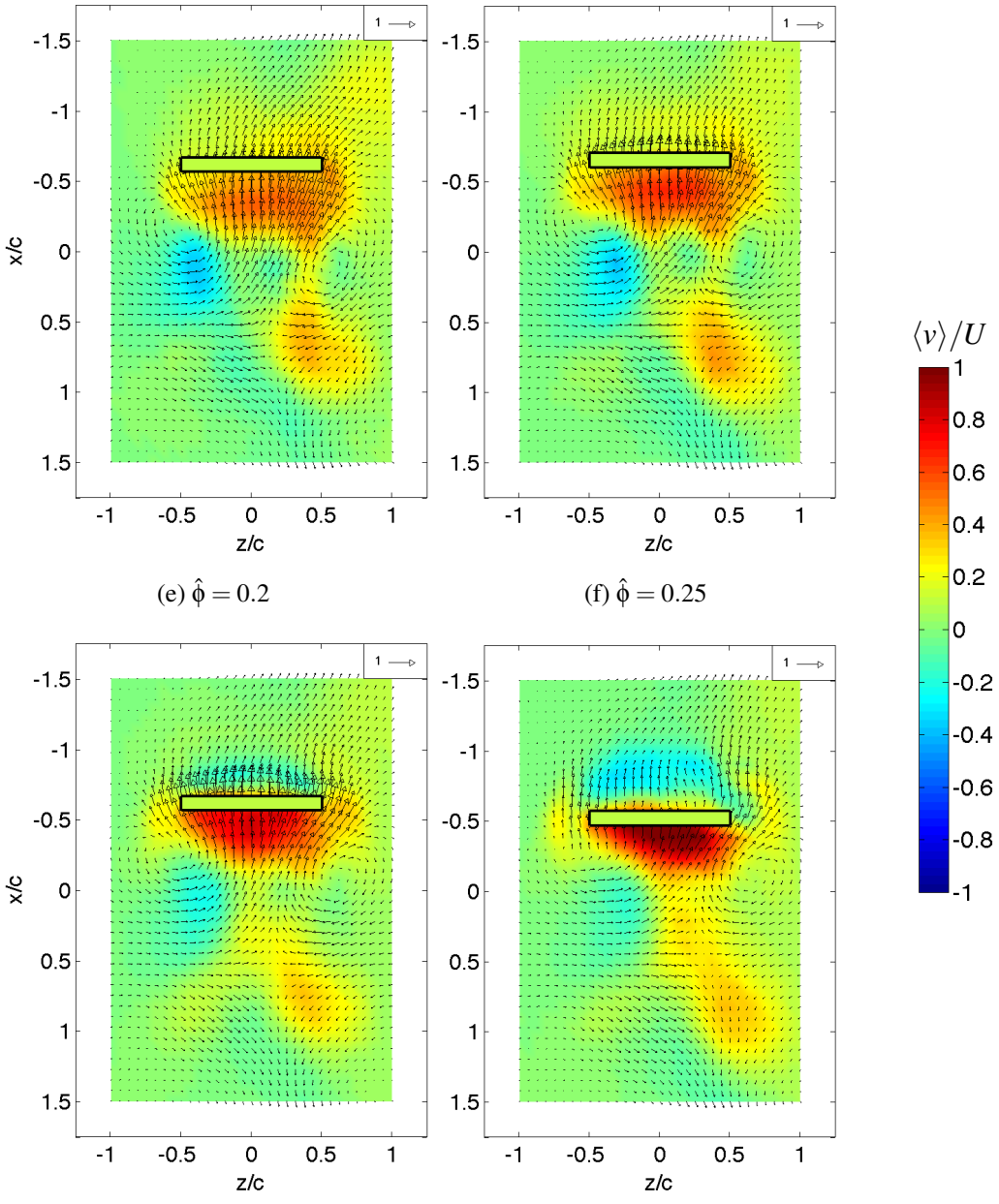

(e) $\hat{\phi} = 0.2$ (f) $\hat{\phi} = 0.25$

(g) $\hat{\phi} = 0.3$ (h) $\hat{\phi} = 0.35$

Figure A.8: Velocity distribution of Re=3160, $y = 0$. (*Continued*)

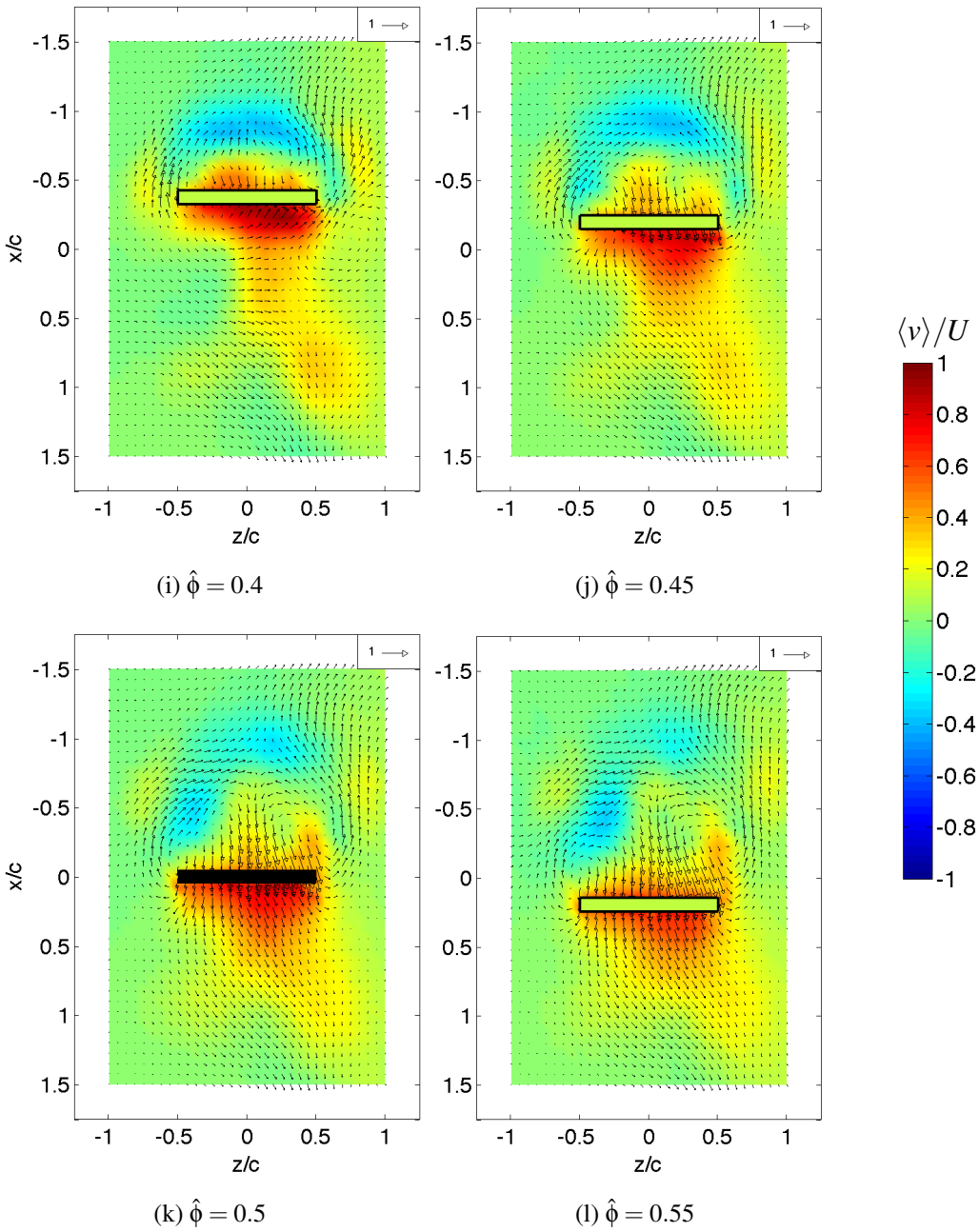

(i) $\hat{\phi} = 0.4$ (j) $\hat{\phi} = 0.45$

(k) $\hat{\phi} = 0.5$ (l) $\hat{\phi} = 0.55$

Figure A.8: Velocity distribution of Re=3160, $y = 0$. (*Continued*)

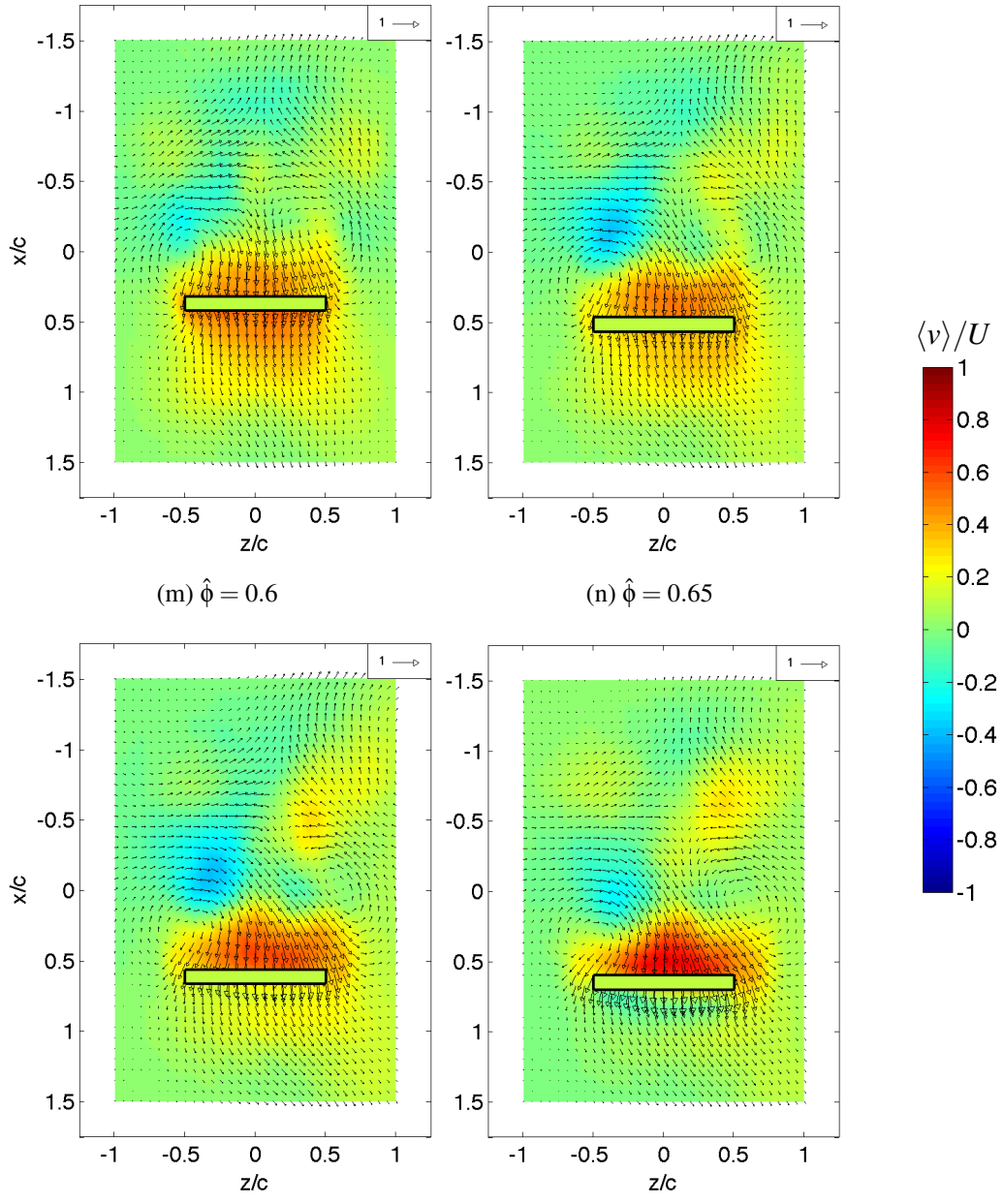

(m) $\hat{\phi} = 0.6$ (n) $\hat{\phi} = 0.65$

(o) $\hat{\phi} = 0.7$ (p) $\hat{\phi} = 0.75$

Figure A.8: Velocity distribution of Re=3160, $y = 0$. (*Continued*)

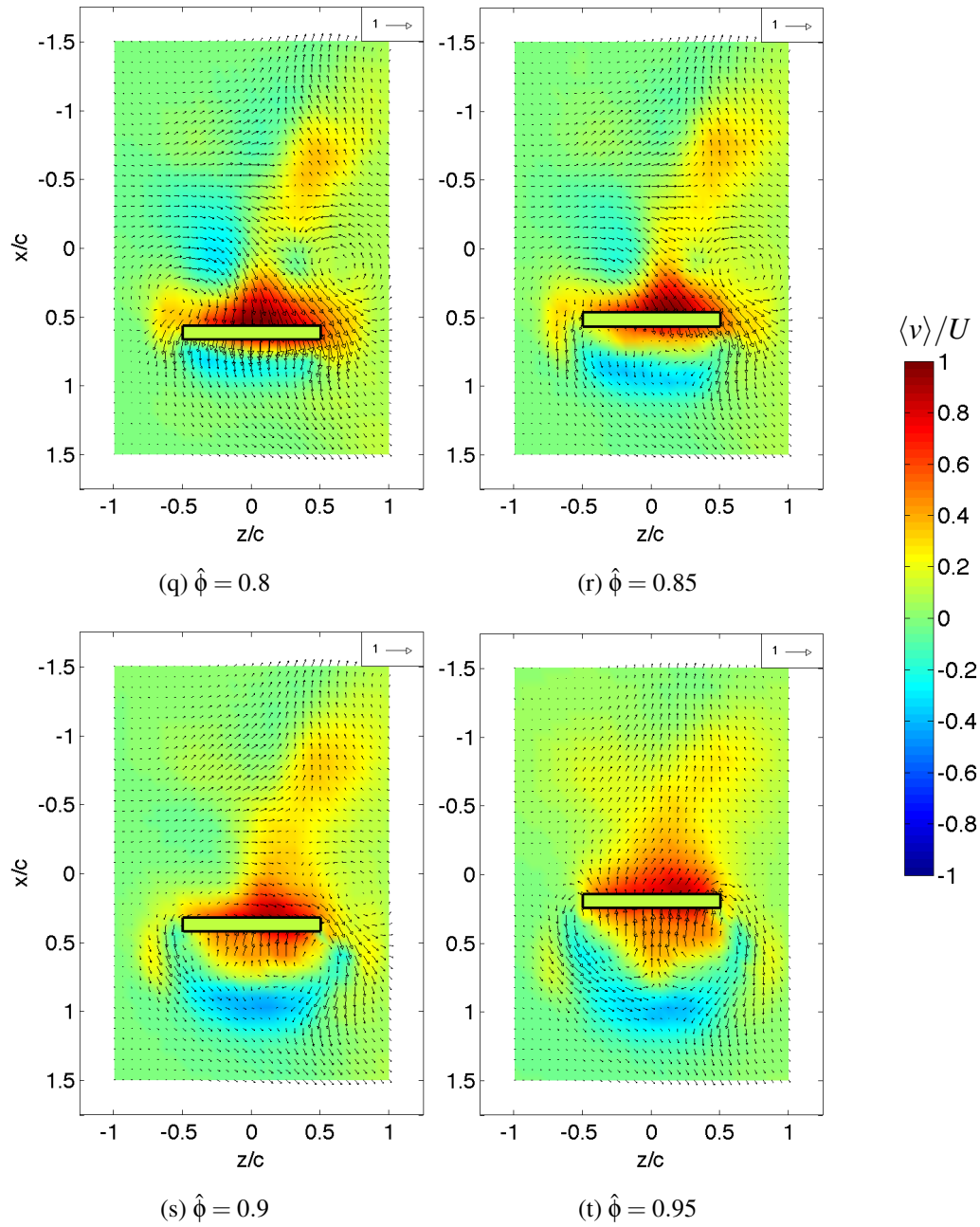

(q) $\hat{\phi} = 0.8$ (r) $\hat{\phi} = 0.85$

(s) $\hat{\phi} = 0.9$ (t) $\hat{\phi} = 0.95$

Figure A.8: Velocity distribution of Re=3160, $y = 0$.

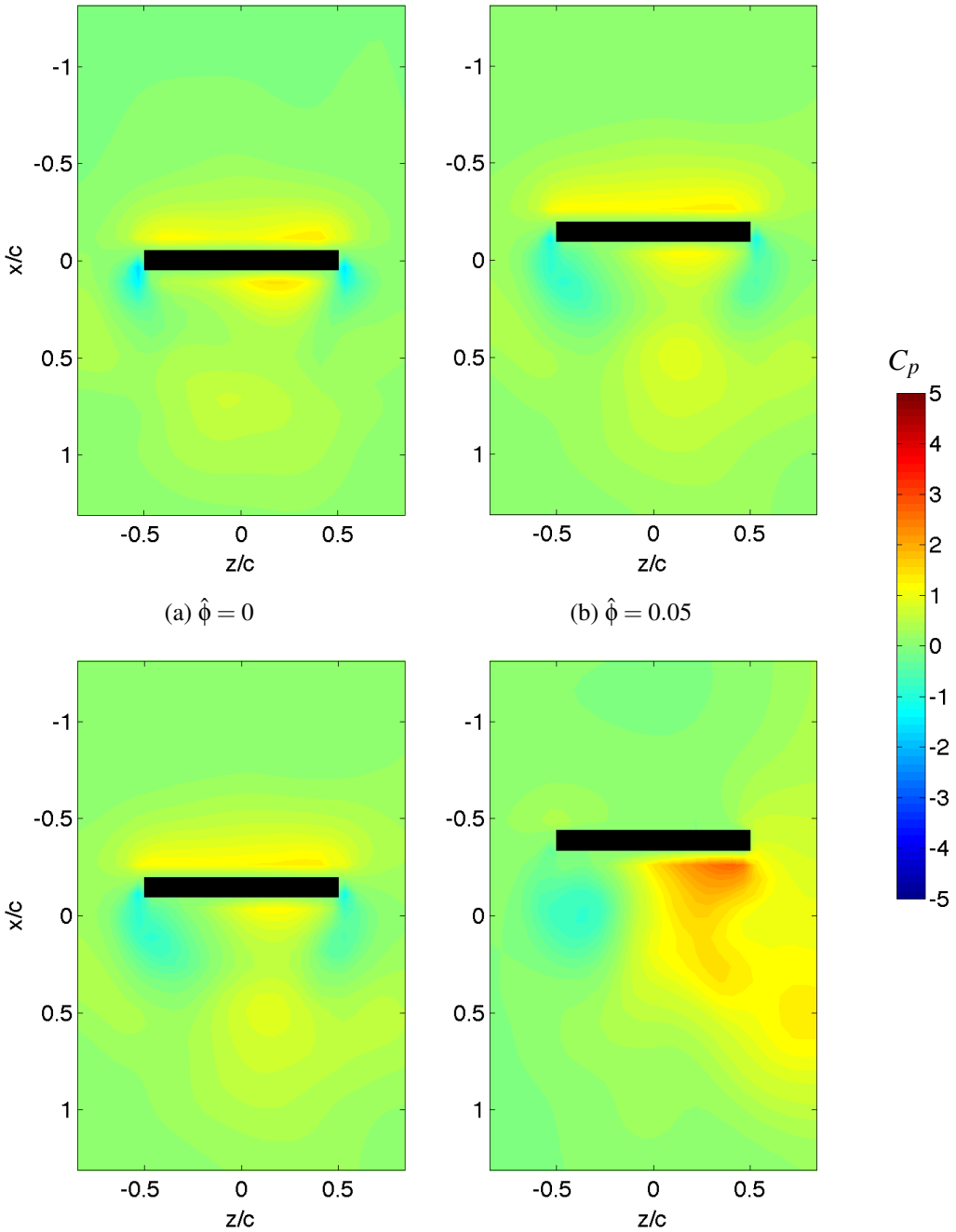

(a) $\hat{\phi} = 0$ (b) $\hat{\phi} = 0.05$

(c) $\hat{\phi} = 0.1$ (d) $\hat{\phi} = 0.15$

Figure A.9: Pressure distribution of Re=3160, $y = -c/2$. (*Continued*)

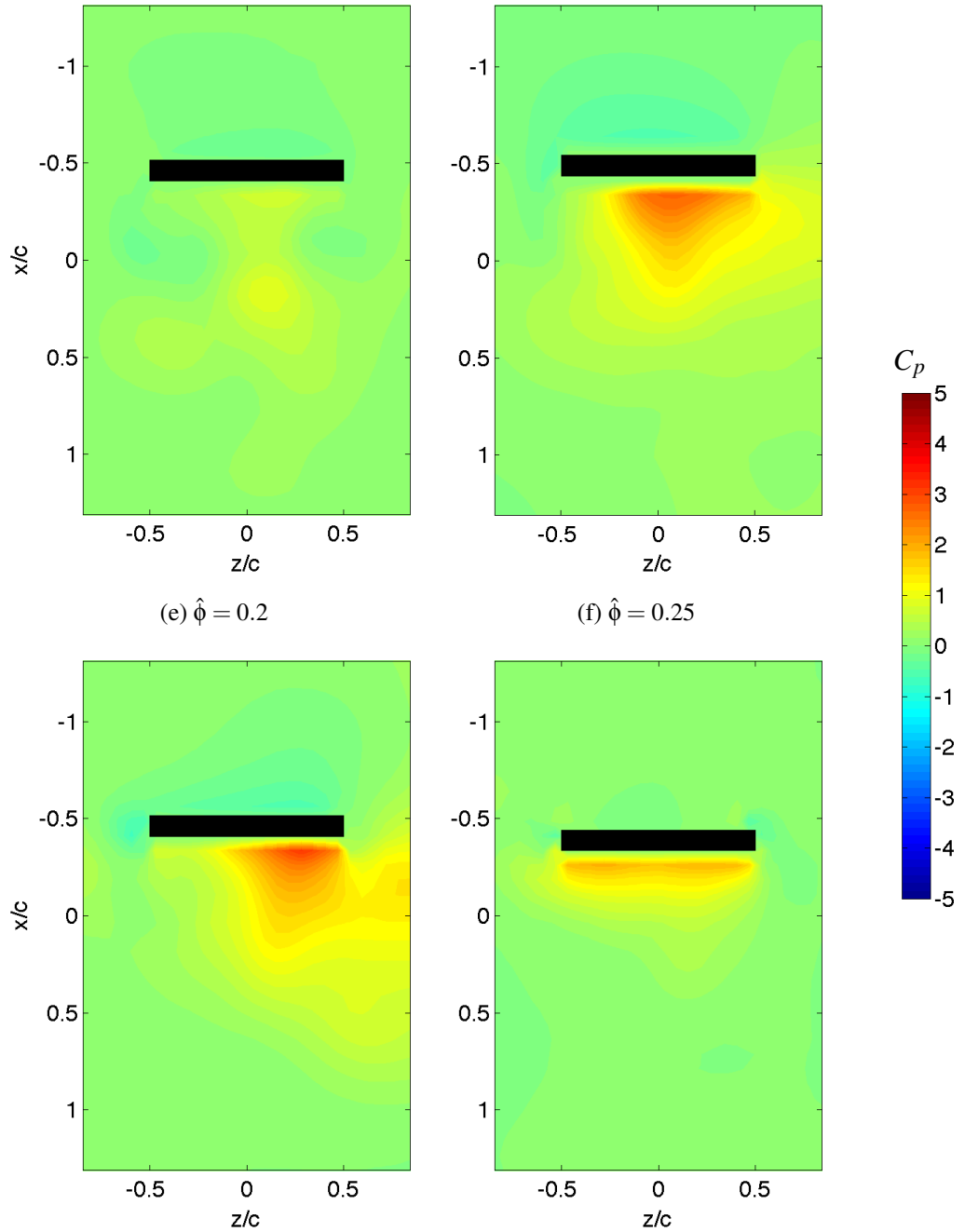

(e) $\hat{\phi} = 0.2$

(f) $\hat{\phi} = 0.25$

(g) $\hat{\phi} = 0.3$

(h) $\hat{\phi} = 0.35$

Figure A.9: Pressure distribution of Re=3160, $y = -c/2$. (*Continued*)

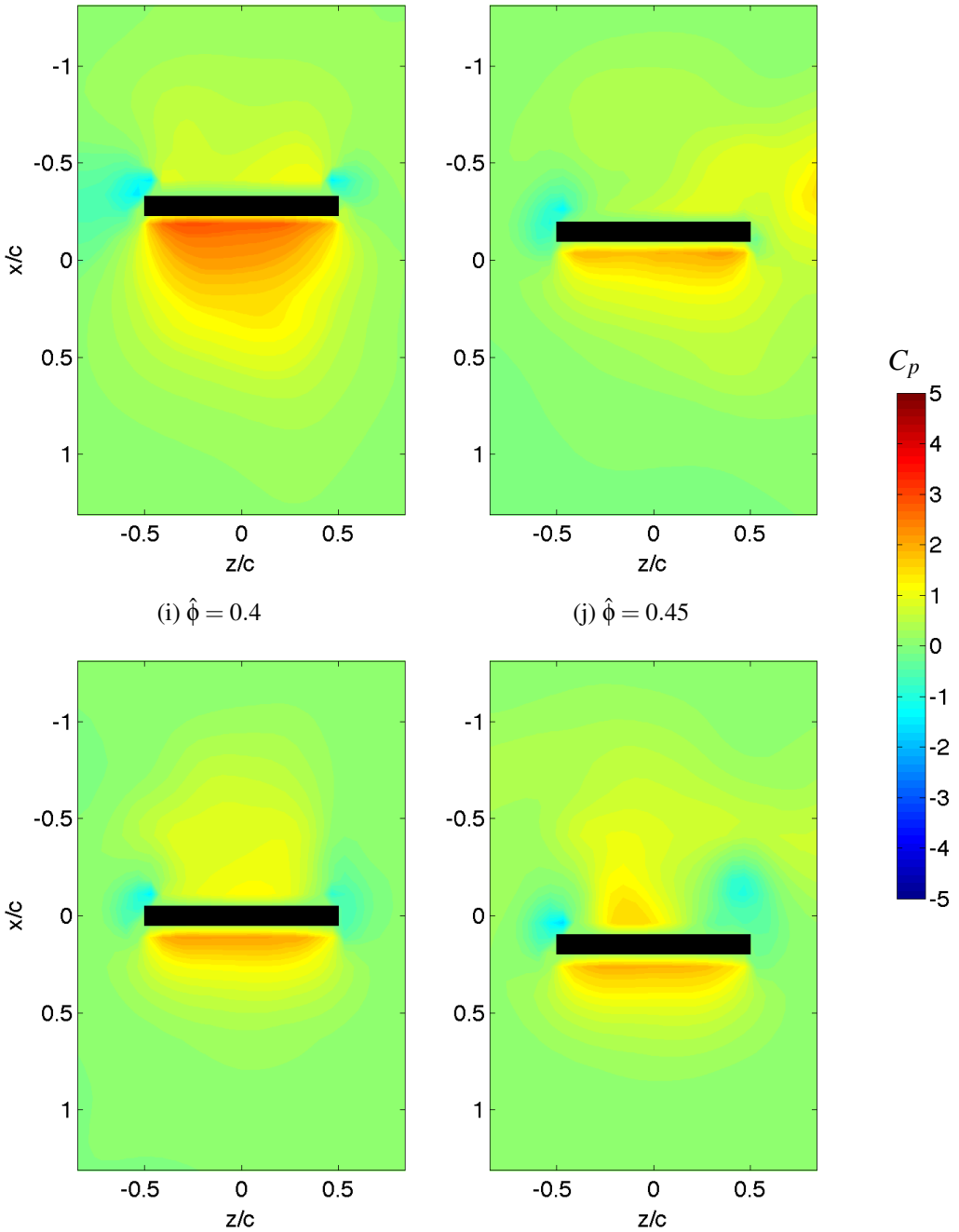

(i) $\hat{\phi} = 0.4$ (j) $\hat{\phi} = 0.45$

(k) $\hat{\phi} = 0.5$ (l) $\hat{\phi} = 0.55$

Figure A.9: Pressure distribution of Re=3160, $y = -c/2$. (*Continued*)

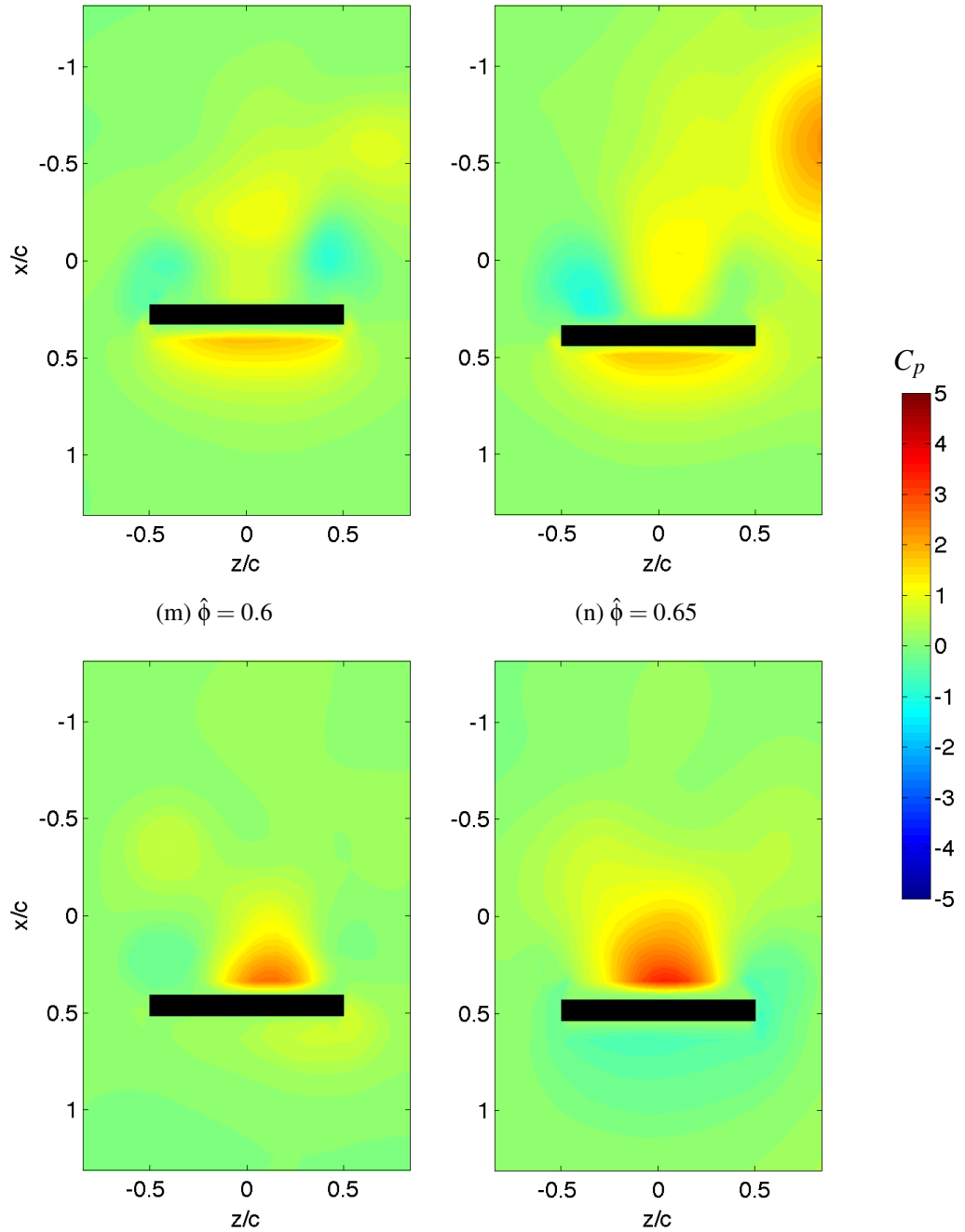

(m) $\hat{\phi} = 0.6$ (n) $\hat{\phi} = 0.65$

(o) $\hat{\phi} = 0.7$ (p) $\hat{\phi} = 0.75$

Figure A.9: Pressure distribution of Re=3160, $y = -c/2$. (*Continued*)

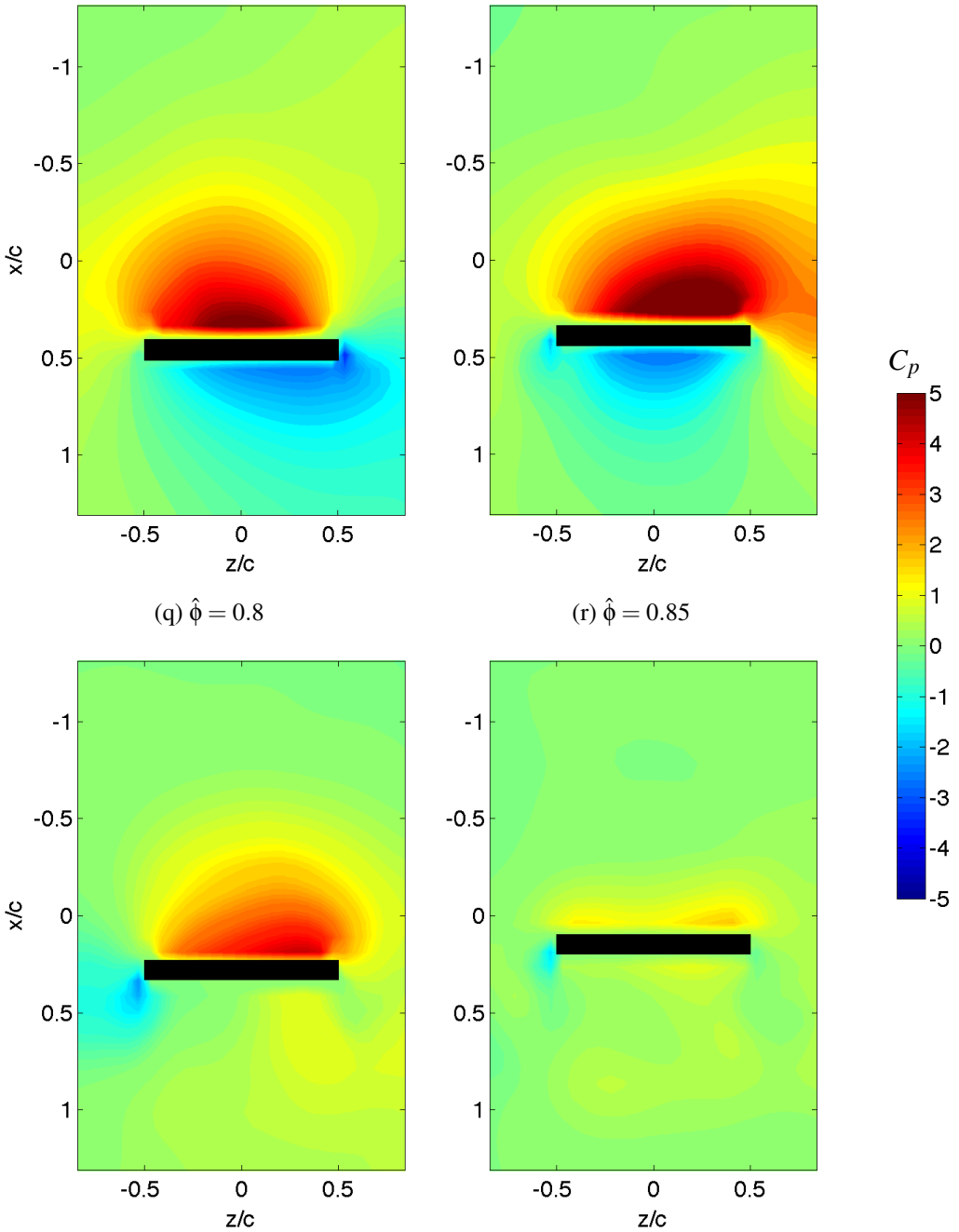

(q) $\hat{\phi} = 0.8$ (r) $\hat{\phi} = 0.85$

(s) $\hat{\phi} = 0.9$ (t) $\hat{\phi} = 0.95$

Figure A.9: Pressure distribution of Re=3160, $y = -c/2$.

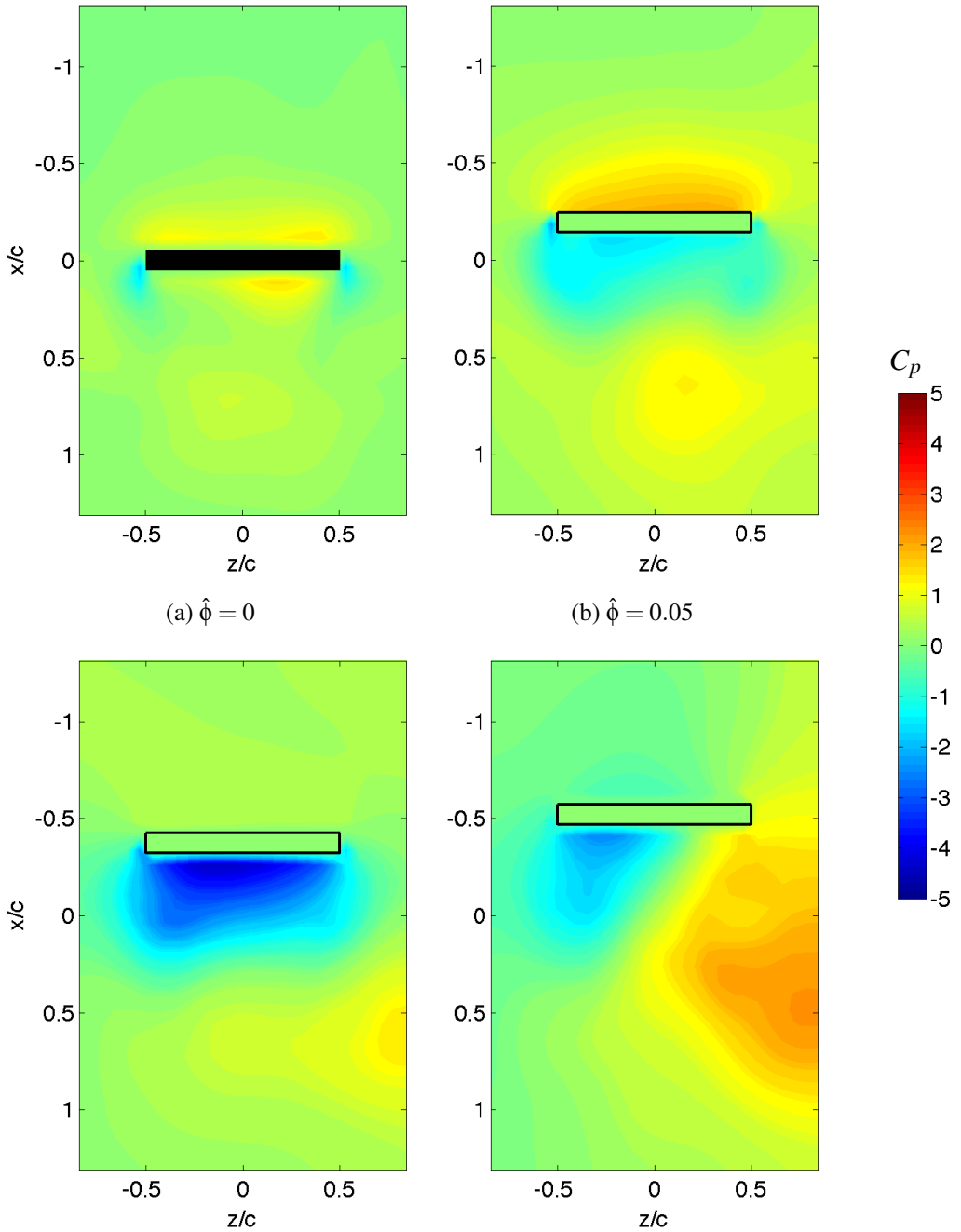

(a) $\hat{\phi} = 0$ (b) $\hat{\phi} = 0.05$

(c) $\hat{\phi} = 0.1$ (d) $\hat{\phi} = 0.15$

Figure A.10: Pressure distribution of Re=3160, $y = 0$. (*Continued*)

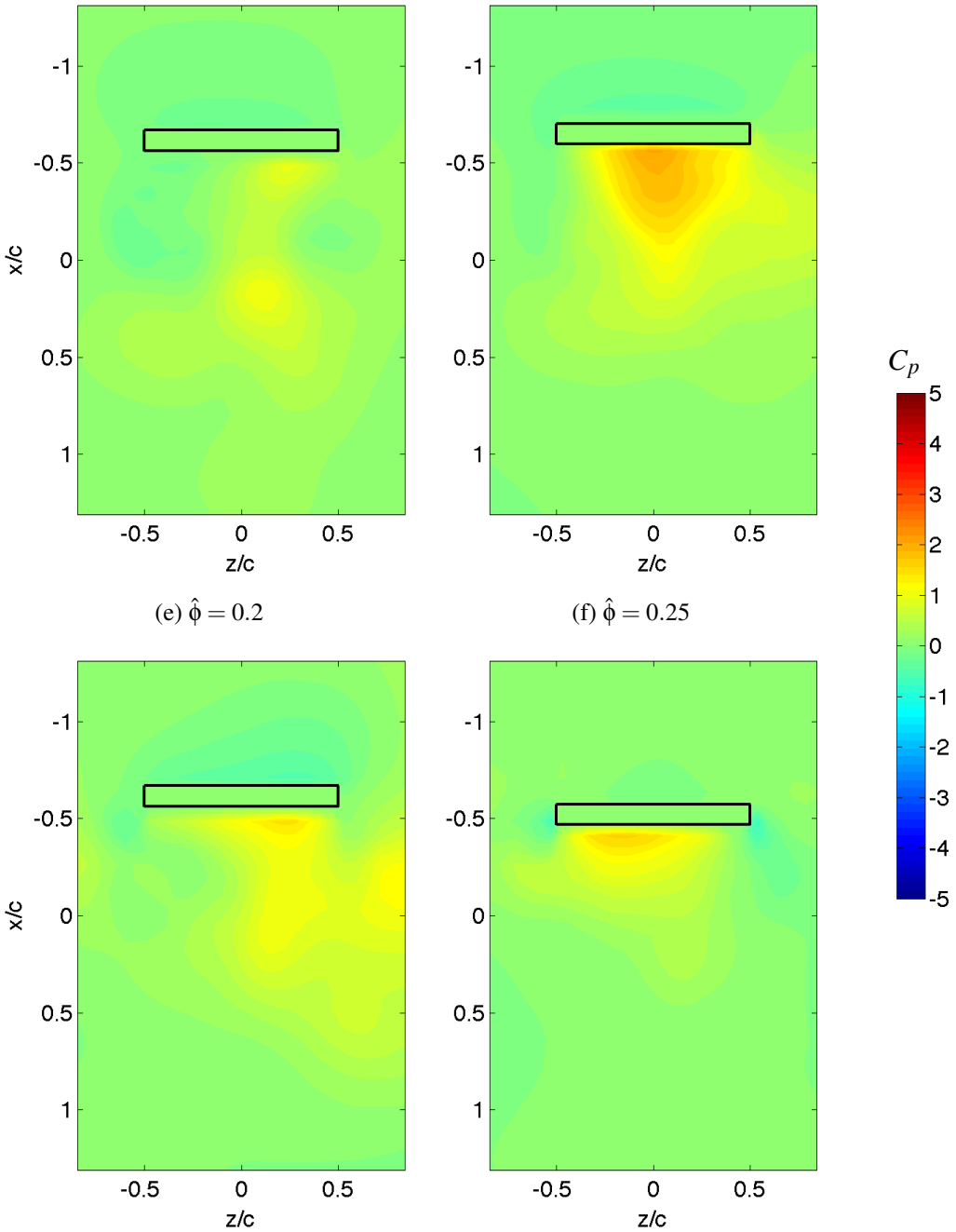

(e) $\hat{\phi} = 0.2$ (f) $\hat{\phi} = 0.25$

(g) $\hat{\phi} = 0.3$ (h) $\hat{\phi} = 0.35$

Figure A.10: Pressure distribution of Re=3160, $y = 0$. (*Continued*)

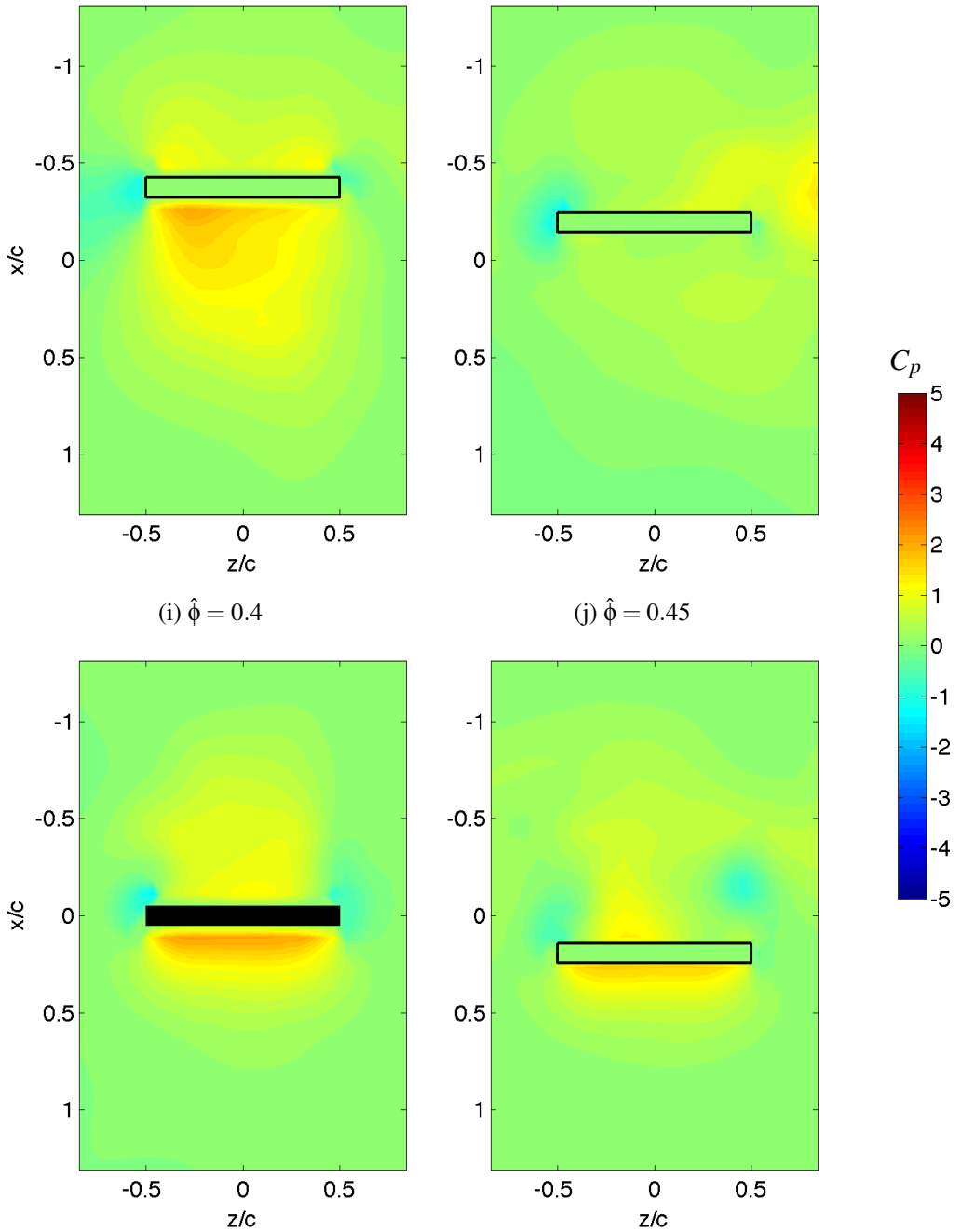

(i) $\hat{\phi} = 0.4$

(j) $\hat{\phi} = 0.45$

(k) $\hat{\phi} = 0.5$

(l) $\hat{\phi} = 0.55$

Figure A.10: Pressure distribution of Re=3160, $y = 0$. (*Continued*)

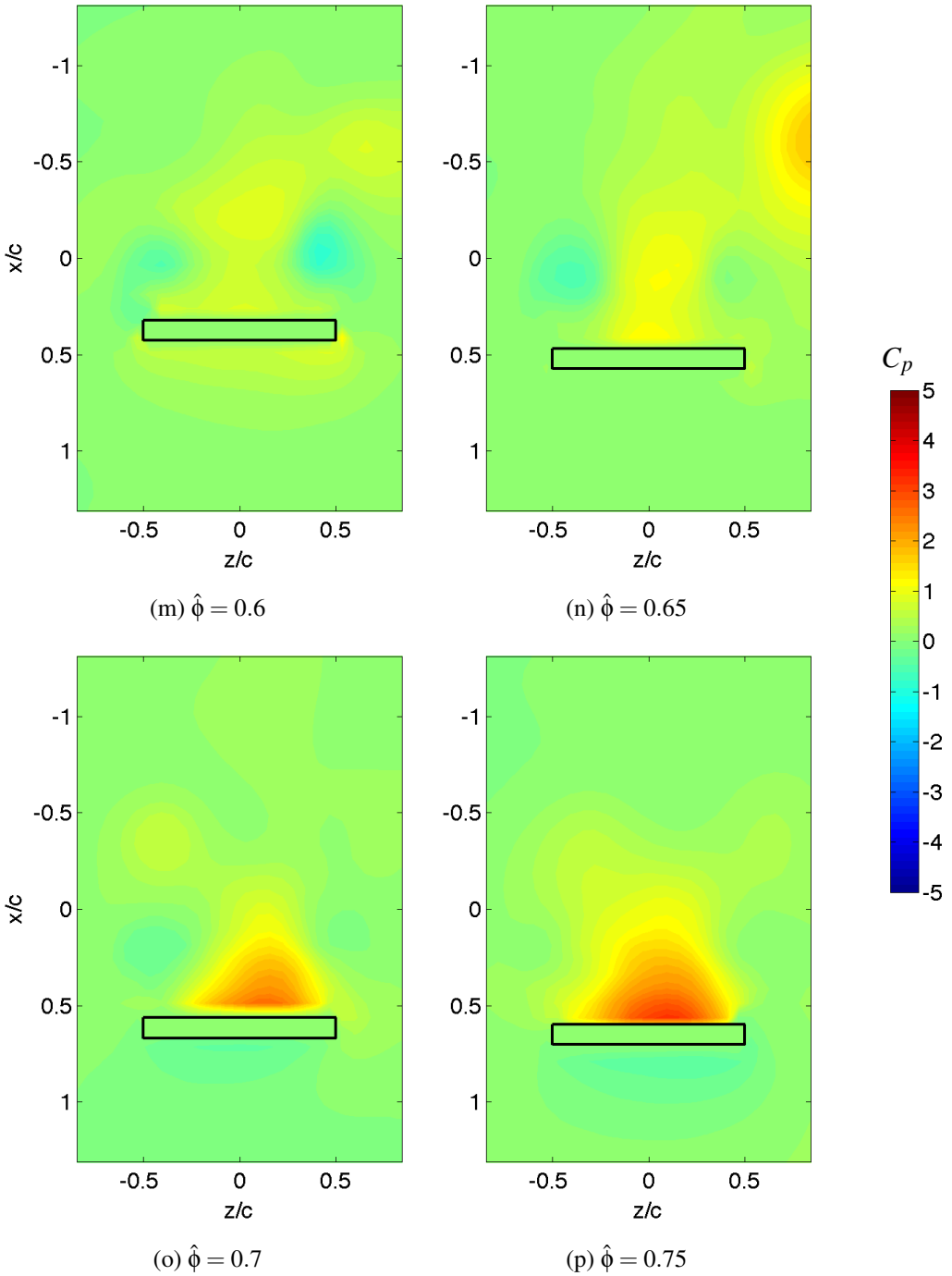

(m) $\hat{\phi} = 0.6$ (n) $\hat{\phi} = 0.65$

(o) $\hat{\phi} = 0.7$ (p) $\hat{\phi} = 0.75$

Figure A.10: Pressure distribution of Re=3160, $y = 0$. (*Continued*)

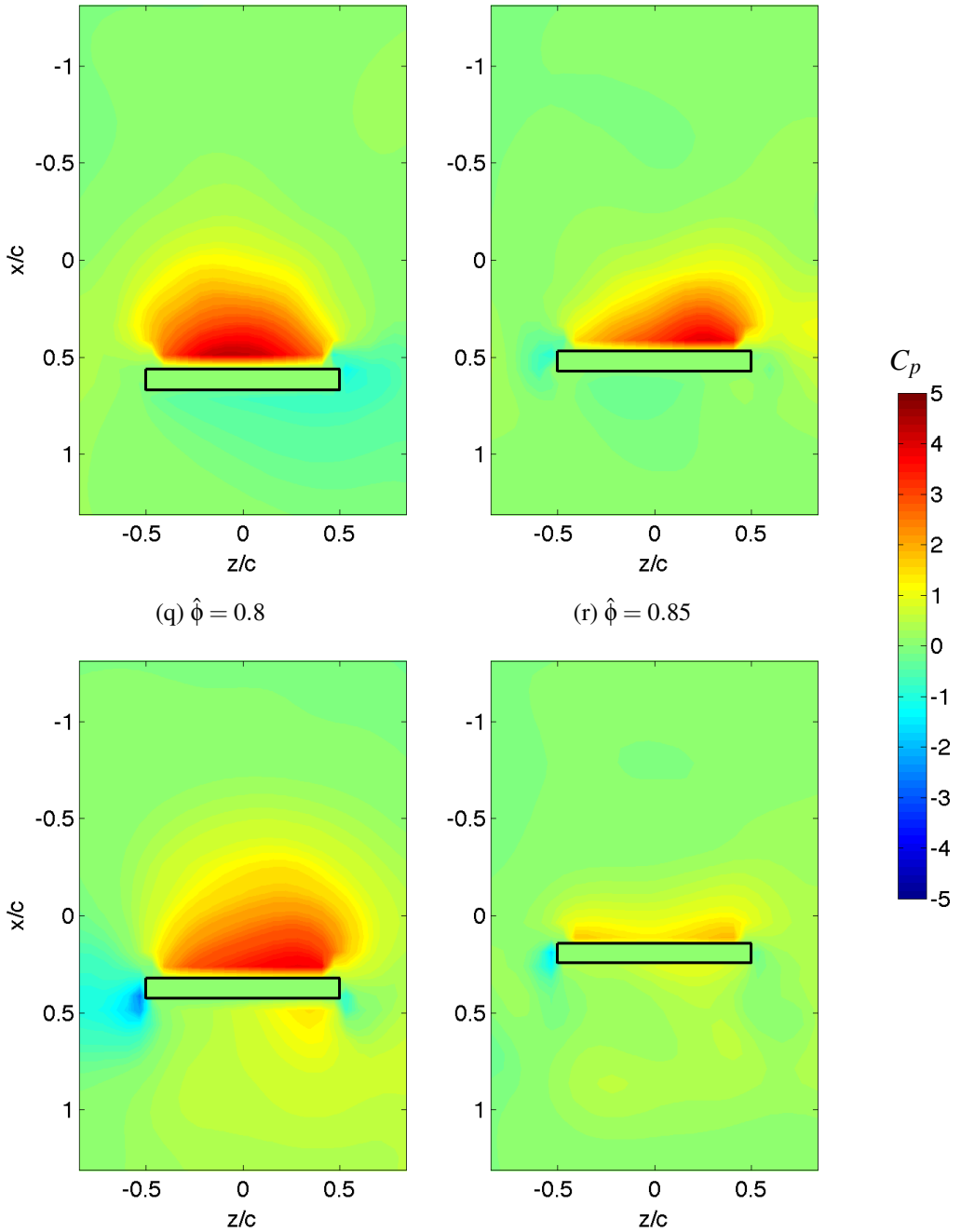

(q) $\hat{\phi} = 0.8$

(r) $\hat{\phi} = 0.85$

(s) $\hat{\phi} = 0.9$

(t) $\hat{\phi} = 0.95$

Figure A.10: Pressure distribution of Re=3160, $y = 0$.

Appendix B

Poisson solver for circular cylinder in potential flow

```
clear;
clf;

eps = 1e-12;

%% flow domain
dx = 0.2; dy = 0.2;
[x,y] = meshgrid(-4:dx:4, -4:dy:4);
initVarPressure2D(x)
ufree = 3000;
rho = 1.225;
releaseVer = '4.2'; % Gauss-Seidel Method

%% local mesh grid setup, at nodes
nmesh = 16;
dr = 0.0625;
dtheta = pi/50;
Rb = sqrt(10000/2/pi/ufree);
xb = Rb * cos(0:dtheta:2*pi);
yb = Rb * sin(0:dtheta:2*pi);
meshb = Rb:dr:Rb+(nmesh*dr);
xmeshb = zeros(size(length(meshb)), length(0:dtheta:2*pi));
ymeshb = xmeshb;
for i = 1:length(meshb)
  xmeshb(i,:) = meshb(i) * cos(0:dtheta:2*pi);
  ymeshb(i,:) = meshb(i) * sin(0:dtheta:2*pi);
end
rb = sqrt(xmeshb.^2 + ymeshb.^2);
thetab = 0:pi/50:2*pi;
```

```
30 for i=1:size(rb,1); thetab(i,:) = thetab(1,:); end
31
32 %% global mesh grid setup simulates PIV velocity data,
33 %% (V in the body = 0) @ nodes
34 theta = get_angle(x,y);
35 r = sqrt(x.^2 + y.^2);
36
37 utheta = -(1+Rb^2./r.^2) * ufree.* sin(theta);
38 ur = (1-Rb^2./r.^2) * ufree .* cos(theta); % velocities in polar
       coordinates
39 [nan_i, nan_j] = find(isnan(utheta))
40 for i = 1:length(nan_i)
41   utheta(nan_i(i), nan_j(i)) = 0;
42 end
43
44 [nan_i, nan_j] = find(isnan(ur))
45 for i = 1:length(nan_i)
46   ur(nan_i(i), nan_j(i)) = 0;
47 end
48
49 u = ur.*cos(theta) - utheta.*sin(theta);
50 v = ur.*sin(theta) + utheta.*cos(theta);
51 % velocities in cartesian coordinates
52
53 for i = 1:size(x,1) % velocity distribution in the body
54   for j = 1:size(x,2)
55     if r(i,j) <= Rb
56       u(i,j) = 0;
57       v(i,j) = 0;
58     end
59   end
60 end
61
62 urb = interp2(x,y,ur,xmeshb,ymeshb,'cubic');
63 uthetab = interp2(x,y,utheta,xmeshb,ymeshb,'cubic');
64
65 rb = [rb(:,end-1) rb(:,:)];
66 uthetab = [uthetab(:,end-1) uthetab(:,:)];
67 urb = [urb(:,end-1) urb(:,:)];
68
69 %%% local mesh, set up boundary condition and source term
70 %%% interpolate velocity
71 [erw, ethetaw] = set_polar_component(urb,uthetab,rb,dr,dtheta);
72 [bAw] = set_bodyCirc_source(rb,rho,erw,ethetaw,dr,dtheta);
73 [bprw] = set_bodyCirc_pressureBoundary(rho,erw);
74
75 edge.global.u = u;
76 edge.global.v = v;
77 edge.global.utheta = utheta;
```

```
78 edge.global.ur = ur;
79 edge.global.x = x;
80 edge.global.y = y;
81 edge.local.xmeshb=xmeshb;
82 edge.local.ymeshb=ymeshb;
83 edge.local.uthetab = uthetab;
84 edge.local.urb = urb;
85
86 %% finite volume coordinates and velocities. @ center points
87 [midglobal.x,midglobal.y] = meshgrid(-4+dx/2:dx:4-dx/2, -4+dy/2:dy:4-
       dy/2);
88 midglobal.u = interp2(x,y,u,midglobal.x,midglobal.y,'cubic');
89 midglobal.v = interp2(x,y,v,midglobal.x,midglobal.y,'cubic');
90 midglobal.r = sqrt(midglobal.x.^2+midglobal.y.^2);
91 midglobal.theta = get_angle(midglobal.x,midglobal.y);
92 for i = 1:size(midglobal.x,1)
93   for j = 1:size(midglobal.x,2)
94     if midglobal.r(i,j) <= Rb
95       midglobal.u(i,j) = 0;
96       midglobal.v(i,j) = 0;
97     end
98   end
99 end
100
101 meshbmid = Rb+dr/2:dr:Rb+(nmesh*dr)+dr/2;
102 for i = 1:length(meshbmid)
103   midlocal.xmeshb(i,:) = meshbmid(i)*cos(dtheta/2:dtheta:2*pi+dtheta
        /2);
104   midlocal.ymeshb(i,:) = meshbmid(i)*sin(dtheta/2:dtheta:2*pi+dtheta
        /2);
105 end
106 midlocal.ub = interp2(x,y,u,midlocal.xmeshb,midlocal.ymeshb,'cubic');
107 midlocal.vb = interp2(x,y,v,midlocal.xmeshb,midlocal.ymeshb,'cubic');
108 midlocal.uthetab = interp2(x,y,utheta,midlocal.xmeshb,midlocal.ymeshb
       ,'cubic');
109 midlocal.urb = interp2(x,y,ur,midlocal.xmeshb,midlocal.ymeshb,'cubic'
       );
110 midlocal.rb = sqrt(midlocal.xmeshb.^2 + midlocal.ymeshb.^2);
111 for i=1:length(meshbmid)
112   midlocal.thetab(i,:) = dtheta/2:dtheta:2*pi+dtheta/2;
113 end
114
115 clear x y u v utheta ur xmeshb ymeshb ub vb uthetab urb r rb theta
       thetab
116
117 x = midglobal.x;
118 y = midglobal.y;
119 u = midglobal.u;
120 v = midglobal.v;
```

```
121 r = midglobal.r;
122 theta = midglobal.theta;
123
124 xmeshb = midlocal.xmeshb;
125 ymeshb = midlocal.ymeshb;
126 ub = midlocal.ub;
127 vb = midlocal.vb;
128 uthetab = midlocal.uthetab;
129 urb = midlocal.urb;
130 rb = midlocal.rb;
131 thetab = midlocal.thetab;
132
133 xmeshb = [xmeshb(:,end-1) xmeshb(:,:)];
134 ymeshb = [ymeshb(:,end-1) ymeshb(:,:)];
135 rb = [rb(:,end-1) rb(:,:)];
136 thetab = [thetab(:,end-1) thetab(:,:)];
137 uthetab = [uthetab(:,end-1) uthetab(:,:)];
138 urb = [urb(:,end-1) urb(:,:)];
139
140
141 %% numerical mask
142 uu = zeros(size(u));
143 vv = zeros(size(v));
144 maskoff = [2 2 2 2];
145 masktemp = (u ~= 0);
146 maskflow = zeros(size(u));
147 maskbody = zeros(size(u)); % "u" is the values at center points
148
149 maskflow(1+maskoff(1):end-maskoff(2), ...
150   1+maskoff(3):end-maskoff(4)) = 1;
151 [mxb,myb] = gradient(maskflow,1,1);
152 mxb = mxb.*maskflow;
153 myb = myb.*maskflow;
154
155 maskbody(1+maskoff(1):end-maskoff(2), ...
156   1+maskoff(3):end-maskoff(4)) = ...
157   masktemp(1+maskoff(1):end-maskoff(2), ...
158   1+maskoff(3):end-maskoff(4));
159 [mx,my] = gradient(maskbody,1,1);
160 mx = mx.*maskbody;
161 my = my.*maskbody;
162
163 maskbody = maskbody - round(abs(mx)) - round(abs(my));
164 [imask,jmask] = find(maskbody == -1);
165 for i = 1:length(imask); maskbody(imask(i),jmask(i)) = 0; end;
166
167 %% perimeter of mesh interface (outer boundary of local mesh)
168 count = 0;
169 for i = 1:size(x,1)
```

```
170    for j = 1:size(x,2)
171      if (mx(i,j)-mxb(i,j)) || (my(i,j)-myb(i,j))
172        count = count + 1;
173        x2(count) = x(i,j);
174        y2(count) = y(i,j);
175      end
176    end
177  end
178
179  %% global mesh, velocity derivatives
180  [ux,uy,vx,vy,uxvy,uyvx] = set_Flowrect_velocityGradient ...
181    (x,y,u,v,dx,dy,mx,my,mxb,myb,maskbody);
182
183  %% source term and boundary condition in global domain
184  [px,py] = set_flowRect_pressureGradient(x,y,u,v,ux,uy,vx,vy,rho);
185  [A] = set_flowRect_source(x,y,uxvy,uyvx,rho);
186
187  %% local mesh, set up boundary condition and source term
188  %% interpolate velocity
189  disp('advection components, body domain')
190  disp('pressure gradient components, body domain')
191  [er, etheta] = set_polar_component(urb,uthetab,rb,dr,dtheta);
192
193  disp('source term and boundary condition, body domain')
194  [bA] = set_bodyCirc_source(rb,rho,er,etheta,dr,dtheta);
195  [bpr] = set_bodyCirc_pressureBoundary(rho,er);
196  %\\\\\\\\\\\\\\\\\\\\\\\\\\
197
198  %% setup coefficient matrix for the solver
199  [Acart,ax,ay,Alist1,flagx,flagy,flagxw,flagyw,XX2] = ...
200    PDMAneumann(dx^2,dy^2, mxb,myb,maskbody);
201  listx = flagx.*Alist1;    listy = flagy.*Alist1;
202  listxw = flagxw.*Alist1; listyw = flagyw.*Alist1;
203
204  %% setup coefficient matrix with Dirichlet boundary condition near
       the body
205  [Acart_d,ax_d,ay_d,Alist1_d,flagx_d,flagy_d,flagxw_d,flagyw_d,XX2_d]
       = ...
206    PDMAdirichlet(dx^2,dy^2, mxb,myb,maskbody);
207  listx_d  = flagx_d.*Alist1_d;
208  listy_d  = flagy_d.*Alist1_d;
209  listxw_d = flagxw_d.*Alist1_d;
210  listyw_d = flagyw_d.*Alist1_d;
211
212  %% setup coefficient matrix with Dirichlet boundary on the farthest
213  % point for circular coordinate
214  r_lower = 2; r_upper = size(rb,1)-1;
215  [Apolar, XX, Alist, frad, ftht] = PDMApolar(dr,dtheta, rb,r_lower,
       r_upper);
```

```
216
217 %% Iteration
218 disp('iteration')
219 %//////////////////////decompose coefficient matrices
220 A1D = diag(diag(Acart));
221 A1L = tril(-Acart,-1);
222 A1U = triu(-Acart,1);
223 A1OD = A1L + A1U;
224
225 A2D = diag(diag(Acart_d));
226 A2L = tril(-Acart_d,-1);
227 A2U = triu(-Acart_d,1);
228 A2OD = A2L + A2U;
229
230 A3D = diag(diag(Apolar));
231 A3L = tril(-Apolar,-1);
232 A3U = triu(-Apolar,1);
233 A3OD = A3L + A3U;
234
235 rho_cart   = max(abs(eig(A1D\A1OD)));
236 rho_cart_d = max(abs(eig(A2D\A2OD)));
237 rho_local  = max(abs(eig(A3D\A3OD)));
238 disp([num2str(rho_cart) '  ' num2str(rho_cart_d) '  ' num2str(
      rho_local) ])
239 CONV1 = 1e-5;
240 CONV = 1e-5;
241 %\\\\\\\\\\\\\\\\\\\\\\\\\\\\\\\\\\\\\\\\
242
243 for w = 1:1
244   P = zeros(size(x));
245   Pb = zeros(size(xmeshb,1), size(xmeshb,2));
246
247   %% //(flow domain)*pressure calculation on global mesh
248   disp('Pressure calculation 1 on global mesh')
249   [pxn,pyn] = set_flowTDMA_NumericalRHS(mxb,myb,listx,listy,px,py);
250   [pxw,pyw] = set_flowTDMA_wallRHS(ax,ay,listxw,listyw,px,py);
251   S = A(Alist1) - 2/3*pxn/dx - 2/3*pyn/dy - 2/3*pxw/dx - 2/3*pyw/dy;
252
253   count2 = 1;
254   res_cart(count2) = 100;
255   gconv1(count2) = 100;
256   Ptemp = P(Alist1');
257   Tw1 = (A1D-w*A1L)\((1-w)*A1D+w*A1U);
258   cw1 = w*((A1D-w*A1L)\S');
259   while gconv1(count2) > CONV1
260       if ~mod(count2,100)
261       disp([ num2str(count2) ' ' num2str(gconv1(count2))])
262     end
263     count2 = count2 + 1;
```

```
264
265       Ptemp = Tw1*Ptemp + cw1;
266       res_cart(count2) = sum(abs(Acart*Ptemp - S'));
267       gconv1(count2) = abs(res_cart(count2) - res_cart(count2-1));
268     end
269     P = reorder_flow(mxb,myb,maskbody,Alist1,Ptemp,P);
270     P1 = P;
271 %\\\\\\\\\\\\\\\\\\\\\\\\\\
272
273
274     %% ////////////////////pressure calculation on local mesh
275     %% *interpolate pressure from global mesh to local mesh
276     %%    at outermost circle
277     disp('Pressure calculation 2 on local mesh')
278     Pb(end,2:end-1) = interp2(x,y,P,xmeshb(end,2:end-1),ymeshb(end,2:
            end-1),...
279       'cubic');
280     Pb = [Pb(:,end-1) Pb(:,2:end-1) Pb(:,2)];
281
282     %% (body domain) *PDMA on circular mesh
283     [bp1,bp2] = set_bodyTDMA_NumericalRHS(Pb,bpr,rb,dr,frad,r_lower,
            r_upper);
284     Sb = bA(Alist) + bp1 + bp2;
285
286     count2 = 1;
287     res_circ2(count2) = 100;
288     gconv2(count2) = 100;
289     Pbtemp = Pb(Alist');
290     Tw3 = (A3D-w*A3L)\((1-w)*A3D+w*A3U);
291     cw3 = w*((A3D-w*A3L)\Sb');
292     while gconv2(count2) > CONV
293       if ~mod(count2,100)
294         disp([ '*' num2str(count2) ' ' num2str(gconv2(count2))])
295       end
296       count2 = count2 + 1;
297
298       Pbtemp = Tw3*Pbtemp + cw3;
299       res_circ2(count2) = sum(abs(Apolar*Pbtemp - Sb'));
300       gconv2(count2) = abs(res_circ2(count2) - res_circ2(count2-1));
301     end
302     Pb = reorder_body(Alist,rb,Pbtemp,Pb);
303     Pb(1,:)= -2/3*bpr(1,:)*dr+4/3*Pb(2,:)-1/3*Pb(3,:);
304     Pbw = -2/3*bprw(1,:)*dr+4/3*(Pb(2,:)+Pb(1,:))/2 - 1/2*(Pb(3,:)+Pb
            (2,:))/2 ;
305     Pb1 = Pb;
306     count5 = 1;
307
308 %% /////*interpolate pressure from local mesh to global mesh
309     for xklm = 1:6 % iterative method
```

```
310     %%% disp('.. .. back interpolation: flow <- body')
311     %%% at points closest to the inner most circle
312     %%% overlap position -0.75<=x<=0.75, -0.75<=y<=0.75
313     R2 = max(rb(:));
314     [xlow, ylow] = find( x<-R2 & x>-(R2+dx) & y<-R2 & y>-(R2+dy));
315     [xup, yup] =  find( x>R2 & x<R2+dx & y>R2 & y<R2+dy);
316     [xcirc_rect,ycirc_rect] = meshgrid( ...
317       x(xlow,ylow)-eps:dx: x(xup,yup)+eps , ...
318       y(xlow,ylow)-eps:dy: y(xup,yup)+eps );
319     Pb2 = polar2cart_interp(rb,thetab,xcirc_rect,ycirc_rect,Rb,dr,
          dtheta,Pb);
320     for i = 1:length(x2)
321       [ix,iy] = find(x == x2(i) & y == y2(i));
322       [ix2,iy2] = find(xcirc_rect > x2(i)-2*eps & ...
323         xcirc_rect < x2(i)+2*eps & ...
324         ycirc_rect > y2(i)-2*eps & ...
325         ycirc_rect < y2(i)+2*eps );
326       P(ix,iy) = Pb2(ix2,iy2);
327     end
328   %\\\\\\\\\\\\\\\\\\\\\\\\\\\\\\\\\\\\\\\\\\\\\\\\
329
330   %% //////(flow domain) pressure calculation on global mesh
331     disp('pressure calculation 3 on global mesh')
332     [pxn_d,pyn_d] = set_flowTDMA_NumericalRHS(mxb,myb,listx_d,listy_d
          ,px,py);
333     [pxw_d,pyw_d] = set_flowTDMA_dirichletRHS(ax_d,ay_d,listxw_d,
          listyw_d,P);
334     S_d = A(Alist1)- 2/3*pxn_d/dx-2/3*pyn_d/dy-pxw_d/dx/dx-pyw_d/dy/
          dy;
335
336     count3 = 1;
337     res_cart3(count3) = 100;
338     gconv3(count3) = 100;
339     Ptemp = P(Alist1_d');
340     Tw2 = (A2D-w*A2L)\((1-w)*A2D+w*A2U);
341     cw2 = w*((A2D-w*A2L)\S_d');
342     while gconv3(count3) > CONV
343       if ~mod(count3,100)
344         disp([ '**' num2str(count3) ' ' num2str(gconv3(count3))])
345       end
346       count3 = count3 + 1;
347
348       Ptemp = Tw2*Ptemp + cw2;
349
350       res_cart3(count3) = sum(abs(Acart_d*Ptemp - S_d'));
351       gconv3(count3) = abs(res_cart3(count3) - res_cart3(count3-1));
352     end
353     P = reorder_flow(mxb,myb,maskbody,Alist1_d,Ptemp,P);
354     P2 = P;
```

```
355
356     %% second iteration on local mesh
357     %% *interpolate pressure from flow domain to body domain
358     %% *at outermost circle
359     disp('Pressure calculation 4 on local mesh')
360     Pb(end,2:end-1)=interp2(x,y,P, ...
361          xmeshb(end,2:end-1),ymeshb(end,2:end-1),'cubic');
362     Pb = [Pb(:,end-1) Pb(:,2:end-1) Pb(:,2)];
363
364     %% (body domain) *PDMA on circular mesh
365     [bp1,bp2] = set_bodyTDMA_NumericalRHS(Pb,bpr,rb,dr,frad,r_lower,
            r_upper);
366     Sb = bA(Alist) + bp1 + bp2;
367
368     Tw4 = Tw3;
369     cw4 = w*((A3D-w*A3L)\Sb');
370     count4 = 1;
371     res_circ4(count4) = 100;
372     gconv4(count4) = 100;
373     Pbtemp = Pb(Alist');
374     while gconv4(count4) > CONV
375       if ~mod(count4,100)
376         disp([ '***' num2str(count4) ' ' num2str(gconv4(count4))])
377       end
378       count4 = count4 + 1;
379
380       Pbtemp = Tw4*Pbtemp + cw4;
381
382       res_circ4(count4) = sum(abs(Apolar*Pbtemp - Sb'));
383       gconv4(count4) = abs(res_circ4(count4) - res_circ4(count4-1));
384     end
385     Pb = reorder_body(Alist,rb,Pbtemp,Pb);
386     Pb(1,:)= -2/3*bpr(1,:)*dr + 4/3*Pb(2,:) - 1/3*Pb(3,:);
387     Pbw = 15/8 * Pb(1,:) + (-5/4)*Pb(2,:) + 3/8 * Pb(3,:);
388     Pb2 = P;
389
390     save(['circle poisson ' releaseVer num2str(w) num2str(count5) '.
            mat']);
391     count5 = count5 + 1;
392   end
393 end
```

Appendix C

Poisson solver for flapping wing

```
function fn_fw_poisson3d_6_1_mid(nconv1,nconv2,freq,nsec)
% naming convention
% fn = function
% fw = flapping wing
% poisson3d = solves 3d Poisson equation
% 6_1 = program version
%
% nconv1 = 100000;
% nconv2 = 100000;
% freq = 1;
% nsec = 1:3;

%% pressure around flapping wing
% MU, MV (mm/s);
% Mxp, Myp (mm);
% a, b (mm); THETA (rad);
% th2 (thickness/2, mm);
% rho (g.mm^(-3))
load('../statistics_covariance_and_average.mat', ...
    'mu','mv','mw', 'uu','uv','uw','vv','vw','ww');
load('../statistics_measurement_uncertainty.mat', ...
    'sigma_pu2','sigma_pv2','sigma_pw2');
[YP,XP] = meshgrid(-20:1.25:20,-30:1.5:30);

if nsec(1) == 1
  releaseVer = ['6.1.' num2str(freq) '.mid'];
  else if nsec(1) == 4
    releaseVer = ['6.1.' num2str(freq) '.edge'];
  end
end
%============================
a = 12.56;
b = 40;
```

```
34 THETA = 0.1*pi;
35 th2 = 1; % thickness
36 rho = 0.001;
37 visc = 8.9e-4;
38 baseCONV = [1e-5 1e-5 1e-5 1e-5 1e-5 1e-5 1e-5 1e-5 1e-5 1e-5 ...
39               1e-5 1e-5 1e-5 1e-5 1e-5 1e-5 1e-5 1e-5 1e-5 1e-5 ];
40 gCONV = 5e2* baseCONV;
41 lCONV = 1e0* baseCONV;
42 Stime = 1;  Ntime = 20;
43
44 %% global mesh spatial lengths
45 dx = 1.5;  %(mm)
46 dy = 1.25; %(mm)
47 dz = 2;    %(mm)
48 dt = 1/freq/20; disp(dt) %s
49
50 %% local mesh spatial lengths
51 dxmesh = 1;
52 dymesh = 1;
53 dzmesh = dz;
54
55 %% Data preparation for numerical procedure
56 MU = cell(1,20); MV=MU; MW=MU;
57 Muu=MU;Mvv=MU;Mww=MU;Muv=MU;Muw=MU;Mvw=MU;eu=MU;ev=MU;ew=MU;
58 Mxp=zeros([size(XP),3]);Myp=Mxp;Mzp=Mxp;fsec=zeros(1,3);
59
60 csec = [-2 0 2 8 10 12];
61 count0 = 0;
62 for sec = nsec
63   count0 = count0 + 1;
64   for phase = 1:20
65     MU{phase}(:,:,count0)  = reshape(mu{freq}{sec,phase},33,41)';
66     MV{phase}(:,:,count0)  = reshape(mv{freq}{sec,phase},33,41)';
67     MW{phase}(:,:,count0)  = reshape(mw{freq}{sec,phase},33,41)';
68     Muu{phase}(:,:,count0) = reshape(uu{freq}{sec,phase},33,41)';
69     Muv{phase}(:,:,count0) = reshape(uv{freq}{sec,phase},33,41)';
70     Muw{phase}(:,:,count0) = reshape(uw{freq}{sec,phase},33,41)';
71     Mvv{phase}(:,:,count0) = reshape(vv{freq}{sec,phase},33,41)';
72     Mvw{phase}(:,:,count0) = reshape(vw{freq}{sec,phase},33,41)';
73     Mww{phase}(:,:,count0) = reshape(ww{freq}{sec,phase},33,41)';
74     eu{phase}(:,:,count0) = reshape(sigma_pu2{freq}{sec,phase},33,41)
           ';
75     ev{phase}(:,:,count0) = reshape(sigma_pv2{freq}{sec,phase},33,41)
           ';
76     ew{phase}(:,:,count0) = reshape(sigma_pw2{freq}{sec,phase},33,41)
           ';
77   end
78   Mxp(:,:,count0) = XP;
79   Myp(:,:,count0) = YP;
```

```
80    Mzp(:,:,count0) = csec(sec)*ones(size(XP));
81    fsec(count0) = csec(sec);
82  end
83  %% set up local mesh, which is  moving with the plate. The plate's
84  %% kinematics is represented by an analytical equation
85  xmesh = -10:dxmesh:10;
86  ymesh = -40:dymesh:5;
87  [YMESH,XMESH]=meshgrid(ymesh,xmesh);
88
89  for i=1:20
90    disp(['time ' num2str(i)]);
91    % set plate kinematics: t(characteristic time) and theta
92    % (plate's deflection angle)
93    t(i) = (i-1)/20;  % characteristics time index
94    theta(i) = -THETA*sin(2*pi*t(i)); % phase angle
95    cutoff_1 = 28; % cuts the plate to define the part of the plate
96    % overlapping with the measurement plane
97    for kk = 1:3
98      YMESHT1{i}(:,:,kk) =  (YMESH+40)*cos(-theta(i))+XMESH*sin(-theta(
          i))-40;
99      XMESHT1{i}(:,:,kk) = -(YMESH+40)*sin(-theta(i))+XMESH*cos(-theta(
          i));
100     YMESHT{i}(:,:,kk) = YMESHT1{i}(:,cutoff_1:end,1);
101     XMESHT{i}(:,:,kk) = XMESHT1{i}(:,cutoff_1:end,1);
102   end
103   % surface coordinate of local mesh from hub to tip for plane 1 edge
104   % nodes coord. of local mesh in the computational domain for plane
        1-3
105
106
107 % CREATE MASKS TO INDICATE COMPUTATIONAL AND WALL BOUNDARIES
108 %! template
109   MASK = ones(size(XMESHT{1}(:,:,1)));
110   % template of edge node MASK from local mesh
111   PLATE1 = MASK;  FLOW = MASK;
112   % PLATE1= mask for the local mesh
113   % PLATEX, PLATEY, PLATEZ= mask for the edges of the local mesh
114   lx = (length(xmesh)-1)/2; % location(index) of the surface of the
        plate
115   PLATE1(lx:lx+2, 1:1+41-cutoff_1)= 0;
116   PLATE1(1,:) = 0;
117   PLATE1(:,1) = 0;
118   PLATE1(end,:) = 0;
119   PLATE1(:,end) = 0;
120 % % % MASKING FOR THE EDGE NODES, INCLUDES WALL BOUNDARY
121 % % % AND COMPUTATIONAL DOMAIN BOUNDARY
122   [PLATEY1,PLATEX1] = gradient(PLATE1);
123   PLATEY1 = PLATEY1 .* PLATE1;
124   PLATEX1 = PLATEX1 .* PLATE1;
```

```
125    PLATEX1(2       ,2:end-1) = PLATEX1(2       ,2:end-1)*4;
126    PLATEX1(end-1,2:end-1) = PLATEX1(end-1,2:end-1)*4;
127    PLATEY1(2:end-1,2       ) = PLATEY1(2:end-1,2       )*4;
128    PLATEY1(2:end-1,end-1) = PLATEY1(2:end-1,end-1)*4;
129    for kk = 1:3
130      PLATEX(:,:,kk) = PLATEX1;
131      PLATEY(:,:,kk) = PLATEY1;
132      PLATE(:,:,kk) = PLATE1;
133    end
134    PLATEZ = zeros([size(PLATE1) 3]);
135    PLATEZ(:,:,1) = PLATE1;
136    PLATEZ(:,:,3) = -PLATE1;
137    clear PLATE1 PLATEX1 PLATEY1
138
139 %%% CREATE MASK TO INDICATE THE WALL BOUNDARY.
140    FLOW(1x+1,1:1+41-cutoff_1) = 0;
141    FLOW(:,:,2) = FLOW(:,:,1);
142    FLOW(:,:,3) = FLOW(:,:,1);
143    MASK = ones(size(XMESHT1{1}(:,:,1)));
144    PLATE2 = MASK;
145    PLATE2(1x:1x+2,1:1+41)= 0;
146    [XY2,XX2] = gradient(PLATE2);
147      XY2 = XY2 .* PLATE2;
148      XX2 = XX2 .* PLATE2;
149      PLATEX2 = XX2;
150      PLATEY2 = XY2;
151    PLATE2(:,:,2) = PLATE2(:,:,1);
152    PLATE2(:,:,3) = PLATE2(:,:,1);
153    %%% MASKING FOR THE EDGE NODES, ONLY FOR THE WALL BOUNDARY
154
155 %%% CREATE COORDINATES, DATA, AND MASKS FOR THE CENTER NODES IN
156 %%% THE mid VARIABLE [for global mesh and local mesh]
157    [mid.Myp, mid.Mxp] = meshgrid(-20+dy/2:dy:20-dy/2,-30+dx/2:dx:30-dx
           /2 );
158    for kk = 1:3
159      mid.Myp(:,:,kk) = mid.Myp(:,:,1);
160      mid.Mxp(:,:,kk) = mid.Mxp(:,:,1);
161      mid.Mzp(:,:,kk) = fsec(kk) * ones(size(mid.Myp(:,:,1)));
162      mid.MU{i}(:,:,kk)=interp2(Myp(:,:,kk),Mxp(:,:,kk),MU{i}(:,:,kk),
             ...
163                                mid.Myp(:,:,kk), mid.Mxp(:,:,kk));
164      mid.MV{i}(:,:,kk)=interp2(Myp(:,:,kk),Mxp(:,:,kk),MV{i}(:,:,kk),
             ...
165                                mid.Myp(:,:,kk),mid.Mxp(:,:,kk));
166      mid.MW{i}(:,:,kk)=interp2(Myp(:,:,kk),Mxp(:,:,kk),MW{i}(:,:,kk),
             ...
167                                mid.Myp(:,:,kk),mid.Mxp(:,:,kk));
168      mid.Muu{i}(:,:,kk)=interp2(Myp(:,:,kk),Mxp(:,:,kk) Muu{i}(:,:,kk)
             , ...
```

```
169                             mid.Myp(:,:,kk),mid.Mxp(:,:,kk));
170       mid.Muv{i}(:,:,kk)=interp2(Myp(:,:,kk),Mxp(:,:,kk),Muv{i}(:,:,kk)
              , ...
171                             mid.Myp(:,:,kk),mid.Mxp(:,:,kk));
172       mid.Muw{i}(:,:,kk)=interp2(Myp(:,:,kk),Mxp(:,:,kk),Muw{i}(:,:,kk)
              , ...
173                             mid.Myp(:,:,kk), mid.Mxp(:,:,kk));
174       mid.Mvv{i}(:,:,kk)=interp2(Myp(:,:,kk),Mxp(:,:,kk),Mvv{i}(:,:,kk)
              , ...
175                             mid.Myp(:,:,kk), mid.Mxp(:,:,kk));
176       mid.Mvw{i}(:,:,kk)=interp2(Myp(:,:,kk),Mxp(:,:,kk),Mvw{i}(:,:,kk)
              , ...
177                             mid.Myp(:,:,kk), mid.Mxp(:,:,kk));
178       mid.Mww{i}(:,:,kk)=interp2(Myp(:,:,kk),Mxp(:,:,kk),Mww{i}(:,:,kk)
              , ...
179                             mid.Myp(:,:,kk), mid.Mxp(:,:,kk));
180       mid.eu{i}(:,:,kk)=interp2(Myp(:,:,kk),Mxp(:,:,kk),eu{i}(:,:,kk),
              ...
181                            mid.Myp(:,:,kk), mid.Mxp(:,:,kk));
182       mid.ev{i}(:,:,kk)=interp2(Myp(:,:,kk),Mxp(:,:,kk),ev{i}(:,:,kk),
              ...
183                             mid.Myp(:,:,kk), mid.Mxp(:,:,kk));
184       mid.ew{i}(:,:,kk)=interp2(Myp(:,:,kk),Mxp(:,:,kk),ew{i}(:,:,kk),
              ...
185                             mid.Myp(:,:,kk), mid.Mxp(:,:,kk));
186     end
187     % center point coordinates for (X,Y) and center-face coord for Z,
188     % and the values associated to them in global mesh.
189
190
191 % % coordinate for the local mesh
192 % % % coordinates associated with the full-length of the plate.
193     mid.ymesh0{i} = YMESHT1{i}(1:end-1,1:end-1,:)+dymesh/2;
194     mid.xmesh0{i} = XMESHT1{i}(1:end-1,1:end-1,:)+dxmesh/2;
195 % % % coordinates associated with the overlapping length of the plate
        .
196     mid.ymesh{i} = YMESHT{i}(1:end-1,1:end-1,:) ...
197                     + dymesh/2*cos(-theta(i)) + dxmesh/2*sin(-theta(i));
198     mid.xmesh{i} = XMESHT{i}(1:end-1,1:end-1,:) ...
199                     - dymesh/2*sin(-theta(i)) + dxmesh/2*cos(-theta(i));
200     xmesh_wall = size(mid.xmesh{i},1)/2;
201 % % MASKING OF THE CENTER NODES ENCOMPASSING THE FULL LENGTH OF THE
        PLATE
202     mid.flow0{i} = ones(size(mid.xmesh0{i}));
203     mid.flow0{i}(xmesh_wall:xmesh_wall+1 ,1:40,:) = 0;
204     mid.mask{i} = ones(size(mid.xmesh{i}));
205     mid.mask{i}( xmesh_wall:xmesh_wall+1 ,1:41-cutoff_1 ,:) = 0;
206     mid.flow{i} = mid.mask{i};
207 % % MASKING OF CENTER NODES ENCOMPASSING THE LENGTH OF THE PLATE
```

```
208 %% INSIDE THE COMPUTATIONAL DOMAIN
209    mid.mask{i}(1    ,:    ,:) = 0;   mid.mask{i}(:    ,1    ,:) = 0;
210    mid.mask{i}(end,:    ,:) = 0;   mid.mask{i}(:    ,end,:) = 0;
211    [mid.ymask{i}, mid.xmask{i}] = gradient(mid.mask{i});
212    mid.xmask{i} = mid.mask{i}.*mid.xmask{i};
213    mid.xmask{i}(2      ,:      ,:) = mid.xmask{i}(2      ,:      ,:) * 4;
214    mid.xmask{i}(end-1,:      ,:) = mid.xmask{i}(end-1,:      ,:) * 4;
215    mid.ymask{i} = mid.mask{i}.*mid.ymask{i};
216    mid.ymask{i}(:      ,2      ,:) = mid.ymask{i}(:      ,2      ,:) * 4;
217    mid.ymask{i}(:      ,end-1,:) = mid.ymask{i}(:      ,end-1,:) * 4;
218    mid.zmask{i}(:,:,1) = mid.mask{i}(:,:,1);
219    mid.zmask{i}(:,:,3) = -mid.mask{i}(:,:,1);
220
221 %% ANGULAR VELOCITY AND ACCELERATION OF THE PLATE [local mesh]
222    %% plate kinematics
223    theta(i) =              -1 * THETA * sin(2*pi*t(i)); % phase angle
224    OMEGA(i) = -(2*pi*freq)    * THETA * cos(2*pi*t(i));
225    ALPHA(i) =  (2*pi*freq)^2 * THETA * sin(2*pi*t(i));
226    for kk = 1:3
227 %% %(ON THE FACE)
228       umesh{i}(:,:,kk) = interp2(Myp(:,:,kk), Mxp(:,:,kk), MU{i}(:,:,kk
           ), ...
229                                  YMESHT{i}(:,:,kk), XMESHT{i}(:,:,kk));
230       vmesh{i}(:,:,kk) = interp2(Myp(:,:,kk), Mxp(:,:,kk), MV{i}(:,:,kk
           ), ...
231                                  YMESHT{i}(:,:,kk), XMESHT{i}(:,:,kk));
232       wmesh{i}(:,:,kk) = interp2(Myp(:,:,kk), Mxp(:,:,kk), MW{i}(:,:,kk
           ), ...
233                                  YMESHT{i}(:,:,kk), XMESHT{i}(:,:,kk));
234       uumesh{i}(:,:,kk) = interp2(Myp(:,:,kk), Mxp(:,:,kk), Muu{i}(:,:,
           kk), ...
235                                   YMESHT{i}(:,:,kk), XMESHT{i}(:,:,kk));
236       uvmesh{i}(:,:,kk) = interp2(Myp(:,:,kk), Mxp(:,:,kk), Muv{i}(:,:,
           kk), ...
237                                   YMESHT{i}(:,:,kk), XMESHT{i}(:,:,kk));
238       uwmesh{i}(:,:,kk) = interp2(Myp(:,:,kk), Mxp(:,:,kk), Muw{i}(:,:,
           kk), ...
239                                   YMESHT{i}(:,:,kk), XMESHT{i}(:,:,kk));
240       vvmesh{i}(:,:,kk) = interp2(Myp(:,:,kk), Mxp(:,:,kk), Mvv{i}(:,:,
           kk), ...
241                                   YMESHT{i}(:,:,kk), XMESHT{i}(:,:,kk));
242       vwmesh{i}(:,:,kk) = interp2(Myp(:,:,kk), Mxp(:,:,kk), Mvw{i}(:,:,
           kk), ...
243                                   YMESHT{i}(:,:,kk), XMESHT{i}(:,:,kk));
244       wwmesh{i}(:,:,kk) = interp2(Myp(:,:,kk), Mxp(:,:,kk), Mww{i}(:,:,
           kk), ...
245                                   YMESHT{i}(:,:,kk), XMESHT{i}(:,:,kk));
246
247       umesh_ntz{i}(:,:,kk) = umesh{i}(:,:,kk) * cos(theta(i)) ...
```

```
248             - vmesh{i}(:,:,kk) * sin(theta(i)) - OMEGA(i)*(40+YMESHT
                    {1}(:,:,kk));
249         vmesh_ntz{i}(:,:,kk) = umesh{i}(:,:,kk) * sin(theta(i)) ...
250             + vmesh{i}(:,:,kk) * cos(theta(i));
251         wmesh_ntz{i}(:,:,kk) = wmesh{i}(:,:,kk);
252         cua = uumesh{i}(:,:,kk) * cos(theta(i))^2;
253         cub = vvmesh{i}(:,:,kk) * sin(theta(i))^2;
254         cuc = uvmesh{i}(:,:,kk) * cos(theta(i)) * sin(theta(i));
255         cud = uwmesh{i}(:,:,kk) * cos(theta(i));
256         cue = vwmesh{i}(:,:,kk) * sin(theta(i));
257         cuf = wwmesh{i}(:,:,kk);
258
259         uu_ntz{i}(:,:,kk) = cua + cub - 2*cuc;
260         uv_ntz{i}(:,:,kk) = cua - cub;
261         uw_ntz{i}(:,:,kk) = cud - cue;
262         vw_ntz{i}(:,:,kk) = cud + cue;
263         vv_ntz{i}(:,:,kk) = cua + cub + 2*cuc;
264         ww_ntz{i}(:,:,kk) = cuf;
265
266 % % % (ON THE NODE)
267         mid.umesh{i}(:,:,kk)=interp2(Myp(:,:,kk),Mxp(:,:,kk),MU{i}(:,:,kk
                ), ...
268                                 mid.ymesh{i}(:,:,kk), mid.xmesh{i}(:,:,kk));
269         mid.vmesh{i}(:,:,kk)=interp2(Myp(:,:,kk),Mxp(:,:,kk),MV{i}(:,:,kk
                ), ...
270                                 mid.ymesh{i}(:,:,kk), mid.xmesh{i}(:,:,kk));
271         mid.wmesh{i}(:,:,kk)=interp2(Myp(:,:,kk),Mxp(:,:,kk),MW{i}(:,:,kk
                ), ...
272                                 mid.ymesh{i}(:,:,kk), mid.xmesh{i}(:,:,kk));
273         mid.umesh_ntz{i}(:,:,kk)=mid.umesh{i}(:,:,kk)*cos(theta(i)) ...
274             - mid.vmesh{i}(:,:,kk)*sin(theta(i)) - OMEGA(i)*(40+mid.ymesh
                    {1}(:,:,1));
275         mid.vmesh_ntz{i}(:,:,kk)=mid.umesh{i}(:,:,kk)*sin(theta(i)) ...
276             + mid.vmesh{i}(:,:,kk)*cos(theta(i));
277         mid.wmesh_ntz{i}(:,:,kk)=mid.wmesh{i}(:,:,kk);
278         mid.umesh_ntz{i}(:,:,kk)=mid.umesh_ntz{i}(:,:,kk) .* mid.flow{i
                }(:,:,kk);
279         mid.vmesh_ntz{i}(:,:,kk)=mid.vmesh_ntz{i}(:,:,kk) .* mid.flow{i
                }(:,:,kk);
280         mid.wmesh_ntz{i}(:,:,kk)=mid.wmesh_ntz{i}(:,:,kk) .* mid.flow{i
                }(:,:,kk);
281     end
282     MASK2 = zeros(size(mid.xmesh{1}(:,:,1)));
283     MASK2(1,:) = 1; MASK2(:,1) = 1;  MASK2(end,:) = 1; MASK2(:,end) =
            1;
284 end
285  clear MASK umesh1 vmesh1 wmesh1
286
```

```
287 %% calculate acceleration of flow on NODES with forward marching
        scheme
288 [utmesh,vtmesh,wtmesh] = getAcceleration(mid.umesh_ntz, ...
289                                mid.vmesh_ntz, mid.wmesh_ntz, dt);
290 [MUt,MVt,MWt] = getAcceleration(mid.MU, mid.MV, mid.MW, dt);
291 [eut,evt,ewt] = getAcceleration(mid.eu, mid.ev, mid.ew, dt);
292
293
294 %>> phase averaged solutions starts here <<
295 %=========================================
296 for time = Stime:Ntime
297   disp(['Convergence limit 1: ' num2str(gCONV(time))])
298   disp(['Convergence limit 2: ' num2str(lCONV(time))])
299   %% (local mesh) source term and pressure gradients
300   ux = zeros(size(mid.xmesh{1}));
301   uy = zeros(size(mid.xmesh{1}));
302   uz = zeros(size(mid.xmesh{1}));
303   vx = zeros(size(mid.xmesh{1}));
304   vy = zeros(size(mid.xmesh{1}));
305   vz = zeros(size(mid.xmesh{1}));
306   wx = zeros(size(mid.xmesh{1}));
307   wy = zeros(size(mid.xmesh{1}));
308   wz = zeros(size(mid.xmesh{1}));
309   [ux,uy,uz,vx,vy,vz,wx,wy,wz] = get_local_velocityGradient( ...
310       umesh_ntz{time}, vmesh_ntz{time}, wmesh_ntz{time}, ...
311       mid.flow{1}, dxmesh,dymesh,dzmesh, ux,uy,uz,vx,vy,vz,wx,wy,wz);
312
313   [vv_ntz_y2,uu_ntz_x2,ww_ntz_z2,uv_ntz_xy,vw_ntz_yz,uw_ntz_xz] = ...
314       getReSecondDerivatives( ...
315       vv_ntz{time},uu_ntz{time},ww_ntz{time}, ...
316       uv_ntz{time},vw_ntz{time},uw_ntz{time},dy,dx,dz);
317
318   bA1 = ux.^2 + vy.^2 + wz.^2 + 2*uy.*vx + 2*uz.*wx  + 2*vz.*wy;
319   bA2 = uu_ntz_x2 + vv_ntz_y2 + ww_ntz_z2 + ...
320         2*uv_ntz_xy + 2*vw_ntz_yz + 2*uw_ntz_xz;
321   bA = -rho*( bA1 + bA2 - 2*OMEGA(time).^2 + 2*OMEGA(time)*( uy-vx )
          );
322
323   [uv_ntz_y, uu_ntz_x, uw_ntz_z] = getReFirstDerivatives( ...
324       uv_ntz{time},uu_ntz{time},uw_ntz{time},dy,dx,dz);
325   [vv_ntz_y, vu_ntz_x, vw_ntz_z] = getReFirstDerivatives( ...
326       vv_ntz{time},uv_ntz{time},vw_ntz{time},dy,dx,dz);
327   [wv_ntz_y, wu_ntz_x, ww_ntz_z] = getReFirstDerivatives( ...
328       vw_ntz{time},uw_ntz{time},ww_ntz{time},dy,dx,dz);
329   pxmesh = -rho*( utmesh{time} ...
330     + mid.umesh_ntz{time}.*ux ...
331     + mid.vmesh_ntz{time}.*uy ...
332     + mid.wmesh_ntz{time}.*uz ...
333     + uv_ntz_y + uu_ntz_x + uw_ntz_z+...
```

```
334       - ALPHA(time).*(40 + mid.ymesh{1}) ...
335       - OMEGA(time)^2.*mid.xmesh{1} ...
336       - 2*OMEGA(time)*mid.vmesh_ntz{time} );
337     pymesh = -rho*( vtmesh{time} ...
338       + mid.umesh_ntz{time}.*vx ...
339       + mid.vmesh_ntz{time}.*vy ...
340       + mid.wmesh_ntz{time}.*vz ...
341       + vv_ntz_y + vu_ntz_x + vw_ntz_z+...
342       + ALPHA(time).*mid.xmesh{1} ...
343       - OMEGA(time)^2.*(40 + mid.ymesh{1}) ...
344       + 2*OMEGA(time)*mid.umesh_ntz{time} );
345     pzmesh = -rho*( wtmesh{time} ...
346       + mid.umesh_ntz{time}.*wx ...
347       + mid.vmesh_ntz{time}.*wy ...
348       + mid.wmesh_ntz{time}.*wz ...
349       + wv_ntz_y + wu_ntz_x + ww_ntz_z );
350     %%% pressure gradient and RHS of Poisson equation, local mesh
351     pxmesh0 = zeros(size(pxmesh)); pymesh0 = zeros(size(pymesh));
352     for kk = 1:3
353       pxmesh0(xmesh_wall ,1:41-cutoff_1,kk) = -rho * ( ...
354           ALPHA(time).*(40 + (-12.5:1:-0.5)) + OMEGA(time)^2.*(-0.5) );
355       pxmesh0(xmesh_wall+1,1:41-cutoff_1,kk) = -rho * ( ...
356           ALPHA(time).*(40 + (-12.5:1:-0.5)) + OMEGA(time)^2.*( 0.5) );
357       pymesh0(xmesh_wall ,1:41-cutoff_1,kk) = -rho * ( ...
358          -ALPHA(time).*(-0.5) + OMEGA(time)^2.*(40 + (-12.5:1:-0.5)));
359       pymesh0(xmesh_wall+1,1:41-cutoff_1,kk) = -rho * ( ...
360          -ALPHA(time).*( 0.5) + OMEGA(time)^2.*(40 + (-12.5:1:-0.5)));
361     end % set boundary condition on the wall
362
363     %% (global mesh) source term and pressure gradients
364     [mid.gmask,mid.gx,mid.gy,mid.gz] = set_flowRect_mask( ...
365       mid.Mxp, mid.Myp, mid.xmesh0{time}, mid.ymesh0{time}, mid.flow0{
              time} );
366     % set flow area for global mesh at center nodes
367     msize = size(mid.Mxp);
368
369     gux = zeros(msize);       gvx = zeros(msize);       gwx = zeros(msize
          );
370     guy = zeros(msize);       gvy = zeros(msize);       gwy = zeros(msize
          );
371     guz = zeros(msize);       gvz = zeros(msize);       gwz = zeros(msize
          );
372     [gux,guy,guz,gvx,gvy,gvz,gwx,gwy,gwz] =
            get_global_velocityGradients( ...
373           MU{time},MV{time},MW{time},dx,dy,dz,(mid.gmask==0),mid.gx,mid
                .gy,...
374           gux,guy,guz,gvx,gvy,gvz,gwx,gwy,gwz); %=velocity gradients
375     [vv_y2,uu_x2,ww_z2,uv_xy,vw_yz,uw_xz] = getReSecondDerivatives(...
```

```
376        Mvv{time},Muu{time},Mww{time},Muv{time},Mvw{time},Muw{time},dy,
               dx,dz);
377    A1 = gux.^2 + gvy.^2 + gwz.^2 + 2*guy.*gvx + 2*guz.*gwx + 2*gvz.*
           gwy;
378    A2 = uu_x2 + vv_y2 + ww_z2 + 2*uv_xy + 2*uw_xz + 2*vw_yz;
379    A = -rho*( A1 + A2 );
380
381    [uv_y,uu_x,uw_z]=getReFirstDerivatives(Muv{time},Muu{time},Muw{time
           },...
382                           dy,dx,dz);
383    [vv_y,vu_x,vw_z]=getReFirstDerivatives(Mvv{time},Muv{time},Mvw{time
           },...
384                           dy,dx,dz);
385    [wv_y,wu_x,ww_z]=getReFirstDerivatives(Mvw{time},Muw{time},Mww{time
           },...
386                           dy,dx,dz);
387    px= -rho*(MUt{time} + mid.MU{time}.*gux + mid.MV{time}.*guy ...
388          + mid.MW{time}.*guz + uu_x + uv_y + uw_z);
389    py= -rho*(MVt{time} + mid.MU{time}.*gvx + mid.MV{time}.*gvy ...
390          + mid.MW{time}.*gvz + vu_x + vv_y + vw_z);
391    pz= -rho*(MWt{time} + mid.MU{time}.*gwx + mid.MV{time}.*gwy ...
392          + mid.MW{time}.*gwz + wu_x + wv_y + ww_z);
393
394
395    %% ambiguity
396    eux = zeros(msize);        evx = zeros(msize);        ewx = zeros(msize
           );
397    euy = zeros(msize);        evy = zeros(msize);        ewy = zeros(msize
           );
398    euz = zeros(msize);        evz = zeros(msize);        ewz = zeros(msize
           );
399    [eux,euy,euz,evx,evy,evz,ewx,ewy,ewz] =
           get_global_velocityGradients( ...
400          eu{time},ev{time},ew{time}, dx,dy,dz, ...
401          (mid.gmask==0),mid.gx,mid.gy, eux,euy,euz,evx,evy,evz,ewx,ewy
                 ,ewz);
402    %=velocity gradients
403    epx = -rho*(eut{time} + mid.eu{time}.*gux + mid.MU{time}.*eux ...
404                          + mid.ev{time}.*guy + mid.MV{time}.*euy ...
405                          + mid.ew{time}.*guz + mid.MW{time}.*euz);
406    epy = -rho*(evt{time} + mid.eu{time}.*gvx + mid.MU{time}.*evx ...
407                          + mid.ev{time}.*gvy + mid.MV{time}.*evy ...
408                          + mid.ew{time}.*gvz + mid.MW{time}.*evz);
409    epz = -rho*(ewt{time} + mid.eu{time}.*gwx + mid.MU{time}.*ewx ...
410                          + mid.ev{time}.*gwy + mid.MV{time}.*ewy ...
411                          + mid.ew{time}.*gwz + mid.MW{time}.*ewz);
412    sigma_p=sqrt(((px./gux).^2+(gux.*epx).^2+(px.*eux).^2).*mid.eu{time
           }.^2 ...
```

```
413                 + ((py./gvy).^2+(gvy.*epy).^2+(py.*evy).^2).*mid.ev{time
                        }.^2  ...
414                 + ((px./gwz).^2+(gwz.*epz).^2+(pz.*ewz).^2).*mid.ew{time
                        }.^2   );
415
416 %%% another procedure to create mask
417     plate_on_rect=griddata(mid.ymesh0{time}(:,:,kk),mid.xmesh0{time
            }(:,:,kk),...
418       ~mid.flow0{time}(:,:,kk), mid.Myp(:,:,kk), mid.Mxp(:,:,kk) );
419     for i=1:size(plate_on_rect,1)
420       for j=1:size(plate_on_rect,2);
421         if isnan(plate_on_rect(i,j)); plate_on_rect(i,j) = 0; end
422         if plate_on_rect(i,j)~=0; plate_on_rect(i,j) = 1; end
423       end
424     end
425     [mask_y2,mask_x2] = gradient(plate_on_rect);
426     mask_x2= mask_x2.*~plate_on_rect;
427     mask_y2= mask_y2.*~plate_on_rect;
428     temp2 = round(abs(mask_x2)+abs(mask_y2));
429     mask_x3 = temp2.*mid.Mxp(:,:,1);
430     mask_y3 = temp2.*mid.Myp(:,:,1);
431     gmask2 = plate_on_rect + temp2;
432     gmask2(:          ,1:2        ) = 1;    gmask2(1:2        ,:          ) =
            1;
433     gmask2(end-1:end,:          ) = 1;    gmask2(:          ,end-1:end ) =
            1;
434     gmask2(:,:,2) = gmask2(:,:,1);  gmask2(:,:,3) = gmask2(:,:,1);
435     [gy2,gx2] = gradient(gmask2(:,:,1),1,1);
436     gx2         = gx2.*(gmask2(:,:,1)==0);
437     gy2         = gy2.*(gmask2(:,:,1)==0);
438     gx2(3,3:end-2)      = gx2(3,3:end-2)*4;
439     gx2(end-2,3:end-2) = gx2(end-2,3:end-2)*4;
440     gy2(:,3)       = gy2(:,3)*4;
441     gy2(:,end-2) = gy2(:,end-2) *4;
442     gx2(:,:,2) = gx2(:,:,1);
443     gx2(:,:,3) = gx2(:,:,1);
444     gy2(:,:,2) = gy2(:,:,1);
445     gy2(:,:,3) = gy2(:,:,1);
446     gz2 = zeros(size(gmask2));
447     gz2(:,:,1) = (gmask2(:,:,1)==0);
448     gz2(:,:,3) = -double(gmask2(:,:,3)==0);
449     sigma_p = sigma_p.*(gmask2==0);
450
451 %% >>>>> CALCULATING MATRICES
452     disp('calcuting matrices');
453     P  = zeros(size(mid.Mxp));
454     Pb = zeros(size(mid.xmesh{time}));
455
456     clear P2 mask_x4 mask_y4
```

```
457    Pbx = zeros(size(mid.xmask));
458    Pby = zeros(size(mid.xmask));
459    Pbz = zeros(size(mid.xmask));
460
461 % procedure 1: apply Dirichlet boundary condition on the numerical
        boundary
462 % procedure 2: apply mixed boundary in the local mesh
463 %% >>>>> PROCEDURE #1, CALCULATE PRESSURE ON GLOBAL MESH
464    disp('procedure 1: Aglobal1');
465    [Aglobal1,Alist1,flagy1,flagx1,flagz1,flagyw1,flagxw1,Xglobal1] =
           ...
466      PDMAglobal_neumann_neumann(dy,dx,dz,-gy2,-gx2,gz2,~gmask2);
467    Aglobal1 = single(Aglobal1);
468    A1D = diag(diag(Aglobal1)) ;
469    A1U = triu(-Aglobal1, 1)    ;
470    A1L = tril(-Aglobal1,-1)    ;
471    [p1o,p2o,p3o] = set_global_NeumannBC(-gx2,-gy2,gz2, ...
472         flagx1,flagy1,flagz1,px,py,pz,Alist1);
473         %=boundary condition on numerical boundary
474    [p1i,p2i,~] = set_global_NeumannBC(-gx2,-gy2,gz2, ...
475         flagxw1,flagyw1,flagz1,px,py,pz,Alist1);
476         %=boundary condition on wall
477    [~,~] = set_global_dirichletBC(-gx2,-gy2,flagxw1,flagyw1,P,Alist1);
478
479    S1 = A(Alist1) + 2/3*p1o/dx+2/3*p2o/dy+2*p3o/dz + 2/3*p1i/dx+2/3*
           p2i/dy;
480    w1 = 1;
481    count1 = 1;
482    gconv1(count1) = 100;
483    res0 = 0;
484    Ptemp = P(Alist1');
485    Ta1 = (A1D-w1*A1L)\((1-w1)*A1D+w1*A1U);
486    ca1 = w1*((A1D-w1*A1L)\S1');
487
488    while gconv1(count1) > gCONV(time) && count1 < nconv1
489      if ~mod(count1,100)
490        disp([num2str(count1) ' ' num2str(gconv1(count1))])
491      end
492      Ptemp = Ta1 * Ptemp + ca1;
493      count1 = count1 + 1;
494      res = sum(abs(Aglobal1*Ptemp - S1'));
495      gconv1(count1) = abs(res - res0);
496      res0 = res;
497
498      if count1 ==3
499        gCONV(time) = gCONV(time) .* gconv1(3);
500      end
501    end %=solution of pressure
502    P = flowRect_reorder(gmask2, Alist1, Ptemp, P);    Pg_temp1 = P;
```

```
503         % CHECK RESULT #1
504     P = get_pressure_global(-gy2,-gx2,py,px,dy,dx,P); Pg_temp2 = P;
505         % CHECK RESULT #2 % pressure AT INNER boundary
506
507
508 %% >>>>> Interpolate and specify Plocal (@outer BOUNDARY) from
        P_Global
509     for kk = 1:3
510       x6 = 0;     y6 = 0;     clear ai;
511       ai = find(MASK2 == 1);
512       xtemp = mid.xmesh{time}(:,:,1);
513       ytemp = mid.ymesh{time}(:,:,1);
514       x6(1:length(ai)) = xtemp(ai(1:length(ai)));
515       y6(1:length(ai)) = ytemp(ai(1:length(ai)));
516       Pb1 = griddata(mid.Myp(:,:,kk), mid.Mxp(:,:,kk), P(:,:,kk), y6,x6
            );
517       for i=1:length(ai)
518         [bi,bj] = find( ...
519               mid.xmesh{time}(:,:,kk) == x6(i) ...
520             & mid.ymesh{time}(:,:,kk) == y6(i));
521         Pb2(bi,bj,kk) = Pb1(i);
522       end
523     end
524     Pb3(:,:,1) = ( pzmesh(:,:,1)*2*dz + Pb(:,:,2)).*mid.mask{time
          }(:,:,1);
525     Pb3(:,:,3) = (-pzmesh(:,:,1)*2*dz + Pb(:,:,2)).*mid.mask{time
          }(:,:,3);
526
527
528 %% >>>>> PROCEDURE#2, CALCULATE PRESSURE ON LOCAL MESH
529     disp('decompose Alocal2');
530     [Alocal2  ,Alist2,flagy2,flagx2,flagz2,flagyw2,flagxw2,Xlocal2] =
          ...
531       PDMAlocal_neumann_dirichlet(dymesh,dxmesh,dzmesh, ...
532       mid.ymask{time},mid.xmask{time},mid.zmask{time},mid.mask{time});
533     Alocal2  = single(Alocal2);
534     A2D = diag(diag(Alocal2)) ;
535     A2U = triu(-Alocal2, 1)   ;
536     A2L = tril(-Alocal2,-1)   ;
537
538     [pbxd,pbyd,pbzd] = set_local_dirichletBC(flagx2,flagy2,flagz2, ...
539       mid.xmask{time},mid.ymask{time},mid.zmask{time},Pb2,Pb2,pzmesh,
            Alist2);
540     pbyn2 = set_local_neumannBC2(flagy2, mid.ymask{time}, pymesh,
          Alist2);
541     [pbxn,pbyn,pbzn] = set_local_neumannBC(flagxw2,flagyw2,flagz2, ...
542       mid.xmask{time},mid.ymask{time},mid.zmask{time},...
543       pxmesh0,pymesh0,pzmesh,Alist2);
544
```

```

%% >>>>> TEST the boundary condition
%                 index (convert column vector to matrix)
% >>>>>>>>>>>>>>>>>>>>>>>>>>>>>>>>>>>>>>>>>>>>>>>>>>>>>>>>>>>>>>>>>>>
  listx2  = flagx2 .*Alist2;
  listy2  = flagy2 .*Alist2;
  listz2  = flagz2 .*Alist2;
  listxw2 = flagxw2.*Alist2;
  listyw2 = flagyw2.*Alist2;
  [mm1,mm2,mm3] = size(mid.mask{1});

  [mm1,mm2,mm3] = size(mid.xmesh{1});
  p1xn = zeros(mm1,mm2,mm3);
  p2xn = zeros(mm1,mm2,mm3);
  p3xn = zeros(mm1,mm2,mm3);
  p1xd = zeros(mm1,mm2,mm3);
  p2xd = zeros(mm1,mm2,mm3);
  p3xd = zeros(mm1,mm2,mm3);
  p4xn = zeros(mm1,mm2,mm3);

  for mmi=1:mm1
    for mmj=1:mm2
      for mmk=1:mm3
        idx = (mmk-1)*(mm1*mm2) + (mmj-1)*mm1 + mmi;
        idx1 = find(listxw2 == idx);
          if ~isempty(idx1); p1xn(mmi,mmj,mmk) = pbxn(idx1); end
        idx2 = find(listyw2 == idx);
          if ~isempty(idx2); p2xn(mmi,mmj,mmk) = pbyn(idx2); end
        idx3 = find(listz2 == idx);
          if ~isempty(idx3); p3xn(mmi,mmj,mmk) = pbzn(idx3); end
        idx4 = find(listx2 == idx);
          if ~isempty(idx4); p1xd(mmi,mmj,mmk) = pbxd(idx4); end
        idx5 = find(listy2 == idx);
          if ~isempty(idx5); p2xd(mmi,mmj,mmk) = pbyd(idx5); end
        idx6 = find(listz2 == idx);
          if ~isempty(idx6); p3xd(mmi,mmj,mmk) = pbzd(idx6); end
        idx7 = find(listy2 == idx);
          if ~isempty(idx7); p4xn(mmi,mmj,mmk) = pbyn2(idx7); end
      end
    end
  end
  p1xn1 = p1xn(:,:,1); %pbxn &
  p2xn1 = p2xn(:,:,1); %pbyn &
  p3xn1 = p3xn(:,:,1); %pbzn &

  p1xd1 = p1xd(:,:,1); %pbxd &
  p2xd1 = p2xd(:,:,1); %pbyd &
  p3xd1 = p3xd(:,:,1); %pbzd

```

```
594    p4xn1 = p4xn(:,:,1); %pbyn2 &
595
596    count2 = 1;  gconv2(count2) = 100;  res0 = 0;
597    w2 = 1;  Pbtemp = Pb(Alist2');
598    S2 = bA(Alist2) ...
599      + pbxd/dxmesh/dxmesh
600      + pbyd/dymesh/dymesh
601      + 2/3*pbyn2/dymesh ...  %=gradients on numerical boundary
602      + pbxn/dxmesh
603      + pbyn/dymesh
604      + 2*pbzn/dzmesh; %=gradients on the wall
605      %% pbzd is ignored because forward and backward difference
           scheme was
606      %% set on the coefficient matrix Alocal2.
607    Ta2 = (A2D-w2*A2L)\((1-w2)*A2D+w2*A2U);
608    ca2 = w2*((A2D-w2*A2L)\S2');
609
610    while gconv2(count2)>lCONV(time) && count2 < nconv2
611      if ~mod(count2,100)
612        disp([num2str(count2) ' ' num2str(gconv2(count2))])
613      end
614      Pbtemp = Ta2*Pbtemp + ca2;
615      count2 = count2 + 1;
616      res = sum(abs(Alocal2*Pbtemp - S2'));
617      gconv2(count2) = abs(res0 - res);
618      res0 = res;
619      if count2 ==3
620        lCONV(time) = lCONV(time) .* gconv2(3);
621      end
622    end
623
624    Pb = bodyRect_reorder(mid.mask{time},Pbtemp,Alist2,Pb2,Pb2,Pb,
         cutoff_1);
625    Pl_temp1 = Pb;
626    Pl_temp2 = Pb;
627    Pb = get_pressureLocal_outer(mid.xmask{time},mid.ymask{time},...
628      dxmesh,dymesh,pxmesh,pymesh,Pb);
629    Pl_temp3 = Pb;
630
631 % force component normal to wing's surface AND torque
632 % in the direction of the rotation
633    Pn_plus=15/8*Pb(9,1:13,1:3)+(-5/4)*Pb(8,1:13,1:3)+(3/8)*Pb
         (7,1:13,1:3);
634    Pn_minus=15/8*Pb(12,1:13,1:3)+(-5/4)*Pb(13,1:13,1:3)+(3/8)*Pb
         (14,1:13,1:3);
635    dP = Pn_plus - Pn_minus;
636    for kk=1:3
637      Fn.val(kk) = sum( dP(:,:,kk).*dymesh*dzmesh );
```

```
638     Tz.val(kk) = sum( dP(:,:,kk).*(40 + [-12.5:1:-0.5])*dymesh*dzmesh
            );
639   end
640   Fn.note = 'not normalized';
641   Tz.note = 'not normalized';
642
643   save(['pressure flapping3d ' releaseVer '_' num2str(2000+time) '.
          mat'])
644   clear Pb1 mask* temp plate_on_rect Aglobal1 Alocal2 Aglobal3
645   clear A1D A1L A1U A1LU   A2D A2L A2U A2LU   A3D A3L A3U A3LU
646   clear gconv*
647 end
648
649 beep
```